# Functional Applications of $Al{\cdot}Al_2O_3$ Nanowires: Laser Assisted $\alpha$-$Al_2O_3$ Synthesis and Fabrication of Micro-/Nanostructured Surfaces for Cell Compatibility Studies

**Dissertation**

**zur Erlangung des Grades des Doktors der Ingenieurwissenschaften**
**der Naturwissenschaftlich-Technischen Fakultät III**
**Chemie, Pharmazie, Bio- und Werkstoffwissenschaften**
**der Universität des Saarlandes**

von

**Oral Cenk Aktaş**

**Saarbrücken, Germany**
**2009**

**Tag des Kolloquiums:** 30.03.2009

| | |
|---|---|
| **Dekan:** | Prof. Dr. U. Müller |
| **Vorsitzender:** | Prof. Dr. U. Kazmaier |
| **Berichterstatter:** | Prof. Dr. M. Veith<br>Prof. Dr. W. Possart<br>Prof. Dr. F. Faupel |
| **Akad. Mitarbeiter:** | Dr. Ing. A. Barnoush |

# Abstract

Recently, one-dimensional (1D) nanostructures have attracted considerable interest of nanoscience studies as well as nanotechnology applications. Especially 1D hetero-structural nanowires with a combination of two different materials, for instance metal/metal oxide composites, hold a great potential for various photonic and electronic applications. Thus, $Al{\cdot}Al_2O_3$ core-shell nanowires, which were firstly reported by Veith et al., form an interesting class of such hetero-nanostructures.

This thesis describes the preparation of functional surfaces composed of 1D nanostructures by CVD of a $(^t BuOAlH_2)_2$ [bis(*t*ert-butoxyaluminum dihydride)] precursor and laser treatment of such structures. Firstly, main attention is given to understand the underlying mechanisms controlling the 1D growth of $Al{\cdot}Al_2O_3$ nanostructures. By applying systematically different deposition temperatures and flow rates, various nanostructures were synthesized. At high deposition temperatures chaotic $Al{\cdot}Al_2O_3$ nanowires form, whereas at low deposition temperatures worm- and loop-like nanostructures are achieved. A new mask-less local deposition method, named selective CVD (SCVD), is introduced by selective heating of the substrate with electro magnetic induction. A controlled thermal gradient leads to the observation of stepwise 1D growth of nanostructures. As a continuation the of the local deposition approach, an LCVD system has been designed and fabricated to show the possibility to grow 1D complex structures.

$\alpha$-$Al_2O_3$ layers were synthesized by laser induced heating of deposited $Al{\cdot}Al_2O_3$ nanowires. In particular, two laser processing approaches were investigated: continuous wave (CW) laser and pulsed laser treatments. CW laser treatment is useful to produce dense and fully crystalline $\alpha$-$Al_2O_3$ layers which may be employed as hard and protective coatings. Pulsed laser treatment produces a large variety of nanostructures (nanopores, nanoprotrusions, nanospheres etc.) of $Al_2O_3$ which is interesting for studying cell-surface interactions.

Micro-/nanostructured surfaces prepared by direct deposition of $(^t BuOAlH_2)_2$ and laser treatment were tested for biocompatibility. Jurkat cells seem to adhere selectively on $Al{\cdot}Al_2O_3$ nanowires which may lead to applications in cancer diagnosis and therapy. Laser treated $Al{\cdot}Al_2O_3$ layers exhibit a better biocompatibility for normal human dermal fibroblast (NHDF) cells. In addition, a preliminary study on neurons showed that $Al{\cdot}Al_2O_3$ nanowires provide enhanced cellular adhesion and growth which can be interesting for various applications in medical fields as well as in biosciences.

# Kurzfassung

In jüngster Zeit konnten eindimensionale (1D) Nanostrukturen beträchtliches Interesse sowohl der Nanowissenschaften als auch der Anwender der Nanotechnologie auf sich ziehen. Insbesondere 1D heterostrukturelle Nanodrähte, kombiniert aus zwei unterschiedlichen Materialien, beispielsweise Metall-Metalloxid-Zusammensetzungen, verfügen über bedeutendes Potential für verschiedenste photonische und elektronische Anwendungen. So bilden die zuerst von Veith et al. beschriebenen $Al{\cdot}Al_2O_3$-Kern-Hülle-Nanodrähte eine Klasse dieser Hetero-Nanostrukturen.

Diese Dissertation behandelt die Herstellung funktionaler 1D-Oberflächen mittels Chemical Vapor Deposition (CVD) mit einem $(^tBuOAlH_2)_2$-Präkursor und anschließender Laser-Prozessierung. Zunächst gilt das Hauptinteresse dem Verständnis des zugrundeliegenden Mechanismus, der das Wachstum der $Al{\cdot}Al_2O_3$-Nanostrukturen beeinflusst. Durch systematische Verwendung unterschiedlicher Depositionstemperaturen und Präkursorflussraten werden verschiedene Nanostrukturen synthetisiert. Bei hohen Temperaturen bilden sich chaotische, unregelmäßige $Al{\cdot}Al_2O_3$-Nanodrähte, während bei niedrigen Temperaturen wurm- und schleifenartige Nanostrukturen erhalten werden. Als eine neue Depositionsmethode, ohne Verwendung einer Maske und durch selektives Erhitzen des Substrats mittels elektromagnetischer Induktion, wird das sogenannte selektive CVD-System (SCVD) eingeführt. Ein kontrollierter Temperaturgradient führt zu der Beobachtung des schrittweisen eindimensionalen Wachstums von Nanostrukturen. Desweiteren wird als Fortsetzung des lokalen Depositionsverfahrens ein Laser-CVD-Verfahren erarbeitet und entwickelt, um die Möglichkeit des Erzeugens komplexer 1D-Strukturen aufzuzeigen.

$\alpha$-$Al_2O_3$-Beschichtungen werden mittels laserinduzierter Erhitzung der $Al{\cdot}Al_2O_3$-Nanodrähte synthetisiert. Im Einzelnen kommen zwei Laser-Prozessierungsverfahren zur Anwendung: Continuous-wave(CW)-laser-Behandlung und die Prozessierung mittels gepulstem Laser. Die CW-Laser-Behandlung ist anwendbar für die Herstellung dichter und vollständig kristalliner $\alpha$-$Al_2O_3$-Kompositschichten, die als harte, schützende Beschichtungen Verwendung finden können. Die Behandlung mit einem gepulsten Laser hingegen erzeugt eine große Bandbreite von Nanostrukturen (nanopores, nanoprotrusions, nanospheres etc.) aus $Al_2O_3$, die dem Studium von Zell-Oberflächen-Interaktionen dienen können.

Durch direkte $(^tBuOAlH_2)_2$-Deposition und anschließende Laserbehandlung erzeugte mikro- beziehungsweise nanostrukturierte Oberflächen werden auf ihre Biokompatibilität hin untersucht. Jurkat-Zellen adhärieren selektiv an $Al{\cdot}Al_2O_3$-Nanodrähten, was zu der Verwendung

dieser Strukturen in der Diagnose und Therapie von Karzinomerkrankungen führen kann. Laserbehandelte $Al{\cdot}Al_2O_3$-Schichten zeigen eine gute Biokompatibilität für normale Fibroblasten der menschlichen Dermis (normal human dermal fibroblasts, NHDF). Desweiteren zeigen erste Untersuchungen an Neuronen (Nervenzellen), dass $Al{\cdot}Al_2O_3$-Nanodrähte zu gesteigerter Adhäsion und vermehrtem Wachstum dieser Zellen führen, was für verschiedene Anwendungen sowohl im medizinischen Bereich als auch in den Biowissenschaften von Interesse ist.

# Acknowledgements

I desire to take the opportunity to record my deep sense of gratitude to my supervisor **Prof. Dr. Michael Veith** for giving me the chance to join his research group. He offered me an ideal scientific atmosphere and helped me a lot to gain knowledge and ability in different fields. In passing years, I learned a lot from him and his enthusiasm has been most inspiring to me throughout my research career. I am very grateful for his keen and continuous interest and believe in my work right from the rudimentary stages and his endless encouragement throughout. I must thank him very much for giving time (even on holiday) for the precise and detailed correction of my manuscript without missing a single comma.

I would also like to express my thanks to **Prof. Dr. Wulf Possart** (Chair for Adhesion and Interphases in Polymers, Saarland University, Saarbrücken) for his willingness to be my second examiner and for giving his precious time to referee this work. I appreciated his valuable advices in the preparation of the manuscript.

I have to mention my indebtedness to **Prof. Dr. Franz Faupel** (Chair for Multicomponent Materials, Christian-Albrechts-University, Kiel), for all moral encouragements and contributions at various stages of my academic life. Discussions with him and his group members have been a crucial step for a deeper understanding of different aspects of this thesis.

**Dr. Abhijit Biswas** (Department of Physics and Astronomy, The University of Oklahoma) was the second supervisor of my master thesis. I must thank him for his discussions and advices. He is also gratefully acknowledged for accepting the correction of my manuscript during his tough time.

This PhD thesis is an end-product of the cooperation with various groups. I would like to sincerely acknowledge some institutions who contributed a lot to my work:

**Dr. Frank Narz** (Qiagen Corporate Research, Hilden) for his collaboration concerning the investigation of cell responses on nanostructured surfaces prepared by CVD,

**Dr. Wolfgang Metzger, Dr. Martin Oberringer, Prof. Dr. Tim Pohlemann** (Clinic of Trauma, Hand and Reconstructive Surgery, Saarland University, Homburg) for their collaborations to study fibroblast cell-surface interactions on different surfaces and their interesting suggestions,

**Prof. Dr. Gunther Wennemuth** (Department of Anatomy and Cell Biology, Saarland University, Homburg) for his fantastic SEM images showing cell-surface interactions,

**Prof. Karl-Herbert Schäfer and Dr. Ulrich Rauch** (Department of Biotechnology, University of Applied Sciences, Zweibrücken) for giving a new direction to my work in the field of neuroscience,

**Dr. Afrooz Barnoush and Prof. Dr. Horst Vehoff**, (Department of Materials Science, Saarland University, Saarbrücken) for nanomechanical characterisation of laser treated layers.

I would also like to thank my colleagues (**INM)** and especially people who helped me a lot in non-result coming and tough days: Dr. Ingrid Grobelsek, Dr. Herbert Schmid, Dr. Marcus Koch and Mrs. Aude Haettich for giving time to characterize my samples; Dr. Hao Shen for his helps in XPS analysis and suggestions; Dipl. Chem. Benny Siegert for his assistance in some part of my work; Dr. Peter Olivera for introducing the "laser world" to me; Dr. Marcus Geerkens for his helps for the application of the patent covering the results of this thesis work; Dipl. Ing. Dietmar Serwas, Herbert Beerman, Uwe Magar, Michael Schneider and Werner Schneider for their technical helps for the preparation of new deposition systems, Elke Galli and Melanie Groh for their continuous supports and kind understandings for longer-term book lending; Dr. Stefan Gerbes and Margit Müller for their collaborations during the CellPROM project; Mr. Wolfgang Türk and the EDV group for their helps to solve my computer problems.

Some experimental part of this work was carried out at the Institute for Inorganic Chemistry, Saarland University. I would also like to express my thanks to all of Prof. Veith`s group members. Special acknowledgments should be addressed to; Lab. 350 co-workers (Dr. Nils Köhler, David Kolano, Tatjana Kirs and Hameed Ullah) for the nice working atmosphere; Dr. Volker Huch for XRD analysis and discussions; Günther Berlin, Hermann Recktenwald and Sylvia Beetz for technical helps for my crazy ideas.

Of course, this long time was not full of experiments, graphs, and tables only. Some people encouraged me a lot. Without them this thesis could not have been finished. Dr. Sener Albayrak, with whom I shared the office for most of the time, has always had an open ear for experimental and other problems. I am thankful for fruitful discussions and making me feel at home with our long talks in Turkish lasting also in lunch breaks. Similarly, Dr. Mesut Aslan helped me to overcome the home-sickness that appeared in some instances.

And I can not forget the continuous support of my friends Kaan, Erdem, Tankut and their families who never let me walk this long way alone.

Last but not least, I have to thank my family for their great support during the time of my university education and for their understanding for the little time I was able to spend with them during the past years.

Finally, special thanks go to my girlfriend Jasmin who always believed in me and helped a lot in every condition. From her I learned new vowels different from "I" for the passing two long years. I will not forget how we got out of such tough days together.

# Contents

# Symbols and Abbreviations

**List of Symbols**

| | |
|---|---|
| $\alpha$ | optical absorption coefficient |
| $\alpha^L$ | linear expansion coefficient |
| A | area |
| $c_p$ | specific heat at constant pressure |
| $\Delta$ | interference |
| E | Young's modulus |
| $E_A$ | activation energy |
| G | shear modulus |
| $\Delta H$ | enthalpy |
| $\Delta T$ | change in temperature after laser heating |
| $I_a$ | absorbed laser intensity |
| $I_{(0)}$ | maximum irradiance |
| l | length |
| $\kappa$ | thermal conductivity |
| $\lambda$ | wavelength |
| n | molar amount |
| $\Phi$ | laser fluence |
| P | power |
| $P_I$ | contact pressure |
| $P_T$ | total power over an area |
| Q | power density |
| $\rho$ | density |
| $r^*$ | normalized radius |
| r, R | radius |
| $R_a$ | surface roughness |
| $R_I$ | interface radius |
| $R_s$ | reflection of the substrate |
| $\sigma_r$ | radial stress |

| | |
|---|---|
| $\sigma_t$ | hoop stress |
| $\tau_{max}$ | maximum shear stress |
| $\tau_{th}$ | theoretical shear stress |
| $t_i$ | time of irradiance |
| T | temperature |
| $T_o$ | initial temperature |
| $T_m$ | melting point |
| $T_{max}$ | maximum temperature rise |
| V | volume |
| $\nu$ | Poisson's ratio |
| $v_s$ | scanning speed |
| $w_o$ | Gaussian half-width of the laser beam |
| $z_{\tau(max)}$ | position of the maximum shear stress |

**List of Abbreviations**

| | |
|---|---|
| 1D | one dimensional |
| AIP | aluminum isopropoxide |
| APTS | aminopropyl-triethoxy silane |
| BCA | bicinchoinic assay |
| CMC | ceramic matrix composites |
| CMOS | complementary metal oxide semiconductor |
| CNT | carbon nano-tubes |
| CVD | chemical vapor deposition |
| CW | continuous wave |
| DOS | densities of state |
| DRG | dorsal root ganglia |
| EBL | electron beam lithography |
| ECM | extra cellular matrix |
| EDX | energy dispersive X-ray spectroscopy |
| EL | electroluminescence |

| | |
|---|---|
| ESEM | environmental scanning electron microscope |
| EUV | extreme-ultraviolet |
| FET | field effect transistor |
| FIB | focused ion beam |
| FT-IR | Fourier-transform infrared spectroscopy |
| FWHM | full width at half maximum |
| HAZ | heat affected zone |
| HF | high frequency |
| HR-TEM | high resolution transmission electron microscopy |
| IR | infrared |
| JCPDS | joint committee on powder diffraction standards |
| LASER | light amplification by stimulated emission of radiation |
| LCVD | laser assisted chemical vapor deposition |
| LIGA | Lithographie, Galvanoformung, Abformung |
| MEMS | micro-electromechanical systems |
| MMC | metal matrix composites |
| MOCVD | metal-organic chemical vapor deposition |
| Nd:YAG laser | neodymium-doped yttrium aluminum garnet laser |
| NHDF | normal human dermal fibroblast |
| NIR | near-infrared |
| NWFET | nanowire field effect transistor |
| OAG | oxide catalyst growth |
| PAA | porous anodic alumina |
| PACVD | plasma assisted chemical vapor deposition |
| PBS | phosphate buffered saline |
| PDF | powder diffraction file |
| PECVD | plasma enhanced chemical vapor deposition |
| PEPVD | plasma enhanced physical vapor deposition |
| PL | photoluminescence |
| PMC | polymer matrix composites |
| PU | polyurethane |

| | |
|---|---|
| PVD | physical vapor deposition |
| SAED | selected area electron diffraction |
| SCVD | selective chemical vapor deposition |
| SEM | scanning electron microscopy |
| SHG | second harmonic generation |
| SL | stencil lithography |
| SPMS | single particle mass spectrometry |
| SPR | surface plasmon resonance |
| TEM | transmission electron microscopy |
| THG | third harmonic generation |
| UV | ultraviolet |
| VIS | visible |
| VLS | vapor-liquid-solid |
| VS | vapor-solid |
| XPS | X-ray photoelectron spectroscopy |

# 1. Introduction

One-dimensional (1D) nanostructures such as nanowires, nanobelts and nanotubes have enormously attracted the attention of nanoscience as well as nanotechnology applications due to their highly anisotropic geometry and size confinements. Several research groups have reported various synthetic routes to fabricate carbon nanotubes (CNTs), semiconductor, metal and metal oxide nanowires. Especially 1D metal oxide nanostructures are used in different applications, such as piezoelectricity, chemical sensing and photo-detection, due to their unique properties and functionalities [1]. In particular, metal oxide nanowires are the ideal structures to understand the fundamental 1D electronic and transport properties of oxides and their relation to the surface chemistry of the nanowire [2].

In recent years, 1D metal/metal oxide or semiconductor/metal oxide hetero-structures, such as co-axial core-shell, super lattice and composite nanowires, began to attract significant attention. Such hetero-structures exhibit superior or new functional properties compared to their individual constituent materials. 1D heterostructures with a well defined core/shell structure hold a great potential for photonic and electronic applications, such as scanning probes, field emission tips, resonant tunneling devices, nanobarcodes, injection lasers and thermoelectrics [3]. Co-axial nanocable of SiC core and carbon shell [4], side-by-side silica-SiC nanowires [5], metal silver nanowires sheathed with silica [6], tape structured nanobelts of $SnO_2$ and $TiO_2$ [7], core-shell structured Si-Ge nanowires [8] and ZnO-$In_2O_3$ core-shell nanostructures [9] have been synthesized.

This PhD thesis presents the synthesis of 1D Al·$Al_2O_3$ hetero-structures and their preparation for functional applications. Earlier studies showed that the Al·$Al_2O_3$ system is known to form highly chaotic 1D nanostructures. In this context, the investigation of experimental factors that govern the growth of such structures and the development of controlled deposition strategies for future applications are the main interests of this work. As an example of applications, laser treatment of deposited 1D Al·$Al_2O_3$, showing the possibility to fabricate α-alumina layers, is discussed. In addition to the α-alumina synthesis, laser treatment of deposited layers leads to exotic nano-/microstructured alumina surfaces which attract the attention of cell-surface interaction studies. The use of

laser treated $Al{\cdot}Al_2O_3$ layers as bio-compatible surfaces is also discussed. The behaviors of cells on as-deposited and laser treated layers are compared.

The first two chapters give a brief introduction of this work. In **Chapter 2** different methods used so far to synthesize 1D nanostructures are reviewed and basic properties of such structures are explained. Among other physical and chemical approaches, the main attention is given to gas phase synthesis methods. After giving a concise background about gas phase synthesis methods of 1D nanostructures, earlier studies on 1D $Al_2O_3$ and Al structures are reviewed.

**Chapter 3** presents the synthesis of 1D $Al{\cdot}Al_2O_3$ nanostructures by CVD of the molecular precursor $(^tBuOAlH_2)_2$. Prior to experimental details, previous studies on CVD of $(^tBuOAlH_2)_2$ are reviewed and different approaches are discussed. Afterwards, deposition techniques followed in this thesis are explained. Thermal CVD, selective CVD (SCVD) and laser assisted CVD (LCVD) methods are introduced. In the thermal CVD approach the effect of the flow rate, deposition temperature and period on the deposit morphology is studied in detail. This systematic study covers the synthesis of various 1D structures including nanowires, nanorods, nanoloops etc. by applying different temperatures and other process parameters. In addition, this chapter presents the use of SCVD to induce a controlled temperature gradient on the substrate surface in order to understand the effect of the temperature on the growth mechanism of 1D nanostructures. An LCVD apparatus has been developed during this thesis work to locally deposit nanostructures. The use of this specially designed LCVD apparatus to deposit nanofibrous structures is also discussed.

**In Chapter 4** the laser treatment of deposited layers is presented. Firstly, basics of the laser-material interaction and laser assisted material processing are explained briefly. After that a detailed review of earlier studies on laser processing of alumina ceramics is provided. Additionally, the formation of alumina polymorphs and especially the synthesis of α-alumina are discussed in detail. In the experimental part two different laser processing approaches are described. Firstly, a systematic study on continuous wave (CW) laser treatment of $Al{\cdot}Al_2O_3$ nanostructures is presented. The main attention of CW laser processing is the synthesis of α-alumina by local heating of $Al{\cdot}Al_2O_3$ layers. The effect of laser induced heating on the morphology, surface and mechanical

properties of $Al{\cdot}Al_2O_3$ layers is also presented in depth. As a second approach, pulsed laser treatment of the deposited layers is presented. The main aim of the pulsed laser treatment is to fabricate nano/micro structures by applying different laser fluences and numbers of pulses. Such structures are interesting for studying cell-surface interactions due to their combination of nano and micro topographic features.

**Chapter 5** presents a detailed study covering the cell interactions on various nano-/microstructured surfaces prepared by CVD and laser treatment. Before the experimental work, basics of cell-surface interaction and particularly cell responses on alumina surfaces are introduced. In the experimental part biocompatibility and responses of different cell types on fabricated surfaces are discussed. The results of this experimental work highlight the selective adhesion of Jurkat cells on $Al{\cdot}Al_2O_3$ nanowires and improvement of NHDF (normal human dermal fibroblast cells) cell adhesion on laser treated surfaces. As a future aspect, preliminary results of enhanced neuron cell growth on $Al{\cdot}Al_2O_3$ nanowires is also presented.

**Chapter 6** summarizes the main results of this work, draws the conclusion and provides an outlook for future research interests.

# 2. One Dimensional (1D) Nanostructures

## 2.1 Introduction

After the discovery of carbon nanotubes (CNTs) by Iijima [10], there has been a great interest in the synthesis and characterization of other one-dimensional (1D) structures. Especially, 1D nanostructures are attractive for fundamental nanoscience studies as well as nanotechnology applications due to their unique geometry and possible quantum confinement effects [11].

It is generally accepted that a 1D nanostructure provides a good system to investigate the dependence of the electrical and thermal transport or mechanical properties on dimensionality [12]. While it is difficult to obtain an accurate control of fabrication parameters, 1D nanostructures are ideal systems to study transport phenomena at a nanometer scale compared to 0D and 2D systems. Besides their importance for studying the basic physical and chemical properties, 1D nanostructures attract the attention of technological applications including the electronic interconnect units [13], solar cells [14], photonics [15], thermoelectric [16], electromechanical [17] and fluidic nanoscaled devices [18] and magnetic data storage [19].

1D nanostructures consist of a wide variety of morphologies, such as nanowires, nanorods, nanofibers, nanotubes and nanobelts. Nanotubes are the first discovered 1D nanomaterials and especially the CNT is the most commonly known type of such nanotube structures. A nanotube is a tubular and hollow 1D nanostructure with a diameter below 100 nm, while the length may be as long as a few micrometers to millimeters. Nanowires and nanorods form another category of 1D nanostructures which differ from the nanotubes in terms of their filled solid tubular structures. The cross-section of a nanowire is negligibly small compared to its extremely long length. In contrast, the cross-section and the length of the nanorods are within an order of magnitude of each other. The nanobelt represents a quasi-one-dimensional nanostructure which does not only have a specific growth direction. Furthermore its top/bottom surfaces and side surfaces exhibit well-defined crystallographic facets.

Although 1D nanostructures may be fabricated using various advanced nanolithography and other physical patterning techniques, chemical methods have been

shown to be more versatile and effective in the synthesis of large quantities of 1D nanostructures [20]. Thus, chemical methods including the precursor decomposition, solvothermal, hydrothermal and carbothermal reactions as well as chemical vapor deposition (CVD) have been widely employed to synthesize 1D nanostructures of different materials. CVD methods have been used successfully in fabrication of fibers, filaments, nanotubes and nanowires of various materials for more than 20 years. CVD has a number of advantages as a method for depositing thin films [21]. One of the primary advantages is that CVD films are generally quite conformal, which is critical for coating the complex-shaped objects. Another advantage of CVD is that the wide variety of materials can be deposited with a precise thickness control. In comparison to physical vapor deposition (PVD) techniques, CVD methods do not need high vacuum conditions and provide much higher deposition rates [22].

## 2.2 Gas Phase Synthesis of 1D Nanostructures

### 2.2.1 Vapor-Liquid-Solid (VLS) Growth Process

The VLS process is one of the intensively used vapor phase growth methods to fabricate various 1D nanostructures including nanotubes, nanowires and nanorods. The VLS growth mechanism was developed by Ellis and Wagner in the late 1960s [23]. A typical VLS process is illustrated schematically in Figure 2.1. The substrate material contains some catalyst particles prior to the gas phase deposition. Upon heating the substrate, the catalyst seeds transform into the liquid droplets which act as preferred deposition sites for the gaseous reactants. The gaseous reactants dissolve into the droplets of the molten catalyst material and the absorption of the source vapor by the catalysts forms an alloy (in the ideal case a eutectic alloy). While the alloy becomes supersaturated, the source materials will precipitate out of the droplet and start forming 1D growth. The growth will continue with further precipitation until all the source vapor has vanished.

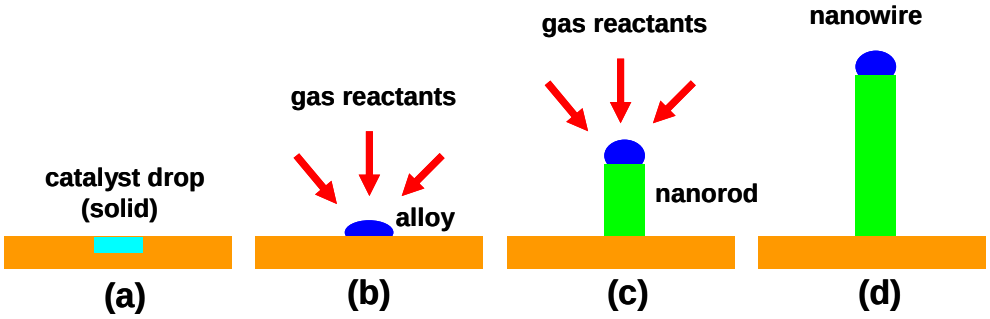


**Figure 2.1 Schematic illustration of the 1D growth steps in a typical VLS process.**

The VLS mechanism is used for the fabrication of nanowires of different materials, especially Ge and Si. The work of Wu and Yang on the growth of Ge nanowires [24] is one of the most cited works in the field of VLS research. They used an in-situ TEM characterization technique to observe the growth stages of Ge nanowires in the presence of Au catalyst particles. Three different stages in the nanowire growth were reported by them: alloying, nucleation and directional growth. The real time images of such a growth can be seen in Figure 2.2.

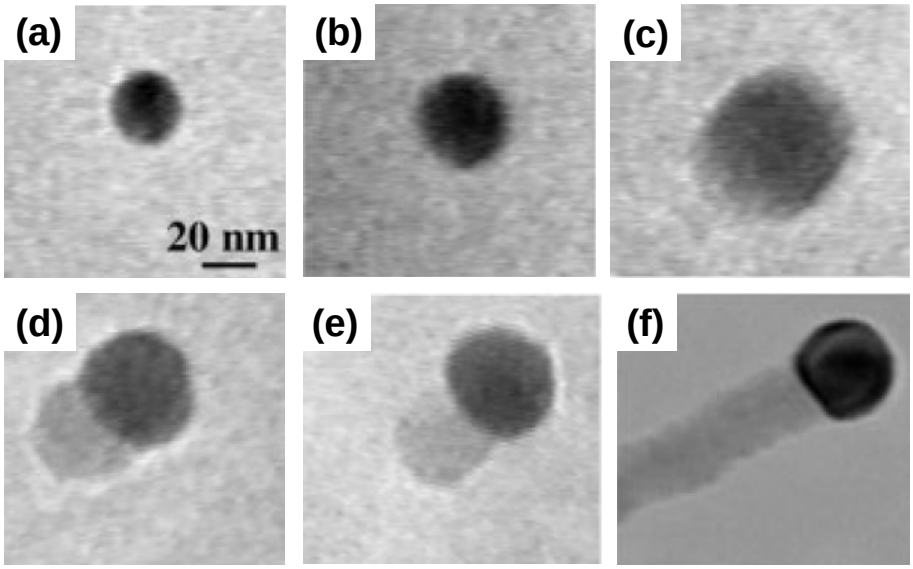


**Figure 2.2 Illustration of the growth stages of a Ge nanowire on an Au nanoparticle using an in-situ TEM analysis [24]. (a) Au nanoparticle in solid state. (b) Formation of Ge-Au alloy. (c) Increase in the liquid droplet size during the condensation of Ge vapor. (d) Nucleation of first Ge nanostructures. (e) Growth of a Ge nanorod pushing the liquid-solid interface. (f) Further growth of the Ge nanowire.**

At the beginning of the growth process an Au nanoparticle is in the solid state, as it is shown in Figure 2.2a. Following the condensation of the Ge vapor, a Ge-Au binary alloy forms (Figure 2.2b). After the condensation of more Ge vapor, a eutectic point appears in the Ge-Au alloy system and this is followed by the formation of a liquid droplet of the corresponding alloy, as shown in Figure 2.2c. When the Ge concentration exceeds a critical value (supersaturation), the nucleation of the first Ge nanocrystals starts (Figure 2.2d) and more Ge vapor condensates at the solid/liquid interface. As seen in Figure 2.2e, following the further condensation, the interface is pushed forward and a nanorod grows. The continuous growth ends up with a Ge nanowire having an Au cap at the end, as shown in Figure 2.2f.

Besides the synthesis of Ge nanowires, the VLS approach was also applied successfully to fabricate Si nanowires. Lieber et al. showed the synthesis of Si nanowires of 10-50 nm in diameter using Au as catalyst and $SiH_4$ as Si source [25]. It is also possible to use other catalyst materials instead of Au. Liu et al. and Williams et al. for example used Au-Pd and Ti particles as catalysts respectively, to synthesize Si nanowires [26, 27]. Recently, the VLS growth process has been used to synthesize various 1D semiconductors including; GaN [28], GaS [29], InAs [30] and oxides including ZnO [31] and $SiO_2$ [32].

### 2.2.2 Vapor-Solid (VS) Growth Process

In the VS growth process 1D structures form directly after the condensation of the vapor without the need of any liquid phase in comparison to the VLS growth process. Therefore the process can be thought as a self catalytic approach. In spite of the fact that the first use of the VS process goes beyond the 1970s [33], the mechanism is not completely understood yet. After the generation of gaseous reactants by physical or chemical methods, the vapor is transported and condensed on the substrate which is kept at a lower temperature. The method is also known in the literature as "*direct vapor phase deposition*".

Using the VS process, various 1D nanostructured oxide materials, such as ZnO [34], $SnO_2$, $In_2O_3$ [35], CdO [36] and $Ga_2O_3$ [37], have been synthesized without applying any external catalyst. In addition to oxides, nanowires of non-oxide materials, such as $Si_3N_4$

[38] and SiC [39], were also synthesized by applying this direct-vapor deposition process. Dai et al. [40] and Wang et al. [41] proposed a model describing the VS growth process for the synthesis of ZnO nanobelts. Their proposed model is illustrated schematically in Figure 2.3. Firstly, the source materials is vaporized into molecular species at high temperature and transported to the substrate by a carrier gas. The vapor is condensed onto the substrate which is at a lower temperature (Figure 2.3a).

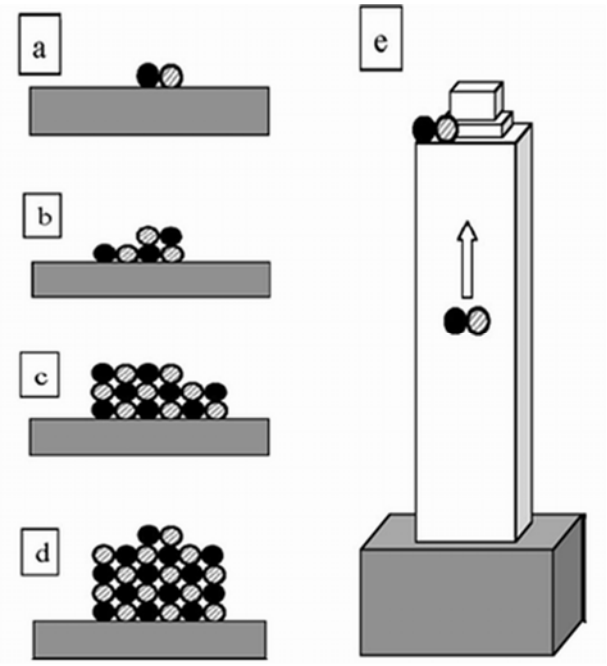


**Figure 2.3 Growth mechanism of a ZnO nanobelt [40 and 41]. (a) Condensation of the vapor on the substrate. (b) Molecular arrangement to preserve cation-anion coordination. (c) Preferential growth on former nucleus. (d) Expanding of side surface due to sticking of more molecules on the growth front. (e) Formation of a long nanobelt.**

During the condensation the cation and anion molecules arrange themselves in such a way to balance the local charge and structural symmetry. This coordination leads to the formation of a small nucleus (Figure 2.3b). Arriving molecules continue to deposit on this freshly formed nucleus (Figure 2.3c). At high temperatures, more molecules stick on the rough growth front rather than accumulating onto the side surfaces (Figure 2.3d). The rough structure of the tip leads to a rapid accumulation of incoming molecules, resulting in the fast formation of a nanobelt (Figure 2.3e). The newly arriving molecules randomly diffuse on the surface and finally they find the lower-energy sites at the

growth front. They do not stick to the edge of the nanobelts because of the unbalanced coordination and possibly higher energy.

### 2.2.3 Carbothermal Synthesis Processes

Various carbothermal reactions were applied successfully in the vapor phase synthesis of 1D nanostructures. Such approaches are based on a chemical reaction of the sub-oxide vapors with the other reactive chemical species. The chemical reaction of a typical carbothermal process is shown schematically in Figure 2.4. In the first step a mixture of carbon and metal oxide is prepared. After that the mixture is heated up to generate the sub-oxides. In the last step the sub-oxides are reacted with the carbon, oxygen or nitrogen to fabricate 1D carbides, oxides or nitrides, respectively.

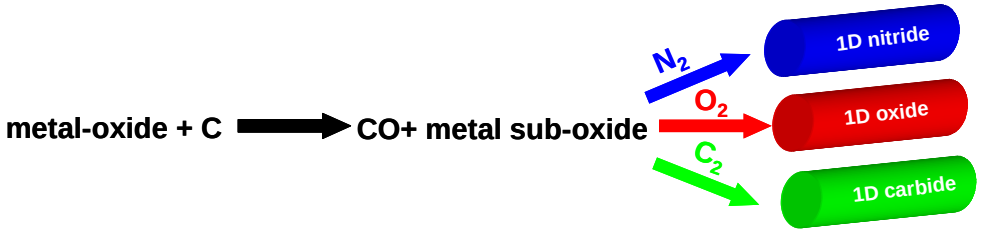


**Figure 2.4 Carbothermal growth process of 1D nitrides, carbides and oxides.**

In the literature there are plenty of examples using the carbothermal reactions to synthesize various types of 1D ZnO nanostructures, such as nanowires, nanobelts or nanosheets [42 and 43]. In most of these presented works firstly a mixture of C(s) and ZnO(s) is prepared. Afterwards this mixture is heated up in the presence of a carrier gas mixed with $O_2$ to generate the sub-oxide vapor. 1D ZnO nanostructures form after the condensation of the sub-oxide vapor on the substrate which is kept at relatively lower temperatures.

Carbothermal chemical reactions can be modified easily by altering the stoichiometry and process conditions. Carbothermal processes were also used to synthesize crystalline nanowires of other oxides; $SiO_2$ [44], $Al_2O_3$ [45], $Ga_2O_3$ [46] and $In_2O_3$ [47], nitrides; $Si_3N_4$ [48], AlN [49], BN [50] and GaN [51], and carbides; SiC [52], as well as elemental Si [53] and Se [54].

### 2.2.4 Oxide Catalyst Growth (OAG) Process

Alternatively to the metal catalyst supported VLS process, Lee and his co-workers proposed a new method to synthesize Si nanowires [55]. They produced bulk-quantities of Si nanowires without using any metal catalyst. They called this new approach "*oxide assisted growth* (OAG)" where the oxide phase rather than the metal assists the nucleation and growth of the 1D nanostructure. In their pioneering work Lee et al. prepared a target material by mixing Si and $SiO_2$ powders. By laser ablation or thermal evaporation of this target material, $SiO_x$ (x>1) vapor formed and following the chemical reactions as expressed in (2.1) and (2.2), Si nanoparticles precipitated.

$$Si_xO \longrightarrow Si_{x-1} + SiO \qquad \textbf{(2.1)}$$

$$2SiO \longrightarrow Si + SiO_2 \qquad \textbf{(2.2)}$$

The authors suggested that Si nanoparticles act as seeds for the growth of Si nanowires encapsulated by the oxide layer, as explained schematically in Figure 2.5 [56]. The real electron microscopy images of such structures are given in Figure 2.6 [56]. The observation of the dense nucleation especially at colder regions is an indication that the temperature gradient has an effect on the 1D growth.

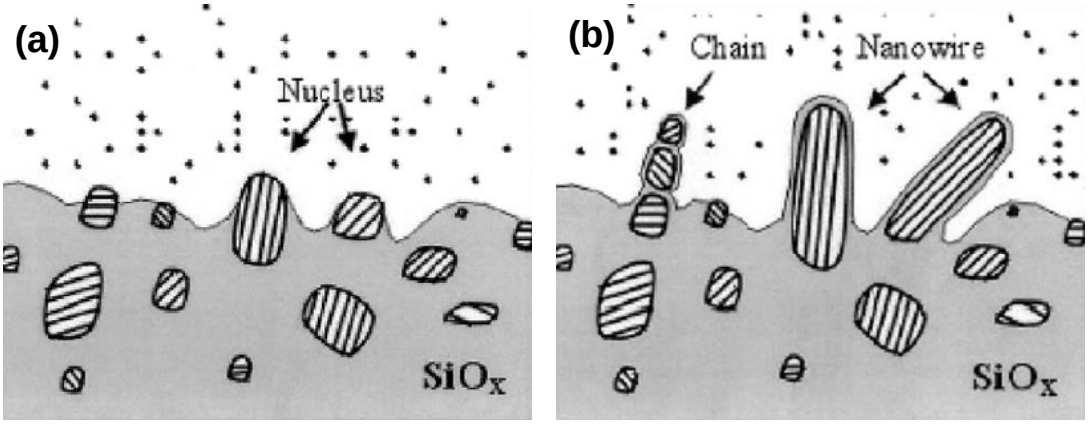


**Figure 2.5 Schematic description of the nucleation and growth of Si nanowires [56]. (a) Si oxide vapor is deposited firstly and afterwards Si nanoparticles precipitate. (b) Precipitated Si nanoparticles grow in a preferred orientation and form 1D nanostructures.**

Lee and his co-workers showed the effectiveness of the OAG process to synthesize 1D nanostructures of other materials including GaN [57], GaAs [58], GaP [59], as well as elemental Ge [60]. Xia et al showed the synthesis of CuO and MgO nanowires applying the same approach [61].

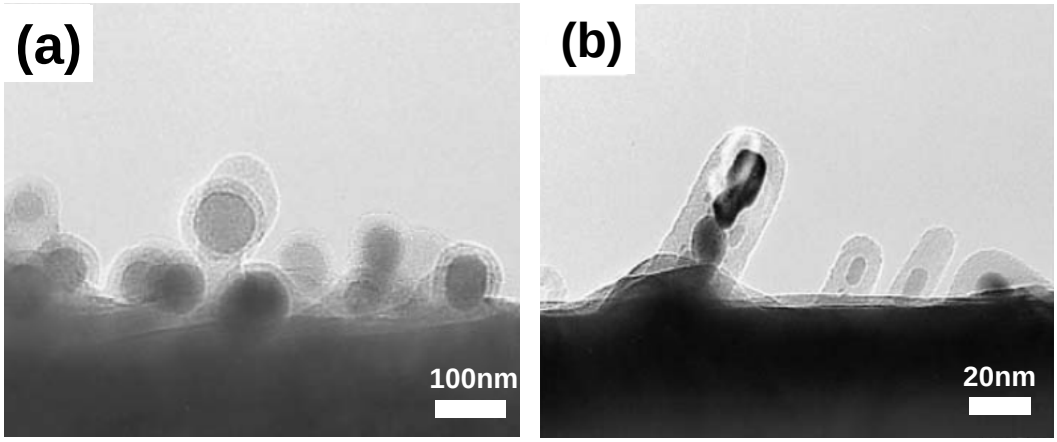


**Figure 2.6 TEM micrographs of (a) Si nanowire nuclei and (b) initial stages of the nanowire growth [56].**

On the other hand, the direct effect of the oxide phase on the chemical and morphological nature of the 1D growth is not clear. There may be a complicated growth mechanism which is composed of a stepwise VLS or OAG process. For instance, the nucleation step can start in the presence of an impurity, but the growth can be assisted by the oxide phase. Therefore the approach is not completely understood.

## 2.3 Synthesis of 1D Aluminum and Aluminum Oxide Structures

### 2.3.1 1D $Al_2O_3$ Structures: Microfibers to Nanowires

Among various 1D nanostructures, a special attention has been given to the preparation of nanotubes/nanowires of metal oxides because of their use in electrochemical and catalysis processes [62]. $Al_2O_3$, alumina, is one of the most known metal oxides which attracted much interest in the recent years for several technical applications, e.g. hard coatings [63], antireflective coatings on glass substrates [64], electrical insulators in electronic devices [65] and diffusion barriers which are protecting steel against high temperature oxidation [66]. While α-alumina is desired in wear-resistant and hard coatings due to its excellent mechanical properties and chemical and

thermal stability, metastable alumina phases such as γ-alumina are preferred in catalysis applications where the high surface area is the critical issue. In addition, alumina is expected to have potential application especially in high-temperature composite materials and nanodevices due to its high elastic modulus and superior optical characteristics [67].

In recent years there is an increasing interest to synthesize anodic porous alumina as templates for the controlled fabrication of low dimensional nanostructures beyond the current limits of the lithographic techniques. Alumina nanowires with diameters down to 5 nm have been fabricated by etching alumina membranes made of highly ordered arrays of uniform pores [68]. Actually, long before the synthesis of such extremely small 1D alumina nanostructures, 1D alumina microstructures were used extensively in the composite materials for mechanical applications. Alumina-whisker-reinforced ceramic, metal and polymer composites, which have exhibited excellent properties, such as low density, high strength and toughness, are accepted as promising structural materials for high performance applications [69].

In comparison to whiskers, alumina fibers have more defined structures and geometries and such fibers have been used to reinforce the structural materials due to their high melting points, high strength, light weight and good wear resistances [70]. Such fibers were mostly added to ceramics, metals and polymers to obtain ceramic matrix composites (CMCs), metal matrix composites (MMCs) and polymer matrix composites (PMCs) respectively to increase the flexibility, strength and high temperature resistance of the matrix material.

Mostly such fibers have been produced by a melt spinning technique, which is a well known process for the glass fiber production [71]. But alternative methods were also applied because of the technical restrictions, for instance the high melting point and low viscosity of molten alumina. Different sol-gel and colloidal synthesis approaches were developed to synthesize such 1D microstructures of alumina. In these approaches the main problem is the control of the size, shape and especially the porosity within the fiber or whisker.

Following the developments in the synthesis of nano-ceramics, 1D alumina nanostructures, which are much smaller than conventional alumina whiskers and fibers

up to date, are fabricated. Porous alumina has been used as a template to synthesize CNTs [72]. On the contrary, CNTs were used as templates to prepare different types of nanotubes and nanowires of $Al_2O_3$ [73]. The use of a porous anodic alumina (PAA) membrane with ordered nanopores is accepted as one of the simplest methods to generate 1D $Al_2O_3$ nanostructures [74]. In addition to pure alumina nanostructures, the pores of PAA can be filled with different materials including Ni, Au, Ag and Al to create arrays of 1D composite nanostructures, which may exhibit superior magnetic, optical and electrical properties. Besides template assisted methods, various lithography based top-down processes and bottom-up chemical approaches, such as thermal evaporation, catalyst supported CVD or carbothermal reactions, are also developed to synthesize such 1D $Al_2O_3$ and metal-$Al_2O_3$ composite structures.

### 2.3.2 Gas Phase Synthesis of 1D $Al_2O_3$ Nanostructures

Among other methods, gas phase synthesis methods are intensively employed in the fabrication of 1D $Al_2O_3$ nanostructures. Actually, gas phase methods provide a better controlled process and a wide spectrum of flexibility to fabricate structures with different shapes and geometries including nanobelts, nanoribbons, nanowires, nanorods or nanosheets, since these approaches are not based on any template which defines the final shape and structure of the 1D growth.

On the other hand, there are some approaches which combine the template assisted processes with the gas phase deposition. Satiskumar et al. used CNTs as templates and coated them with $Al_2O_3$ [75]. In the first step CNTs were prepared by the arc vaporization of graphite rods in an inert atmosphere. Then a gel prepared from aluminum isopropoxide (AIP) was coated on the acid treated CNTs. After 12 hours heat treatment at 770 K, $Al_2O_3$ coated CNTs with a diameter of 30-40 nm were achieved. Similarly, by heating a mixture of Al and $Al_2O_3$ powders, alumina nanotubes have been fabricated using CNTs as templates at 1473 K [76]. It was reported that these $Al_2O_3$ nanotubes (with an outer diameter less than 100 nm and an inner diameter of some tens of nanometers) were polycrystalline.

Che et al. used the VLS method, which was mostly applied for synthesis of Si and Ge nanowires so far, to synthesize crystalline 1D $Al_2O_3$ structures [77]. In that approach

basically Pt droplets were deposited on a basal sapphire substrate and prior to the deposition the substrate was heated up. At high temperatures the Pt droplets melted and acted as catalytic sites for the 1D growth. The main disadvantage of the process is the extremely high deposition temperature and the need for unusual and expensive raw materials such as "*basal sapphire*". The actual mechanism of the growth was not understood before Wu et al. showed the growth steps in a typical VLS process by the help of an in-situ TEM analysis [24].

Valcarcel et al. used a similar approach by thermal evaporation of a mixture of Al and $SiO_2$ [78]. Following two to four hours of heating at 1300-1500°C, he observed the formation of $\alpha$-$Al_2O_3$ fibers of white cotton-like appearance. It was also reported that the fibers had hexagonal cross-sections with a diagonal length varying from 100 nm to 10 μm. The hexagonal structure could be a direct proof of the $\alpha$-$Al_2O_3$ phase and the X-ray photoelectron spectroscopy (XPS) analysis showed that the Al within the fibers was in the form of $Al^{+3}$. Moreover, the Energy Dispersive X-ray Spectroscopy (EDX) analysis showed that droplets at the end of the fibers contain Si, Al and, interestingly, Fe. The authors proposed that molten Si droplets act as catalytic sites for the growth of $Al_2O_3$ fibers. Since the deposition temperature was below the melting point of Si, it was proposed that the liquid droplets might appear as a product of the following chemical reactions (2.3) and (2.4).

$$4Al(s,l) + 3SiO_2 \longrightarrow 2Al_2O_3 + 3Si(l) \qquad \textbf{(2.3)}$$

$$Al_2O(g) + 2SiO(g) \longrightarrow Al_2O_3 + 2Si(l) \qquad \textbf{(2.4)}$$

On the other hand, the reason for the presence of Fe at the end of the fibers and its effect on the growth mechanism was not discussed in detail and clearly.

Tang et al. used nearly the same approach as Valcarcel et al. He and his co-workers synthesized 1D $Al_2O_3$ and Si nanostructures with wrapping layers of amorphous $Al_2O_3$ by heating a mixture of Al, $SiO_2$ and $Fe_2O_3$ powders at different temperatures [79]. A fibrous layer was obtained by heating the prepared powder mixture to 1400°C. The authors suggested that the formation of whiskers rather than nanowires might be due to

the gas aggregation of catalyst drops. The whisker growth (VLS) takes place considering the following two reactions (2.5) and (2.6).

$$4Al(l) + 3SiO_2(s) \longrightarrow 2Al_2O_3(s) + 3Si(s) \quad \textbf{(2.5)}$$

$$4Al(l) + Al_2O_3(s) \longrightarrow 3Al_2O(g) \quad \textbf{(2.6)}$$

The authors mentioned that SiO vapor might form in addition to $Al_2O$ vapor due to the existence of a eutectic point in the Si–$SiO_2$ system or as a product of the reaction given in (2.7). The proposed overall VLS reaction is shown in (2.8).

$$Si(s) + SiO_2(s) \longrightarrow 2SiO(g) \quad \textbf{(2.7)}$$

$$Al_2O(g) + 2SiO(g) \longrightarrow Al_2O_3(s) + 2Si(s) \quad \textbf{(2.8)}$$

Zhou followed the same idea and used Fe as catalyst to synthesize smaller and branched 1D $Al_2O_3$ nanostructures [80]. Peng et al., similar to previously presented works, used an Al and $SiO_2$ powder mixture as the source material [81]. This mixture was evaporated at relatively lower temperatures (1100-1200°C) in comparison to higher deposition temperatures employed by Tang [79] and Valcarcel [78]. Different from the other presented results, the synthesis of $Al_2O_3$ nanobelts was presented in addition to fiber-like structures. The authors showed also interesting photoluminescence (PL) properties of these nanobelts and nanowires. They proposed that the emission peaks at 394 nm and 392 nm from $\alpha$-$Al_2O_3$ nanowires and nanobelts respectively, might be attributed to the oxygen vacancies.

Fang et al followed the VLS process and synthesized $\alpha$-$Al_2O_3$ nanowires in bulk quantity by evaporation of the mixture of pure Al powders (vapor source) and nanometer-sized $TiO_2$ powders (catalyst) at 1150°C [82]. SEM and TEM observations showed that $\alpha$-$Al_2O_3$ nanowires had diameters varying from 20 to 60 nm and lengths up to several tens of micrometers. The compositional analysis showed that there was an Al/Ti alloy formation at the tip of the nanowires which may be a natural effect of a

catalyst supported VLS growth. The authors also showed a strong blue luminescence band in the wavelength range of 400–500 nm with two peaks at 415 nm and 440 nm. These peak positions are different from the findings of Peng et al. [81].

In most of these catalyst supported processes the synthesis of 1D $Al_2O_3$ nanostructures is based on the formation of a nanoscaled liquid-phase catalyst and the existence of a eutectic point in the corresponding phase diagram between the vapor source and the catalyst. It is clear that a catalyst-free method may be more practical to produce 1D $Al_2O_3$ nanostructures. There are different approaches to develop such methods using only a mixture of Al and $Al_2O_3$ as vapor source excluding any other external catalyst support similar to the OAG process proposed by Lee and his co-workers [55].

For example, Zhao and his co-workers synthesized nanowires on a large-area silicon substrate by simple thermal evaporation of a mixture of Al and $Al_2O_3$ powders [83]. Their detailed TEM analysis showed that such nanowires usually had a straight morphology and were single crystalline with the wire axis parallel to the (001) direction. The growth of such nanowires can be explained with the VS mechanism since no catalyst particle is used. It is proposed that the VS growth takes place following the chemical reactions given in (2.9) and (2.10).

$$4Al(l) + Al_2O_3(s) \longrightarrow 3Al_2O(g) \qquad \textbf{(2.9)}$$

$$Al_2O(g) + O_2(g) \longrightarrow Al_2O_3(s) \qquad \textbf{(2.10)}$$

Since the deposition temperature is below the melting point of $Al_2O_3$, only the Al may be in the molten form. Indeed, this brings the question whether molten Al acts as a self catalyst. The authors observed that the orientated growth of nanowires started from the big particles. This is explained by the authors in the following way. Firstly, some big particles (approximately 10 μm) are deposited on the Si substrate and these particles act as preferred nucleation sites for the next species to be adsorbed. The growth effect becomes very significant due to the high density of nuclei on the surface of a big particle. The interaction forces between individual nanowire seeds induce a directional

growth. On the other hand, there is no detailed information about the nature of the particles acting as seeds. These particles may be the molten Al droplets or the sub-oxides of Al which support the directional growth.

Similarly, Wang et al. also used the mixture of Al and $Al_2O_3$ to prepare $Al_2O_3$ nanowires [84]. Such nanowires differ from the ones synthesized by Zhao et al. [83] in terms of their U- and L-shaped morphologies and larger sizes (ca. 100 nm). Although a VS model is proposed to explain the growth, the mechanism is not completely understood. The authors proposed that the growth mechanism might be related to the existence of the structural defects formed during the growth. Zhao et al reported a similar growth process for the synthesis of 1D MgO nanostructures and it is believed that mechanical stresses play an important role on such a directional growth [85].

Boxel et al. showed the effect of mechanical stresses on the directional growth of $Al_2O_3$ nanowires [86]. He and his co-workers synthesized 1D nanostructures of $\alpha$-$Al_2O_3$ successfully by evaporation of commercially available high-purity $Al_2O_3$ powders. The 1D growth was driven by the condensation of the generated vapor onto a sapphire substrate under controlled conditions of supersaturation. No external catalyst was used in the process. The authors believe that two sub-oxides, $Al_2O$ and AlO, act as vapor sources during the deposition process since their vapor pressures are higher than $Al_2O_3$ at the reported deposition temperature. The chemical reactions involved in the growth process are given in (2.11) and (2.12).

$$Al_2O_3(l) \longrightarrow Al_2O(g) + O_2(g) \qquad \textbf{(2.11)}$$

$$Al_2O_3(l \longrightarrow) 2AlO(g) + 1/2\, O_2(g) \qquad \textbf{(2.12)}$$

The authors proposed that firstly a 2D layer forms and during this growth a strong bi-axial compressive stress occurs. This stress formation drives the extrusion of 1D structures out of the initial thin film. This reminds of the explanation of Zhao [83] which points out that the directional growth of the nanowires starts from the bigger particles in the presence of interaction forces between them.

In these presented approaches using the mixture of Al and $Al_2O_3$ as the source material, the growth mechanism is mostly explained with various chemical reaction routes where Al is mostly in the molten state and $Al_2O_3$ stays in the solid form. Gundiah et al. proved this idea by employing a low temperature deposition at 900°C and showed that sub-oxides play the major role rather than $Al_2O_3$ itself [87]. He tried a different approach using a mixture of Al and graphite or active carbon powders to synthesize $Al_2O_3$ nanowires. The growth mechanism of the nanowires was explained on the basis of a VS approach, since extensive microscopic investigations revealed no catalyst/liquid droplets at the ends of the nanowires. Although the presented approach is different from the previous VS growth processes which mostly employ a mixture of Al and $Al_2O_3$ as the vapor source, the results show that sub-oxides of Al play an important role in the vapor transport. The relevant chemical reactions are shown in (2.13) and (2.14).

$$Al(s) + C(s) + O_2(s) \longrightarrow AlO_X(v) + CO(g) \qquad \textbf{(2.13)}$$

$$AlO_X(s) + O_2(g) \longrightarrow Al_2O_3(g) \qquad \textbf{(2.14)}$$

After the examination of all presented synthesis routes using the mixture of $Al/Al_2O_3$ as the vapor source, one can easily see a similarity with the synthesis of Si nanowires from the evaporation of a $Si/SiO_2$ mixture. On the other hand, while the evaporation of the $Si/SiO_2$ mixture leads to the formation of 1D Si nanostructures covered by an oxide shell [55], such a core-shell structure is not observed in any of the experimental works using a $Al/Al_2O_3$ mixture as the vapor source.

### 2.3.3 1D Al Nanostructures

Electron beam lithography (EBL) is one of the well established techniques for high resolution patterning of metal nanostructures. Different from the conventional EBL approaches, Ma et al. demonstrated the fabrication of Al nanowires by electron beam induced diffusion of $AlF_3$ [88]. By controlling the accelerating voltage, beam current and scanning time, Al nanowires of different sizes were synthesized. Alternatively to EBL, optical lithography methods were also employed to fabricate 1D nanostructures of Al.

Vazquez-Mena et al. produced sub-100 nm Al nanowires by applying stencil lithography (SL) [89]. Such a process is quite slow and applicable only to small areas. In addition, the stencil should be changed with a new one after using it a few times, which makes the whole process costly. Using extreme-ultra-violet (EUV) interference lithography Ekinci et al. fabricated sub-100 nm Al nanowires on a larger area [90]. In all these lithography based approaches there is no detailed investigation about the Al structure and especially it is not clear whether the Al stays in a metallic form or is covered with an oxide skin.

In addition to lithography processes, template assisted methods have been used also to fabricate 1D structures of Al as well as other metals. In a typical template assisted method, the main idea is the filling of the metal into a previously prepared porous material which mostly is alumina. Sung et al. introduced a joint method which combines PVD and atmospheric pressure injection methods. He used the anodic alumina layer as a template to synthesize Al nanowires [91]. This approach provides a better process control compared to the template assisted wet-chemical approaches. Hammrick et al. used polymer fibers as template and coated them with Al by plasma enhanced physical vapor deposition (PEPVD) [92]. The main problem of this approach is the inhomogeneous thickness of Al covering the fibers. Chen synthesized Al nanowires of 20-30 nm using another gas phase approach [93]. He prepared an equimolar mixture of Al and Si powders and heated this mixture up to 900°C in the presence of an $Ar/H_2$ carrier gas. Following one hour heating and cooling steps, the formation of bended nanowires was observed on the surfaces of the powders. Although the authors proposed that such structures are Si doped Al nanowires, the growth mechanism is not clear.

## 2.4 Properties and Applications of 1D Nanostructures

As discussed in the previous sections, 1D nanostructures, such as nanorods, nanotubes and nanowires, are the ideal systems to investigate the dependence of the thermal, electronic, mechanical and optical properties on dimensionality. In the recent years, in addition to the increasing basic research interest on the unique properties of such structures, 1D nanostructures attracted the attention of technological applications.

1D nanostructures below a distinct critical size exhibit singularities in the electronic density of states (DOS), called “van Hove singularities”, which is totally different from

the behavior of other low dimensional structures and of the bulk state as schematically illustrated in Figure 2.7. Following the discovery of CNTs in 1992, Odom et al. [94] and Kim et al. [95] showed the specific behavior of 1D structures experimentally by presenting sharp peaks in the DOS with the help of tunneling spectroscopy.

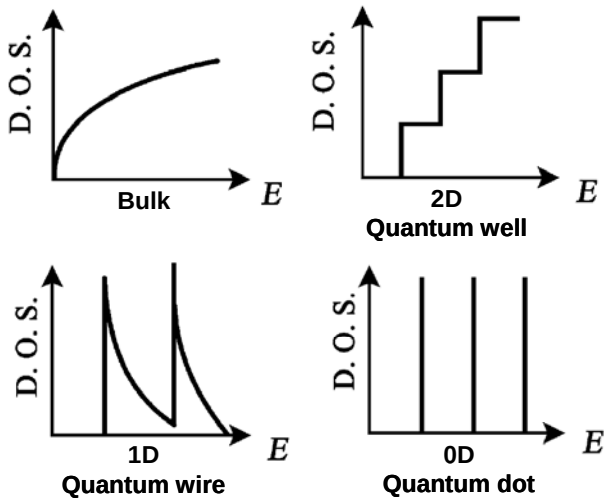


**Figure 2.7 Electronic densities of states (DOS) of materials.**

It is compulsory to understand the electron or charged particle transport properties of nanowires for nano-electronic, optical, magnetic and optoelectronic device applications of the future. The transport mechanisms in nanowires depend on different parameters including wire diameter, wire surface condition, crystal structure and quality, chemical composition and crystallographic orientation [96]. It has been reported that quasi-1D nanowires exhibit both ballistic and diffusive type electron transport mechanisms, which depend on the wire length and diameter [97].

Semiconductor nanowires have been employed successfully in some of the electronic device applications. One famous example is the nanowire field-effect transistor (NWFET). Although the mass production of such transistors is still behind the prototype stage, some NWFETs have already been fabricated from boron and phosphorous doped Si nanowires [98]. In addition, nanowires were used in the fabrication of several semiconductor nano-devices, such as junction diodes [99], memory cells [100], electro-mechanical switches [101], LEDs [102] and inverters [103].

Metal nanowires are one of the most attractive materials because of their unique properties that may lead to a variety of applications. Examples include interconnects for

nano-electronics, magnetic devices, chemical and biological sensors and biological labels. Makita et al. reported the first-principle electronic-state calculations for Al nanowires which received much attention as a new device material [104]. 1D Al microstructures have been used in microelectronics for more than 40 years. Since the 1970s the semiconductor industry has used vacuum deposited 1D Al structures for interconnection both in bipolar and CMOS (complementary metal oxide semiconductor) devices [105]. The major disadvantage of Al structures, however, is their early failure due to electro-migration. Alternatively, the $Al/Al_2O_3$ alloy has been shown to exhibit superior electro-migration resistance and it has been postulated that this might be related to higher creep resistance [106].

On the other hand, nanoscaled $Al/Al_2O_3$ interfaces attract also the attention of high density circuit applications, for instance Josephson devices [107]. $Al/Al_2O_3/Al$ structures are well known tunnel junctions for diode applications for a long time. Tumienen et al. showed a single-electron tunneling transistor composed of two ultra small capacitance $Al/Al_2O_3/Al$ tunnel junctions and a capacitively coupled gate electrode [108]. Very recently Lee et al. fabricated a nanowire field effect transistor (FET) using metallic Al cores and $Al_2O_3$ shells as a nanoscaled gate electrode and high-k dielectric layer respectively [109]. In such nano-electronic applications well aligned straight core-shell $Al/Al_2O_3$ nanowires are definitely desired.

In addition to the use of Al in electronic applications, the high-frequency plasmon resonance of Al nanostructures opens up new possible applications in plasmonic and other photonic applications. While spherical noble metal nanoparticles have an optical absorption in a narrow wavelength band, in the case of rod- or wire-like 1D nanostructures the plasmon band splits into two separate bands which correspond to oscillation of the free electrons along (longitudinal) and perpendicular (transverse) to the long axis of the 1D structure [110]. It is shown by various types of metal nanowires that this phenomenon strongly depends on the size and especially the aspect ratio of the 1D structure. In this context, nanowires can be employed as plasmon tuning tools.

Tamada et al. showed that sub-micron Al wire grids can be used effectively as optical polarizers at a 0.8 μm wavelength band. [111]. Similarly, Wang et al. showed that grid polarizers made of Al nanowires with smaller diameters down to 30 nm exhibit

a high extinction ratio contrast up to 10.000:1 in the visible range with a good transmittance of 83-87 % [112]. Recently, Ekinci et al. showed that bi-layer Al nanowire grids can be employed as broad band polarizers [113]. Different from well known plasmonic Ag and Au quantum dots and wires, Al exhibits a plasmon resonance in the UV region. Actually, there is not so much work conducted on the plasmonic properties of Al nanostructures in comparison to intensive studies carried out on the plasmon effects of noble metals. The main reason is the difficulty in preparation of non-agglomerated and oxide isolated Al nanostructures. Most of the optical calculations concerning 0D and 1D Al nanostructures consider also the effect of the oxide skin. Mostly 1D Al nanostructures are fabricated by the lithography processes.

Their non-linear optical properties are another interesting feature of 1D nanostructures. Johnson et al. showed the second harmonic generation (SHG) and third harmonic generation (THG) within a single nanowire by using near-field optical microscopy [114]. Yamada et al. showed a real device application employing such non-linearity of the nanowires. He and his co-workers used Si nanowires as waveguides and presented a non-linear transmittance due to two photon absorption [115].

1D nanostructures also exhibit interesting photoluminescence properties. The p-n junction of nanowires has been found to be capable of light emission by their unique photoluminescence (PL) or electroluminescence (EL) properties [116]. The crossed nanowire approach, where nanoscaled p–n diodes were created by crossing well-defined p-type and n-type InP nanowires, was the first demonstration of the real nanoscale LEDs [117]. The use of p–n junction nanowires was extended to laser applications. Huang et al. showed that ZnO nanowires with diameters smaller than the wavelength of the emitted light exhibit lasing actions at lower threshold energies compared to their bulk counterparts [118].

Ferromagnetic arrays of 1D nanostructures have the potential for ultra-high density perpendicular data storage applications. Such ferromagnetic 1D nanostructures are considered viable alternatives to the present state-of-the-art magnetic quantum dot-based data storage media. In a pioneering work Thurn-Albrecht et al. showed cobalt nanorods for magnetic data storage applications [119]. They fabricated parallel arrays of cobalt

nanorods using pores of alumina. These nanorods exhibited a very high coercive field with appropriate magnetic anisotropy.

In recent years nanowires also became an attractive class of materials for bio-applications. Especially, an intensive research interest has grown up in the field of bio-sensor technology using nanowires. The working principle of these sensors is based on the detection of any change in the conduction or other physical properties after attaching of the bio-molecules to the surface of the nanowires. Elfström showed that 1D Si nanostructures modified with biotin receptors are capable to detect label free streptavidin molecules efficiently [120]. Patolsky et al. demonstrated the application of nanowire sensors for ultra sensitive detection of proteins down to individual virus particles as well as multiplexed recording of these species using distinct nanowire elements within a sensor device [121]. There is an intensive research on the bio-sensor applications using nanowires.

Considering the enormous potential of 1D nanostructures, it is believed that the research on such fascinating nanomaterials will continue to grow in the coming years. Exciting opportunities exist for scientists and engineers for creativity and innovation in research and development to realize the full potential of 1D nanostructures.

# 3. Synthesis of 1D $Al{\cdot}Al_2O_3$ Nanostructures

## 3.1 Background: CVD of $(^tBuOAlH_2)_2$

Veith et al. showed the existence of HAlO (aluminumoxyhydride), a compound which may be derived from the oxohalide by formal substitution of the halide by hydride [122]. Instead of using a classical solid-state reaction to synthesize this compound, the authors used a molecular route. The easiest way to synthesize a HAlO layer is to direct a constant stream of $(^tBuOAlH_2)_2$ on inductively heated substrates in a cold-wall reactor. In such a decomposition process the deposition temperature is critical in terms of the de-hydration proportion.

In the late 1990s Veith and Faber demonstrated the growth of interpenetrating spherical particles by the decomposition of $(^tBuOAlH_2)_2$ at temperatures above 300°C [123]. Using TEM it was shown that globular species of 400 nm diameter, which had spherical particles of 40 nm on their surfaces, covered the substrate. The authors proposed that these particles might be in the form of $Al{\cdot}Al_2O_3$ core-shell structures. Using small angle neutron scattering, a theoretical approach was introduced to explain the structure of these particles. On the other hand, an electron microscope image supporting such a core-shell structure was not provided. In the X-ray diffraction analysis an $Al_2O_3$ shell could not be detected also. The main reason of this may be the nanocrystallinity and extremely thin oxide layer which are also believed to cause a broadening effect in the X-ray diffractograms.

In another work of Veith and Faber a bi-phasic nanocomposite (composed of metallic Al and its oxide phase) was synthesized by the decomposition of $(^tBuOAlH_2)_2$ at 450°C [124]. It was stated that the composite $Al{\cdot}Al_2O_3$ could be the product of disproportionation of an $Al_2O_2$ intermediate. Similarly, Andres showed the formation of the $Al{\cdot}Al_2O_3$ composite layer by applying a deposition temperature above 500°C [125]. In addition to this direct deposition method, Andres applied also a two-step process to synthesize the $Al{\cdot}Al_2O_3$ composite layer free from any carbon residual. In the first step the intermediate glassy HAlO layer was deposited at 300°C. In the second step this layer was transformed into $Al{\cdot}Al_2O_3$ by heating it up to 600°C. During the heating stage the hydrogen was eliminated and AlO intermediately disproportionated to $Al^0$ and $Al^{+3}$.

Alternatively, a $CO_2$ laser was used to transform the HAlO layer into the $Al{\cdot}Al_2O_3$ composite [126]. However, in both cases the microstructure of the $Al{\cdot}Al_2O_3$ layer achieved upon transformation was not discussed in detail.

In the PhD thesis of Wolf a core-shell structure was proposed for the $Al{\cdot}Al_2O_3$ composite layer which was deposited by the decomposition of the same precursor [127]. Although the existence of a bi-phasic composite structure was proposed in most of these studies, a TEM or SEM image was not provided as a direct proof. In his PhD thesis Petersen studied the effect of the deposition rate and temperature on the morphology systematically by depositing $(^tBuOAlH_2)_2$ at temperatures above 550°C [128]. At a controlled and reduced pressure he observed the formation of randomly growing nanowires. The TEM and EDX analysis indicated that nanowires were composed of an Al core and an $Al_2O_3$ shell. Such nanowires were discussed for their potential bio-applications. However, a clear growth mechanism of such nanowires was not proposed. Sow carried out a more detailed work especially on the growth mechanism of such nanowires [129]. She was able to show the core-shell nature clearly with the help of HR-TEM. She explained the growth of $Al{\cdot}Al_2O_3$ nanowires with a catalyst-free mechanism different from the catalyst supported VLS methods. However, she also observed the formation of self assembling particles in addition to nanowires at some instances. In this context, the main difficulty is to find out a mechanism which may also explain the nanoparticle-nanowire transformation. Sow mostly used metal substrates. Actually, it is difficult to get a stable temperature regime on metallic or other conductive surfaces (especially in case of low temperature depositions) since the electromagnetic induction may cause local fluctuations on the heated surfaces.

It is clear that in functional applications using such 1D nanostructures, it is important to control the growth precisely. In this current work we present the controlled synthesis of different 1D $Al{\cdot}Al_2O_3$ nanostructures including nanowires, nanorods and nanoloops by the decomposition of $(^tBuOAlH_2)_2$. The growth mechanism of 1D structures is also discussed. The effect of the substrate temperature, precursor flow rate, pressure and other process parameters on the morphology of the deposited layers is studied in detail. In addition to thermal CVD, selective CVD (SCVD) and laser assisted CVD (LCVD) methods are employed for the local deposition purpose.

## 3.2 Experimental Approach

Basically, thin solid films were deposited by the decomposition of the single source molecular precursor $(^tBuOAlH_2)_2$ on the heated substrates under a reduced pressures of 2-5x$10^{-2}$ mbar. Prior to the deposition, the precursor compound $(^tBuOAlH_2)_2$ was synthesized following the routes described elsewhere [130] under dry $N_2$ using standard Schlenk techniques.

Three different approaches were followed for the deposition. Most of the depositions were performed using a cold-wall horizontal reactor where only the substrate material was heated directly by the electromagnetic induction. In addition to this conventional approach, a selective CVD (SCVD) method was employed by inducing controlled thermal gradients on partially metal coated glass substrates. As an alternative to induction heating, the surface of the substrate was heated locally by a focused laser beam. This approach is known in the literature as pyrolytic laser assisted CVD (LCVD).

The next chapters will cover the synthesis route and general experimental setups. Each experimental set-up and the corresponding procedure will be explained separately. As it will be shown later in detail, slight changes in the experimental parameters in these three technical approaches can have a significant impact on the morphology and structure of the deposited layers.

### 3.2.1 Precursor Synthesis

According to well known routes [130], the synthesis of $(^tBuOAlH_2)_2$ starts with dissolving 120mmol (4.554 g) $LiAlH_4$ in 80 ml diethyl ether in a flask including a reflux cooler. Afterwards 40 mmol (5.334 g) of aluminium trichloride are dissolved in 80 ml diethyl ether under cooling and added to the LiAlH4 solution at room temperature with a steady flow, which is followed by the precipitation of lithium chloride. To the suspension which is left, 160 mmol (11.859 g) tert-butanole is added to produce hydrogen after 4 to 5 hours of stirring at ambient temperature. By filtration, lithium chloride is separated from the mixture and the solvent is evaporated *in vacuo* subsequently. To achieve 15.2 g bis(tert-butoxy aluminium dihydride), the remaining solid phase was sublimated at a pressure of $10^{-3}$ bar and ambient temperature:

93 % yield, decomposition temperature > 120 °C, melting point 71 °C, 1H NMR (in C6D6): δ = 1, 21 ppm (s); 4,43 ppm (s, breit). 13C NMR (in C6D6): δ = 30, 36 ppm (s); 76,42 ppm (s).

Values according to the literature [130]: 1H NMR (in C6D6): δ = 1, 22 ppm (18H, C(CH3)3); 4,43 ppm (breit, 4H, AlH2). 13C NMR (in C6D6): δ = 30, 36 ppm (CH3); 76,43 ppm (C(CH3)3).

### 3.2.2 Cold-wall Reactor Deposition

Most of the deposition processes were carried out in a home-built horizontal cold-wall type reactor, as schematically shown in Figure 3.1. The substrate was heated directly by the induction coil coupled to a high frequency (HF) generator (running at 300-400 kHz with a maximum power of 1500 W) while the rest of the reactor remained cool or at least cooler. While the metallic substrates were heated directly with the induced electromagnetic field, in the case of glass and similar non-conducting substrates, an indirect heating approach was applied by using a graphite holder.

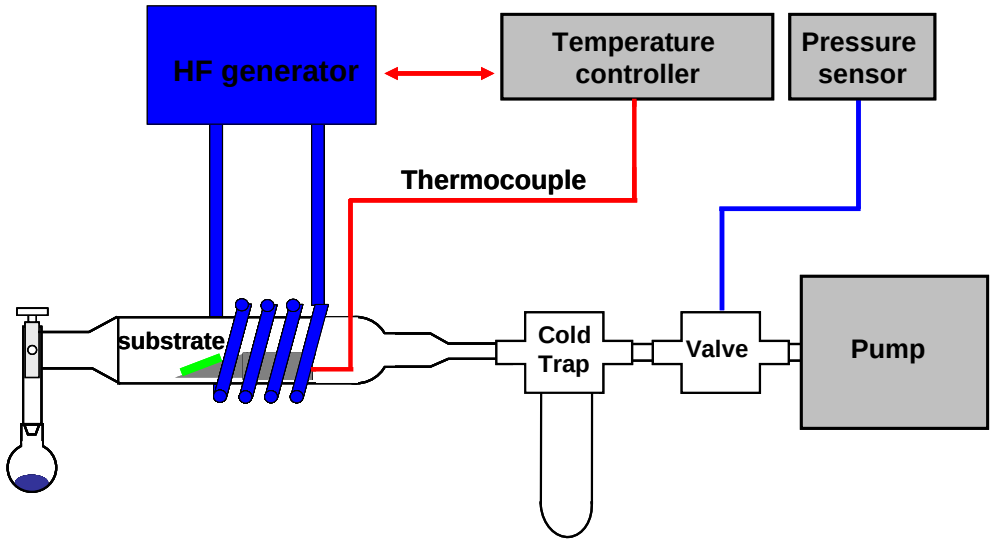


**Figure 3.1 Schematic illustration of the cold-wall CVD reactor.**

An electronic temperature controller was used to regulate the substrate temperature at desired values. The main principle of such a controller is based on the feed-back between the thermocouple attached to the substrate holder and the HF generator. The pressure level was kept at 2-3x$10^{-2}$ mbar with the help of a mechanical pump. A standard

Pirani gauge was used to monitor the pressure during the deposition. The vacuum system includes a cold trap to collect the solid or gaseous exhaust materials, which otherwise may damage the pump.

Prior to the deposition process, the whole apparatus was heated, flooded and pumped several times with nitrogen or argon in order to eliminate residual oxygen and water in the apparatus. After heating the substrate up to the desired deposition temperature, the precursor was sent by controlling the flow rate with a manual valve. The flow rate was monitored indirectly by observing the change of the over-all pressure with the help of a sensitive Pirani gauge. During the deposition processes parametric studies were carried out on the flow rate, pressure, temperature and the deposition time.

### 3.2.3 Selective CVD (SCVD)

SCVD is the acronym used in the CVD research group at Leibniz-Institute of New Materials (INM) to define a modified version of the cold-wall CVD approach. The main idea is to create a controlled thermal gradient on the substrate using partially metal coated glass substrates.

Electromagnetic induction is used to heat bulk materials in various applications including mostly the state-of-the-art metallurgy processes such as melting, soldering and hardening of metals [131]. The induction heating is also a promising method for MEMS (**M**icro-**E**lectro-**M**echanical **S**ystem) processes and devices. Recently Yang et al showed the selective heating of micro-structures by applying the electromagnetic induction [132]. In this work the LIGA (German acronym for ″**Li**thographie, **G**alvanoformung, **A**bformung”) method was employed to deposit Ni microstructures on Si substrates and such structures were heated locally by applying a HF electromagnetic field.

The selective heating approach was also used in the CVD processes. Semancik et al. used a micro hot-plate array to induce different heating levels on the substrate material to observe the effect of the temperature on the thin film growth [133]. They observed that the micro hot-plate array structure permitted a local temperature control between 30°C and 550°C on every micro-plate. On the other hand, preparing such micro array plates using lithography techniques is costly.

In this current work we employed a simple selective heating method to decompose $(^{t}BuOAlH_2)_2$ locally. The process is based on inducing a local temperature rise only on the metal coated portions of the glass substrate by applying induction. The template preparation steps are shown in Figure 3.2. Firstly, the surface of the bare glass substrate (Figure 9a) was covered with a metal mask (Figure 3.2b). Then Au was deposited selectively through this mask (Figure 3.2c). After the deposition step the mask was removed and Au structures were created on the glass surface (Figure 3.2d).

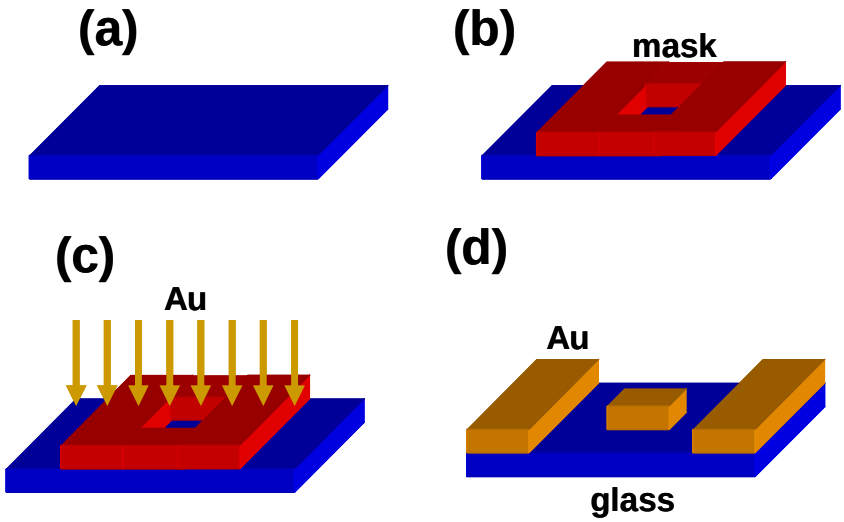


**Figure 3.2 Preparation of the template. (a) Bare glass substrate. (b) Masking of the bare glass with a metal mask. (c) Sputtering of Au through the mask under vacuum conditions. (d) Removing the mask.**

It is known that thin Au layers are heated poorly in the electromagnetic field [134]. Thus, partially Au coated glass substrates were heated on the graphite substrate holders. The main aim is to induce a thermal gradient between Au coated and non-coated regions by using a combination of contact and induction heating.

### 3.2.4 Laser-Assisted CVD

In most of the LCVD processes the laser beam is positioned parallel or perpendicular to the substrate surface. The parallel beam configuration is only used in photolytic LCVD. In such processes the laser beam is absorbed directly by the gas phase species and a photo-assisted decomposition takes place. The present work covers the pyrolytic LCVD method which uses a perpendicular laser beam configuration.

In pyrolytic LCVD the laser beam acts as the local heat source in the reaction zone. In comparison to the thermal CVD, the reaction zone is confined to an extremely small area in the case of the LCVD. In LCVD processes, the growth rate is high due to the effective, nearly three-dimensional mass transport of the gaseous species to the deposition zone. Theoretically, any material which is deposited as a thin film by conventional CVD can be deposited as lines, dots or three dimensional structures by applying LCVD.

In this PhD thesis a small cold-wall static-type reactor was developed to be used with a CW argon ion laser (mixed line: 457-514 nm) for local heating of the substrate material, as illustrated schematically in Figure 3.3. The laser beam was focused on the substrate by the help of a simple plano-convex lens. The focal spot diameter was determined to 10 μm ($1/e^2$ decrease in intensity) by using the scanning knife-edge technique [135].

The LCVD chamber is made of stainless steel and has inlet and outlet connections for the precursor and residual gases respectively. The chamber has a cylindrical shape with a height of 4 cm and a diameter of 8 cm. It is equipped with a quartz window for the entrance of the laser beam.

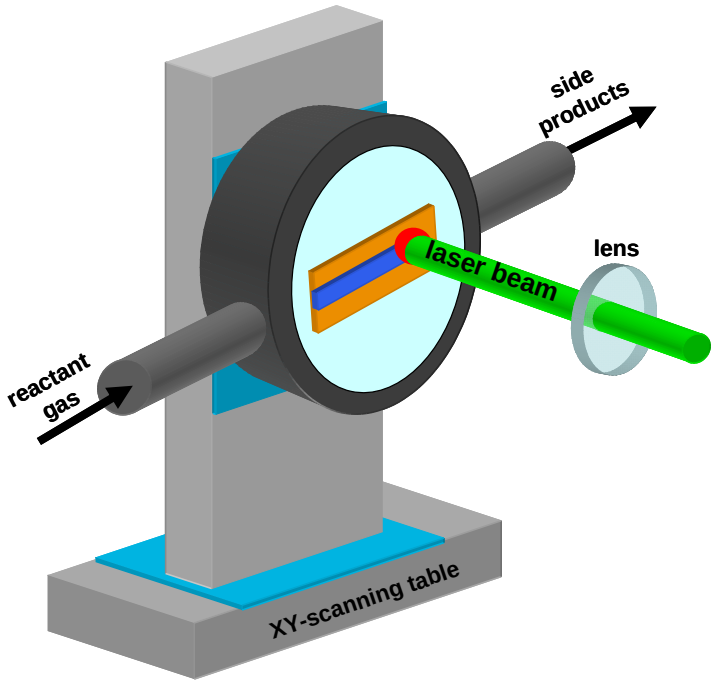


**Figure 3.3 Schematic illustration of the home-built LCVD apparatus.**

The reactive precursor, $(^{t}BuOAlH_2)_2$, was fed into the chamber by controlling the pressure of the chamber with a Pirani gauge and a butterfly valve. An XY-micro-positioning system was used to move the chamber in X- and Y-axes under the focused laser beam. The laser intensity was measured online using a beam sampler and a sensitive powermeter. The LCVD process is explained schematically in Figure 3.4. Basically, it is similar to the thermal CVD method. The only difference is the use of a laser beam to heat the surface of the substrate material locally.

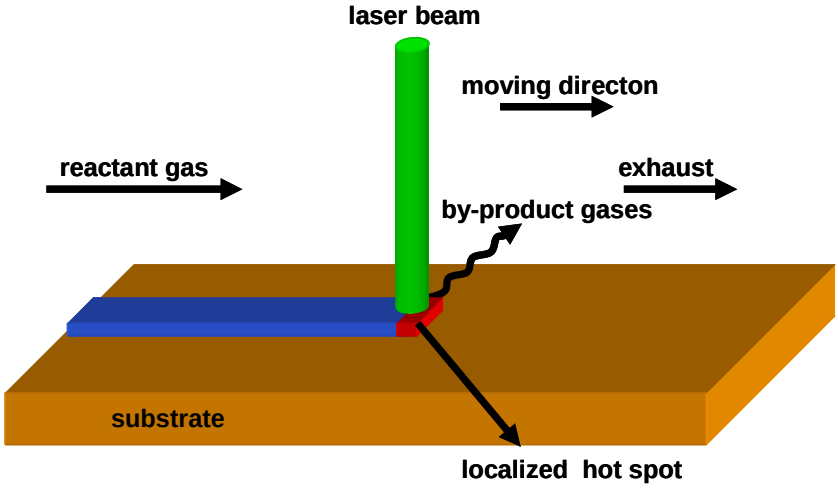


**Figure 3.4 Local deposition process using the LCVD method.**

## 3.3 Results and Discussions

### 3.3.1 Structural Characterisation

After the deposition of $(^{t}BuOAlH_2)_2$ on stainless steel substrates at 550°C for 10 minutes, the substrate was left to cooling under vacuum conditions, followed by the SEM analysis of the morphology of the deposited layers. Figure 3.5a shows a SEM image of deposited nanowires. The chaotic arrangement of randomly distributed nanowires on the surface reminds of a spaghetti shape. The length of the nanowires reaches up to several micrometers while the diameters of the nanowires are in the range of 20-30 nm. The thickness of the layer is about l µm, as it is estimated from the cross-sectional SEM micrograph shown in Figure 3.5b. The cross-sectional image also shows the highly chaotic arrangement of the nanowires.

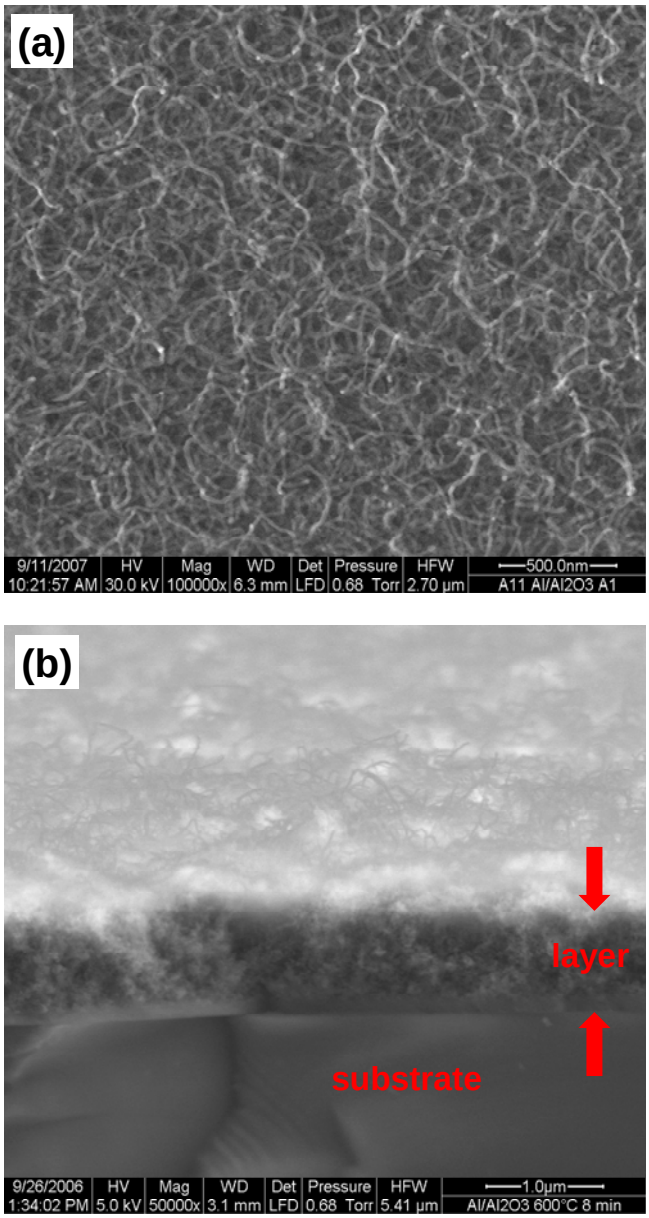


**Figure 3.5 SEM micrographs of deposited nanowires. (a) Surface of the substrate. (b) Cross-sectional view.**

It is believed that the diameters observed in the SEM micrographs appear larger than the actual wire diameters due to the local charging effects. After the analysis of more than 150 nanowires from randomly recorded TEM images, it is seen that most of the nanowires have diameters in the range of 17-23 nm, as shown in the size distribution (Figure 3.6a). Figure 3.6b shows the typical morphology of a composite nanowire with a clearly seen Al-$Al_2O_3$ core-shell structure.

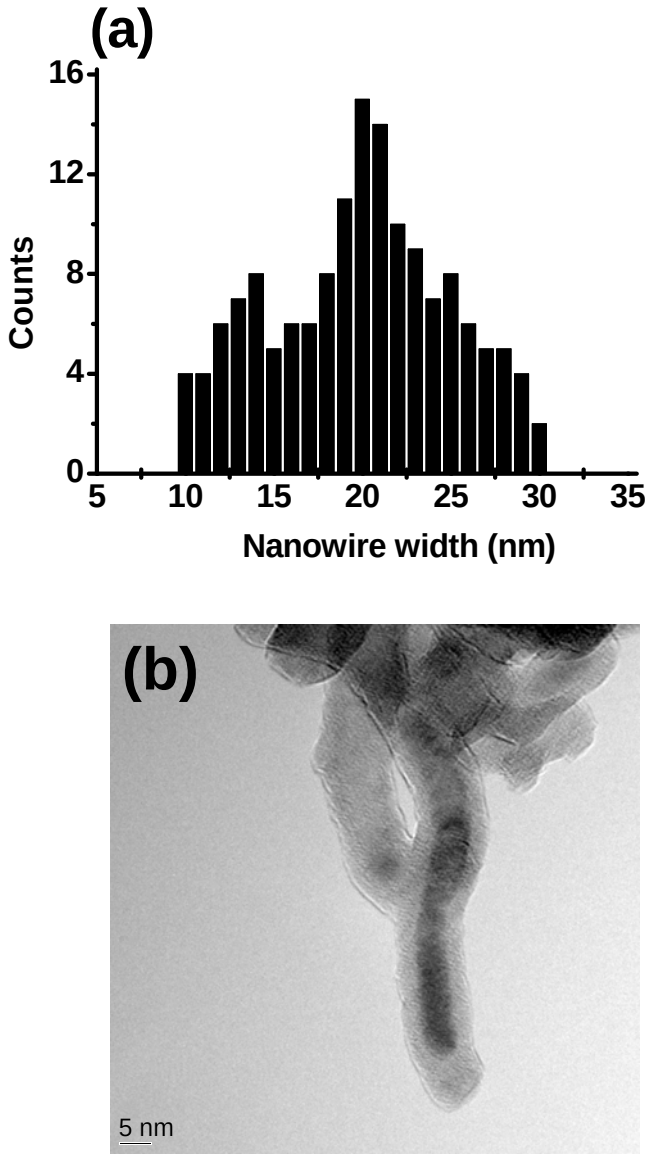


**Figure 3.6 (a) Size distribution of the deposited nanowires. (b) TEM image of a core-shell Al·$Al_2O_3$ nanowire.**

The X-ray diffractogram given Figure 3.7 shows that only the detectable crystalline phase, apart from the steel substrate (PDF: 85-1410), is aluminum (PDF: 85-1327). A crystalline oxide phase is not seen in the diffraction pattern. This may be due to the nanocrystallinity and extremely thin oxide layer. These two effects are known to lead to very broad features in the diffractograms. On the other hand, the oxide layer can be totally or partially amorphous (with a very low crystallinity) since the deposition

temperature is not so high. The existence of metallic Al is also confirmed with the analysis of the SAED pattern, as given in Figure 3.8.

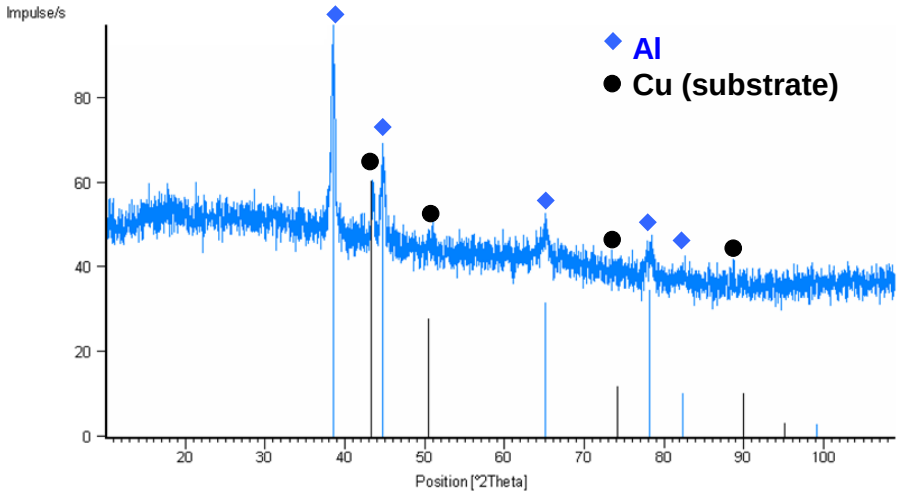


**Figure 3.7 X-ray diffractograms of the layers deposited on Cu substrate.**

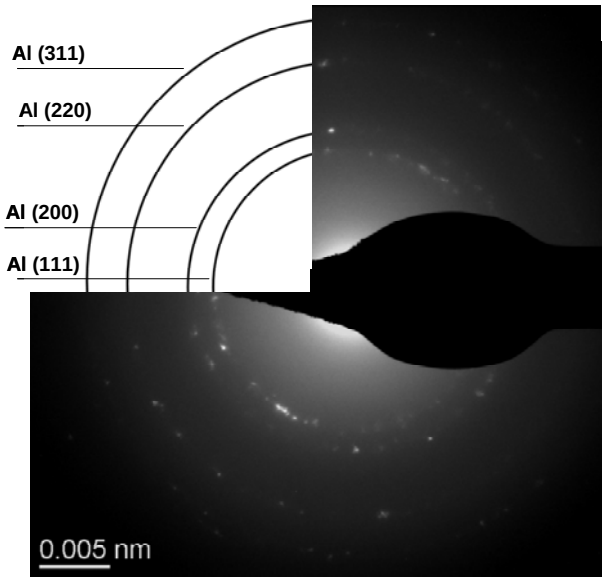


**Figure 3.8 SAED pattern of deposited layers.**

On the other hand, we observed at some instances, especially at high temperature depositions (>650°C), additional rings in the SAED pattern, which are not corresponding to metallic Al, as shown in Figure 3.9. Although several analyses have been carried on the electron diffraction patterns of the different deposits, a clear crystalline identification concerning these additional rings (shown by *) could not be achieved. These rings may be attributed to γ-$Al_2O_3$ (cubic, JCPDS 10-425) or δ-$Al_2O_3$ (tetragonal, JCPDS 16-394).

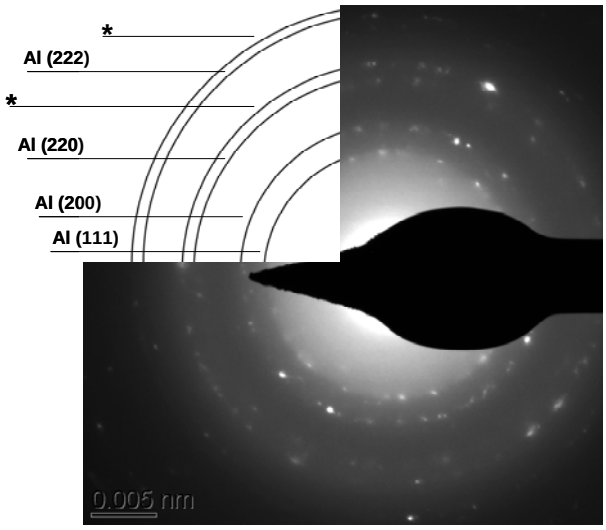


**Figure 3.9 SAED pattern of the layers deposited at high temperatures (> 650° C).**

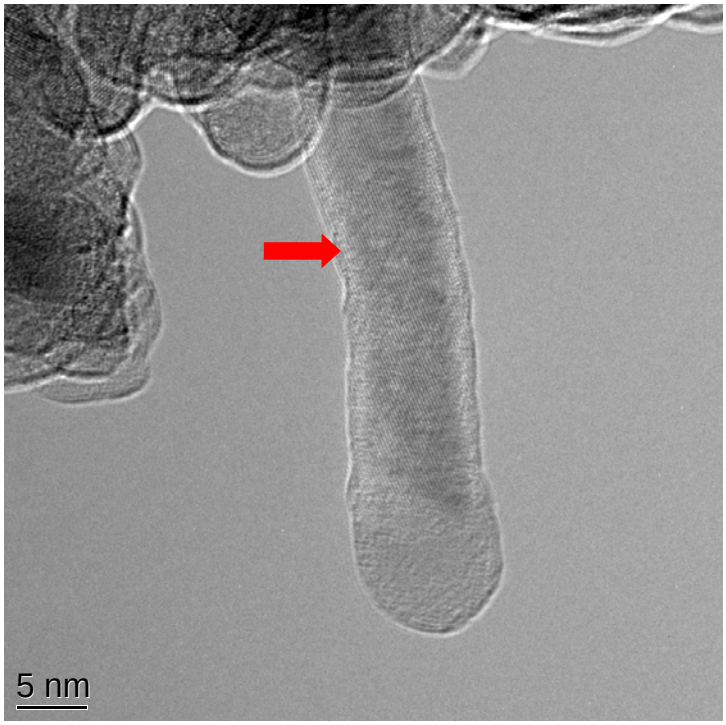


**Figure 3.10 HR-TEM image of an Al·$Al_2O_3$ nanowire.**

The crystalline structure of the core is further confirmed by HR-TEM. In Figure 3.10 it is clearly seen that the core exhibits lattice fringes which are attributed to metallic Al. In some of the nanowires the shell also exhibits a fringe structure (Figure 3.11) which is an indication of a crystalline phase. As we mentioned previously, it is not easy to distinguish whether the oxide layer is a δ- or γ-phase $Al_2O_3$. Petersen also discussed

similar difficulties in the identification of the crystal structure of the shell in his PhD thesis [128].

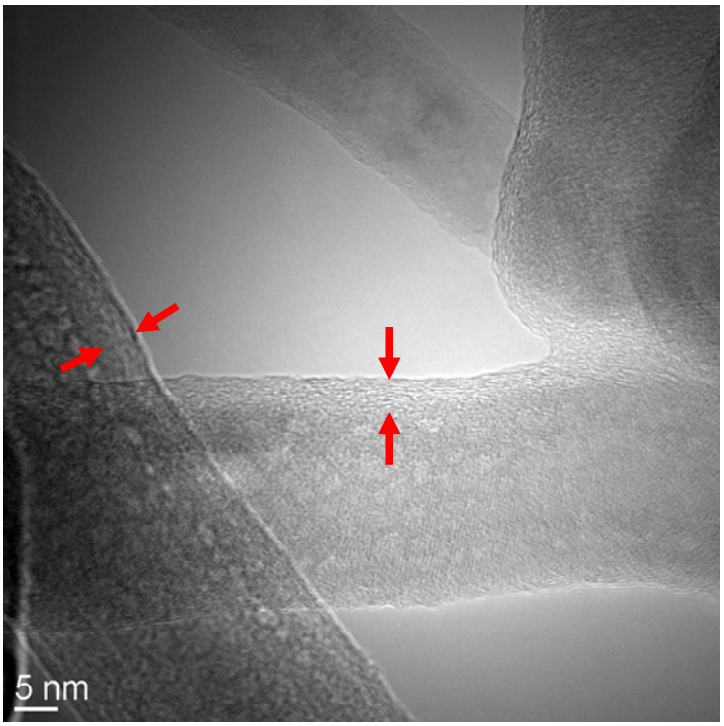


**Figure 3.11 HR-TEM image of Al·$Al_2O_3$ nanowires. The arrows show the lattice grating structures within the shell.**

It is confirmed by EDX attached to the TEM that the shell consists of aluminum and oxygen, which is a clear indication of the presence of $Al_2O_3$. While the Al content reaches to a maximum in the middle of the wire (Al:O=56:44 at. %), the oxygen content reaches its maximum (O:Al=68:32 at. %) within the shell. Similarly, Petersen and Sow presented in their theses, that the amount of Al (at. %) is higher in the core of the nanowire [128 and 129]. Using several TEM images of the nanowires, it was found out that there is a constant ratio between the radius of the Al core, r(Al), and the total radius of the core/shell wire, R(Al/$Al_2O_3$). With the help of the interference contrast in the two-dimensional cut of the wire, we found out that this ratio, r(Al)/R(Al/$Al_2O_3$), is ca. 0.47 which matches nicely with the theoretical value of 0.53, which is calculated using a co-axial composite cylinder model for the Al ($\rho$=2.70 g·$cm^{-3}$) -core surrounded by the $\gamma$-$Al_2O_3$ ($\rho$=3.97 g·$cm^{-3}$) –shell, as shown schematically in Figure 3.12.

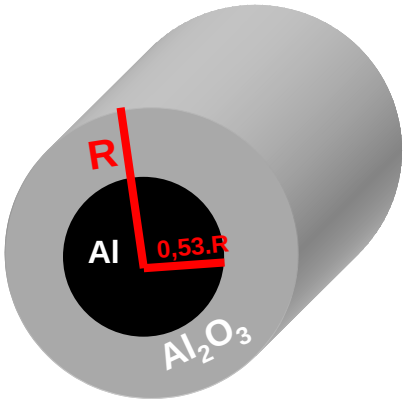


**Figure 3.12 Co-axial composite cylinder model for an Al·$Al_2O_3$ core-shell nanowire.**

The co-axial composite cylinder model is based on the assumption that the decomposition of ($^t$BuOAl$H_2$)$_2$ follows the stoichiometry shown in (3.1);

$$n(Al) = n(Al_2O_3) \qquad \textbf{(3.1)}$$

where ***n(Al)*** and ***n($Al_2O_3$)*** are the molar amounts of Al and $Al_2O_3$, respectively. *n(Al)* can be calculated from the ratio of the Al core volume, $V_{core}$, to the molar volume of Al, $V_{Al\ (molar)}$, as shown in Equation (3.2). Similarly, *n($Al_2O_3$)* can be calculated from the ratio of the volume of the shell, $V_{shell}$, to the molar volume of the $Al_2O_3$, $V_{oxide\ (molar)}$, as given in Equation (3.3).

$$n(Al) = \frac{V_{core}}{V_{Al(molar)}} = \frac{\pi r^2 l}{V_{Al(molar)}} \qquad \textbf{(3.3)}$$

$$n(Al_2O_3) = \frac{V_{oxide}}{V_{Oxide(molar)}} = \frac{\pi(R^2 - r^2)}{V_{Oxide(molar)}} \qquad \textbf{(3.4)}$$

Taking the assumption given in (3.2) into account and using $V_{Al\ (molar)}$=9.99 cm$^3$/mol and $V_{oxide\ (molar)}$=25.7 cm$^3$/mol, we found a relation between the core radius (r) and the total wire radius (R) in the following form (3.5).

$$r = 0.53R \qquad \textbf{(3.5)}$$

Only in some of the nanowires a continuous core structure can be seen directly due to the good contrast between Al and its oxide in TEM. On the other hand, in most of the nanowires a continuous tubular core structure is not observed within the $Al_2O_3$ shell. It is believed that the core is grown up with a curvature rather than a linear direction. Therefore, the Al core becomes visible partially at specific angles, which satisfy the Bragg condition as shown in the TEM images recorded at different tilt angles (Figure 3.13). The arrows in the images show that the Al core becomes visible with the change of the tilt angle.

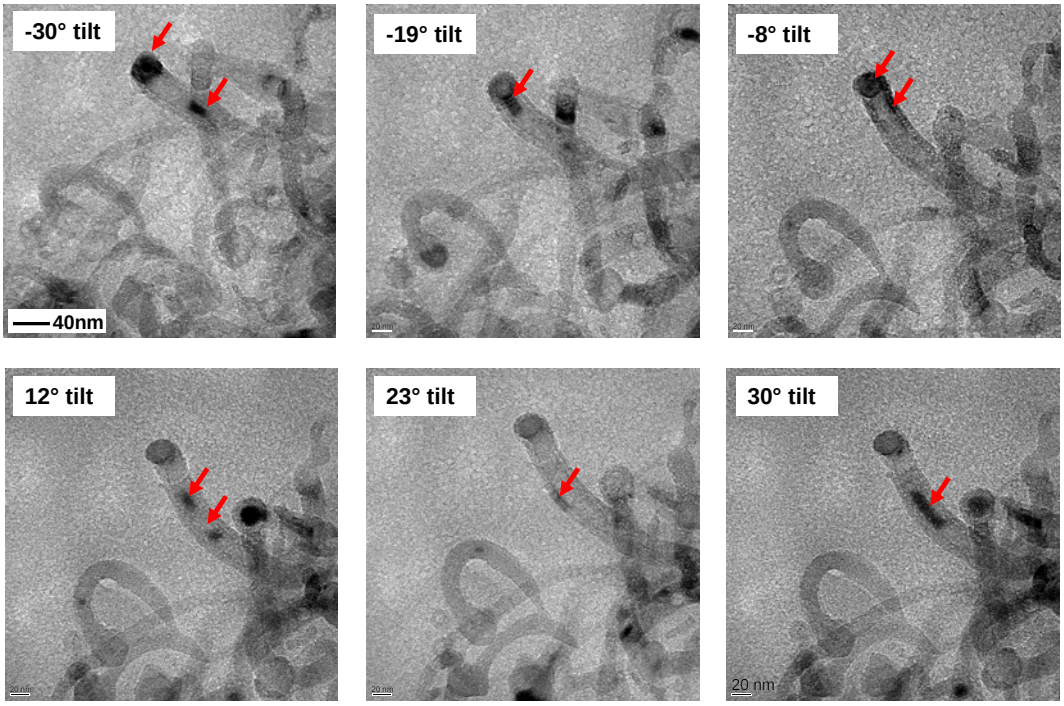


**Figure 3.13 TEM images of Al·$Al_2O_3$ core-shell nanowires recorded at different tilt angles.**

It is believed that the temperature is the main factor in the growth of $Al_2O_3$ nanowires. The temperature of the substrate determines whether nucleated Al seeds are in the solid or liquid state, which is critical for the 1D growth. In this context, differently from Sow and Petersen who synthesized similar structures [128 and 129], the temperature and heating level of the substrate was monitored with a thermal camera. Additionally, non-conducting and non-metallic substrate materials were employed in order to control the surface temperature precisely and to eliminate any possible metal supported catalyst effect. In the next chapters detailed information will be provided on the growth mechanism of 1D nanostructures.

### 3.3.2 Growth Mechanism

#### 3.3.2.1 Deposition at a Temperature above the Melting Point of Al

Figure 3.14a shows a TEM image of Al·$Al_2O_3$ nanowires deposited on a glass substrate at 650°C. The size of the nanowires is approximately 20 nm in diameter. The diameters remain constant throughout the length of the nanowires. In the TEM image of the nanowire (a) one can see clearly a core-shell structure with a spherical particle at the tip. While other nanowires (b and c) have similar spherical particles at their tips, they do not exhibit the core-shell structure in the TEM analysis. As explained previously, the Al core grows with a curvature, so only some portions of the core which satisfy the Bragg condition may be seen. At some angles the core is not seen at all. The spherical particles at the tips of the deposited nanowires remind of a catalyst supported VLS type growth mechanism. The EDX spectrum in Figure 3.14b shows that the tip contains only elements of Al and O. In this context, the growth process is considered different than an external catalyst supported growth.

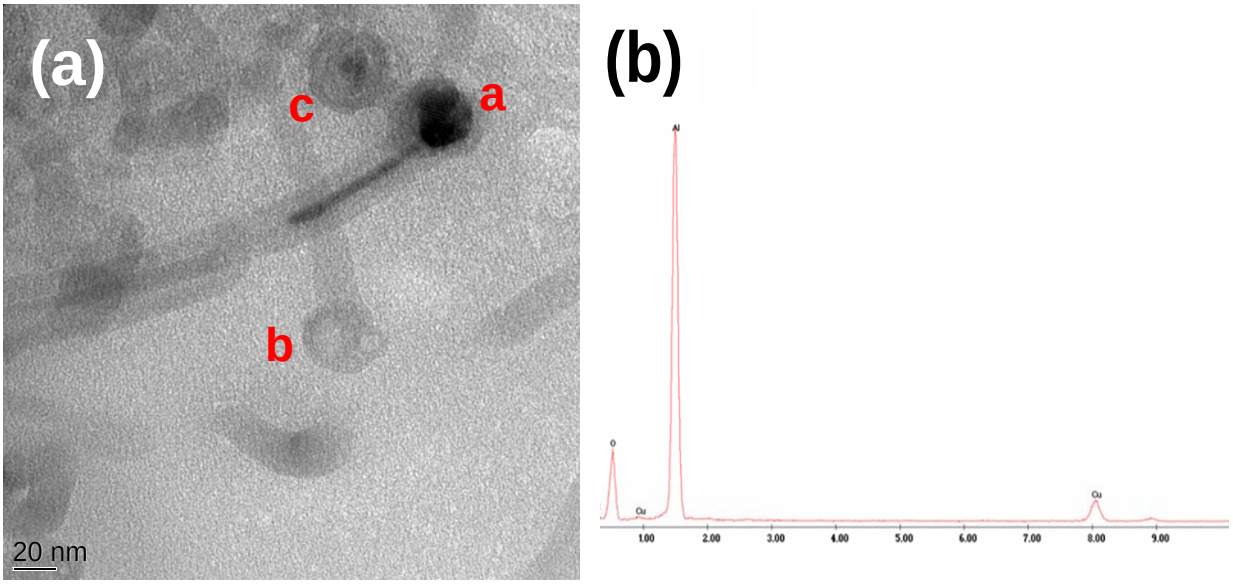


**Figure 3.14 (a) TEM image of Al·$Al_2O_3$ nanowires (b) EDX spectrum of the spherical particle found at the tip of the nanowire labelled with "a".**

In Figure 3.15 the HR-TEM image of the spherical particle found at the tip of a nanowire is shown. It is confirmed that the particle exhibits a core-shell type structure. A dark contrast exhibiting core is surrounded by a rather transparent shell, whose thickness

is ca. 4-5 nm. The shell and core both exhibit lattice fringes which resemble to crystalline phases. The lattice gratings of the core correspond to metallic Al. Although one can see a clear difference between lattice spacings of the shell and the core, it is difficult to mention the presence of a crystallographic orientation relation between them.

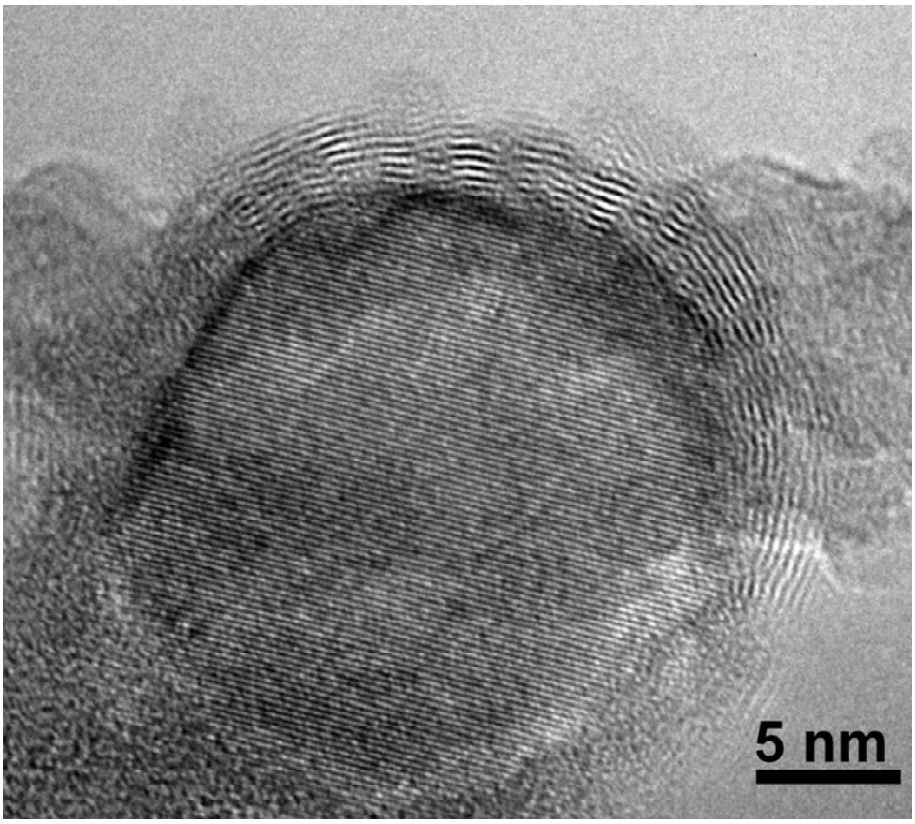


**Figure 3.15 HR-TEM image of a spherical particle found at the tip of a nanowire.**

In order to image the Al-$Al_2O_3$ interface in HR-TEM and derive the atomic structure, the interface must be observed edge-on to eliminate interference effects, for instance "Fresnel fringes". The interfaces have to be straight and without steps along the beam direction to be able to interpret the structure correctly. Our observations do not show such a well defined sharp transition between the core and the shell. The spacing between the lattice fringes and the contrast stay constant through the shell thickness. There is no additional high contrast fringe at the edge which is mostly seen at such interfaces due to Fresnel interference. In this context, we believe that such artefacts due to Fresnel fringes are not observed in our HR-TEM images.

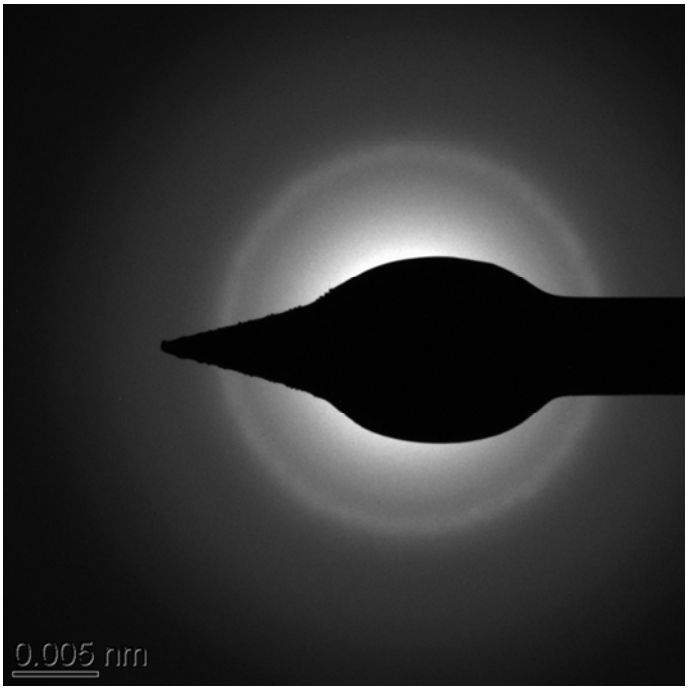


**Figure 3.16 Diffuse SAED pattern from deposited layers.**

The lattice spacings observed in the oxide shell may be attributed to δ- or γ-phase $Al_2O_3$. As we discussed previously in Chapter 3.3.1, it is not easy to distinguish between these two phases since the lattice spacings show little variations at some portions of the bend structure of the shell. Due to the curvature it is believed that some defects form which causes also discontinuities in the lattice fringes. The shell may be thought as a continuous arched ribbon which is composed of little crystallites separated from each other by small angle grain boundaries. It is known that such small crystallites may behave as cross-gratings which yield a poor resolving power [136]. Such an effect may also cause broadening of diffraction rings or, in some cases, overlapping of some rings. In addition, in the case of orientation of small crystallites along some definite directions, some diffraction rings may disappear [137]. These effects may lead to diffuse electron diffraction patterns. We observed such diffuse ring patterns in some of our SAED analyses, as shown in Figure 3.16. It is difficult to identify crystalline phases from such electron diffraction patterns.

Another difficulty in HR-TEM imaging of the deposited layers is the fast reduction of $Al_2O_3$ during the electron beam exposure. Especially when the beam is focused on a small area, $Al_2O_3$ transforms into Al within a very short time. This also affects our

interpretation. Sow observed similar difficulties during the TEM analysis of $Al{\cdot}Al_2O_3$ nanowires [129].

Based on our findings, a first growth mechanism is proposed which is valid for temperatures around 650±30°C (the melting point of pure Al is 660.4°C) where the metallic Al seems to serve as a catalyst, which forms from the phase separated metal entities in the fractal ball-like entities by an arrangement similar to Oswald ripening [138].

It seems that intermediate AlO vapor plays a major role in the growth of $Al{\cdot}Al_2O_3$ nanowires. The formal $Al^{+2}$ should be stabilized by the disproportionation into $Al^0$ and $Al^{+3}$, giving a stoichiometric ratio of 1:2 between $Al^0$ and $Al^{3+}$.This resembles findings from $Si/SiO_2$ core-shell particles and wires which are thought to evaluate from intermediate SiO by disproportionation into $Si^0$ and $Si^{4+}$ as shown by Lee et al.[55].

In an agreement with the earlier findings of Veith et al [139] we propose the following chemical routes which seem to govern the growth of $Al{\cdot}Al_2O_3$ nanowires. It is known that $(^t\text{BuOAlH}_2)_2$ decomposes into a glassy layer of HAlO at low temperatures, as shown in (3.6). We believe that at higher deposition temperatures this reaction may act as an intermediate reaction, which is followed by a subsequent de-hydration to AlO vapor, as shown in the reaction (3.7). The condensation of AlO on the substrate, as shown in the reaction (3.8), yields the Al precipitation followed by the growth of 1D Al structures covered by an oxide shell. It is believed that at extremely high deposition temperatures $(^t\text{BuOAlH}_2)_2$ decomposes directly into a AlO intermediate not following the pre-step given in (3.6) and condensation takes place directly.

$$1/2\,(^t BuOAlH_2)_2 \longrightarrow H_2 + H_2C = C(CH_3) + 1/\infty (HAlO)_\infty \qquad \textbf{(3.6)}$$

$$(HAlO)_\infty \longrightarrow \infty/2\,H_2 + \{(AlO)_\infty\} \qquad \textbf{(3.7)}$$

$$3/\infty \{(AlO)_\infty\} \longrightarrow Al + Al_2O_3 \qquad \textbf{(3.8)}$$

We believe that the decomposition of the AlO intermediate vapor on the heated substrate firstly results in the precipitation of Al nanoparticles which act as the nuclei of the Al nanowires covered by oxide shells. At high deposition temperatures the

precipitated Al seems to melt and stay in equilibrium with AlO vapor. This equilibrium drives the continuous 1D growth. On the other hand, it is believed that a temperature gradient provides also an external driving force for the growth of the nanowires. Therefore, local temperature gradients on the surface seem to be the reason for random and highly chaotic arrangement of nanowires. Such local temperature gradients on the substrate were imaged by a thermal camera, as shown in Figure 3.17.

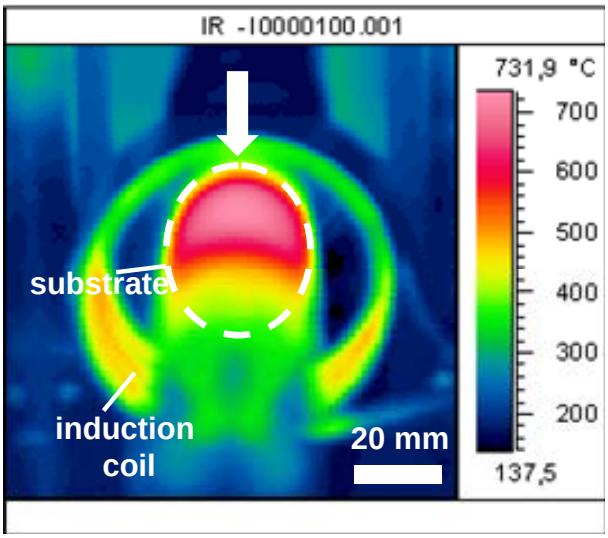


**Figure 3.17 Thermal camera image of the heated substrate during the deposition process.**

As marked by the arrow, upper parts of the substrate are heated more in comparison to the bottom parts. This may be a result of the inhomogeneous electromagnetic field distribution within the substrate. It is known that while a solid cylinder is heated by electromagnetic induction, a temperature gradient occurs from the surface to the core of the cylinder [140]. A similar effect is also observed in the cylindrical graphite block which we use as the substrate holder in our experiments. When the graphite block is shifted a few millimeters from the centre axis of the applied field, some parts are exposed to more field lines. This also causes an inhomogeneous heating on the surface of the substrate.

The proposed self catalysis mechanism for the nucleation and growth can help understanding the morphology of some 1D nanostructures. The nucleation and growth continue all the time during evaporation since the AlO vapor phase is generated continuously. These gaseous species may condensate either on the side surfaces or tips of the former nanowires. It is believed that tips containing Al seeds act as preferred

nucleation sites according to the mechanism discussed above. New nuclei may form on the nanowire tips with different crystalline orientations during the growth. The unfavourable nuclei can not grow fast along the nanowire and this may cause the change of the growth direction or trigger the re-nucleation, as shown in Figure 3.18a. The re-nucleation also results in the formation of junctions where new branches grow. The HR-TEM image taken from such a junction shows the branching of the nanowire in Figure 3.18b.

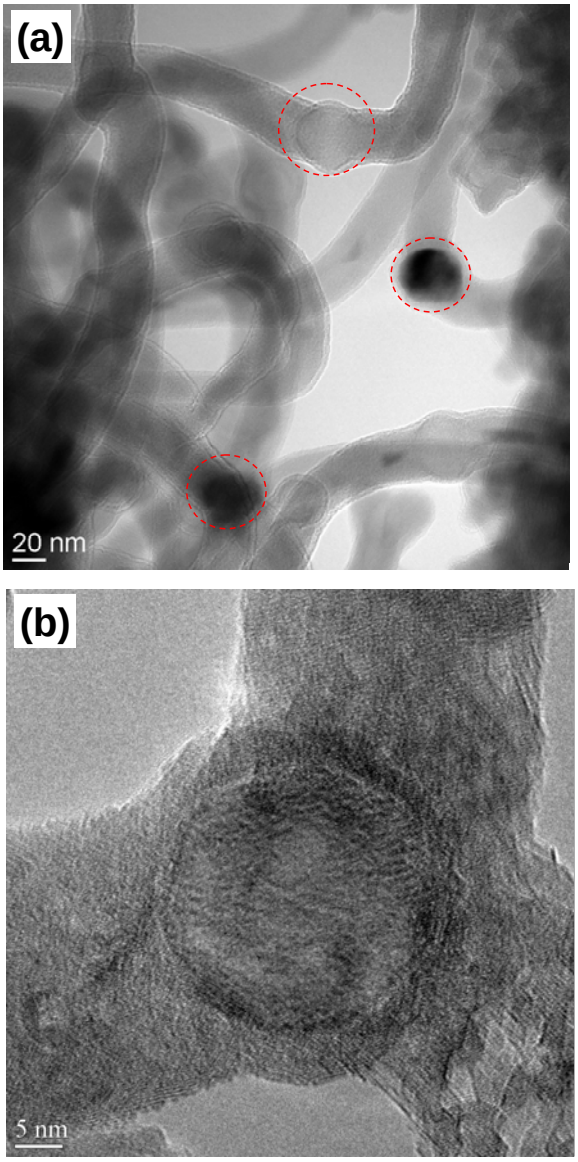


**Figure 3.18 (a) TEM image showing the change of the growth direction of the nanowires at Al seeds (marked with the red circles). (b) HR-TEM image showing the formation of a branched nanowire from the Al seed found at the tip.**

Figure 3.19 shows cross-sectional TEM images of deposited nanowires. The spherical Al particles at the tip of the nanowires are seen darker due to a good density contrast. As one can see clearly in Figure 3.19a, the seed particles are found denser on the surface of the substrate. This supports the idea that the growth starts from the Al molten seeds, which firstly form on the substrate at the beginning of the deposition process. In Figure 3.19b it is also seen that Al seeds at the tips of growing nanowires (marked with red circles) lead to the re-nucleation and growth of new nanowires.

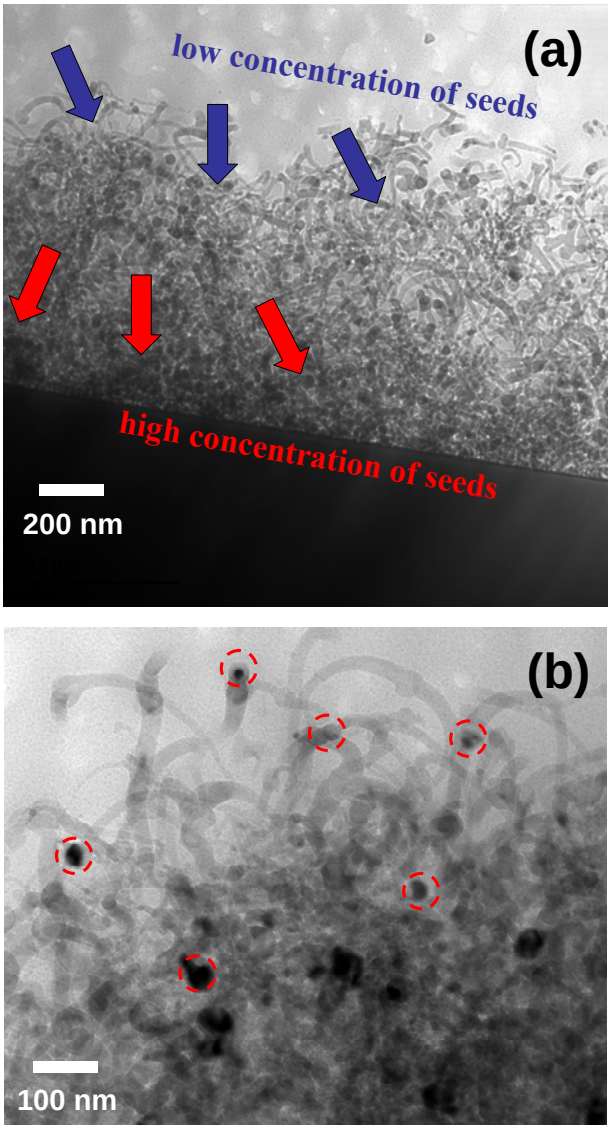


**Figure 3.19 Cross-sectional TEM images of the nanowires deposited on glass substrates. (a) Low magnification. (b) High magnification.**

### 3.3.2.2 Deposition at a Temperature far below the Melting Point of Al

Figure 3.20 shows SEM micrographs of the layers deposited on the glass substrates at 500°C, which is quite lower than the melting point of Al. Figure 3.20a shows that in early stages of the deposition, firstly large particles (200-250 nm) form which is followed by the interaction and clustering of these particles. In Figure 3.20b the SEM image shows that the particles assemble and 1D loop-like structures grow in further stages of the deposition process. These "nanoloops" are observed for the first time and have not been shown in previous research works concerning the synthesis of other 1D nanostructures using the same precursor,$(^{t}BuOAlH_2)_2$ [124,125,127,128 and 129].

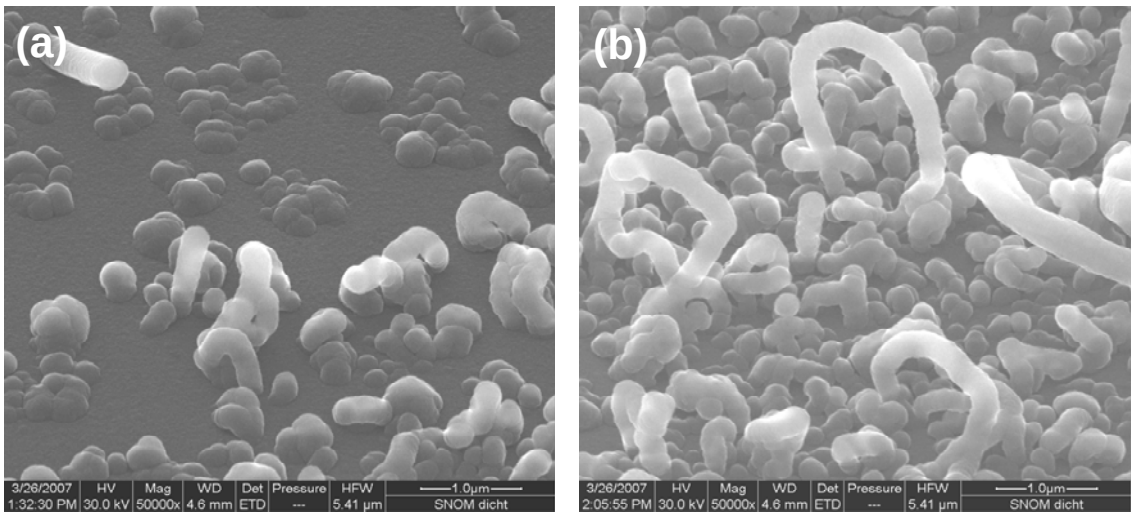


**Figure 3.20 SEM images of the layers deposited at 500°C. (a) Early stages of the deposition. (b) Formation of nanoloops in the further stages of the deposition.**

Such 1D structures differ from nanowires synthesized at high deposition temperatures in terms of their size and geometries. The diameter of a typical worm-like tubular structure is ca. 10 times larger than that of a nanowire presented previously. The growth mechanism of these larger 1D structures may be explained by a second growth mechanism. Taking a closer look, no round shaped seeds are seen, neither at the tips nor on any bended regions of the loop-like structures and this is an indication of a growth mechanism which is different than the catalyst supported nanowire growth. Therefore, it is believed that nanoloops grow basically by assembling of particles which reminds of the formation of nanorods through 1D clustering of nanoparticles by Oswald ripening [141].

Following the deposition at lower flow rates and temperatures slightly below the melting point of Al, firstly very large clusters begin to grow on the surface, as shown in Figure 3.21a. At the beginning of the deposition process the cluster density is very low in comparison to the total surface area of the substrate. It is believed that this may result from the low substrate temperature. Glass substrates are preferred in order to eliminate any metallic catalysis effect. In addition; glass is the optimal substrate for controlling the level of heating at low temperatures, since metallic substrates on a graphite holder are heated additionally due to the electromagnetic induction.

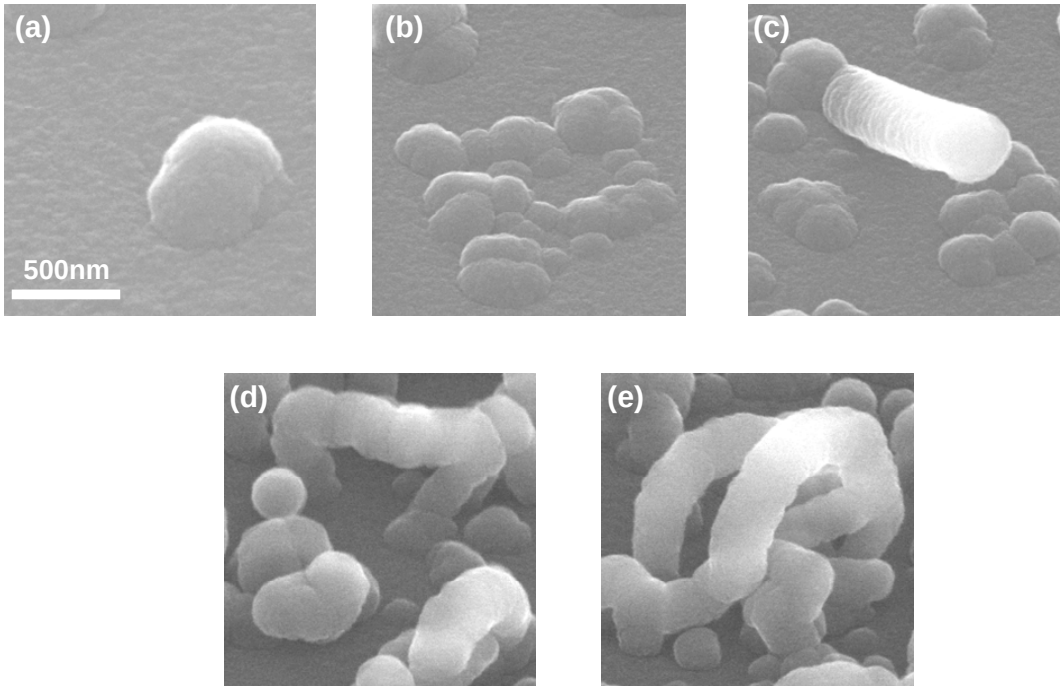


**Figure 3.21 SEM images showing the stepwise growth of nanoloops. (a) Cluster formation (low nucleation density). (b) New clusters nucleated nearby the former clusters. (c) Directional growth between cluster groups. (d) Joining of worm-like structures head-to-head. (e) Closed loop-like structures after the joining of the worm-like structures.**

During the deposition previously nucleated clusters seem to act as preferred nucleation sites for new clusters. Cluster-cluster interaction induces a sort of agglomeration which reminds of Oswald ripening, as one can see in Figure 3.21b. Indeed, the nucleation of new clusters on the former ones rather than a random landing triggers a directional growth (Figure 3.21c). This effect is mostly observed between two adjacent cluster groups. While the directional growth goes on, two or more worm-like

structures may meet head-to-head (Figure 3.22d) and finally this ends up with a closed loop structure as shown in Figure 3.21e. These nanoloops are mostly seen on some parts of the substrate surface where the nucleation density is higher. This is also an evidence for the proposed 1D growth mechanism based on particle-particle interaction and ripening. It is known that Al ion diffuses much faster than the oxygen [142] and during the interaction of the particles, diffusion may lead to a continuous core formation within the shell. The overall proposed growth mechanism is illustrated schematically in Figure 3.22.

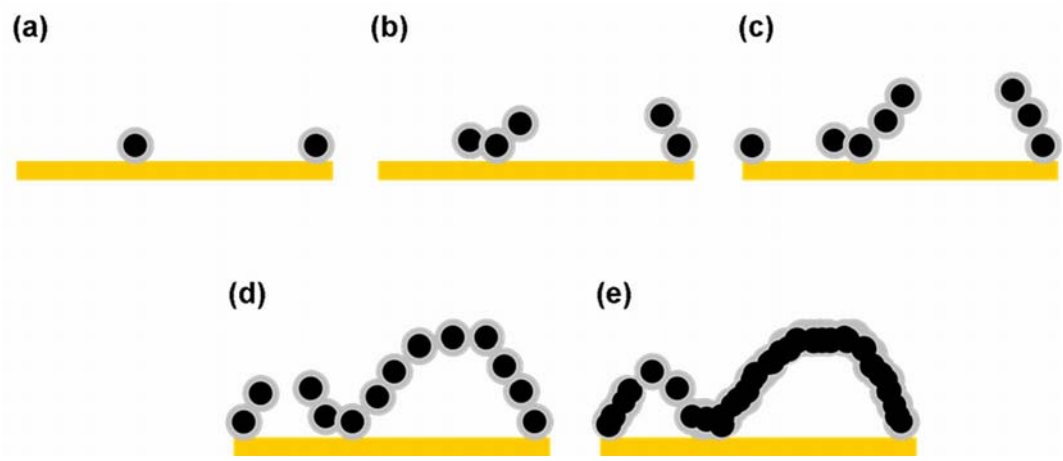


**Figure 3.22 Schematic drawing showing the steps of the loop-like structure formation. (a) Nucleation and growth of particles upon condensation of the gaseous species. (b) Nucleation and impinging of new particles join the former particles. (c) Directional growth starting from the initially nucleated clusters. (d) Joining of worm-like structure and loop formation. (e) Closed loop-like-structures and formation of continuous Al core following the diffusion between attached particles.**

We believe that the deposition temperature is the most critical point determining the growth mode. When the deposition temperature is kept below the melting point of Al, the catalyst based approach seems to fail. In addition to this direct effect, the temperature influences also the nucleation density. Naturally, at low temperatures less gas molecules are adsorbed on the substrate's surface. The formation of fewer nuclei retards the particle-particle interaction on the surface; therefore the growth of isolated particles can be observed clearly. The low nucleation density triggers also the nucleation of new particles preferentially on former particles rather than a random nucleation on the substrate. In this context, the flow rate of the precursor is also critical in the same

manner. The growth process may be governed by controlling the nucleation density with applying different substrate temperatures and precursor flow rates. In the following sections such approaches will be presented in detail.

### 3.3.3 Controlling the Growth of 1D nanostructures: Effect of the Flow rate and Temperature

It is clear that, at temperatures reaching or exceeding the melting point of Al, a self catalytic growth seems to occur. On the other hand, there is a totally different growth mechanism at lower deposition temperatures well below the melting point of Al. In addition to this fact, within both temperature regimes dynamic changes or gradients in temperature are believed to act as the external driving force for the growth. In this context, different deposition temperatures were applied to see the effect on the morphology. As a comparison, the SEM images of the layers deposited at 550°C and 630°C are shown in Figure 3.23a and b, respectively.

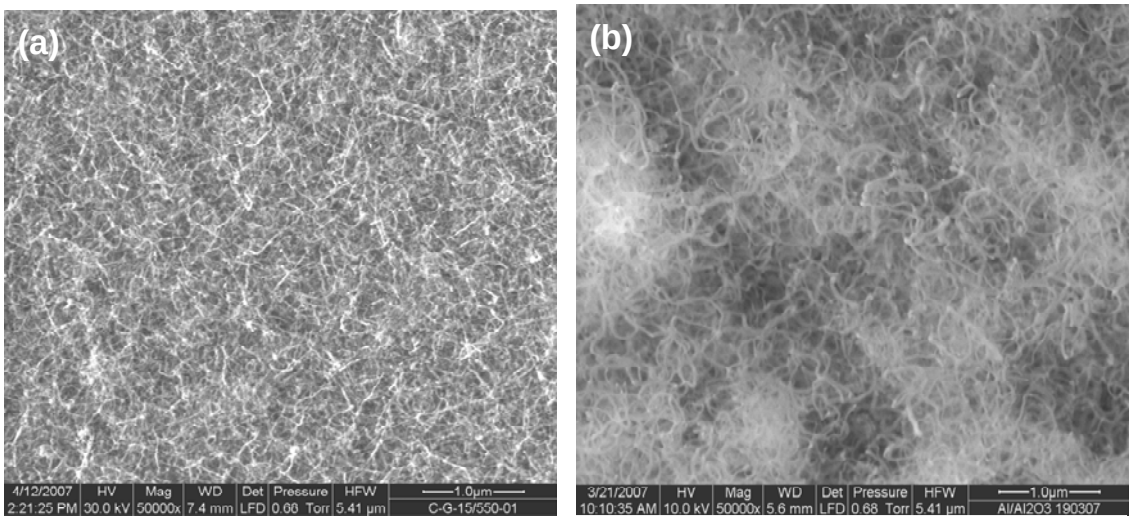


**Figure 3.23 SEM images of nanowires deposited at (a) 550°C and (b) 630°C.**

There is a clear difference between the morphology of the layers deposited at two different temperatures. The layer deposited at 550°C is composed of shorter and less tangled nanowires whereas the layer deposited at 630°C is composed of bundles of longer and more chaotic nanowires. Actually, the size and the geometry of the nanowires deposited at 630°C remind of the growth mechanism which we proposed for the growth of $Al{\cdot}Al_2O_3$ nanowires from Al seeds at high temperatures above the melting point of Al.

In a typical deposition process the substrates are heated by induction heating and the substrate temperature is monitored by the help of a thermocouple contacted to the substrate holder. Although the thermocouple shows a substrate temperature of 630°C, using a thermal camera it is observed that the temperature reaches to 700°C in some parts of the substrate. It is known that the melting temperature of a nanoscaled material is lower than that of its bulk form [143]. According to the mechanism discussed before, it is believed that at a deposition temperature above 600°C, molten Al seeds may form where the 1D growth starts. Due to dynamic temperature fluctuations, the Al seed may switch between the solid and molten states several times. In every change the seed may trigger a new 1D growth which leads to the formation of branched nanowires. As seen in Figure 3.23b, there are some bundles where the nanowires are dense. This may be due to the local temperature rise and nucleation of more Al seeds on more heated regions of the substrate surface.

In addition to the thermal camera analysis, the presence of local temperature gradients can be understood by giving a closer look at the morphology of the layers deposited on different parts of the substrate. The edges of the substrate are in a good contact with the graphite block and the upper half part of the substrate is heated up more due to the high concentration of the electromagnetic field, as shown previously in Figure 3.17. SEM images taken from different regions of the sample are shown in Figure 3.24.

In Figure 3.24a a particle-particle interaction type arrangement is seen which is consistent with the second growth mechanism as we have proposed for the low deposition temperatures. The worm-like structures remind of the early stages of the formation of loop-like structures. There are also a few tiny nanowires grown from the bigger particles. Due to thermal gradients, such particles seem to be heated locally to higher temperatures exceeding the melting point of Al. From the differences in morphologies of the tiny nanowires and the larger 1D particle arrangements it is clear that there should be two different growth mechanisms.

Figure 3.24b shows a SEM image taken from the middle part of the substrate. While larger particles are seen in the background, there are also tiny nanowires and thicker rod-like structures. The rod-like structures have spherical particles at their tips (marked with circles) which remind of the nanowires grown from Al self-catalyst nanoparticles at high

deposition temperatures. Such thick 1D structures should not be mixed with the 1D arrangement of larger particles shown in Figure 3.24a. As one can see, these worm-like structures are in the form of 1D assemblies of particles. Such assemblies do not form 1D continuous tubular structures. In comparison, rod-like structures (Figure 3.24b) are continuous 1D structures. It is believed that the size of the initial Al seed defines the size of the growing 1D nanostructure. Therefore, Al seeds found at tips of rod-like structures are larger than the ones found at the tips of nanowires.

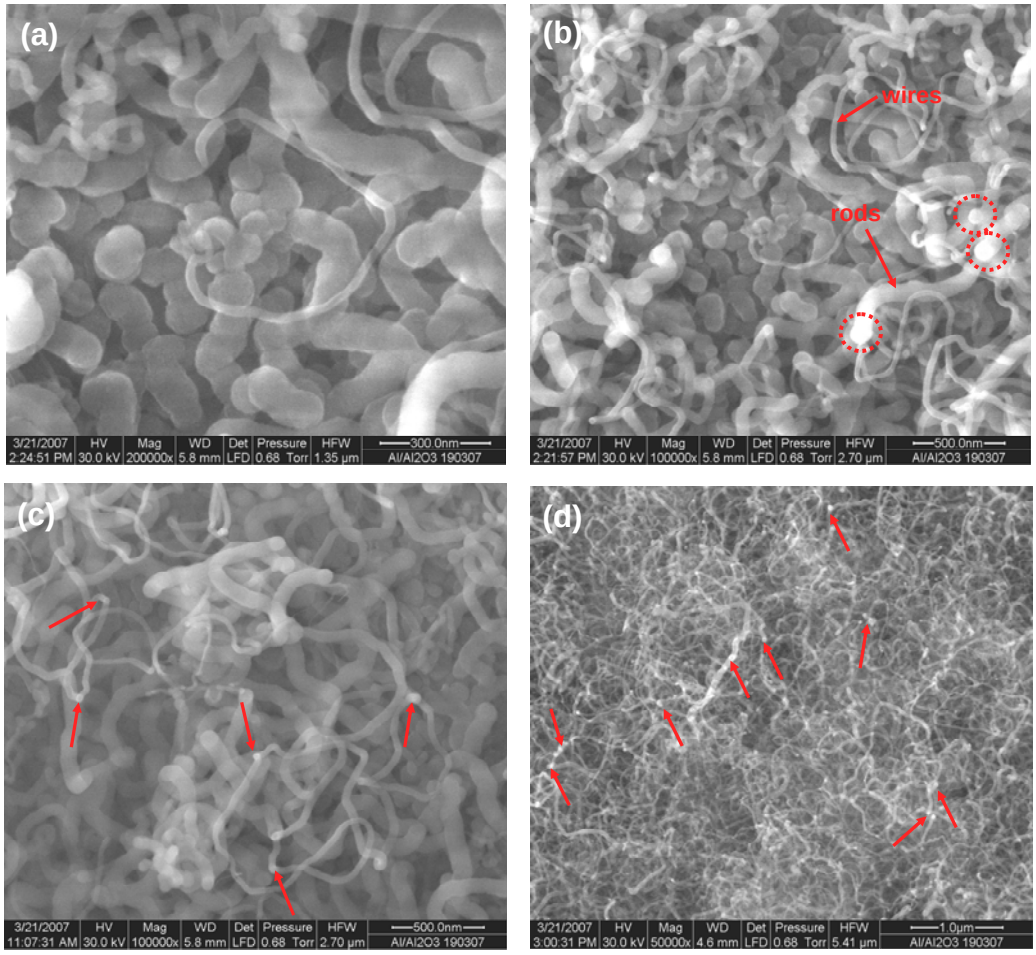


**Figure 3.24 SEM images of the deposited layers taken from different parts of the substrate (a) Bottom part of the substrate which is heated relatively less. (b) Middle part of the substrate. (c) Upper part of the substrate which is heated relatively more. (d) Upper edge of the substrate which is in contact with the graphite substrate holder.**

The SEM image given in Figure 3.24c is taken from a region near the upper edge of the substrate which is heated more in comparison to bottom parts. One can see that there are more tiny nanowires in this region which is a direct indication of a higher substrate

temperature. These nanowires contain spherical nanoparticles as marked with the arrows. Indeed, these particles are the nuclei (Al seeds) of the nanowires. During the deposition process new nanowires seem to be nucleated at the Al seeds found at the tip of former nanowires. This effect is seen more pronounced in the SEM image (Figure 3.24d) taken from the upper edge of the substrate. The arrows in Figure 3.24d show that several junctions form upon the re-nucleation. New nanowires grow from the Al seeds found at the tips of former nanowires. They cause highly interpenetrating and branched nanowires. The proposed mechanism concerning the seed effect and junction formation is explained schematically in Figure 3.25.

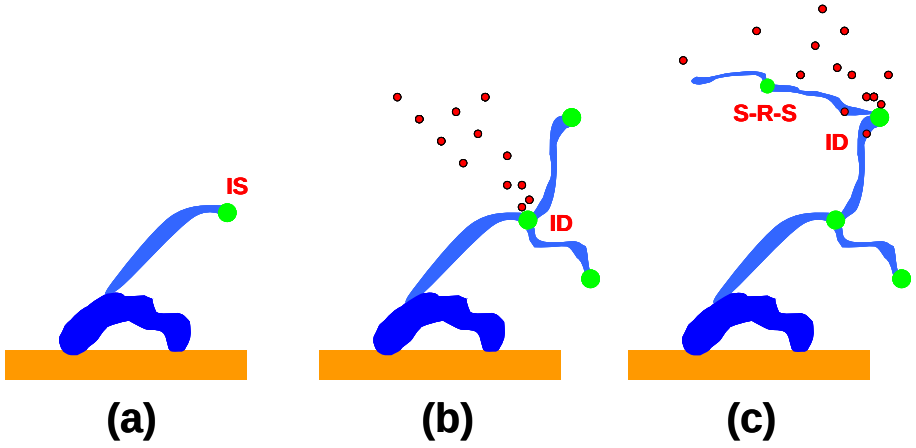


**Figure 3.25 Schematic drawing showing the steps of the branched nanowire formation. (a) Pushing of the Al seed up during the 1D growth. (b) Nucleation of new structures following the condensation of the gaseous species at the former Al seeds and growth of new nanowires. (c) Further condensation of the gaseous species at the former Al seeds which is followed by a re-nucleation and change of the growth direction.**

In the first stage (Figure 3.25a) a tiny nanowire starts growing from an Al seed nucleated on previously grown worm-like structures. The catalytic Al seed is pushed up by the growth of the wire, which usually is observed in a typical VLS growth process. In the second step (Figure 3.25b) new gaseous species are deposited at the tip where the Al seed is still at a meta-state between solid and liquid phases. This initial seed triggers the growth of two new nanowires. In the third stage (Figure 3.25c) it is shown that such a branching repeats at the tip of the freshly grown nanowires. In addition, Al at the tip of a nanowire may solidify for a short period when the surface temperature is slightly lower than the melting point of Al. Following the thermal gradients the solidified tip can be re-

melted due to dynamic heating conditions of the HF electromagnetic induction. This re-melting of Al seeds may induce again a self-catalyst supported growth. It is believed that further nucleation or solidification-re-melting cycles at the Al seeds increase the number of the branched wires.

Another factor which may influence the nucleation and the density of the chaotic arrangement of the wires is the flow rate of the precursor. Keeping the deposition temperature constant at 650°C, different flow rates were used to see the effect of the flow rate on the final morphology. Figure 3.26a and b show the low magnification SEM images of deposited layers at a low flow rate (1/4 open valve) and extremely high flow rate (completely open valve), respectively. At a low flow rate a more regular arrangement of the nanowires is seen (Figure 3.26a). Although the nanowires are randomly orientated, they form a homogenous and continuous layer. The layer deposited at a high flow rate exhibits a highly chaotic structure which reminds of fibrous bundles as presented in Figure 3.26b. This may be attributed to the increased re-nucleation on the active Al seeds found at the tips of the grown nanowires.

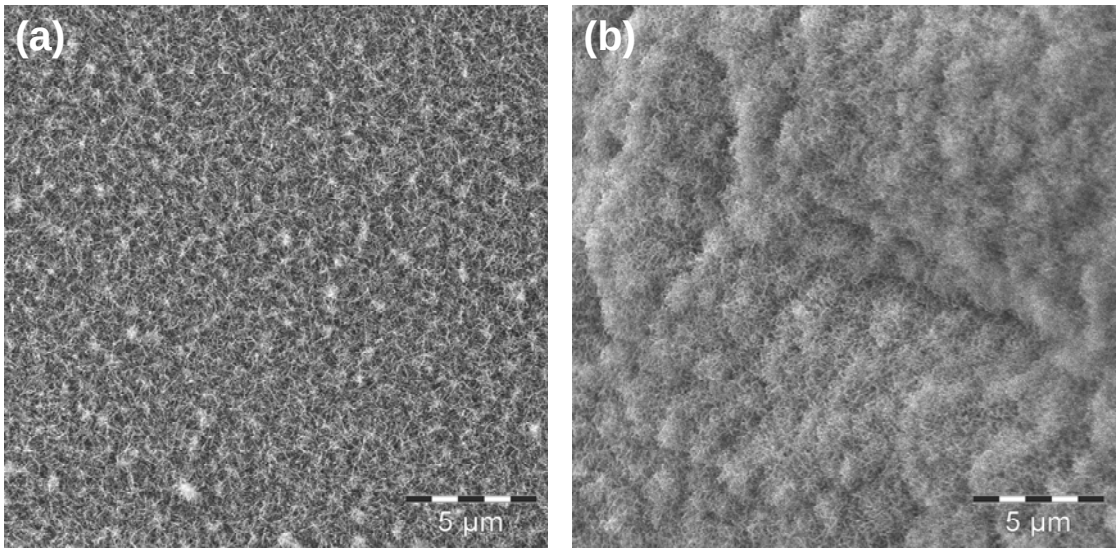


**Figure 3.26 SEM images of the deposited layers at a (a) low flow rate and (b) high flow rate.**

### 3.3.4 Selective CVD (SCVD)

In the previous chapters we presented the effect of the temperature gradient on the growth of $Al{\cdot}Al_2O_3$ nanowires with different examples. It is clear that different structures form depending on the local temperatures on the substrate surface. In this

context, a controlled temperature gradient was induced using partially Au coated glass substrates to control the structure of the deposited layers. The preparation of Au metal coated templates is explained in Chapter 3.2.2. Au is selected purposely due to its inertness at the deposition temperatures and good thermal conductivity.

A partially Au coated template is illustrated schematically in Figure 3.27a. Figure 3.27b shows the thermal camera image of such a template heated by the electromagnetic induction. The temperature at Au coated regions (marked with white arrows) is higher than that of the glass regions (marked with blue arrows).

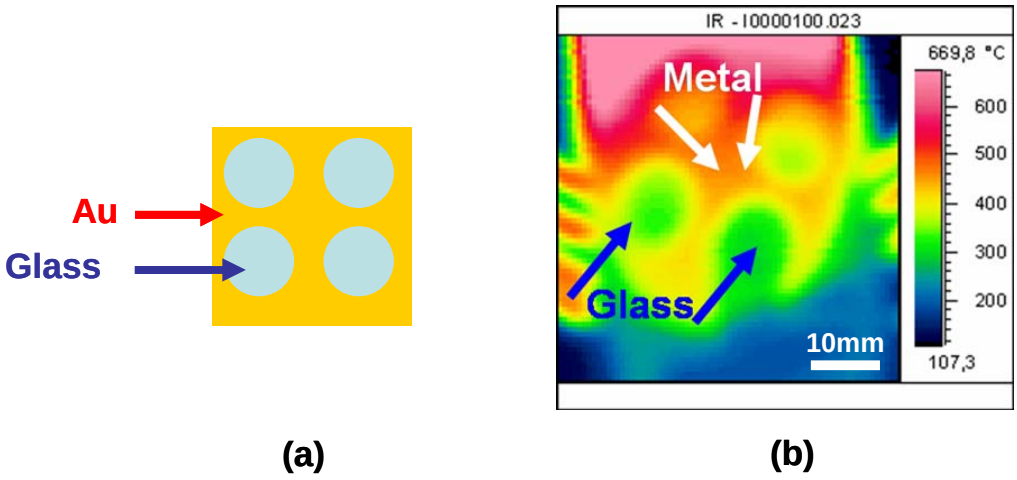


**Figure 3.27 (a) Schematic drawing showing the partially Au coated glass substrate. (b) Thermal camera image of the substrate (Au/Glass) which is heated by electromagnetic induction during the deposition.**

Different substrate temperatures were applied to deposit 1D nanostructures selectively on the Au coated regions. Figure 3.28 shows SEM images taken from the Au coated and non-coated regions of the glass substrate after the deposition process carried out at 575°C. The inserts indicate the part of the template where the corresponding image is recorded. One can see that there are spherical particles on the glass portion of the substrate (Figure 3.28a). This reminds of our previous observations concerning the nucleation of Al seeds prior to the growth of Al·$Al_2O_3$ nanowires. The growth of 1D structures is seen on the glass part near to the Au coated region (Figure 3.28b). This morphology can be attributed to early stages of the 1D growth. The density of such 1D structures increases on the Au coated region (Figure 3.28c). At the edges of the Au coated template (which is in contact with the graphite holder) we found the highest

density of the wires (Figure 3.28d). Such a purposely induced thermal gradient provides a controlled way to observe the intermediate steps of the growth which was explained previously by analyzing the different parts of the substrate in Chapter 3.3.3.

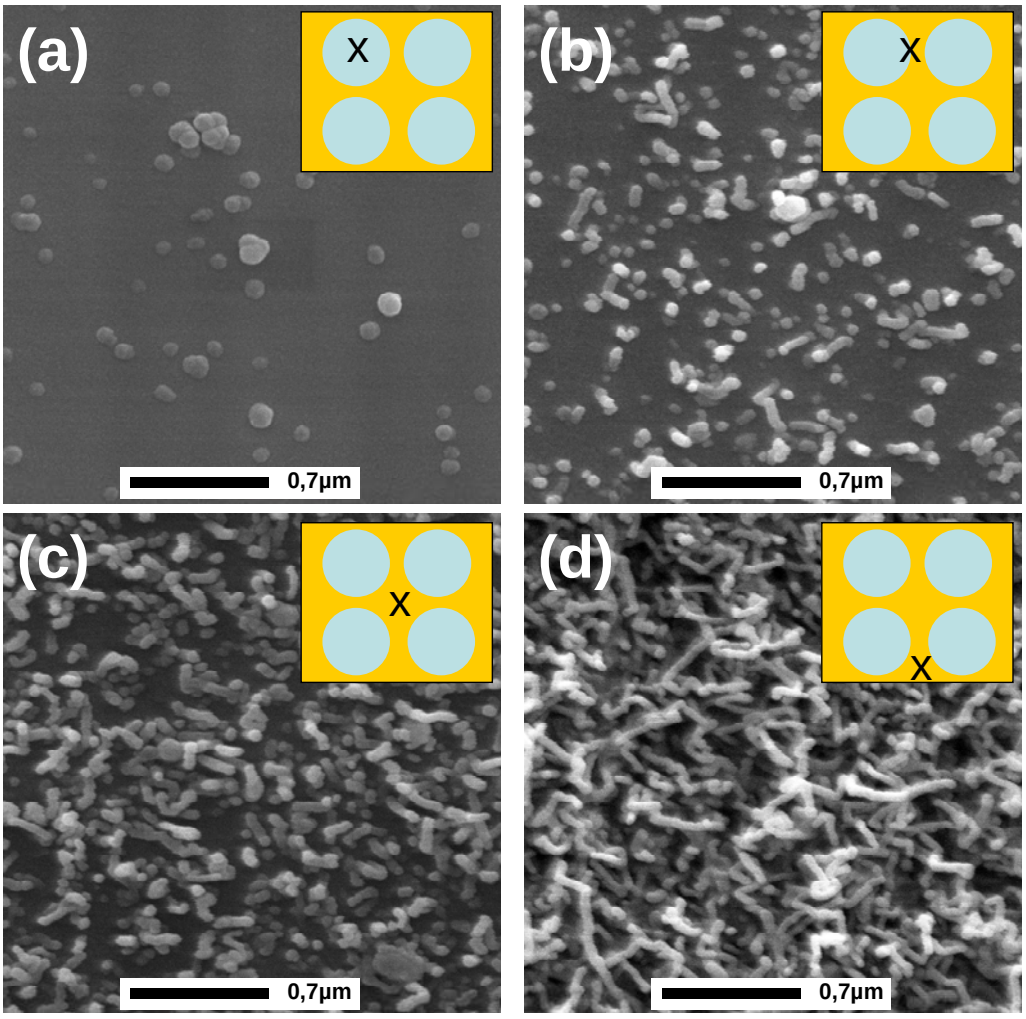


**Figure 3.28 SEM images of the layers deposited at different parts of the partially Au coated glass substrate. (a) Non-coated glass part. (b) The border between the glass and Au coated region. (c) Au coated region. (d) The edge of the Au coated region which is in contact with the graphite holder.**

### 3.3.5 Laser Assisted CVD (LCVD)

#### *3.3.5.1* Thermal Effects

A quantitative analysis of a pyrolytic processing based on local substrate heating requires a detailed knowledge of the laser induced temperature-distributions. Direct temperature measurements have been performed with a reliable degree of accuracy in only a few cases. In our experimental work we used a focused laser beam and this makes

the direct measurement approach fail. In addition, the material properties such as the absorption coefficient, thermal conduction etc. change with the increase of the temperature within a small volume reaction zone. In many cases the measurement techniques can not be applied satisfactorily for practical reasons, so a method of calculating the laser-induced temperatures is desirable.

In our experiments we used tungsten (W) as the substrate material since it exhibits relatively less reflection and a high melting point in comparison to other metals. Assuming the absorption goes to infinity and there is no loss of heat; we calculated the center-temperature rise ($T_{max}$) on the surface of the tungsten substrate using the equation (3.9) which is proposed by Bäuerle et al. [144],

$$T_{\max} = \frac{P(1-R)}{2\sqrt{\pi\kappa w_o}} \approx 0.89 \frac{I_a w_o}{\kappa} \qquad \textbf{(3.9)}$$

where: **P**: laser power; **R**: reflection of the substrate; **κ**: thermal conductivity; $\mathbf{I_a}$: absorbed laser intensity; $\boldsymbol{w_o}$ :half-beam waist. In Figure 3.29 the change of the maximum temperature rise on the W substrate with the increase in the laser power is presented graphically.

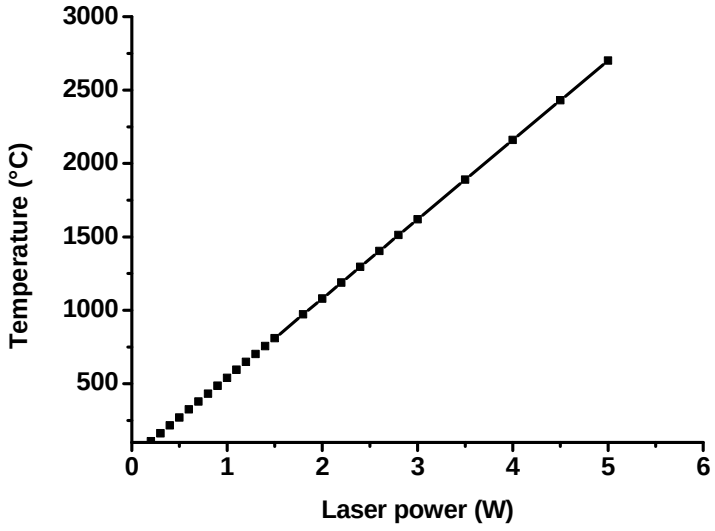


**Figure 3.29 Maximum temperature rise in the center of the focused laser beam.**

While the maximum temperature rise occurs at the center of the focused laser beam, a Gaussian temperature distribution is seen around the center of the irradiated area. This radial temperature distribution can be approximated using the equation (3.10),

$$\Delta T(r^*,0) \approx \frac{T_{\max}}{\sqrt{1+r^{*2}}} \qquad \textbf{(3.10)}$$

where $\boldsymbol{T_{max}}$ is the maximum temperature rise in the center of the focused laser beam and $\mathbf{r}^*$ is the normalized radius (with respect to the beam radius). The curve in Figure 3.30 which is calculated using the equation (3.10) shows the temperature distribution near the center of the laser irradiated area at different laser powers. The insert given in Figure 3.30 is the real thermal camera image recorded during the laser irradiation at a power of 1.5 W.

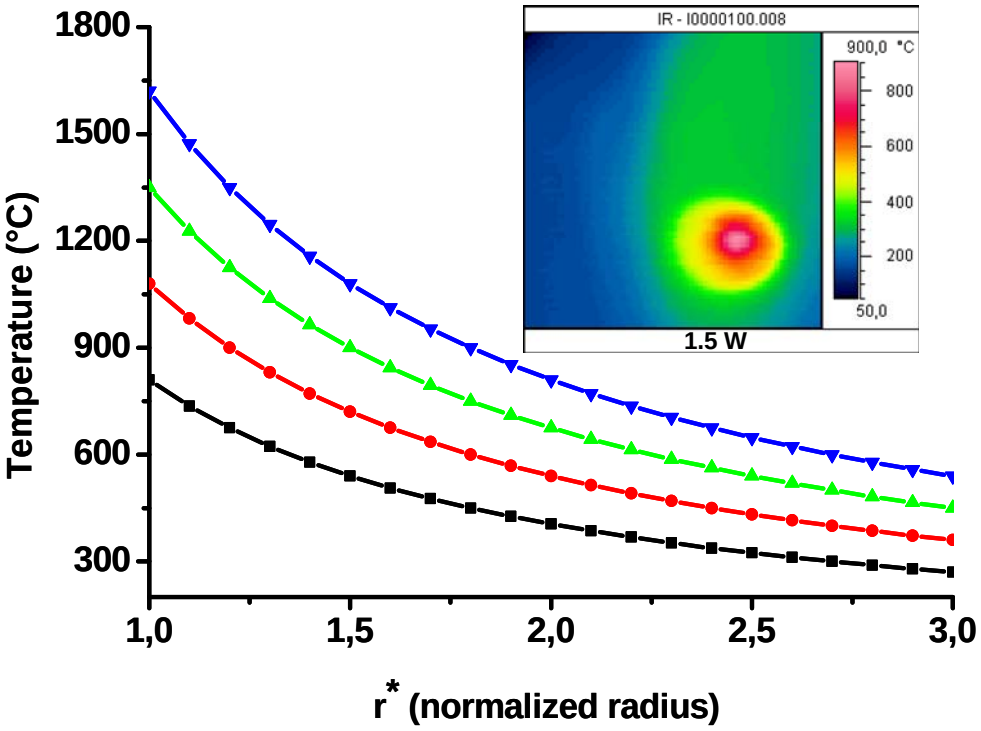


**Figure 3.30 Temperature distribution induced by Gaussian laser beam irradiation on the substrate.**

As seen in the insert of Figure 3.30, there is a clear Gaussian type temperature distribution within the laser irradiated area. On the other hand, it is not possible to get the exact temperature at a specific point due to the low resolution of the thermal camera. In this context, in our LCVD processes the surface temperature is estimated with the help of theoretical calculations presented in (3.9) and (3.10).

In a laser scanning process the average fluence of the laser on the surface changes and a non-stationary heat source model should be taken into consideration. On the other hand, it is known that at a scanning speed of $v_s < 10^4$ μm/s the center temperature rise is essentially unaffected by the scanning speed [145].

#### 3.3.5.2 Morphology: Effects of the Scanning Speed, Laser Energy and Flow Rate

Since the decomposition of precursor molecules is activated thermally in a typical pyrolytic LCVD process, the morphology of the deposits strongly varies with laser induced temperature distributions. In our LCVD process the substrate was moved in one direction perpendicular to the focused laser beam. Therefore, the morphology of the deposits depends on the scanning speed and the laser power which effects the temperature distributions. In addition to temperature-distributions, the transport of reactants into the reaction volume is also critical for the morphology of deposits. In the following sub-chapters such process parameters and their effects on the structure and morphology are discussed separately.

**Effect of the Scanning Velocity**

The effect of the scanning velocity is studied by applying various scanning velocities at a constant average laser power of 2 W and a moderate gas flow rate (1/2 open valve). In Figure 3.31 thermal camera images recorded during the deposition process are presented. When a high scanning velocity of 5 mm/s is applied, the temperature rise seems to be lower than the calculated value of 1080°C, as one can see in Figure 3.31a. Since the calculations are based on a stationary heat source, it is natural to observe less heating in the case of a high scanning speed. At a scanning speed of 1 mm/s

or lower the measured temperatures (shown in Figure 3.31b, c and d) are in a good consistent with the calculations.

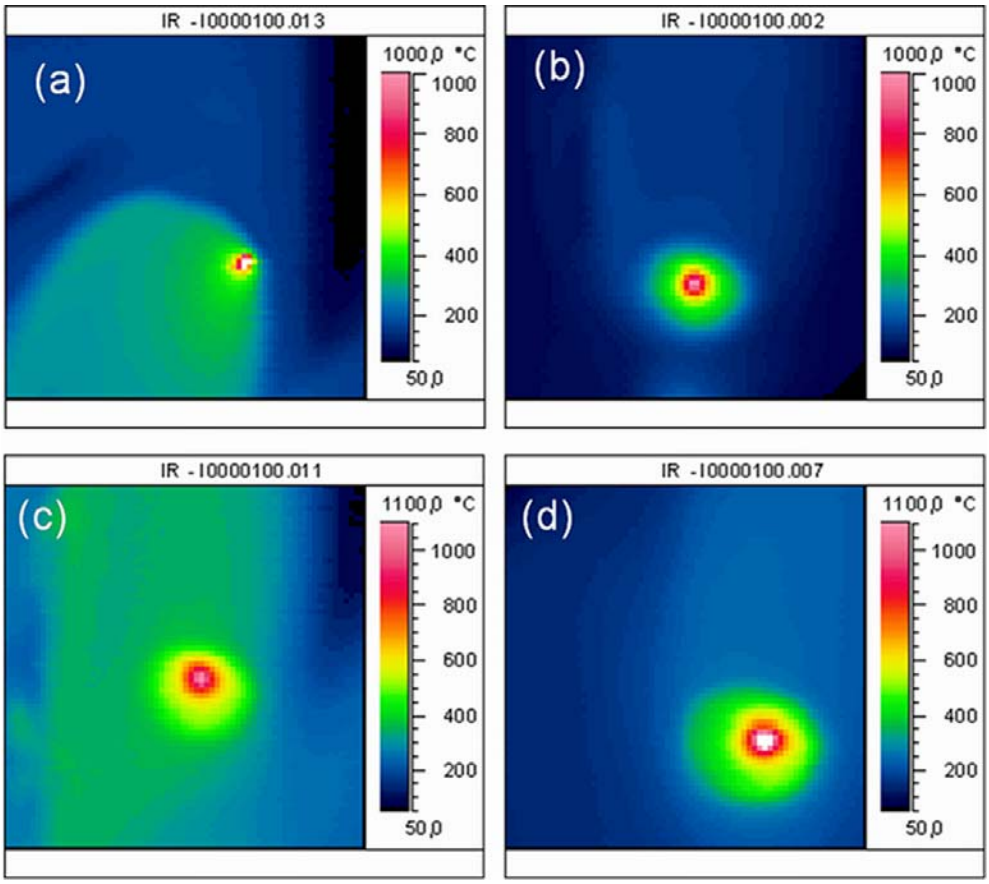


**Figure 3.31 Thermal camera images recorded at different scanning speeds. (a) 5 mm/s. (b) 1 mm/s. (c) 0.5 mm/s. (d) 0.025 mm/s.**

As seen in Figure 3.32a, at a high scanning velocity of 5 mm/s a discontinuous deposit is formed. The temperature seems to be not high enough for the complete decomposition of the precursor. When the scanning speed is decreased to 1 mm/s, a clear increase in the deposit mass is observed, as shown in Figure 3.32b. The deposits are composed of inhomogeneous agglomerates rather than a well defined continuous layer. When the scanning speed is decreased further to 0.5 mm/s, the formation of nanoparticles is observed (Figure 3.32c). It seems that at low scanning speeds enough thermal energy is provided to the reaction zone and this starts the nucleation of particles. This effect is seen more clearly when a much lower scanning speed of 0.025 mm/s is employed (Figure 3.32d). These observations show the effect of the scanning speed or illumination time on the morphology clearly. A high scanning speed leads to a very low

temperature rise on the substrate surface which is not sufficient for a complete decomposition and a proper nucleation.

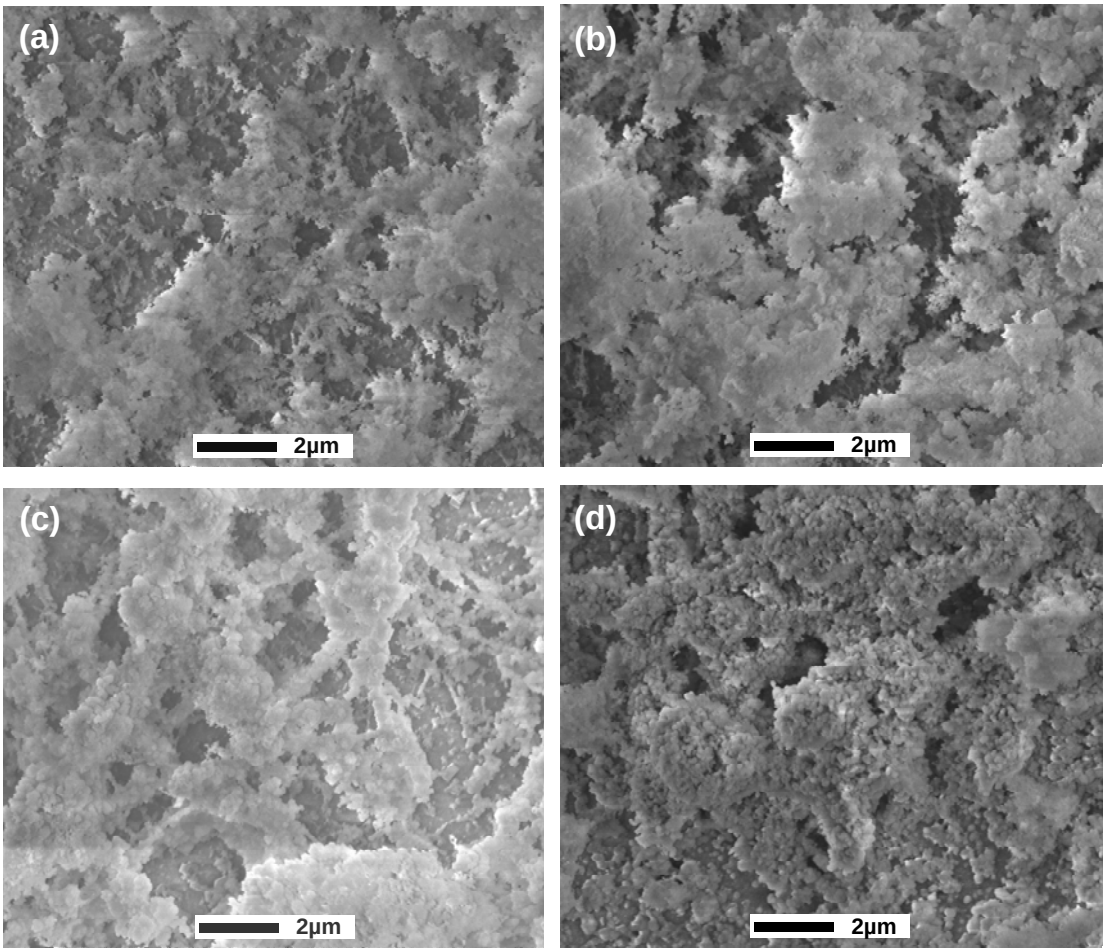


**Figure 3.32 SEM images of deposited layers at scanning speeds of (a) 5 mm/s. (b) 1 mm/s. (c) 0.5 mm/s. (d) 0.025 mm/s.**

### Effect of the Laser Intensity

At very low scanning speeds the maximum temperature rise mainly depends on the laser power. In order to see the effect of the temperature on the morphology, various laser powers were employed at a moderate flow rate and a scanning speed of 0.025 mm/s. At such a low scanning speed the laser beam acts as a stationary heat source. As one can see in the thermal camera images recorded during the deposition (Figure 3.33a), the temperature in the centre of the focused laser beam exceeds 1000°C at a laser power of 2 W, which is in a good agreement with calculated values. At a laser power over 2 W,

the centre temperature rise exceeds the limit of the thermal camera, so the absolute temperature measurement fails (Figure 3.33b and c).

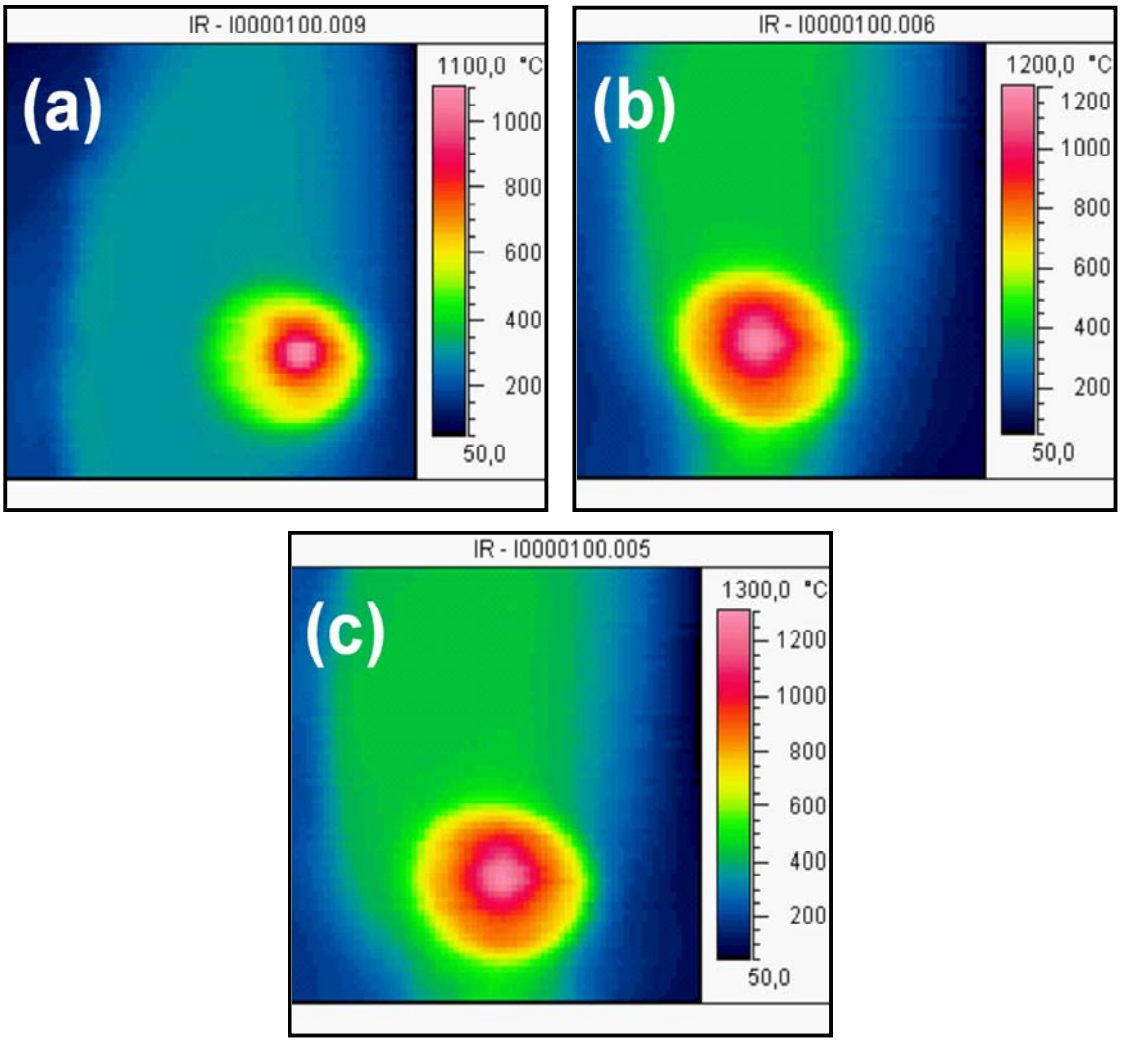


**Figure 3.33 Thermal camera images recorded at different laser powers. (a) 2 W. (b) 2.5 W. (c) 3 W.**

As shown in Figure 3.34a, a layer composed of aggregates reminding of the fractal-like structures form at a laser power of 2 W, which corresponds to a centre temperature of ca. 1000°C as estimated from our calculations.

On the other hand, the temperature distribution (Figure 3.33a) should be taken into account rather than a peak value. When the laser power is increased to 2.5 W under the same conditions (the same scanning speed and flow rate), some nanoparticles start growing (Figure 3.34b). At a higher laser power of 3 W this growth continues and larger microparticles form, as seen clearly in Figure 3.34c.

It is believed that an increase in the laser power triggers the nucleation of the nanoparticles. The growth of the particles with increased laser power is an indication of a kinetically controlled growth regime.

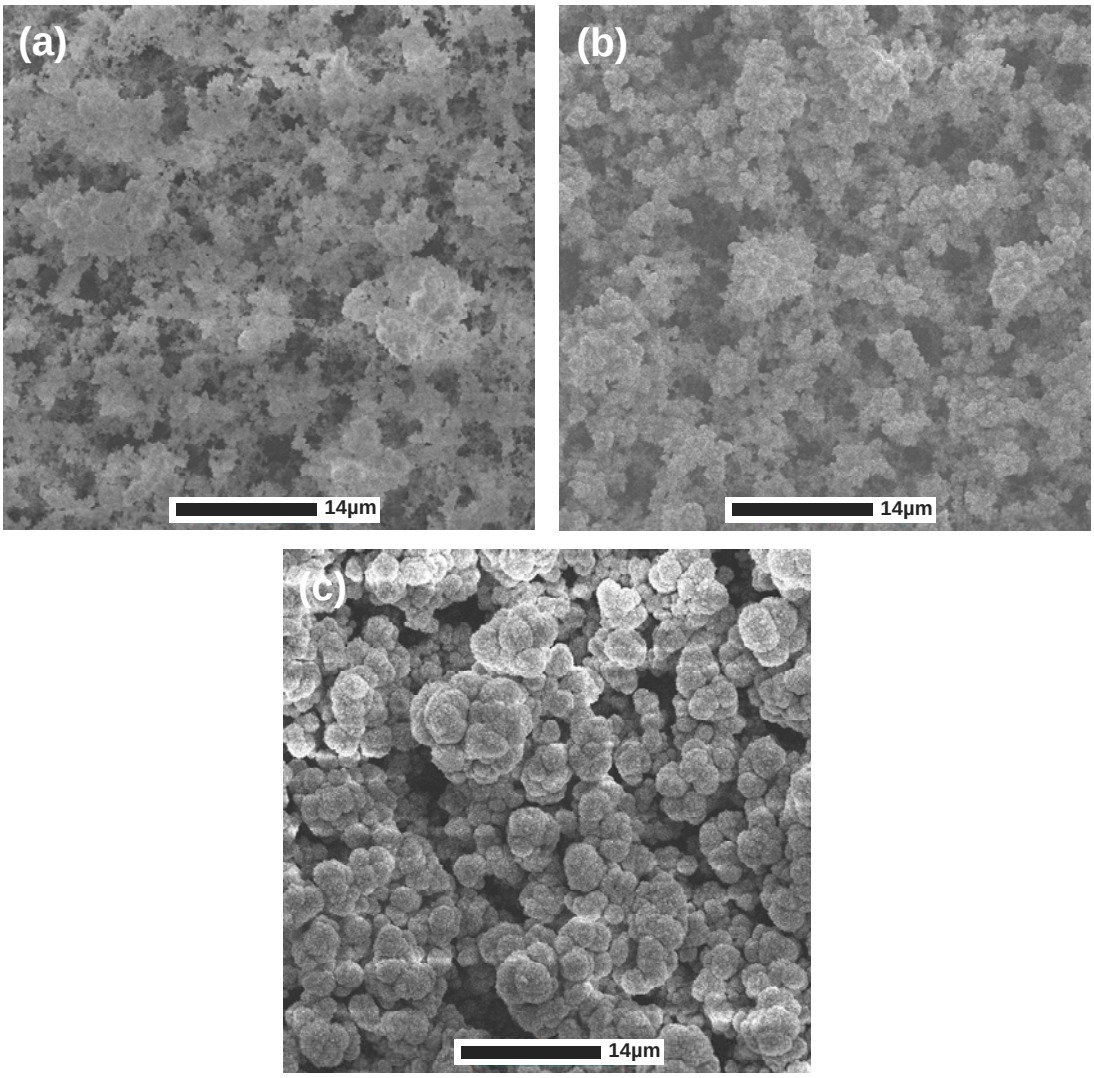


**Figure 3.34 SEM images of the deposited layers at different laser powers of (a) 2 W, (b) 3 W and (c) 4 W.**

### Effect of the Flow Rate

After showing the effect of the laser power and the scanning speed on the morphology, the effect of the flow rate on the deposition is studied by altering the flow rate employing a constant laser power and a scanning speed of 2.5 W and 0.025 mm/s,

respectively. As shown in Figure 3.35a, some fibrous-structures form when a high flow rate is applied by opening the precursor flow valve fully (4/4 open). The layer beneath the fibrous structures reminds of the formation of microparticles, as shown previously in Figure 3.34c.

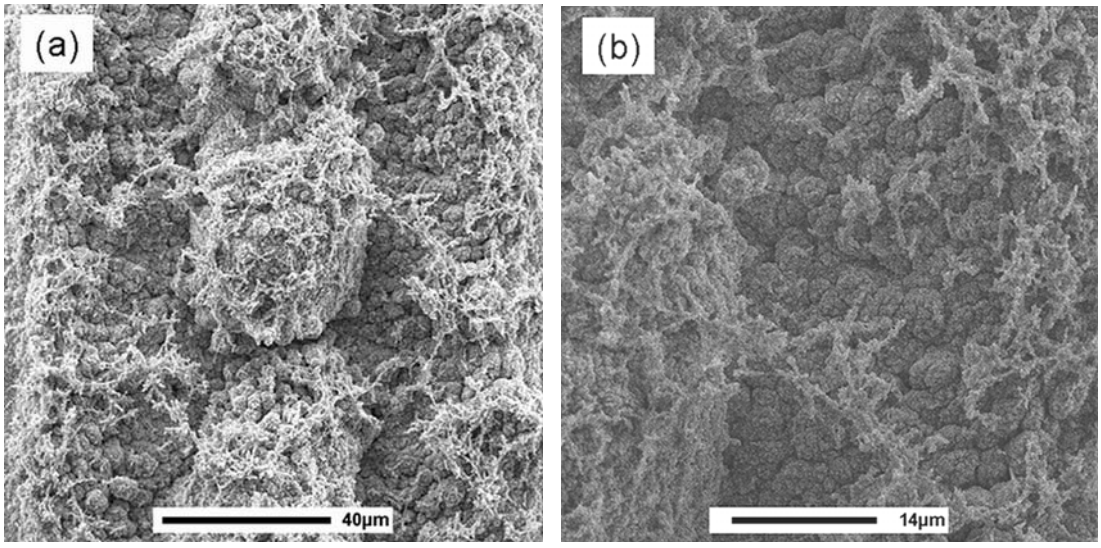


**Figure 3.35 SEM images of deposited layers at a high flow rate of the precursor. (a) Low magnification. (b) Higher magnification.**

It seems that firstly the layer composed of microparticles forms and the fibrous layer is grown up over this pre-deposited layer. The firstly deposited layer has a reflectivity different from the substrate material. Due to this change in the reflectivity the amount of the laser energy absorbed by the deposit may change during the deposition. In addition, the pre-deposited layer has a different thermal conductivity and geometry than the bare metallic substrate. These dynamic changes may induce a temperature gradient which is believed to act as an external driving force for the fibrous growth.

In Figure 3.35b it is seen clearly that the fibrous density is higher on previously formed hill-like particles rather than in the valleys. The possibility of the impingent of random walking reactive molecules on the rough microhill-like surfaces is much higher in comparison to the relatively smooth underlying layers. This resembles to Stranski-Krastanow type of growth where the formation of islands is observed on the preferential nucleation sites. EDX analysis shows that, while Al:O at % is 57:43 on the micro particles, this ratio drops to 51:49 in the case of fibrous structures grown on microparticles. There is no significant change in the composition and these findings

resemble to the compositional analysis of the nanowires deposited by the thermal CVD process.

### 3.3.5.3 Process Optimization and 1D Nanostructure Fabrication using LCVD

We have shown that at high flow rates fibrous structures are deposited. It is believed that excessive heating induces the growth of a layer composed of the microparticles beneath. In this context, the scanning speed is increased to eliminate any excessive heating. It is known that when the scanning speed is kept very low, the laser acts as a stationary heat source. In the case of a high scanning rate (2 mm/s), a high flow rate (4/4 open valve) and a moderate laser energy (2 W), chaotic 1D structures form, as seen in Figure 3.36a.

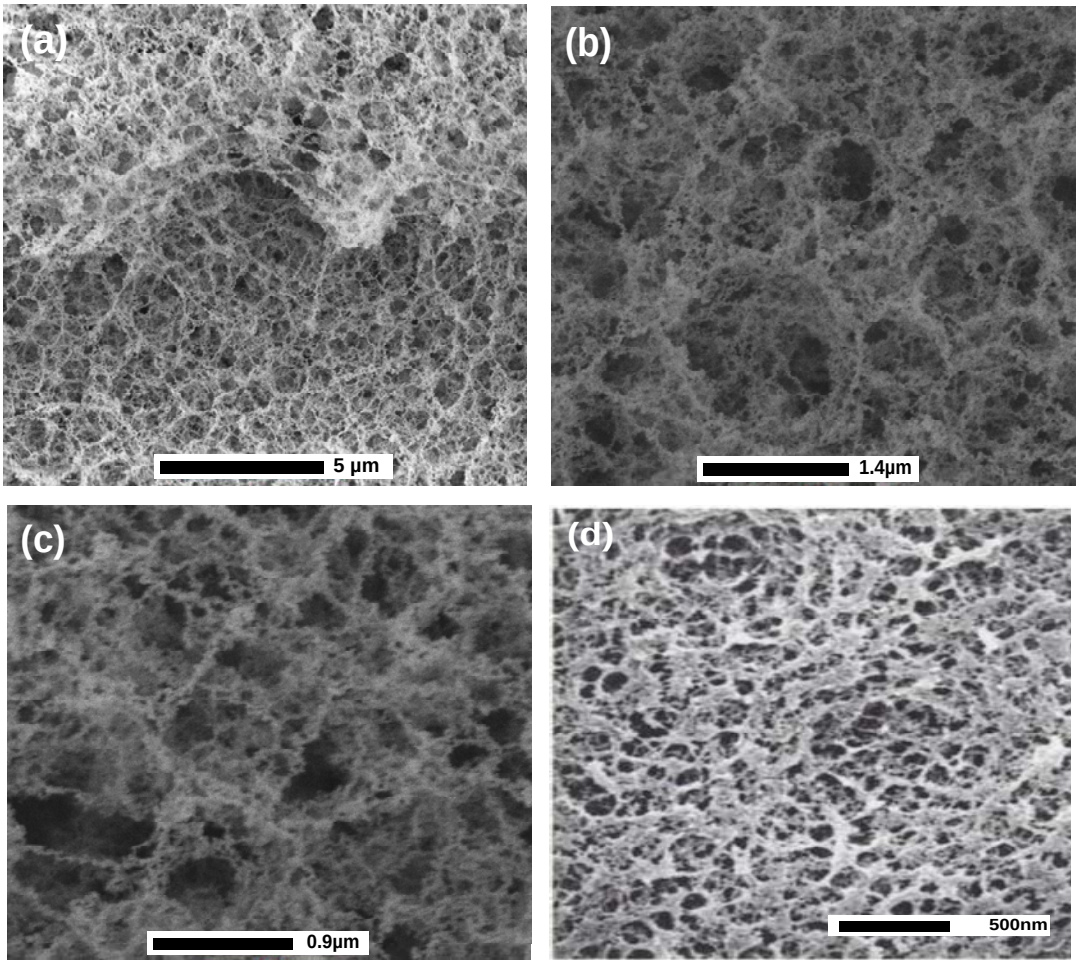


**Figure 3.36 SEM images of deposited layers. (a) Overview. (b) Low magnification. (c) High magnification. (d) SEM image of the basement membrane of a corneal ECM [146].**

In order to understand the 1D structure growth in detail, only the laser power is increased to 3 W while keeping the flow rate and scanning rate constant in another set of the deposition experiments. Basically, again a similar fibrous structure forms. On the other hand, there is a clear increase in the width of 1D structures, as shown in Figure 3.37a. The SEM images in Figure 3.37b and c show that the wire-like structures indeed look like 2D nets formed by 1D assembling of nanoparticles. In some regions the 1D structure is totally lost due to high and random agglomeration. It seems that higher laser powers trigger the formation of particles as presented previously. The EDX compositional analysis shows that Al:O at. % varies in the range of 54:46 to 43:57 which is comparable to our earlier findings.

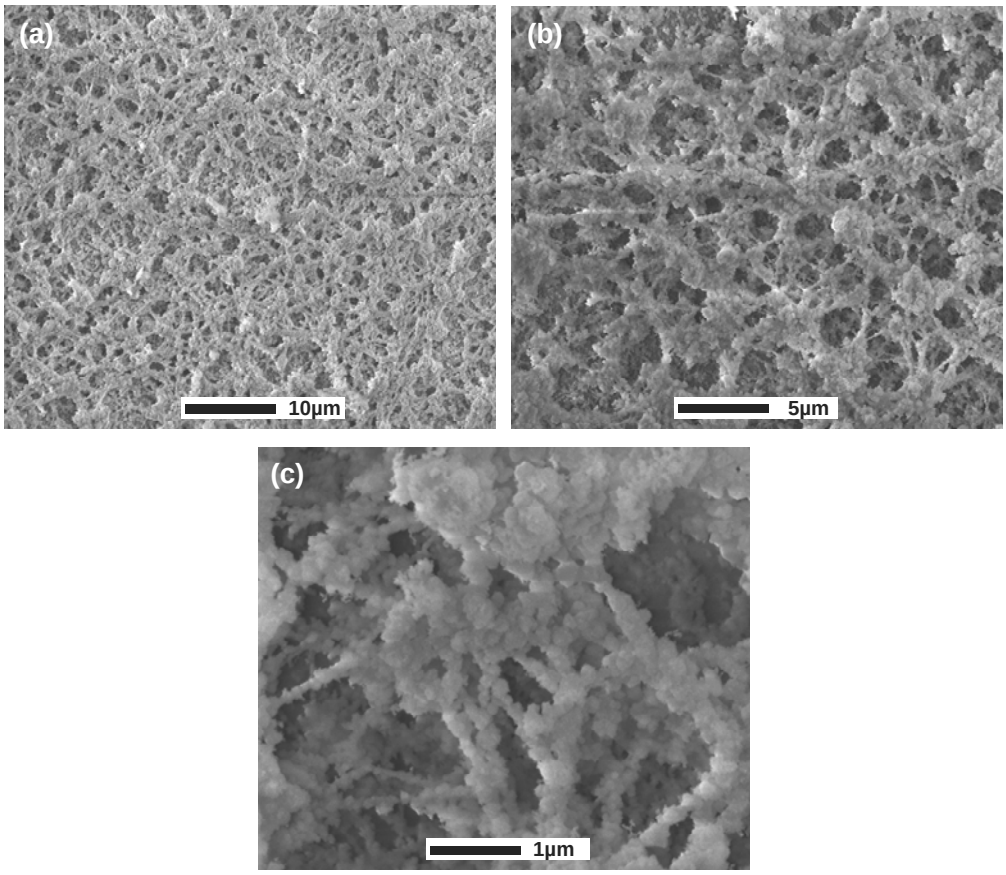


**Figure 3.37 SEM images of deposited layers at 3 W laser power and 2 mm/s scanning speed.**

The temperature distribution induced by the absorbed laser light is believed to act as the external driving force for the directional assembling of particles and growth. The highly chaotic arrangement seems to be the consequence of the dynamic temperature distribution on the substrate which moves under the focused laser beam.

# 4. Laser Treatment of 1D $Al{\cdot}Al_2O_3$ Nanostructures

The surface modification of alumina ceramics is extremely important due to the increasing use of alumina ceramics in structural, electronic and biomedical applications where the performance is determined basically by surface properties [147]. Lasers have been employed successfully to improve the surface properties of alumina ceramics through structural and chemical transformations [148].

Laser treatment of alumina ceramics represents a big challenge because of the high melting point of alumina. In most of these processes a high power laser is required to melt the alumina. At high power densities it is difficult to form dense layers due to large thermal gradients and thermal shocks [149]. Such problems are mostly solved by using a powder mixture of alumina and a second material which has a lower melting temperature. This additive material acts as a binder for alumina powders [150].

Using a low melting temperature inorganic binder normally results in leaving behind an undesired phase, e.g. using ammonium phosphate results in the formation of aluminum phosphate following the laser treatment along with alumina [151]. Alternatively, using organic binders significantly reduces the time and power density required to form dense parts under the laser beam. Since organic binders have low melting temperatures, they require a lower amount of energy to melt and bond the surrounding ceramic powders. On the other hand, organic binders should be removed before further sintering at high temperatures. Unfortunately, this requires careful, long and costly steps [152].

The use of a metal additive, such as aluminum which can be oxidized further to alumina, may be a compromise approach to synthesize dense and pure alumina. In this current work we present laser treatment of $Al{\cdot}Al_2O_3$ composite prepared by CVD of $(^t\mathrm{BuOAlH_2})_2$.

## 4.1 Laser Material Processing

Laser, an acronym for **L**ight **A**mplification by **S**timulated **E**mission of **R**adiation, basically is a coherent and monochromatic beam of electromagnetic radiation. There are different types of lasers operating at different wavelengths ranging from ultra-violet (UV) to infrared (IR). Lasers can deliver a very low (mW) to extremely high (1–100

kW) power with a precise beam size and interaction/pulse time ($10^{-3}$ to $10^{-15}$ s) on any kind of substrate through any medium [153].

Experimental investigations of the laser assisted materials processing began to appear soon after the first demonstration of the ruby laser in 1960 [154]. Due to technical limitations in stability and beam quality of early lasers, technological developments in laser assisted material processing have been dominated by the developments of the laser technology itself [155]. After various commercial types of lasers became standard products on the market, lasers found more applications in the field of the material science and engineering. Today lasers are used especially in welding, bonding, cutting, drilling and shaping of a wide variety of materials [156].

Above all, laser assisted surface treatment is a subject of a considerable interest because it offers the chance to synthesize new kinds of materials with ideal surface properties. Currently, the use of lasers in surface treatment includes *surface heating* (hardening [157] and annealing [158]), *surface alloying* (wear [159] and corrosion protection [160]), *surface melting* (microstructure control [161], surface sealing [162], rapid solidification [163]), *surface texturing* (roughness altering [164], tribology [165], bio applications [166]), *laser marking* [167] and *micro machining* [168].

The high energy density and directionality of the laser permits strongly localized heat- or photo-treatment of materials with a spatial resolution better than 1 μm [169]. Employing advanced optical approaches, such as "near-field optics", a laser may also be used as a nano-machining tool with a resolution down to 30 nm [170]. The monochromaticy of the laser light allows a precise control of the heat treatment depth or a selective non-thermal excitation within the surface of the material. Different laser modes including pulsed or continuous wave (CW) irradiation can be employed in order to control the laser-material interaction time. The laser may induce physical or chemical changes, or both, on a material. The laser processing can be divided in three main groups in terms of interaction mechanisms [171]:

**1. Photo-thermal processing**

In this type of laser processing thermal effects of the laser beam induce some changes on the surface or within the material. Although a non-thermal excitation by the laser light can be observed also, the rate of thermalization is much higher than that of the

excitation. In this context, the whole process is fully characterized by the temperature and enthalpy of the system [172].

**2. Photo-chemical processing**

This approach is based on a non-thermal interaction of the laser light and the material. Such a non-thermal interaction can occur in different ways including dissociation of chemical bonds, activation of reactive species (photo-initiator, photo-polymers etc.), and change of the concentration [173].

**3. Photo-physical processing**

Photo-physical processing is a combination of the chemical activation and thermal effects induced by the laser light. On the other hand, it is not easy to put sharp borders between photo-thermal and photo-chemical processes. In various photo-chemical processes the thermal effect of the laser on the reaction rate can not be neglected totally. Some photo-polymerization reactions can be thought as a hybrid process where physical and chemical changes occur simultaneously with the laser irradiation [174].

| | | |
|---|---|---|
| **Design Parameters** | **Laser** | Power, $P_l$ [W] |
| | | Wavelength, $\lambda$ [nm] |
| | | Coherency, [mrad] |
| | | Mode, $TEM_{xy}$ |
| | | Polarization, ***V/H*** |
| | | Beam diameter, $w$ [mm] |
| | **Material** | Absorption coefficient, $\alpha$ [$cm^{-1}$] |
| | | Reflectance, $R$ [%] |
| | | Thermal conductivity, $\kappa$ [W/cm K] |
| | | Specific heat, $c_p$ [J/g K] |
| | | Melting point, $T_m$ [K] |
| | | Density, $\rho$ [$g/cm^3$] |
| | | Surface roughness, $R_a$ [nm] |
| **Process Parameters** | **Process** | Final spot size, $w_0$ [mm] |
| | | Scanning speed, $v_{scan}$ [cm/s] |
| | | Ambient medium, air/protective gas |

**Table 4.1 Design and process parameters in a laser assisted material processing.**

In this presented work photo-thermal processing (pyrolytic processing) is considered. In such an approach a laser serves as the local heat source. The quantative analysis of the pyrolytic processing based on the local substrate heating requires a detailed knowledge about the laser beam characteristics, material properties and process parameters as listed in Table 4.1.

## 4.2 Characteristics of a Laser

The energy of a laser is in the form of a concentrated beam of electromagnetic radiation. In industrial laser applications mostly Gaussian laser beams (profile for the cross-section of the irradiance $I(x,y)$) are preferred. Figure 4.1 shows the irradiance distribution of a Gaussian beam operating in the fundamental mode ($TEM_{00}$).

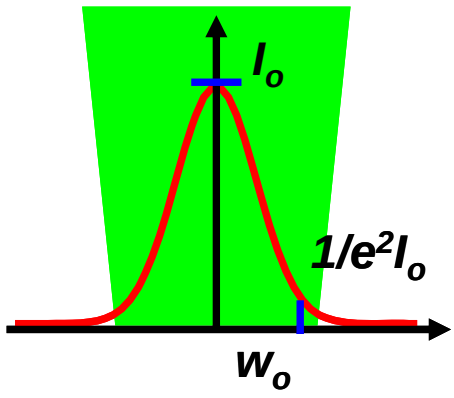


**Figure 4.1 Gaussian laser irradiance.**

For a position exactly on the surface of the material, the irradiance of the beam can be described by the expression [145] given in (4.1),

$$I(x,y,0) = I(r,0) = I_0 \exp\left(\frac{2r^2}{w_0^2}\right) \qquad \textbf{(4.1)}$$

where $r^2=x^2+y^2$ and $w_o$ corresponds to the "Gaussian Half-width", which occurs at $1/e^2$ of the maximum irradiance, $I_o$. The total power $P_T$ of the laser beam acting over the surface area **A** is thus defined in (4.2).

$$P_T = \int_{r=0}^{r\to\infty} I(r,t)dA = \int_{r=0}^{r\to\infty} I_0 \exp\left(-\frac{2r^2}{w_0^2}\right) 2\pi r dr = \frac{\pi}{2} w_0^2 I_0 \qquad \textbf{(4.2)}$$

Apart from the power, the wavelength, coherency, mode and polarization define the characteristics of a laser. The wavelength of the laser depends on the transitions taking place by the stimulated emission. There are various types of lasers operating at different wavelengths, as shown in Figure 4.2. Another important characteristic of a laser is the coherency. In comparison to standard random light, the coherence length may be many meters long in the case of lasers. This long coherence length allows a good interference which is required in some technical applications including the interferometry and holography. In material processing longer coherence lengths are needed in some of the surface treatment processes, for instance "laser interference lithography".

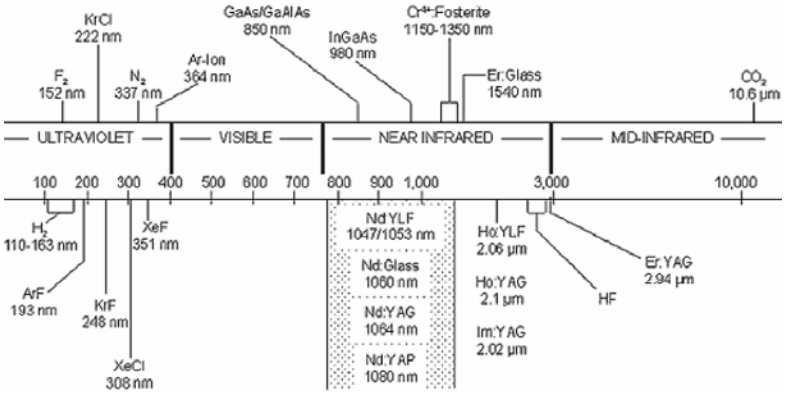


**Figure 4.2 Lasers with different wavelengths.**

The mode pattern of the laser affects the distribution of the output beam energy, which is a critical point in laser material processing. Modes are the standing and oscillating electromagnetic waves which are defined by the cavity geometry of a laser. When these modes oscillate, they interfere with each other, forming the transverse standing wave pattern on any transverse intersection plane. The $TEM_{(pql)}$ sign is used to specify the TEM mode, where p is the number of radial zero fields, q is the number of angular zero fields, l is the number of longitudinal fields and usually the $TEM_{(pq)}$ sign is used to specify the TEM mode without the third index. A table of TEM patterns is shown in Figure 4.3. The higher the order of the mode, the more difficult is it to focus the beam on a fine spot, since the beam is no longer coming from a virtual point.

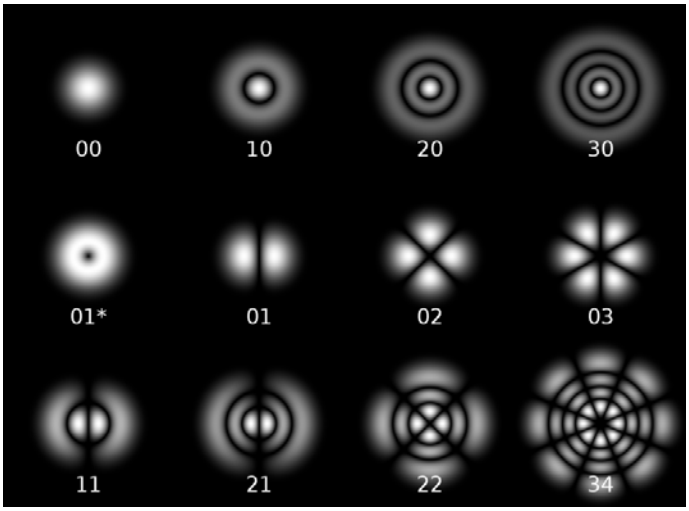


**Figure 4.3 Various mode patterns of a laser.**

Current laser systems provide polarized beams. The polarization plays a role in the reflection and scattering of the light. If the electric vector is aligned in one direction, then the laser beam is "linearly polarized". If the electric vector has two components at right angles to each other of equal intensity, the beam is said to be "circularly polarized". When one component of the electric vector is stronger than the other, the beam is "elliptically polarized". Polarized beams have a directional effect in certain processes, for example laser assisted cutting, cladding or marking.

## 4.3 Laser-Material Interaction

In laser assisted material processing firstly the laser light must be absorbed by the material in order to induce any physical or chemical changes. When the laser beam impinges on the surface of the material, the energy is partially reflected, absorbed and transmitted depending on the material type and the laser wavelength. The light is absorbed in the form of electronic and/or vibration excitation of the atoms and the energy is converted into heat which dissipates to adjacent atoms [175].

When the laser beam irradiates the surface of the metal, firstly photons are absorbed by free electrons. If the photon energy is large enough, the excited electrons can be removed from the metal. This phenomenon is known as "photo-electric effect" [176]. Such an effect can be observed at extremely high energy radiations only. $CO_2$ and Nd:YAG lasers, which are mostly used in conventional laser material processing, do not

provide such high energies to induce any electron ejection from metal surfaces. Mostly, the electrons excited by the photons return back to the equilibrium state by losing their excess energy. This can happen by the scattering or interaction of the excited electrons with lattice defects and other non-continuous structures within the material [177].

Although the basic mechanism is similar, there is a certain difference between the interaction of the laser light with metals and non-metals. In the absence of excitation insulators and semiconductors only have bound electrons and basically their absorption can be attributed to resonances. The most important resonance arises from transitions of valance-band electrons to the conduction band which is known as interband transitions. In order to induce an interband transition, the incident photon must have energy at least equal to the band-gap energy, $E_g$. Semiconductors have band gaps in the visible or infrared part of the spectrum. On the other hand, free carriers contribute to the optical properties of the semiconductors. In case of insulators, for instance ceramics, carrier concentrations may be negligible. Most of the insulators have band gaps corresponding to light frequencies in the vacuum ultraviolet. On the other hand, in addition to electronic transitions, most non-metals show resonant coupling to high frequency optical phonons located in the infrared region of the optical spectrum. Due to this phonon coupling most of the non-metals exhibit strong absorption at infrared wavelengths and weak absorption at intermediate wavelengths which shows a stepwise increase as the photon energy approaches the band gap [178]. In this context, in laser processing of ceramic materials mostly $CO_2$ and Nd:YAG lasers are preferred.

It is known that grain boundaries and inclusions induce scattering in ceramic materials [179]. The inclusions which are small compared to the wavelength of the light may be treated as components of an effective dielectric medium. As such small structures induce various resonances, this leads to absorption peaks which are not present, neither in the pure host ceramic nor in the inclusion material.

## 4.4 Thermalization by the Laser

The majority of laser materials processing techniques are essentially thermal processes in which the absorption of a large number of photons heats the material and leads to physical and chemical changes. The laser provides unique properties for local

heating. In fact, the applied energy can be placed precisely on the surface only where it is needed. The depth, chemistry, microstructure and associated properties of the laser heated zone depend on the suitable choice of laser/process parameters, such as incident power/energy, beam diameter/profile, interaction time/pulse width and physical properties like reflectivity, absorption coefficient, thermal conductivity, melting point and density [180]. Laser induced local heating is used successfully in various surface modification processes, such as transformation hardening, annealing, re-crystallization, glazing and shock hardening.

The laser light may be absorbed in the form of the particle excess energy, excitation energy of bound electrons, kinetic energy of free electrons and perhaps excess phonons. Thus, the absorption of the laser energy does not lead to a direct heating. Basically, laser heating is composed of three different steps [181]. The first step is the spatial and temporal randomization of the motion of the particles which are excited by the photons. The next step is the energy equipartition by different energy transfer mechanisms which can be distinguished by specific time constants. For example, while the overall energy relaxation time in metals is ca. $10^{-13}$ seconds, this value rises up to $10^{-6}$ seconds in the case of non-metals. The last step is the heat flow. On the other hand, when the laser energy is converted into heat, it still tends to be highly localized on a macroscopic scale.

The conversion of the laser energy into heat usually occurs on a time scale shorter than the laser interaction time [182]. The temperature distribution of the heated region depends on the laser characteristics and thermal diffusion rate during the laser radiation. The thermal diffusivity $\boldsymbol{D}$ is related to the thermal conductivity $\boldsymbol{k}$ and the specific heat $\boldsymbol{C_p}$ as shown in the following equation (4.3),

$$D = k/(\rho\, C_p) \qquad \textbf{(4.3)}$$

where $\boldsymbol{\rho}$ is the density. Under the one dimensional heat flow condition the heat balance equation may be expressed as shown in (4.4),

$$\rho C_p \frac{\partial T(z,t)}{\partial T} = Q(z,t) + \frac{\partial}{\partial z} k \frac{\partial T(z,t)}{\partial z} \qquad \textbf{(4.4)}$$

where $\boldsymbol{T}$ and $\boldsymbol{Q}$ are the temperature and power density at a given vertical distance of depth (z) and time (t), respectively. The heat balance equation may be solved analytically, if the coupling parameters ($\boldsymbol{\alpha}$: absorption coefficient and $\boldsymbol{R}$: reflection) and materials parameters (ρ, k and $C_p$) are not temperature and phase dependent. Such an approximation is presented in Chapter 3. On the other hand, the presence of inclusions, defects or other inhomogeneities makes the temperature calculation difficult.

Lasers enable the delivery of a controlled energy (1–30 J/cm$^2$) or power ($10^4$–$10^7$ W/cm$^2$) with precise temporal and spatial distribution either in short pulses ($10^{-3}$ to $10^{-12}$ s) or as a continuous wave (CW). Such a high and sudden energy input induces extremely fast heating/cooling rates ($10^4$–$10^{11}$ K/s), very high thermal gradients ($10^6$–$10^8$ K/m) and ultra-rapid re-solidification velocities (1–30 m/s) [183]. These extreme processing conditions very often develop an exotic microstructure and composition in the near surface region. Therefore, laser is accepted as an effective thermal processing tool especially for ceramic materials.

Ceramics present an attractive class of materials for structural, engineering, electronics and biomedical applications. Despite excellent properties, the use of ceramics in technological applications is still limited primarily due to their brittleness and low mechanical tolerance. Advanced ceramics are usually produced from powders which are densified to a solid body by pressing and sintering techniques. This procedure determines micro structural elements such as grain sizes, pores and/or flaws and hence the final properties of the product. Laser processing allows the delivery of highly intense energy for re-melting or alloying ceramic materials restricted to a small reaction zone. This may result in a change of chemical composition and micro structural parameters, such as porosity, grain size, secondary phases or flaws and residual stresses within the laser treated zone [184].

## 4.5 Laser Processing and Alumina Ceramics

Lasers have been employed successfully to treat ceramic materials, with the advantage that the process is independent from the high hardness and brittleness of the specific materials. Mostly a $CO_2$ laser is preferred since most of ceramic materials strongly absorb infrared (IR) wavelengths [185]. Relatively extensive work has been

carried out on the surface modification of alumina ($Al_2O_3$) based ceramics because of their wide use in various technological applications. Laser surface treatment has been shown as an effective method for producing pore-free and homogeneous surfaces for high alumina refractory systems.

Alumina has a number of meta-stable phases in addition to the thermally stable rhombohedral α-alumina or corundum phase. The metastable alumina polymorphs include γ- (cubic spinel), η- (either tetragonal or orthorhombic), θ- (monoclinic), η- (cubic spinel), κ- (orthorhombic), χ- (cubic) and β- (hexagonal) phases. These polymorphs can be obtained mostly by the dehydration of different alumina hydroxides, rapid quenching from the melt, vapor deposition, thermal spraying and crystallization of amorphous alumina [186]. These phases have different properties, which is one of the reasons for the broad applicability of alumina. In the following sections α-alumina and a few of the most relevant metastable phases are described.

### *4.5.1* Alumina Polymorphs and Corundum

The crystalline forms of alumina are constructed of stacked, close packed layers of oxygen ions with aluminum ions and the vacancies distributed on the tetrahedral and octahedral sites within the oxygen ions. The polymorphism results out of the possibilities for different oxygen layer stacking sequences and the variations in the distribution of aluminum ions on tetrahedral and octahedral sites and from the ordering of aluminum ions and vacancies on these sites [187].

The metastable alumina phases can be observed within several pathways during the dehydration of aluminum hydroxides to form α-$Al_2O_3$, corundum, a name coming from the mineral composition of $Al_2O_3$ identified by Greville in 1789 [188]. Each metastable phase exhibits a distinct X-ray diffraction pattern. Upon heating, all metastable alumina phases transform into other phases and this transformation irreversibly ends up with formation of the thermodynamically stable α-phase at elevated temperatures (Figure 4.4). The α-alumina transformation temperature is, however, relatively high and it is possible to form many of metastable phases at synthesis conditions between room temperature and 1000 °C. This might cause a problem, e.g., when one is interested with

synthesizing the α-phase in a controlled way at low or intermediate temperatures, but it also opens the possibility to get the different metastable alumina in the same time.

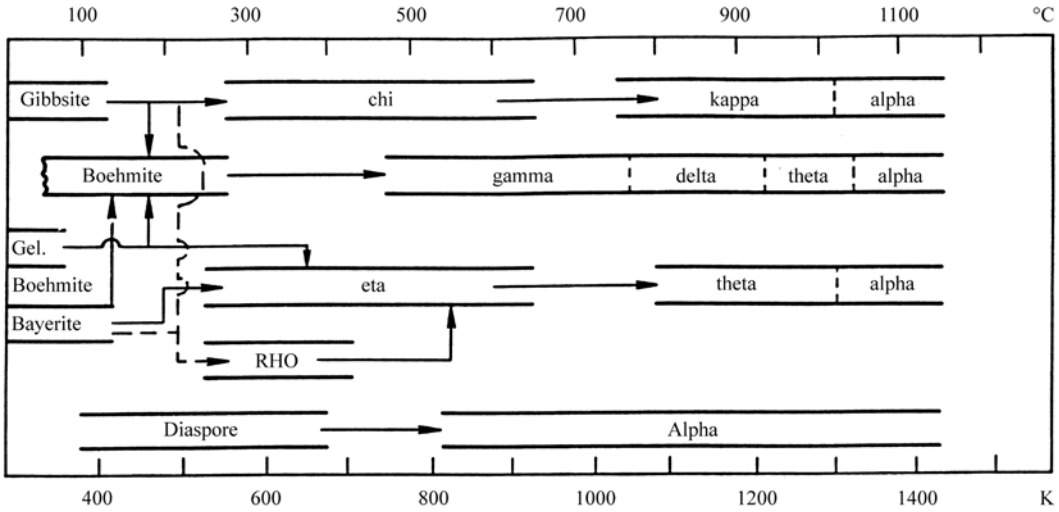


**Figure 4.4 Synthesis and transformation of various alumina polymorphs.**

The metastable phases find use in numerous applications. For example, chemically vapor deposited (CVD) κ-alumina, beside α-alumina, has been used extensively for wear-resistant coatings on cutting tools, since it forms easier than the α-phase under certain CVD process conditions [189]. Another metastable phase; δ-alumina (δ-$Al_2O_3$), has been incorporated in bioactive bone cement composites as a replacement for α-$Al_2O_3$ [190]. It was found to be superior for incorporation in bone cement as it allowed a greater osteoblastic differentiation than α-$Al_2O_3$ allowing for in-vivo bone formation. θ-alumina, (θ-$Al_2O_3$), is used as a precursor for the production of ultra high purity α-$Al_2O_3$ with reduced particle agglomeration [191].

Among other metastable alumina phases, γ-alumina (γ-$Al_2O_3$) has the most immense industrial significance. It is used as a support for automotive and industrial catalysts, especially for the production of various chemicals. Porosity is the main property which makes γ-$Al_2O_3$ attractive as a catalyst support. In addition, similar to other metastable alumina phases, γ-$Al_2O_3$ is used as a polishing abrasive and a coating material because of its low thermal conductivity and relatively high mechanical strength. On the other hand, the phase transformation occurring in high-temperature applications at 700-800 °C constitute a severe problem [192].

The α-phase of alumina is the only thermodynamically stable alumina phase. Some of its properties are summarized in Table 4.2. α-alumina possesses very good mechanical properties. The superior mechanical properties are preserved also at higher temperatures. These properties combined with its chemical inertness make α-alumina one of the technologically most important ceramic materials. Moreover, α-alumina is an excellent electric insulator and optically transparent material which makes it useful for certain applications in electronics and optics [193].

Corundum (α-alumina) crystals can have different names. If they contain, intimately mixed, microcrystals of magnetite ($Fe_3O_4$) or hematite ($Fe_2O_3$), they are called *emery*. If the corundum mono-crystals contain some elements in isomorphic substitution for $Al^{+3}$ in their structure, gemstones and semi-precious gemstones are formed, also receiving specific names for their colors: (a) sapphire-blue (Fe, Ti), (b) ruby–red (Cr), (c) oriental topaz-yellow ($Fe^{3+}$, $Fe^{2+}$), (d) amethyst-purple (Fe, Mn, Ti) and (e) oriental emerald-green ($Fe^{2+}$) [194].

| **Property** | **Value** |
|---|---|
| Density (g/cm$^3$) | 3.96-3.99 |
| Melting point (°C) | ~2050 |
| Bulk modulus (GPa) | 239 |
| Elastic modulus (GPa) | 409-441 |
| Hardness (GPa) | 28 |
| Thermal conductivity (W/m·K) | 46 |
| Relative dielectric constant | 10.5 |
| Band gap (eV) | 8.8 |

**Table 4.2 Physical properties of α-alumina.**

### 4.5.2 Synthetic Approaches to Alumina

A number of processing techniques has been developed for the deposition of alumina coatings and films, such as hydrothermal synthesis, sol-gel, sputtering, physical vapor deposition (PVD) and chemical vapor deposition (CVD) [195]. The last method is particularly interesting because of its high deposition rate and ability to coat complex shaped substrates. Especially plasma assisted/plasma enhanced CVD (PACVD/PECVD) and metal-organic CVD (MOCVD) methods are developing rapidly, since such

processes provide a lower deposition temperature, which permits the use of a broader spectrum of substrates [196].

MOCVD is a specialized area of the CVD and its first use was reported in the 1960s for the deposition of indium phosphide and indium antimonide [197]. These early experiments demonstrated that the deposition of critical semiconductor materials could be obtained at lower temperatures than with conventional thermal CVD and the epitaxial growth could be achieved successfully. In addition to semiconductors, most metals can be deposited by MOCVD and in some cases the process is accepted as an important industrial operation. The technique is also applicable to deposit various carbides, nitrides and oxides with a controlled thickness. Most of the MOCVD reactions occur in the temperature range of 300-800°C and at pressure levels varying from less than 1 Torr to atmospheric [198].

Using aluminum-acetylacetonate, aluminum-isopropoxide and aluminum-ethoxide precursors, MOCVD is employed successfully to deposit alumina thin films at low temperatures [199]. However, at low deposition temperatures, obtained alumina films are usually amorphous. There are different reports on the crystallinity of MOCVD $Al_2O_3$ films. Kim et al. used aluminum-acetylacetonate, $Al(acac)_3$, as a single source precursor to deposit amorphous alumina films below 550°C [200]. Koh et al. reported that $Al_2O_3$ films deposited by a similar MOCVD process at 600°C were also amorphous [201]. In another experimental work Kim et al. showed the preparation of a semi-crystalline alumina film at 700°C [202]. Recently, Devi et al. deposited κ-$Al_2O_3$ films at 600–850°C [203] and Singh and Shivashankar observed 50 nm κ-$Al_2O_3$ crystallites in an amorphous matrix at 600°C [204]. Kohse-Höinghaus et al. using aluminum isopropoxide as precursor showed that γ-$Al_2O_3$ layers can be achieved at deposition temperatures above 800°C [205]. Similarly, a CVD technique assisted by the flame synthesis has been shown as an effective method to deposit γ-$Al_2O_3$ layers above 800°C and these layers were transformed to polycrystalline α-$Al_2O_3$ by heating them up to 1200°C [206]. It is clear that a proper heat treatment is necessary to achieve pure and fully crystalline α-$Al_2O_3$.

In the case of the deposition of alumina layers at high temperatures, the generation of thermal stresses and the subsequent splitting of the coatings are the main problems.

The inadequate adhesion between the alumina coating and the metal substrate is also a critical issue. Due to possible substrate deformations high deposition temperatures can not be applied. The presence of the mixture of metastable phases and high porosity reduces the corrosion and oxidation resistance of deposited alumina layers. At lower temperatures the formation of metastable and amorphous alumina phases instead of pure corundum also means a decrease in mechanical stability and chemical inertness. Such deposited layers are mostly subjected to microwave or laser treatments to end up with dense $\alpha$-$Al_2O_3$ layers. Especially laser surface treatments can produce very dense surfaces and fused bonded layers with short processing time, flexibility in operation and lower cost.

### *4.5.3* Laser Treatment of Alumina

A number of studies demonstrated the effectiveness of producing homogenous, pore-free and smooth alumina surfaces with increased hardness and purity by applying laser treatment. The high melting temperature and low thermal conductivity of alumina-based ceramics however, results in the development of high thermal gradients during the laser processing. These high thermal gradients induce the generation of thermally induced cracks which are oriented parallel and perpendicular to the surface. While the perpendicular cracks are considered beneficial for thermal shock resistance, parallel cracks decrease the mechanical stability of the layers. The cracks also act as sites of slag penetration and splitting of the layer in mechanical contacts. In order to eliminate cracking, the reduction of thermal gradients is essential. Mostly CW laser processing is preferred to pulsed laser processing due to reduced thermal shocks and thermal gradients.

There are two different approaches to tackle such thermal gradient and shock formation. The first one is applying a pre-heating process. The material to be treated with the laser is heated up to some temperatures prior to the processing. Lee and Zumgahr were able to eliminate cracking and produce a smooth and pore-free surface by pre-heating high purity alumina ceramics in a high-temperature electric furnace before and during $CO_2$ laser treatment [207]. In their work the specimen was heated up to 1200°C. Such a temperature is definitely a limiting factor for the selection of the

substrate material. Bradley et al. developed a flame-assisted laser surface treatment process by applying an oxygen/acetylene welding torch to pre-heat the samples in front of a $CO_2$ laser beam [208]. The treated surfaces were crack-free, but such an approach seems to be more suitable for thicker layers or bulk alumina ceramics. Although the method was effective to synthesize a dense alumina layer, the crystallinity of the layer was low.

Modest et al investigated the splitting of a laser beam into two parts to eliminate cracking during drilling and scribing with a highly focused beam [209]. Triantafyllidis et al. treated alumina based ceramics employing a dual laser beam arrangement, consisting of a $CO_2$ laser beam, which was the main processing source, and a diode laser beam, which was the pre- and post-heating source [210]. Crack-free, fully densified, smooth and homogeneous surface tracks were achieved with the treated zone extending from 2.1 mm to 2.5 mm in depth. Even though such efforts have been partially successful, the process was not practical. Especially the method is only suitable for thicker layers, since controlling the combined heat effect induced by dual-laser beam irradiation is complicated in the case of thin films.

The second approach is the modification of the material with some filler or over-layers to increase the absorption and thermal conductivity. Especially in sintering of ceramic powders some additive materials are used to increase the thermal conduction and therefore the penetration depth. Benda et al. showed an efficient laser sintering by using a mixture of opaque and transparent powders and a laser beam having a specific wavelength and sufficient intensity, which can penetrate this powder mixture with a desired depth [211]. Barlow et al. similarly showed the application of an organic binder with inorganic ceramic particles during the laser assisted sintering process [212]. Although a dense layer is achieved by such an approach, the binder material has to be removed applying an additional thermal process. In that method the ceramic particles are not melted and the crystallinity of the layer depends on the raw powder material. Zheng et al. showed that coating the nano-$Al_2O_3$ particles with polystyrene (PS) by emulsion polymerization, prior to laser sintering, improved the optical absorption [213]. Although that approach provided a better densification with a lower laser power, the crystallinity was not improved.

There is still a challenge in preparing dense, defect-free and fully crystalline α-alumina coatings by applying laser technology. In such approaches both laser parameters (wavelength, energy input, beam characteristics, radiation type etc.) and material properties (nano/micro scale size effects, optical absorption, thermal conductivity etc) should be taken into account.

### 4.5.4 Laser Processing and ($^t$BuOAlH$_2$)$_2$ as Molecular Precursor

Actually, aluminum hydrides ($AlH_3$) and aluminum oxides ($Al_2O_3$) are well-characterized, crystalline compounds. Veith and his co-workers firstly showed the existence of an unusual aluminum compound "*HAlO*" in which hydrogen is directly bound to aluminum [122]. HAlO is a new ternary glassy phase of aluminum, oxygen and hydrogen with a 1:1:1 stoichiometry. The same phase has been discovered independently by applying a different approach, which employed a solution reaction between aluminum hydride adducts and siloxanes. This yielded an amorphous powder with some other constituents [214].

The metastability feature of HAlO triggers new possibilities for surface modifications and directed phase transformations. It was shown that heating HAlO layers leads to the elimination of hydrogen and formation of unstable compound $(AlO)_\infty$ [125]. This metastable compound transforms into $Al{\cdot}Al_2O_3$ composite following the disproportionation of $Al^{+2}$. In this context, the laser treatment idea was suggested by Veith et al. in order to induce the local transformation of HAlO into $Al{\cdot}Al_2O_3$ rather than transforming the complete film.

First experimental works on the laser treatment of HAlO layers can be seen in the PhD thesis of Fritscher [215]. Following this work the patent filed by Veith et al. shows the detailed description of the approach [216]. Fritscher gave the main focus on the color change of the hydride upon the elimination of hydrogen and creating optically detectable patterns out of this color change. On the other hand, there is no detailed information on properties of the final material synthesized after the laser treatment. This laser treatment was carried out with a high energy $CO_2$ laser operating at an output power of 300-700 W since aluminum hydrides, similar to other dielectric materials, mostly show strong absorption at IR wavelengths.

A more detailed approach is found in the PhD theses of Andres and Wolf [217, 127]. Andres used a $CO_2$ laser to modify deposited HAlO layers. In her work a laser system operating at a wavelength of 10.6 μm at a maximum output power of 25 W was preferred. A ZnSe lens having a focal length of 25 mm was used to get a focused laser beam. The sample was scanned under the focused laser beam by the help of a computer controlled XY scanner. Andres stated that minimum 30 seconds exposure time was needed to transform HAlO into $Al{\cdot}Al_2O_3$ at a laser power of 12.5 W. Actually, the main indication of the transformation was the colorization of the layer following the laser assisted heating. In her work the laser system was not equipped with an online power-meter to control the intensity of the laser precisely. In addition, the exposure time was controlled manually instead of a fast electronic shutter. Besides such technical restrictions, Andres successfully showed the disappearing of the Al-H band absorption at 1920 $cm^{-1}$ in the IR spectra after the laser treatment. The XRD results also support this transformation by showing the existence of Al and $Al_2O_3$.

Wolf studied similar phase transformations using the $CO_2$ laser [127]. His approach was to increase the absorption of the transparent HAlO layer by applying a double-layer in order to improve the efficiency of the transformation. Firstly he deposited $Al{\cdot}Al_2O_3$ by the thermolysis of $(^tBuOAlH_2)_2$ at higher temperatures. In the second step he deposited a HAlO layer over this $Al{\cdot}Al_2O_3$ layer. Wolf mentioned that the $Al{\cdot}Al_2O_3$ layer beneath gives a roughness to the HAlO layer which seems to increase the optical absorption. He achieved results similar to Andres by applying relatively lower laser intensities. In his work the main uncertainty was the explanation of the heating mechanism. There are various possibilities in heating of the HAlO layer deposited on the $Al{\cdot}Al_2O_3$ layer. The laser light can be absorbed directly by the HAlO layer. Another possibility is the indirect heating by the absorption of the laser energy by the substrate. As Wolf stated, the HAlO layer can be heated more due to its increased roughness induced by the composite layer beneath. Another possibility, which Wolf did not discuss at all, can also be the indirect heating of the $Al{\cdot}Al_2O_3$ layer deposited beneath by the laser beam and dissipation of the heat to the HAlO layer above.

In laser-material interactions the morphology and structure of the deposited layer plays a major role. Actually, Wolf stated the existence of a possible core-shell structure

model to define the morphology of the deposited $Al{\cdot}Al_2O_3$ layer, but there was no direct experimental proof supporting his idea, unless Petersen and Sow showed the existence of such a core-shell structure with the help of high resolution TEM (HR-TEM) [128 and 129]. In the patent covering these new findings Veith et al. showed the existence of biphasic core-shell nanowires [139]. In this context, the mechanism, which Wolf discussed, concerning double layer approach for improving the efficiency of laser induced transformation can be also thought in a totally different manner. Extreme heating of the underlying $Al{\cdot}Al_2O_3$ layer can be followed by the oxidation of the Al core and this can lead to a release of additional heat to the reaction zone. Such excessive sudden heat release can be another reason for heating of the HAlO layer. Although the interaction mechanism was not given in detail in Wolf's work, it was shown that laser treatment of an $Al{\cdot}Al_2O_3$ composite layer leads to the transformation to $Al_2O_3$. In his work the crystal structure and other properties of the $Al_2O_3$ layer, formed upon the laser treatment, were not given in detail.

Veith et al showed the formation of $\gamma$-$Al_2O_3$ following the laser treatment of the HAlO layer [126]. In another work of Veith it was shown that this laser treatment can be confined down to 1-2 μm width by applying laser interference techniques which can be named as "*laser interference metallurgy*" [218]. Similar to earlier $CO_2$ laser treatment results, the authors presented the formation of Al and $\gamma$-$Al_2O_3$.

Following the idea of Fritscher [215], Blin used a pulsed Nd:YAG laser to induce a selective transformation of HAlO layers into an $Al{\cdot}Al_2O_3$ composite [219]. In his work the main focus was given to the local transformation within the 7 μm width reaction zone confined by interference techniques. Similarly, Andres [217] and Liu [220] used also Nd:YAG laser for the treatment of glassy HAlO layers. Andres tried to show the elimination of hydrogen from HAlO upon laser pulses. Liu mostly gave attention to the resolution of the laser interference structuring of the HAlO layer. Although the formation of $Al{\cdot}Al_2O_3$ was discussed basically, further possible changes in the morphology and structure of this composite layer following the repeated laser pulses were not explained in detail.

Chèty-Gimondo also showed the effect of the pulse laser exposure on the hydride layer [221]. Her main aim was to see the effect of the repeated laser pulses on the

properties of the layer formed through the elimination of hydrogen from HAlO. Parallel to results of Andres [217] she also showed the disappearing of the Al-H band after the laser treatment. Similar to Andres, she observed morphology changes on the HAlO surface after repeated pulses. In the PhD thesis of Andres the presentation of the surface changes upon laser pulses was limited with some low resolution optical microscope and macroscopic images. The main supporting data was given in the form of mass spectroscopy spectra showing the change in the Al:O ratio and FT-IR spectra monitoring the disappearance of the Al-H band. Chèty-Gimondo showed a better analysis with an in-situ mass spectroscopy during the laser treatment process. In her work it is stated that the elimination of the hydrogen happens after the first laser pulse and the ablation of $Al_2O_3$ layers occurs following the second and especially the third laser pulse. This may be a fingerprint of a full transformation to $Al_2O_3$ rather than to an $Al{\cdot}Al_2O_3$ biphasic composite.

In most of the presented works the existence of Al and $Al_2O_3$ phases after the laser treatment is seen clearly, especially by XRD analysis. But as mentioned previously, the exact structure of the $Al{\cdot}Al_2O_3$ composite synthesized by direct deposition rather than laser treatment was described firstly in the PhD theses of Petersen [128] and Sow [129] who used HR-TEM.

Previously, Andres proposed that the $Al{\cdot}Al_2O_3$ composite obtained at 450-500°C was made of ball-like structures. Also Sow clearly showed in her PhD thesis that at low temperatures ball-like structures formed. On the other hand, Petersen and Sow observed that the deposited layers at high temperatures are composed core-shell $Al{\cdot}Al_2O_3$ nanowires. Such 1D structures and their synthesis routes were explained in detail by Petersen in his PhD thesis. He also studied laser structuring of HAlO layers by applying the interference technique. In his work he followed a very good systematic study covering the early results of Blin, Andres and Chèty-Gimondo who also worked on the pulsed laser treatment of HAlO layers. Petersen was able to produce lines and dots of $Al{\cdot}Al_2O_3$ on the HAlO layer with a resolution down to 1 µm. He also explained the morphology changes in detail with the help of TEM and FIB combinations [222]. Although Petersen showed that HAlO transformed into $Al{\cdot}Al_2O_3$ after repeated laser pulses, the microstructure of the freshly formed bi-phasic composite layer was not

compared with that of the $Al{\cdot}Al_2O_3$ layer deposited at high temperatures. On the other hand, after repeated laser pulses the formation of fibrous and nanoporous structures is also presented in his thesis. There the uncertainty is the formation mechanism of such structures. It is complicated to understand what happens after repeated laser pulses since we talk about a very high energy input in an extremely short time scale (4-8 nanoseconds). It is difficult to divide the process into two separate steps as; first step, $HAlO\text{-}Al{\cdot}Al_2O_3$ transformation and second step, $Al{\cdot}Al_2O_3\text{-}Al_2O_3$ transformation. Petersen showed the existence of $\gamma\text{-}Al_2O_3$ and Al following the laser pulses in his SAED patterns. In labeling of the electron diffraction pattern, there was a difficulty in resolving the $\gamma\text{-}Al_2O_3$ and Al rings since the diffraction rings are very close to each other . Furthermore, some structural transformation of the $Al{\cdot}Al_2O_3$ system takes place under the heavy electron beam irradiation [128].

In all these presented works concerning the laser treatment of layers prepared by the deposition of $(^t BuOAlH_2)_2$ mostly HAlO was chosen as starting raw material. The main idea is the chemical or structural tuning depending on the metastability of the HAlO layer. As explained above, it is not easy to separate de-hydration and oxidation steps when HAlO is used as the raw material. In order to understand the stepwise transformation and combine the results of Petersen's work on laser treatment of HAlO, a detailed study is needed on the direct laser treatment of $Al{\cdot}Al_2O_3$ composite layers. In the following sections the experimental work on the laser modification of $Al{\cdot}Al_2O_3$ layers will be presented.

## 4.6 Experimental Work

### 4.6.1 Preparation of $Al{\cdot}Al_2O_3$ layers

As described previously in Chapter 3, $Al{\cdot}Al_2O_3$ layers were deposited by directing a constant stream of $(^t BuOAlH_2)_2$ on inductively heated substrates in a cold wall CVD reactor. For CW laser processing, stainless steel and titanium were selected as substrate materials. In the case of pulsed laser processing also glass substrates were employed.

The thickness of the layers was controlled simply by altering the deposition time. The effect of the thickness on the morphology was also taken into consideration prior to any laser treatment. The deposition temperature was kept between 520°C and 600°C

depending on the substrate material. While only a few minutes of deposition was enough for preparing layers of sub-micron thickness, the deposition time was extended to 30 minutes for layers of 1-4 μm thickness.

### 4.6.2 Laser Processing

Prior to laser processing experiments, basic process parameters presented in Chapter 3 were taken into consideration to design the proper laser system for the treatment of $Al{\cdot}Al_2O_3$ layers. Firstly a basic laser system was designed and constructed, following the experimental work and technical needs. Additional optical, mechanical and electronic components were added to improve the performance concerning especially the control of the exposure time, laser power and optical resolution. The basic parameters, which are considered for the direct laser writing process in this current PhD thesis, are listed in Table 4.3.

| | | |
|---|---|---|
| **Laser** | **Wavelength** | IR range<br>• $CO_2$ (10.6 μm)<br>Visible range<br>• $Ar^+$ (514 nm-488 nm)<br>• HeNe (632 nm)<br>• Nd:YAG(SGH) (532 nm) |
| | **Power** | CW **(**0.1-10 W)<br>Pulsed **(**0.1-0.5 J/pulse) |
| | **Mode** | Gaussian, single mode, $TEM_{oo}$ |
| **Process** | **Beam size and shape** | Adjustable by lens systems* |
| | **Exposure time** | Shutter (5 μs accuracy)<br>XY scan. table (0.05 mm/s-5 mm/s) |
| | **Atmosphere** | Vacuum, Protective gas ($N_2$), Air |

**Table 4.3 Laser and process parameters in direct laser writing.**

The parameters can be grouped in two main categorizes: First, *Laser Parameters* and second, *Process Parameters*. Laser Parameters define the characteristics of the raw beam. *Process Parameters* define the modified beam properties with the help of optical components and process conditions in terms of the operation medium and exposure time.

#### 4.6.2.1 Direct Laser Writing System

Basically, the direct laser writing process is based on the modification of the surface under a focused laser beam. The focused laser beam can scan the surface with the help of a galvano-scanner. In the case of such scanning systems it is difficult to synchronize the laser beam movement at the same speed in different axes and the angle of incidence changes during the scanning process. In this current work the laser beam is kept as a stationary source and the sample was moved relatively to the beam with the help of a XY scanner.

The scanner movements can be controlled in X- and Y-axes precisely with an accuracy of 1 µm. In order to write complex 2D structures, a software was developed to synchronize the movement of the scanning table with a fast mechanical shutter. In the literature there are various approaches for controlling 2D linear motions in laser direct-writing systems [223]. In this PhD thesis we gave the main attention to the acceleration rate of the motors driving the motion and the speed of the shutter in addition to the scanning speed, which mostly is defined as the main parameter in similar laser writing processes. The schematic description of the direct-laser writing system is shown in Figure 4.5.

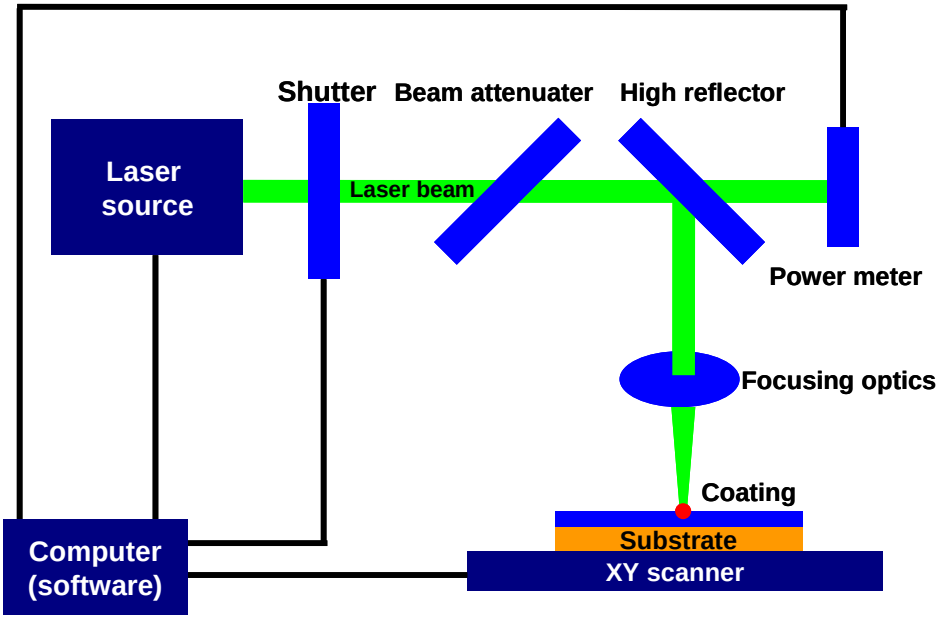


**Figure 4.5 Schematic view of the direct laser writing system.**

A mechanical shutter was placed at the beam exit of the laser source to control the exposure time. Although all lasers used in this experimental work have internal mechanical or electronic shutter systems, an external shutter was employed especially to maintain a stable power regime. In the case of internal electronic shutters, the exposure can be controlled by simply switching on /off the power supply. On the other hand, this disturbs the stability of the optical components since the change of the temperature in every cycle disturbs the optical arrangements within the laser. This effect is observed strongly in the case of pulsed laser experiments. In addition, internal mechanical shutters induce vibrations within the laser source during switching on /off and this affects the beam quality, especially of CW lasers. Such a vibration effect is eliminated by an external shutter placed on an optical table which damps any possible vibration.

Although the lasers used in this current thesis exhibit good output power stability showing a deviation less than ±2 %, the change was monitored with an online powermeter. The primary beam was stirred by a special mirror having 95 % reflection and 5 % transmission. The transmitted beam was directed to a power-meter recording the laser output power online during the process.

The beam was focused by the help of simple plano-convex lenses for CW laser applications. In the case of the $CO_2$ laser a ZnSe lens having a focal length of 55 mm is employed. For visible wavelengths different singlets and combinations having a focal length between 2-80 mm were employed. Especially in the case of vacuum or protective gas exposures, longer working distance lenses were preferred. Due to the high energy outputs and high absorption of the surfaces, no focusing element was used in the case of pulsed laser treatments. On the other hand, the beam coherency of the pulsed laser was improved with the help of a standard injection seeder. In some experiments the beam homogeneity was improved by employing spatial filtering.

The direct writing system provides a local surface patterning which can be in the form of dot arrays or various 2D linear structures. A self-developed software is used to define the line arrays at definite spacings in order to treat the whole surface. Figure 6 shows a schematic of the total surface treatment approach. As it is seen in the schematic view, the overlapping of laser induced tracks is the critical issue and this can be avoided by altering the scanning speed and exposure time intervals. The shutter off/on intervals

can be adjusted and synchronized easily according to the beam positioning by the developed software. This means that the shutter prevents a repeated exposure during the positioning of the beam in the case of multi-line scanning. This switch on/off and scanning mode can be repeated precisely several times in order to scan the whole surface.

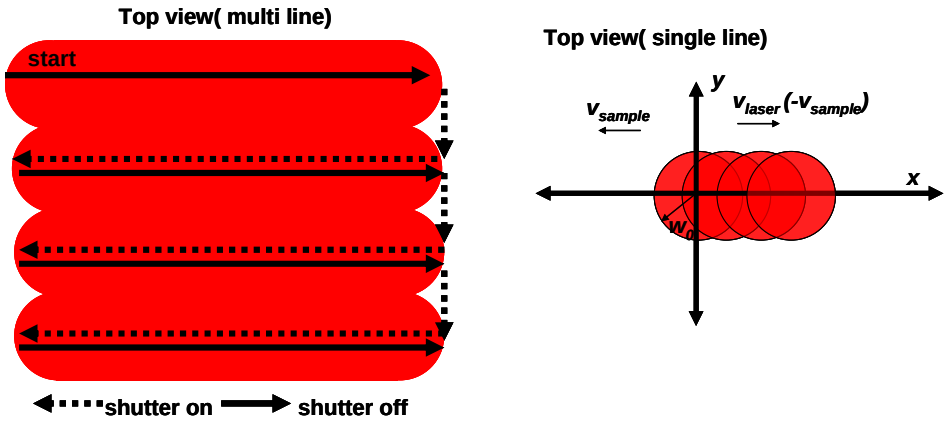


**Figure 4.6 Schematic explanation of the scanning process.**

The laser treatment experiments were conducted in air and under protective atmosphere. The chamber used in the LCVD approach, shown in Chapter 3, was also used in the laser processing experiments to provide a controlled atmosphere. The vacuum chamber can be operated under various protective gases. In this thesis laser treatment of the layers was conducted in air and under vacuum/argon in order to see the oxidization effect and therefore temperature distributions in presence and absence of $O_2$. The characteristics of the lasers used in our experiments are presented in the following section.

#### 4.6.2.2 Laser Work Stations

Laser treatment of thicker layers was carried out using a $CO_2$ laser (D-25, DEOS) operating at a wavelength of 10.6 μm with a maximum output power of 25 W. The laser can be operated in a CW or a chopped operation mode up to 200 Hz. In the chopped mode the laser peak output power typically is five times of the CW level at repetition rates of 100-200 Hz and with pulse widths down to 100 microseconds. Table 4.4 lists the most important parameters of the $CO_2$ laser used in this work.

| | | |
|---|---|---|
| **$CO_2$ Laser (Deos L-25)** | **Wavelength (µm)** | 10.55 to 10.63 |
| | **Power output (W)** | 25 |
| | **Power stability (%)** | ±5 |
| | **Beam size (mm)** | 1.8 ±0.2 |
| | **Beam divergence (mrad)** | 7.5 ±0.5 |
| | **Mode** | $TEM_{00}$, Gaussian |
| | **Polarization** | fixed linear |

**Table 4.4 $CO_2$ laser parameters.**

In the case of treatment of thin layers an air-cooled argon ion laser (Model 2020, Spectra-Physics) operating at multi-line (457.9-514 nm) wavelengths with a maximum output power of 5 W was employed. It is also possible to operate the laser at single-line wavelengths by bending the individual lines (454.5 nm, 457.9 nm, 514.5 nm, 528.7 nm) according to their wavelengths with the help of a dispersion prism. On the other hand, at the single-line wavelength mode the output power decreases. The characteristic properties of the argon laser are given in Table 4.5.

| | | |
|---|---|---|
| **Argon Ion Laser (Spectra 2020)** | **Wavelength (nm)** | 454 to 528.7 |
| | **Power output (W)** | 5 |
| | **Power stability (%)** | ±2 |
| | **Beam size (mm)** | 1.25 ±0.2 |
| | **Beam divergence (mrad)** | 7.5 ±0.5 |
| | **Mode** | $TEM_{00}$, Gaussian |
| | **Polarization** | fixed linear |

**Table 4.5 Argon laser parameters.**

In addition to CW lasers, a Q-switched Nd:YAG laser (Spectra-Physics, USA) which works under four different wavelengths (1064 nm, 532 nm, 355 nm and 266 nm) with a frequency of 10 Hz was used for a high-energy surface treatment of the deposited layers. The fundamental wavelength of the Nd:YAG laser is 1064 nm from which a series of wavelengths (532 nm, 355 nm and 266 nm) can be generated by means of frequency doubling (second-harmonic generation, SHG) and tripling (third harmonic generation, THG). The laser is equipped with an injection seeder which provides a long

coherence length. The main mechanism of the seeder is the synchronization of the laser emission by an external laser source with very narrow line-width. Through the model 6350 injection seeder (Spectra-Physics) the line-width is reduced from 30 GHz to 0.1 GHz, which corresponds to the coherence length of more than 1 meter. The laser parameters associated with surface modifications are wavelength, pulse width, fluence, coherent length, as well as beam profile. Table 4.6 lists the most important parameters of the Nd:YAG laser used in this work.

| | | | | | |
|---|---|---|---|---|---|
| **Nd:YAG Pulsed Laser (PRO-290)** | **Wavelength (µm)** | 1064 nm | 532 nm | 355 nm | 266 nm |
| | **Energy (mJ/p)** | 2000 | 1000 | 550 | 180 |
| | **Pulsed width (nm)** | 8-12 | 1-2 | 2-3 | 2-3 |
| | **Eng. Stability, short term (%)** | ±2 | ±3 | ±4 | ±8 |
| | **Power drift, long term (%)** | 3< | <5 | <6 | <10 |
| | **Beam size (mm)** | <13 | | | |
| | **Beam divergence (mrad)** | 7.5 ±0.5 | | | |
| | **Pulse line width ($cm^{-1}$)** | 1.030 (standard) | | 0.003 (seeded) | |
| | **Mode** | $TEM_{00}$, Gaussian | | | |
| | **Polarization** | fixed linear | | | |

**Table 4.6 Nd:YAG laser parameters.**

Laser pulse energies were varied using a rotable half-wave plate placed in front of the compressor unit. The pulse energy was measured employing a power meter and a pyroelectric detector in the multi- and single-pulse case, respectively. The number of laser pulses per spot was controlled by a pulse counter. The target was mounted on a motorized XYZ translation stage.

## 4.7 Results and Discussions

### 4.7.1 Optical Characterization of Al·$Al_2O_3$ Nanowires

Optical absorption measurements were carried out in a standard Carry Varian 5000 UV/VIS/NIR spectrophotometer operating with a spectral resolution of 2 nm at room temperature, with a deuterium lamp for UV and a tungsten halogen lamp for the visible region. The spectrophotometer is equipped with an integrating sphere to collect diffuse or total reflection.

The absorption spectrum of the deposited layer is plotted in Figure 4.7. Due to technical limitations of the spectrophotometer, the absorption measurement was carried out down to 360 nm. As one can see in the spectrum, there is a strong increase in the absorption in the UV region which reminds of the bulk plasma behavior of Al. It is known that Al exhibits a low absorption down to a wavelength of 200 nm due to its high bulk-plasma frequency [224]. While Au and Ag exhibit sharp absorption edges in visible wavelengths, Al differs from them because of its plasma frequency in the vacuum ultraviolet.

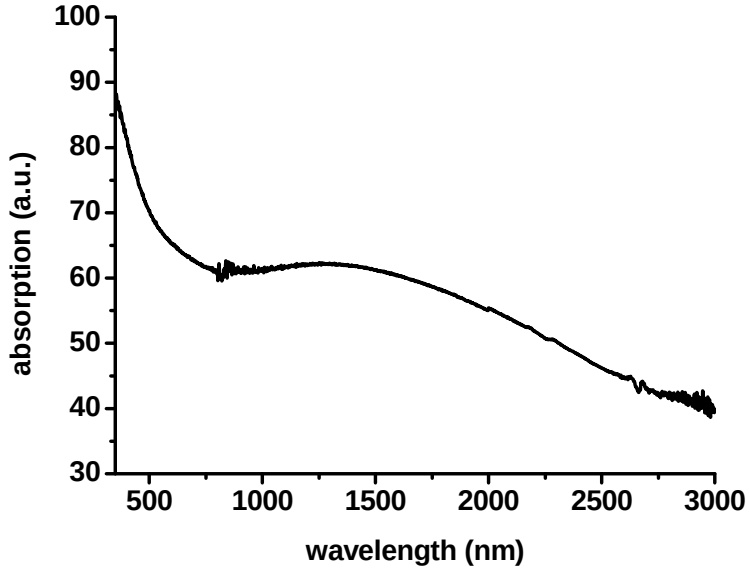


**Figure 4.7 Absorption spectrum of Al.$Al_2O_3$ nanowires**

On the other hand, calculations using Mie's theory show that Al spherical nanoparticles with diameters of 40 nm exhibit two distinct resonances in the UV region [90]. The peak at about 250 nm is due to the dipolar plasmon resonance and the other peak at about 190 nm originates from the quadrupolar mode. In this context, the increase of the absorption in the UV range (Figure 4.7) can also be attributed to the plasmon resonance of Al cores encapsulated by the dielectric $Al_2O_3$ shells. For an explicit observation of the Al plasmon peak, optical experiments in the vacuum ultraviolet region are required. This makes the experimental studies on the plasmonic properties of Al very complicated. As a result limited experimental work on the Al plasmonics is carried out,

whereas various detailed research works are done on the plasmonic properties of Au and Ag nanoparticles embedded in different dielectric materials. In addition, chemical synthesis methods for Au and Ag have reached to an advanced stage, providing particles of different sizes and shapes, whereas the synthesis of Al nanoparticles with a well defined size and geometry remains still a challenge.

Although the exact absorption character of $Al{\cdot}Al_2O_3$ nanowires in the UV region is not clear due to technical limitations, the broad absorption in the VIS-NIR range may result from the shift of the plasmon peak. It is known that inhomogeneities in the size and the geometry of the metallic nanostructures embedded in dielectric materials lead to broadening of plasmon absorptions [226]. For metallic nanoparticles significantly smaller than the wavelength of the light, the absorption is observed within a narrow wavelength range. The wavelength of the absorption peak maximum due to the surface plasmon absorption band is dependent on the size and shape of the nanocrystals, as well as on the dielectric environment surrounding the particles [227]. For extremely small particles the shift of the surface plasmon resonance (SPR) peak position is rather small. For larger nanoparticles the SPR may be strongly red shifted. Nanoparticles with different sizes exhibit different SPR peaks and this may cause a superpositioning of individual peaks which leads to a broad absorption [228].

There are various research works on the broad absorption of $Al_2O_3$-metal composite systems which mostly are used for solar collector applications. In this context, Ni-$Al_2O_3$ [229], Mo-$Al_2O_3$ [230], Fe-$Al_2O_3$ [231], Pt-$Al_2O_3$ [232] and Cu-$Al_2O_3$ [233] composite systems were reported as effective broad absorbers. In such applications mostly the metal filling ratio and percolation phenomena were presented as the critical issues for the optical properties of the composite. On the other hand, the effect of the size and geometry of the metallic structures embedded in the alumina matrix was not studied in detail.

There are various theoretical works on the optical properties of Al nanoparticles. In addition to the size and geometry of particles, the native oxide layer covering the aluminum contributes to plasmon properties. Ekinci et al. showed that aluminum nanoparticles covered by ca. 3 nm native oxide layers exhibit broad plasmon peaks [90].

Recently Langhammer et al. similarly showed the effect of the oxide shell on the Al plasmon resonance shift [234].

The broad absorption of $Al{\cdot}Al_2O_3$ nanowires may result also from the 1D structure. For a wire- or rod-shaped metallic nanostructure the plasmon band splits into two bands corresponding to the oscillation of the free electrons along (longitudinal) and perpendicular (transverse) to the long axis of the nanostructure [235]. The transverse mode resonance is close to that observed for spherical particles, but the longitudinal mode is considerably red-shifted, depending strongly on the aspect ratio, which is the length divided by the width of the 1D structure. As presented in Chapter 3, the lengths of $Al{\cdot}Al_2O_3$ nanowires vary between a few to several micrometers. This means, every single nanowire may exhibit a different plasmon mode (absorption at different wavelengths) depending on its aspect ratio.

In addition, the tangled and highly interacting structure of the $Al{\cdot}Al_2O_3$ nanowires may effect the plasmon mode. Shalev et al. showed that highly interpenetrated random dielectric/metal composite systems induce localized enhancement of electrical fields [236]. More specifically Anno et al showed that Al thin films in the form of random islands exhibit a broad absorption [237]. In his work the main interest was to show the decrease of the parallel band absorption, whereas non-parallel plasmon modes contribute to the optical absorption. Similarly, Hornyak et al. reported a broad absorption spectrum from tubular Al structures embedded in a polyester matrix [238]. Therefore it is believed that $Al{\cdot}Al_2O_3$ nanowires exhibit different plasmon peaks due to different aspect ratios, and superpositioning of these peaks seem to form a broad absorption spectrum.

Actually, the maximum at ca. 1500 nm in the broad absorption spectrum (Figure 4.7) resembles to findings of Lie et al. which show that the plasmon absorption is shifted to wavelengths between 700 and 1200 nm in the case of aluminum hallow nanostructures [239]. In addition, it is stated that the orientation of the nanostructures with respect to the electric field plays a critical role in the absorption behavior. Due to the random distribution of $Al{\cdot}Al_2O_3$ nanowires such an angle dependent absorption or reflection can not be considered. As shown in Figure 4.8, there is no significant change in the absorption behavior with respect to the angle of incidence.

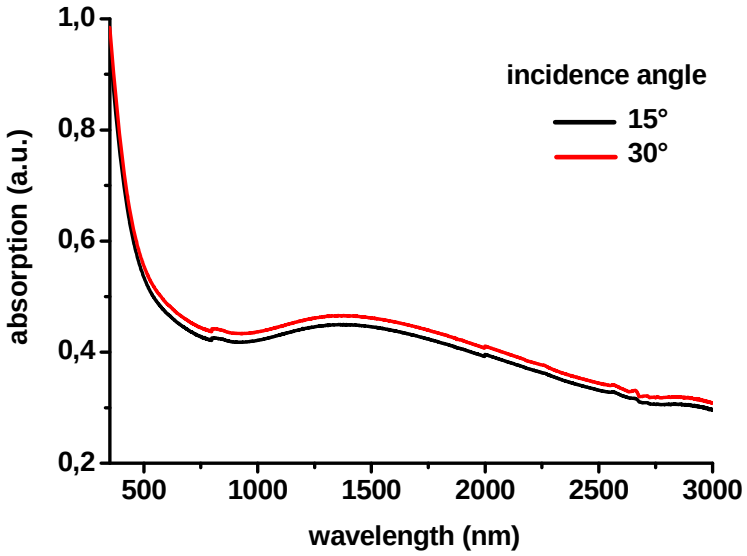


**Figure 4.8 Absorption spectra of Al·$Al_2O_3$ nanowires at different incidence angles.**

On the other hand, the chaotic arrangement, especially the crossing of Al·$Al_2O_3$ nanowires may lead to the formation of hot spots corresponding to very intense electric fields. Podolskiy et al. studied similar geometry effects on metal nanowires and showed that coupled parallel wires, at a very short distance apart, lead to a significantly enhanced coupled plasmon resonance [240]. Such an enhanced plasmon resonance may also occur over a broad spectral range. For instance, Prokes et al showed the enhancement of an electrical field at the crossing of Ag nanowires and their broad surface plasmon absorption [241]. Similarly, Shalev et al. showed the enhancement of an electrical field in semi-continuous metal-dielectric films having different resonating elements at different wavelengths [242].

The chaotic arrangement of the Al·$Al_2O_3$ nanowires and difficulty in controlling the deposition thickness make it complicated to understand their optical behavior. On the other hand, the strong and broad absorption of Al·$Al_2O_3$ nanowires opens up a flexibility to use different wavelength lasers to transform the nanowires into α-$Al_2O_3$. While most of the $Al_2O_3$ based ceramic materials are treated by IR wavelength lasers, such a bi-phasic composite can also be treated with low energy visible wavelength lasers.

### 4.7.2 CW Laser Heating of Al·$Al_2O_3$ Nanowires

#### 4.7.2.1 Laser Fluence and Temperature Rise Measurements

Prior to the detailed investigation of the laser heating mechanism and its effects, the first step was to find the position of the focusing lens that produced the minimum spot size at the working plane. This was performed by adjusting the position of the lens and scanning a straight line on a piece of marking paper. Several lines were scanned and the width of the tracks was measured with an optical microscope. After the best position for the focusing lens was found, some tests were conducted with Al·$Al_2O_3$ samples to corroborate the working position.

Using a moving heat source (scanning the sample under the laser beam) rather than a stationary laser beam affects the laser fluence and therefore the amount of the absorbed energy. In order to estimate the scanning effect, firstly the laser fluence was calculated as a function of the scanning speed using the equation (4.5) proposed by Bäuerle et al. [145],

$$\Phi = \frac{P_T}{A} t_i = \frac{P_T}{A} \cdot \frac{2w_o}{v_s} = \frac{2P_T}{\pi w_o v_s} \qquad \textbf{(4.5)}$$

where $\boldsymbol{P_T}$ is the total power by the beam laser acting on the surface, $\boldsymbol{A}$ is the area on the surface heated by the laser beam, $\boldsymbol{w}_o$ is the Gaussian half-width of the laser beam (50μm) and $\boldsymbol{v}_s$ is the scanning speed.

As shown in Figure 4.9, an increase in the scanning speed decreases the laser fluence gradually. While there is no strong decrease in the laser fluence at slow scanning rates ($v_1$=0.1 cm/s, $v_2$=0.15 cm/s $v_3$=0.25 cm/s, $v_4$=0.4 cm/s) a clear deviation can be observed at scanning speeds higher than 1mm/s ($v_5$=1 cm/s, $v_6$=2 cm/s, $v_7$=3 cm/s). Bäuerle et al. showed that at a scanning speed of $\boldsymbol{v_s}$ <$10^4$ μm/s the centre temperature rise is not affected essentially by the scanning speed $\boldsymbol{v_s}$ [145].

At slower scanning speeds the laser fluence can be approximated to that of a stationary laser beam. Under this assumption using the equation (3.9) the maximum temperature rise on the alumina substrate at the centre of the laser beam is calculated and

presented in Figure 4.10. In this theoretical calculation it is assumed that the thermal conductivity and absorption coefficients do not change with the temperature.

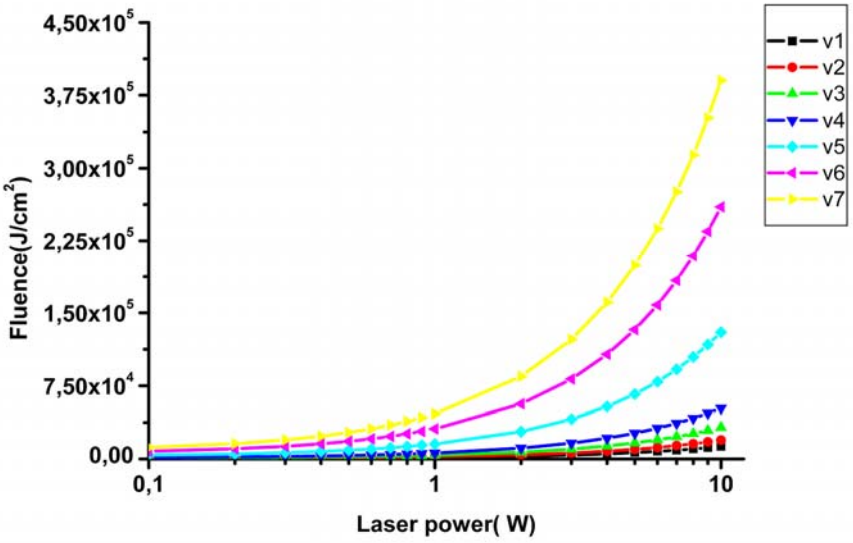


**Figure 4.9 Laser fluence at various scanning speeds ($v_1$=0.1 cm/s, $v_2$=0.15 cm/s, $v_3$=0.25 cm/s, $v_4$=0.4 cm/s, $v_5$=1 cm/s, $v_6$=2 cm/s, $v_7$=3 cm/s).**

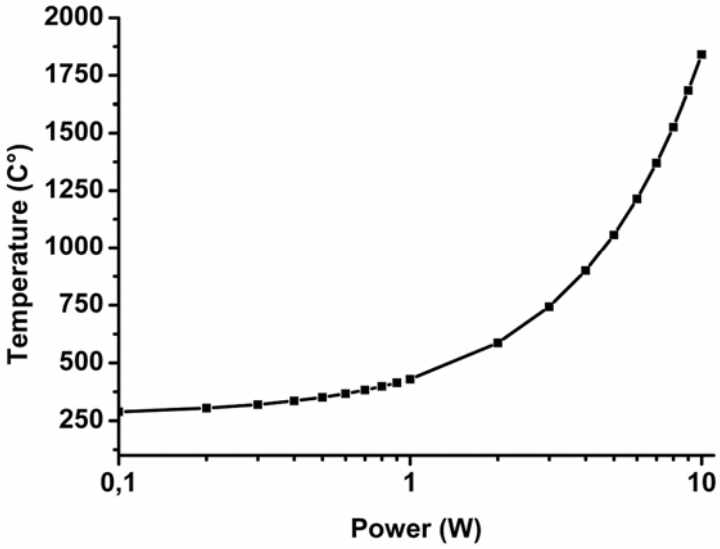


**Figure 4.10 Maximum temperature rise on alumina.**

A real time temperature measurement was also conducted using a thermal imaging system. The temperature rise at the beam center shows variations with the scanning speed. When the surface of the deposited layers is heated 10 seconds with a laser operating at a power of 2 W, the maximum temperature rise at the center of the beam reaches up to 900-1000°C (Figure 4.11a).

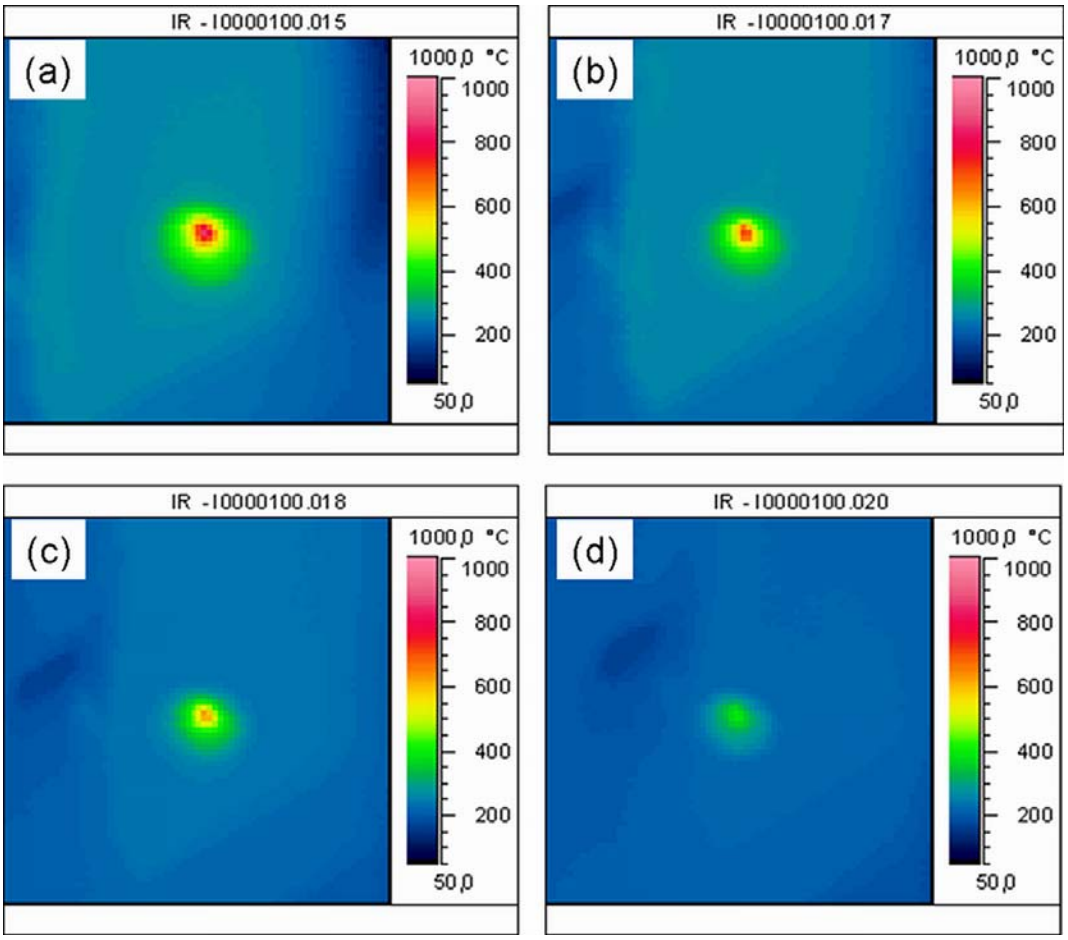


**Figure 4.11 Thermal camera analysis of laser irradiated spot on the deposited layers at various scanning speeds. (a) Stationary, (b) 0.25 mm/s, (c) 0.5 mm/s and (d) 2 mm/s.**

When the same laser power density is applied at a scanning speed of 0.25 mm/s and 0.5 mm/s the temperature rise in the beam center goes down gradually as shown in Figure 4.11b and c. The effect becomes even clearer at higher scanning speeds such as 2 mm/s (Figure 4.11d) There is a large deviation between the calculated and measured temperature profiles. The calculated temperature profile is based on a stationary heat source and also thermal conductivity, absorption and similar material properties are assumed to stay constant. In reality, these factors are temperature dependent. In addition,

$Al{\cdot}Al_2O_3$ nanowires form an extremely complicated model to predict the temperature rise upon laser irradiation. It is believed that there is a strong enhancement of the electrical field due to the tangled geometry of the 1D structures and dielectric-metal interfaces. Moreover, oxidation of the Al cores leads to further local temperature rises since the process is a well known exothermic reaction. In addition, due to resolution limits of the thermal camera the exact temperature measurement at the center of a Gaussian beam is not possible.

#### 4.7.2.2 Thermal Analysis of Al-core Melting and Oxidation

After the estimation of the surface temperature rise depending on the laser intensity and scanning speed, similar measurements were carried out under vacuum and in air. With the help of the thermal camera the temperature rise on the surface of the coating was monitored both under vacuum and in air while keeping the laser intensity and exposure time constant. The temperature rise due to laser induced heating under vacuum is lower than in air, as shown in Figure 4.12 and b respectively. This is a clear in-situ observation of the oxidation of the Al core since it is well known that oxidation of Al is followed by the energy release, which is a common exothermic nature of combustion reaction. In the presence of oxygen, the $Al{\cdot}Al_2O_3$ system is of course metastable at high temperatures, although Al entities are well protected by the $Al_2O_3$ shells.

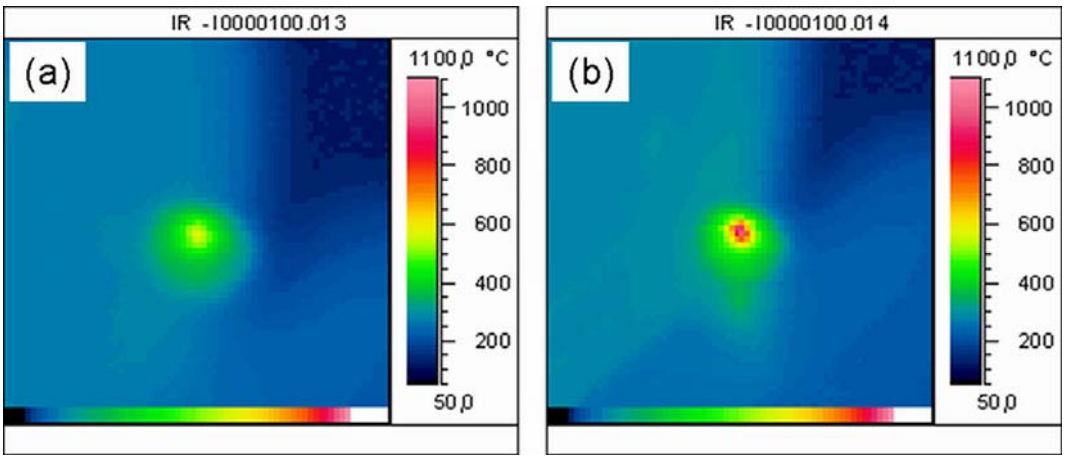


**Figure 4.12 Thermal camera analysis of laser irradiation of $Al{\cdot}Al_2O_3$ nanowires (a) under vacuum and (b) in air.**

If we consider the combustion of aluminum in oxygen, the enthalpy of the combustion of bulk aluminum is about 1675 kJ/mol. As a next step we can consider the

smallest possible aluminum particle, e. g. a particle with only one atom. The enthalpy of combustion of an isolated aluminum atom is about 2324 kJ/mol [243]. Such oxidation mechanism is shown in the following reaction schemes (4.6) and (4.7).

$$Al(bulk) + O_2 \rightarrow Al_2O_3(s) \qquad \Delta H = -1675 \quad KJ/mol \tag{4.6}$$

$$Al + O_2 \rightarrow Al_2O_3(s) \qquad \Delta H = -2324 \quad KJ/mol \tag{4.7}$$

In this context, heating with a low energy laser can cause cracking of the oxide layer and transformation of Al into $Al_2O_3$. It seems that the Al regions in the composite, which have a high surface area because of the nano-scale, react with oxygen very efficiently following the laser destruction of the composite. The liberated energy is trapped in the system and high enough to drive the transformation to high temperature stable $\alpha$-$Al_2O_3$. Basically, the reaction can be written in the following form (4.8).

$$Al \cdot Al_2O_3 + 3/4\,O_2 \xrightarrow{laser} 3/2 \quad \alpha - Al_2O_3 \tag{4.8}$$

A schematic reaction coordinate can be shown in Figure 4.13. $E_A$ is the activation energy needed to destroy the $Al_2O_3$ film on the Al particles. $\Delta H$ is the enthalpy of the oxidation reaction and it has a negative value which corresponds to an exothermic reaction. The destruction and rupture of the oxide layer will be examined in the next sections.

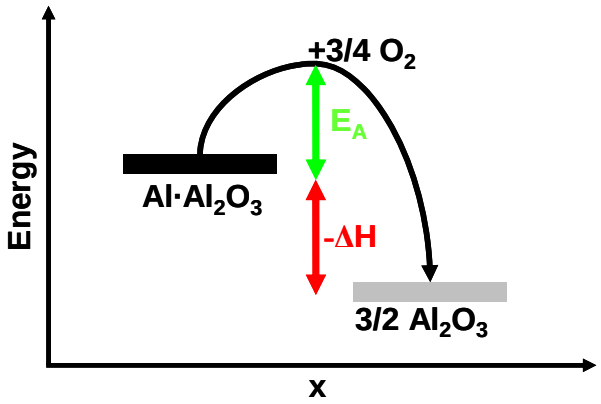


**Figure 4.13 Schematic reaction coordinate showing transformation of $Al \cdot Al_2O_3$ to $Al_2O_3$.**

#### 4.7.2.3 Effect of the Heating Rate and Oxide Shell on the Oxidation of the Al-core

Thick oxide layers encapsulating the Al core can stay non-deformed and mechanically rigid up to 1200°C which is well above the melting temperature of Al [244]. The thickness of the oxide layer, the size and the shape of the Al particles are the critical parameters defining the stability of the oxide layer. Yang et al. showed that oxide layers covering 110 nm nanoparticles keep their mechanical stability up to 550°C. At temperatures above 620°C the crack formation was observed within the thin oxide layer [245]. In addition to material properties, the heating rate also plays a major role on the stability of the oxide layer. Trunov et al. showed, using thermo-gravimetric analysis, that aluminum nanoparticles are oxidized through a stepwise process at slow heating rates [246]. In the first step the amorphous $Al_2O_3$ shell grows in thickness at low temperatures, in the second step it transforms into denser crystalline $Al_2O_3$ polymorphs. As the temperature continues increasing, the crystalline oxide layer grows and gets denser. The formation of a higher density $Al_2O_3$ polymorph results in a reduction of the overall oxide thickness and the diffusion resistance of the oxide layer. An accelerated oxidation continues until the oxide layer transforms into a fully polycrystalline film.

Rai carried out a qualitative study using hot-stage TEM imaging to observe the melting behavior and single particle mass spectrometry (SPMS) to study the oxidation behavior of nano-aluminum particles during heating [243]. While Trunov et al. used low heating rates (1-5°C/min), Rai et al. used a heating rate of about 33°C/min and found that melting of aluminum causes the rupture of the oxide shell and may be the primary step in the oxidation (and ignition) of aluminum nanoparticles. These studies indicate that the oxidation mechanism for Al nanoparticles depends very much on the heating rates. At low heating rates there can be a diffusive and stepwise oxidation, whereas at high heating rates a dispersive mechanism can dominate the oxidation.

In this context, we carried out a comparative study on the oxidation of Al cores within $Al{\cdot}Al_2O_3$ nanowires by applying different types of heat treatments using a laser beam, a conventional oven and inductive heating. Deposited layers firstly were heated in a conventional oven at a rate of 2°C/min up to 700°C and left at this temperature for 3 hours. In Figure 4.14a the SEM image shows the morphology of the nanowires before the heat treatment. After the heat treatment some local agglomerations are seen on the

surface (Figure 4.14b) which may be attributed to the flow of molten Al cores. It is believed that some cracks form within the oxide layer during the heating processes. At 700°C the Al cores seem to melt and flow through these cracks. The molten Al is believed to be oxidized upon re-solidification. On the other hand, since the heating rate is very low, the rupture of the oxide layer can not be the only mechanism to define the oxidation of the Al cores. There might be also a diffusion controlled oxidation mechanism. Furthermore, it should be expected that, because $Al^{+3}$ is a smaller ion, it should diffuse faster than oxygen and thus enhance the rate of oxidation.

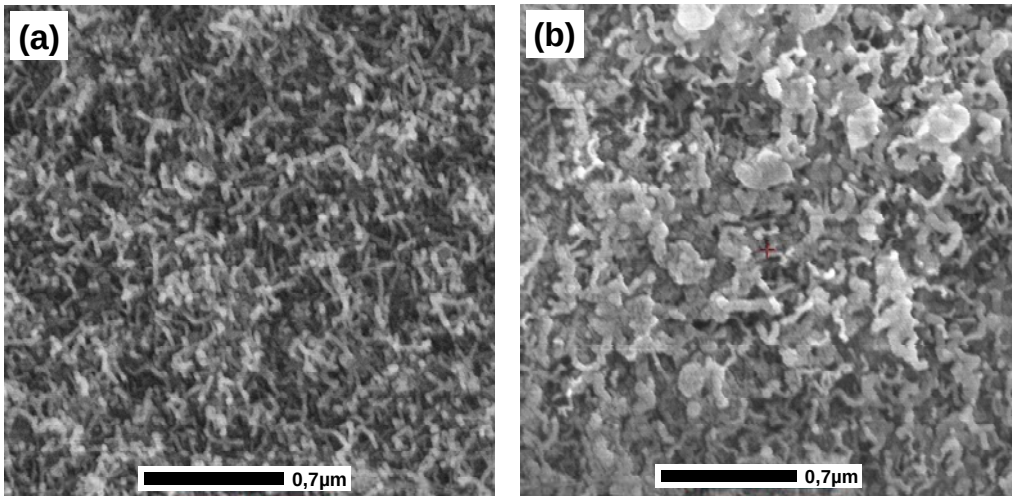


**Figure 4.14 SEM images of Al·$Al_2O_3$ nanowires (a) before and (b) after heating in a conventional oven.**

In comparison, by inductive heating a high heating rate of 10-15°C /min was applied to reach 700°C. The heat treatment was carried out for 3 hours.

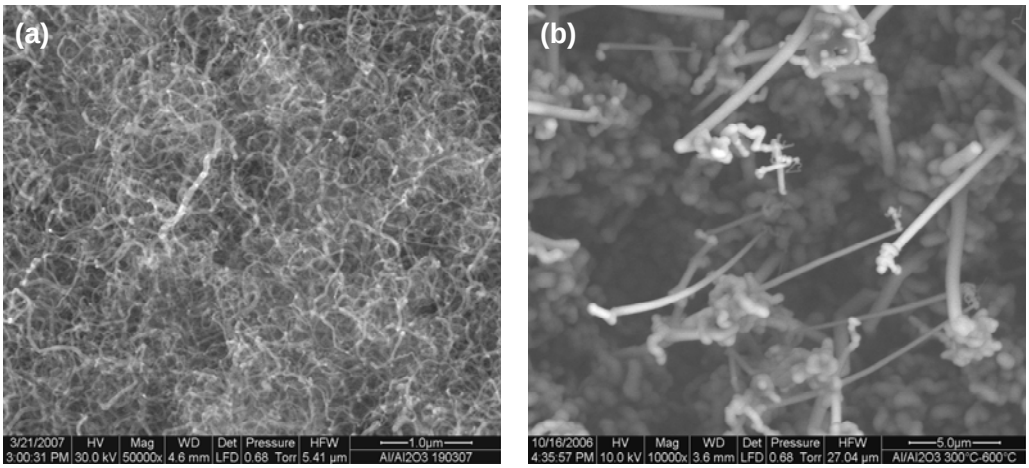


**Figure 4.15 SEM images of Al·$Al_2O_3$ nanowires before (a) and after (b) inductive heating.**

As seen in Figure 4.15a and b, there is a clear difference between the morphology of deposited and heat treated nanowires. After the heat treatment the formation of straight 1D structures is observed. It seems that the melted Al core flows outwards through nano or micro cracks formed within the shell due to high heating rates. When a single and small crack forms on the oxide shell locally, the molten Al core may go out like a "*pressurized water jet*". Theoretical calculations show that during heating of oxidized Al nanoparticles, expansion of the molten Al core can lead to a contact pressure of 3-5 GPa at the $Al/Al_2O_3$ interface [247].

In order to analyze the formation of such a high contact pressure, an analogy can be proposed between core-shell nanowires and co-axial composite cylinders. For composite cylinders one can use an elastic model described elsewhere [248] to define the stress tensors and displacements on the shell as well as the core. During the heating of such a composite cylinder a contact pressure and tensile stress appears at the core-shell interface due to the difference (known as interference, Δ) between the external radius of the Al core and the internal radius of the oxide shell. Such a condition is shown schematically in Figure 4.16 assuming the existence of a core-shell cylinder where r/R is taken as 0.53 (derived from the previous theoretical calculations given in Chapter 3).

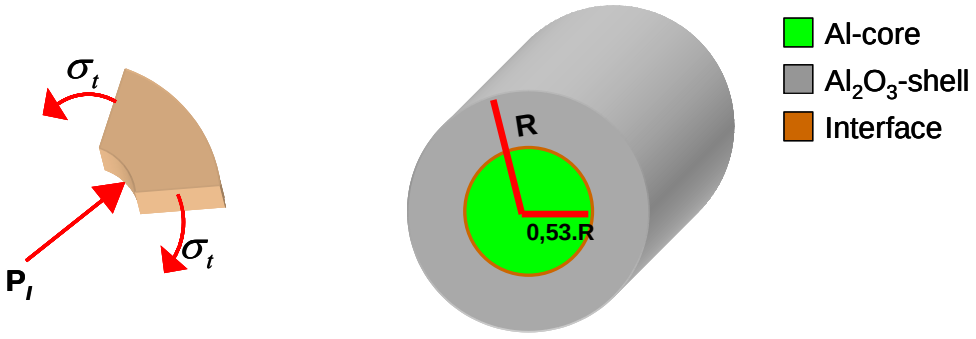


**Figure 4.16 Schematic illustration of the pressure formation at the core-shell-interface.**

The interference forms because of the mismatch between thermal expansion coefficients and densities of Al and its oxide. The radial stress and hoop stress at the metal-oxide interface can be written in the following forms (4.9) and (4.10) respectively, [225],

$$\sigma_r = -P_I \qquad \textbf{(4.9)}$$

$$\sigma_t = \frac{P_I (R_{Al_2O_3} + R_I)}{(R^2_{Al_2O_3} - R^2_I)} \qquad \textbf{(4.10)}$$

where $\boldsymbol{P_I}$ : contact pressure at metal-oxide interface, $R_{Al_2O_3}$ : external radius of the shell, $\boldsymbol{R_I}$: interface radius. Then displacement within the Al core $X_{Al}$ and oxide shell $X_{Al_2O_3}$ can be shown in the following forms (4.11) and (4.12).

$$x_{Al} = -\frac{(1-\nu_{Al}) P_I R_I}{E_1} \qquad \textbf{(4.11)}$$

$$x_{Al_2O_3} = \frac{P_I R_I}{(R^2_{Al_2O_3} - R^2_I) E_2} [(1-\nu_{Al_2O_3}) R^2_I + (1+\nu_{Al_2O_3}) R^2_{Al_2O_3}] \qquad \textbf{(4.12)}$$

The interference, Δ, can be written in the following forms **(4.13)** and **(4.14)**,

$$\Delta = (x_{Al_2O_3} - x_{Al}) \qquad \textbf{(4.13)}$$

$$\Delta = \frac{P_I R_I}{(R_{Al_2O_3} - R_I) E_{Al_2O_3}} [(1-\nu_{Al_2O_3}) R^2_I + (1+\nu_{Al_2O_3}) R^2_{Al_2O_3}] + \frac{1-\nu_{Al}}{E_{Al}} P_I R_I \qquad \textbf{(4.14)}$$

where $\nu_{Al}$, $\nu_{Al_2O_3}$ and $E_{Al}$, $E_{Al_2O_3}$ are Poisson`s ratios and Young`s moduli of the Al and oxide respectively. One can define the interference also using the linear expansion coefficient of Al, $\alpha^L_{Al}$ and $Al_2O_3$, $\alpha^L_{Al_2O_3}$ as shown in **(4.15)**.

$$\Delta = R_I (\alpha^L_{Al} - \alpha^L_{Al_2O_3})(T - T_0) \qquad \textbf{(4.15)}$$

In the case of an $Al{\cdot}Al_2O_3$ core-shell system there can be some additional stresses in the oxide film due to the change in the volume of the Al core upon melting. After melting of aluminum, the density changes from 2.7 g/cm$^3$ to 2.4 g/cm$^3$ resulting in an

expansion of about 6 % and the metallic core increases linearly by 2 %. Then, the interference at the melting point $T_m$ can be written as shown in equation (4.16).

$$\Delta = 1{,}02R_I[1+\alpha^L_{Al}(T_m - T_0)] - R_I[1+\alpha^L_{Al_2O_3}(T_m - T_0)] \qquad \textbf{(4.16)}$$

One can easily calculate the contact pressure at the interface during melting by solving the equations (4.14) and (4.16) using the values given in the Table 4.7. For example, for a nanowire having an outer diameter of 40 nm, the contact pressure $P_I$ reaches a value of 3.77 GPa. This value is very close to calculations of Levitas et al. He stated that in thin oxide shells the pressure levels can reach up to 3-5 GPa [247]. In his detailed work, it is shown that such a high pressure between the core and the exposed surface creates an unloading wave which disperses the molten core via atomic scale clusters. Further increase in the pressure makes these clusters flow through the ruptured oxide shell.

| **Properties** | **Al** | **$Al_2O_3$** |
|---|---|---|
| **Poissons`s ratio (ν)** | 0.34 | 0.27 |
| **Young`s modulus (E)** | 70.6 GPa | 398 GPa |
| **Linear expansion ($\alpha^L$)** | $7.7x10^{-7}\,K^{-1}$ | $2.4x10^{-7}\,K^{-1}$ |
| **Density (ρ)** | 2.55 $g/cm_3$ | 3.97 $g/cm_3$ |

**Table 4.7 Physical properties of Al and $Al_2O_3$** (γ-phase)**.**

A recent molecular dynamic calculation also confirms the presence of such a high pressure on the Al core and negative pressure (tension) on the oxide shell at ca. 700°C [249]. The results of this theoretical study show that the oxide shell is dynamically unstable upon melting of the Al core. In his detailed work Brandon et al. showed also that the pressure rise in smaller particles is higher than that in larger particles, implying that smaller particles should have a higher propensity to rupture. The oxide layer on a small particle is under higher tension because of the high curvature in comparison to a larger particle. Presence of different sized $Al{\cdot}Al_2O_3$ nanowires, local changes in the shell/core widths and inhomogeneous distribution of Al (especially accumulation at the head of nanowires) can trigger the formation of additional pressure gradients and mechanical stresses at the oxide-shell interface.

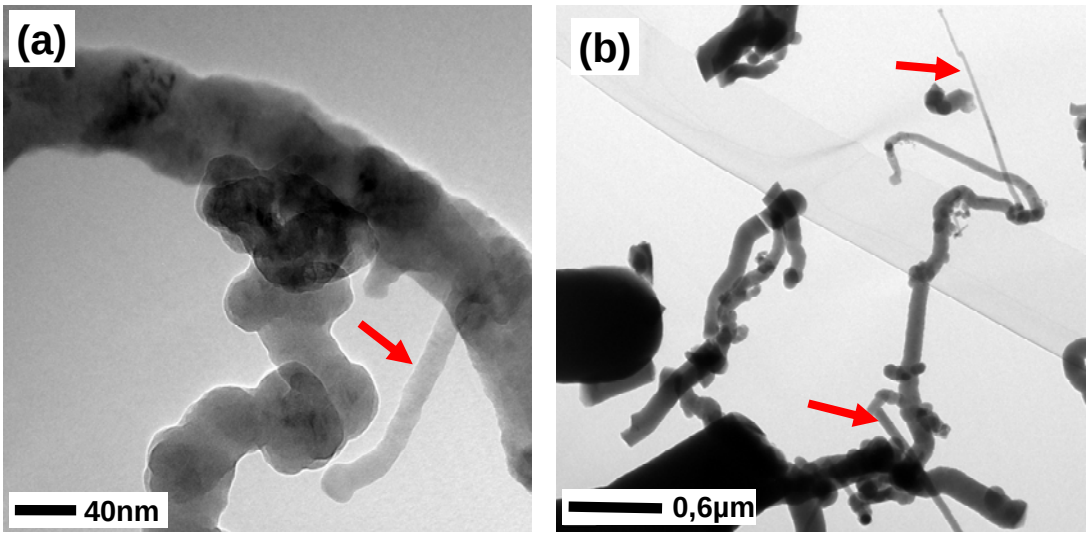


**Figure 4.17 TEM images of Al·$Al_2O_3$ nanowires after inductive heating, (a) high magnification, (b) low magnification (arrows indicate the directional growth).**

In the TEM images given in Figure 4.17a and b such directional growth can be seen more clearly. Straight wires grow after the inductive heat treatment which reminds of our similar observations presented previously in Figure 4.15b. It is believed that the molten Al flows out through a small crack similar to the flow of water in a straight way from a squeezed plastic pipe. It seems that upon solidification, firstly straight tiny nanowires form and they grow due to oxidation and high temperature heat treatment. At the end, larger 1D sub-micro structures form. The final morphology of such 1D structures can be seen in Figure 4.18.

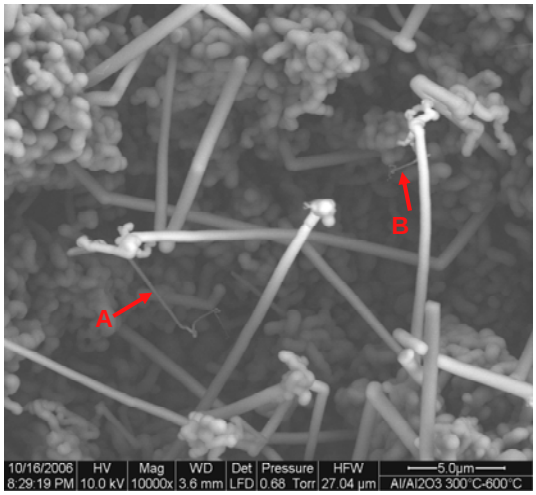


**Figure 4.18 SEM image showing directional growth after inductive heating of Al·$Al_2O_3$ nanowires.**

Although the temperature of the graphite block is measured as 700°C, there can be temperature gradients due to inductive heating. In some regions on the surface, the temperature can stay below the melting temperature or exceed it. If the local heat increase is still enough to re-melt the aluminum within straight micro or nanorods, there can be a release of the molten aluminum again. Such a condition can be seen easily in microrods labeled with A and B shown in Figure 4.18.

Levitas et al. showed that Al can go out as a pressurized fluid at extremely high pressure levels [247]. In addition to the pressure effect, the poor wetting of Al on $Al_2O_3$ may trigger the directional flow rather than covering the whole surface. Storaska et al showed that molten Al flowing through the cracks within the oxide shell agglomerates locally and does not wet the oxide shell, as shown in Figure 4.19 [250]. This also can be the reason for similar local agglomeration of molten Al at the end of grown wires (Figure 4.18).

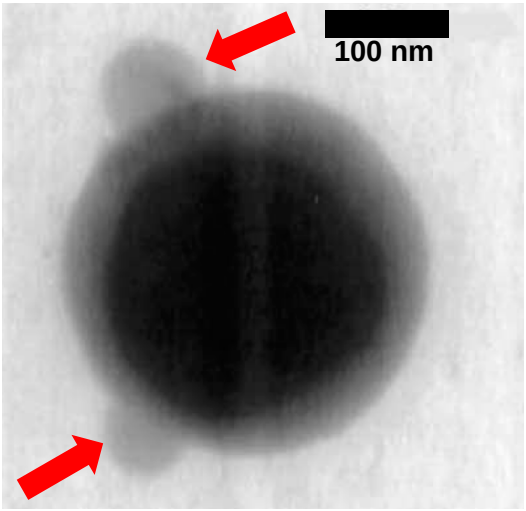


**Figure 4.19 TEM image showing non-wetting behavior of molten Al on the $Al_2O_3$ shell [250].**

#### 4.7.2.4 Effect of Extremely High Heating Rates on Al Oxidation

A $CO_2$ laser operating at 0.5 W was used to heat the deposited Al·$Al_2O_3$ nanowires. The surface temperature was kept at 700°C (similar to oven and inductive heating experiments) with the help of a thermal camera. In comparison to the oven or inductive heating, the laser provides extremely high heating rates, for instance the surface temperature increases to 700°C within ca. 10 seconds. This sudden heating is fast enough to induce thermal cracks in the oxide shell which is also relevant to the results of

Rai et al. [243]. Rai showed that at 4C°/s or higher rates of heating there is a clear rupture on the oxide skin.

As a reference Figure 4.20a shows the SEM image of the $Al{\cdot}Al_2O_3$ composite layer as-deposited. Figure 4.20b demonstrates the surface topography formed after 15 seconds of laser heating, where the characteristic features are random agglomerates and sphere-like nanoprotrusions. Such features mostly are seen on the surface where dense and highly interpenetrating nanowires are found. This phenomenon can be attributed to the extreme enhancement of the electrical field at crossed geometries of nanowires as explained previously in Chapter 4.7.1. On some part of the substrate surface where more dense and interpenetrated nanowires are found, the Al concentration naturally is higher. This means the oxidation of more Al with the laser heating can result in the release of more excessive heat which may increase the temperature of the reaction zone more. The shape of the molten parts observed at the end of the nanowires reminds also of the poor wetting of molten Al on $Al_2O_3$ surface.

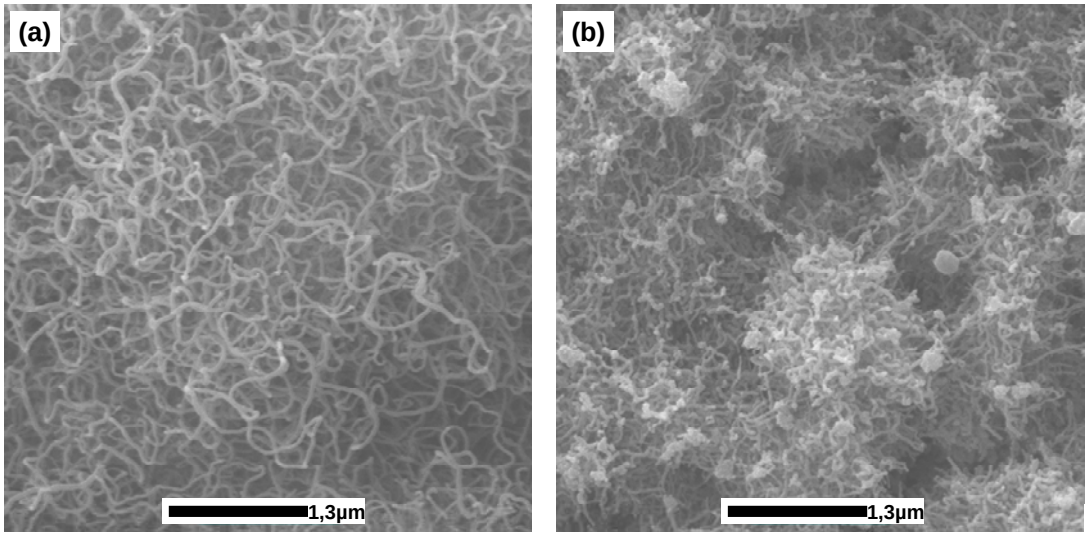


**Figure 4.20 SEM images showing $Al{\cdot}Al_2O_3$ nanowires (a) before and (b) after laser heating.**

When the $Al{\cdot}Al_2O_3$ composite layer is heated with a higher power (2 W) laser, dendrite-like branched structures are observed, as shown in Figure 4.21. It is believed that the sudden melting of Al is followed by cracking of the oxide skin. Then molten and pressurized Al seems to spread randomly through the cracks. In the case of such a sudden ejection of molten Al, a gradual melting approach (oven heating) can not be

considered anymore and non-wetting behavior of molten Al on $Al_2O_3$ becomes not critical for the flow of molten Al.

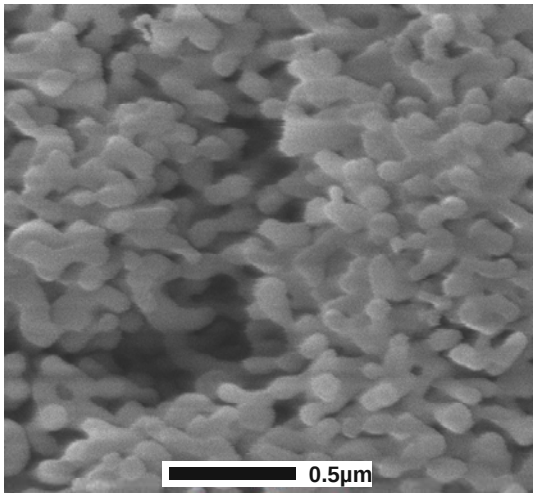


**Figure 4.21 SEM image of dendritic structures after short laser heating of Al·$Al_2O_3$ nanowires.**

### 4.7.3 Morphology Changes upon Laser Heating

#### 4.7.3.1 Macro/Optical Changes upon Laser Heating

It is observed that after scanning a line under the focused laser beam, the color changes from black to white. The width of the laser induced line and the degree of macroscopic color changes depend on the laser power and the scanning speed. At low scanning speeds the laser beam can be assumed as a stationary heat source. In this context, Al·$Al_2O_3$ nanowires were treated with argon ion and $CO_2$ lasers using extremely low scanning speeds to see the effect of the laser intensity on the macro-morphology changes.

Figure 4.22 shows the optical micrographs of tracks induced by the argon ion laser at different laser powers and a constant scanning rate of 3 mm/s. It is obvious that the laser beam induces local changes which can be attributed to the oxidation of Al cores and oxide phase transformations. In laser treatment of alumina surfaces, crack formation is a common problem due to the difference in the expansion coefficients of alumina and the underlying substrate. Interestingly, the optical images given in Figure 4.22 show no macro crack formation. Increase in laser energy broadens the line width of the heat affected zone (HAZ) which is a direct consequence of a Gaussian type heat source ($TEM_{00}$).

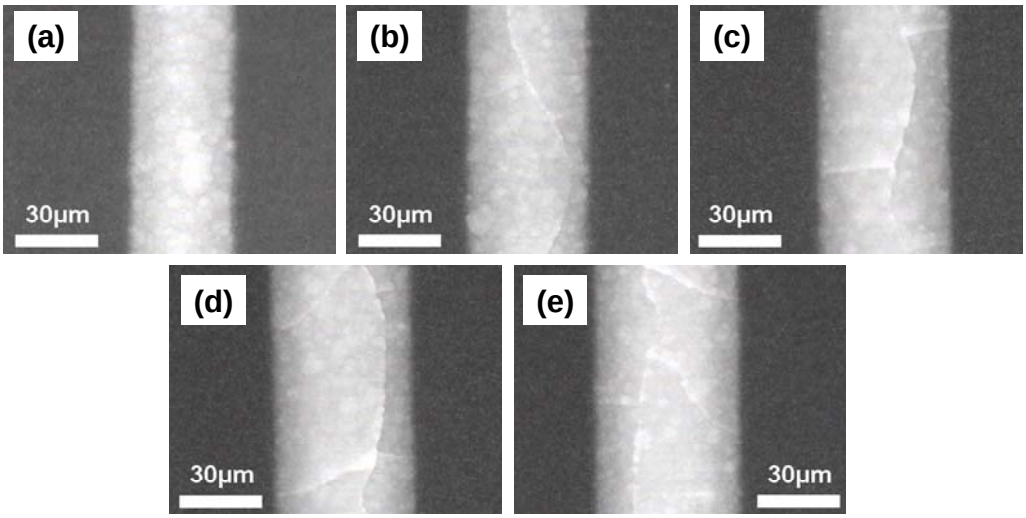


**Figure 4.22 Optical microscope images of Al·$Al_2O_3$ nanowires after argon laser treatment at different powers. (a) 0.5 W, (b) 0.6 W, (c) 0.7 W, (d) 0.8 W and (e) 0.9 W.**

In the case of the $CO_2$ laser, a different effect is observed. Figure 4.23 shows the optical microscope images of a single track treated with a $CO_2$ laser at different intensities.

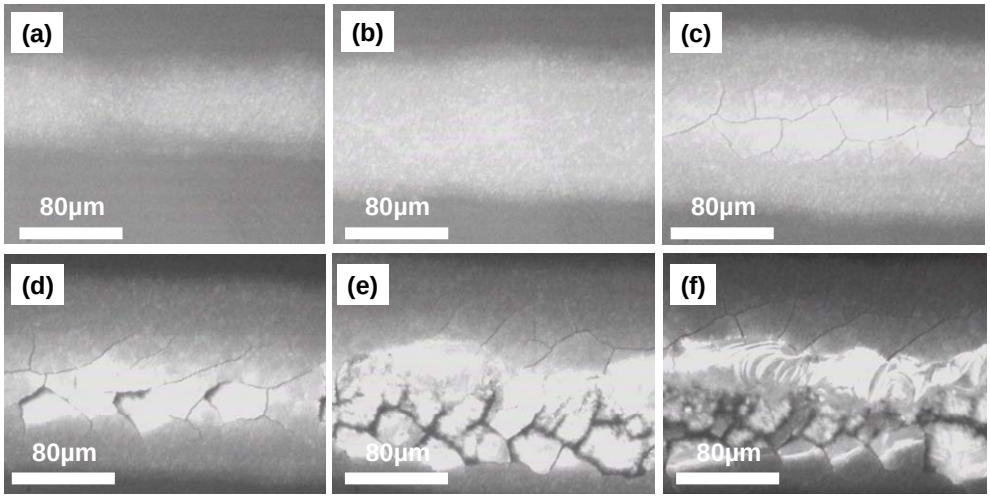


**Figure 4.23 Optical microscope images of Al·$Al_2O_3$ nanowires after $CO_2$ laser treatment at different powers. (a) 0.5 W, (b) 1 W, (c) 1.5 W, (d) 3 W, (e) 4 W, (f) 5 W.**

Due to high power densities, the line width of a track induced by a $CO_2$ laser naturally is larger in comparison to argon ion laser treatment. In addition, the $CO_2$ laser beam can not be focused as much as the argon ion laser, which is a natural consequence of the Abbè diffraction limit ($\lambda/2$). The effect of the high power on the crack formation can be seen directly in Figure 4.23c, d and e. At higher laser intensities the crack

formation starts, which is a common problem in high energy $CO_2$ laser processing of ceramic layers. As seen in Figure 4.23f, at extremely high laser intensities there is a melt flow.

Although a detailed investigation, which will be presented in next chapters, is needed to understand the laser induced morphology and structure changes, the argon ion laser seems to be more suitable for marking or structuring of $Al{\cdot}Al_2O_3$ composite layers, which can be of interest for some applications including permanent labeling and data storage. Lee et al. showed a similar permanent data storage on $Al_2O_3$ using laser induced thermalization [251]. As shown in Figure 4.24a, it is clear that the argon ion laser gives a much better resolution than the $CO_2$ laser (Figure 4.24b).

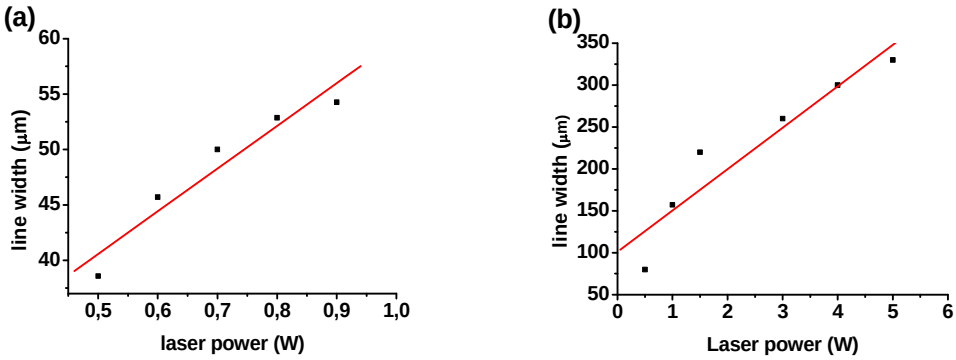


**Figure 4.24 Line width of the laser induced tracks. (a) Argon laser. (b) $CO_2$ laser.**

As shown in Figure 4.25, 2D structures can be written on the $Al{\cdot}Al_2O_3$ composite by using a computer controlled XY scanner. Upon laser induced transformation, the structures exhibit a strong reflection which forms a good contrast with the non-transformed regions. This opens up a new permanent marking approach on ceramic surfaces with low energy visible wavelength lasers, since most of the ceramic marking processes employ high energy $CO_2$ lasers which yield poor resolution in structuring [252].

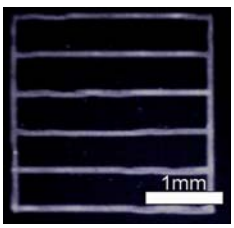


**Figure 4.25 Optical microscope image of 2D structures written on $Al{\cdot}Al_2O_3$ composite.**

A Gaussian laser beam leads to a temperature distribution on the surface. The laser intensity drops to $1/e^2$ at Gaussian-half width of the beam. The surface of the deposited layers was treated with the $CO_2$ laser at a laser power of 4 W and a scanning speed of 0.05mm/s in order to see the effect of the Gaussian distribution on the morphology. The laser beam was focused on a spot with a diameter of ca. 200 µm using a ZnSe lens. Figure 4.26 shows the SEM image of the laser treated layer, where the temperature distribution effect can be seen clearly.

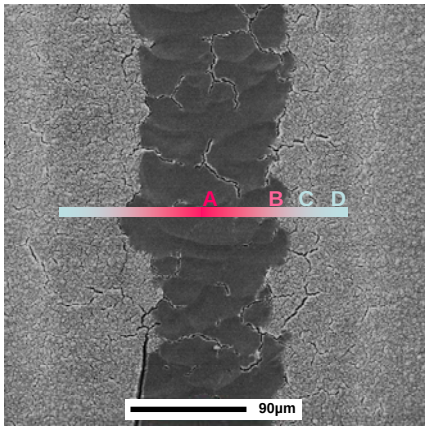


**Figure 4.26 SEM image showing the Gaussian type temperature profile on the laser induced track .**

The label given in the image indicates the different levels of the heating on the surface (red: hot and blue: cold). Whereas a complete densification is observed in the A-B region, a partial densification is observed in the B-C region. There are thermal cracks due to the extremely high heating and cooling rates. In the C-D region only the heat induced growth is the characteristic feature of the morphology. This is a clear indication of a Gaussian type temperature distribution profile.

In the following sections a detailed analysis is carried out on the morphology changes upon the laser treatment. Since the laser beam acts as a Gaussian heat source, the main attention is given to the morphology changes at the beam center in order to analyze the direct effect of the laser heating.

#### 4.7.3.2 Effect of the Scanning Speed on the Morphology

$Al{\cdot}Al_2O_3$ nanowires were treated with an argon ion laser operating at a constant power of 750 mW. The sample was scanned under the focused laser beam at various scanning speeds with the help of a computer controlled XY scanner.

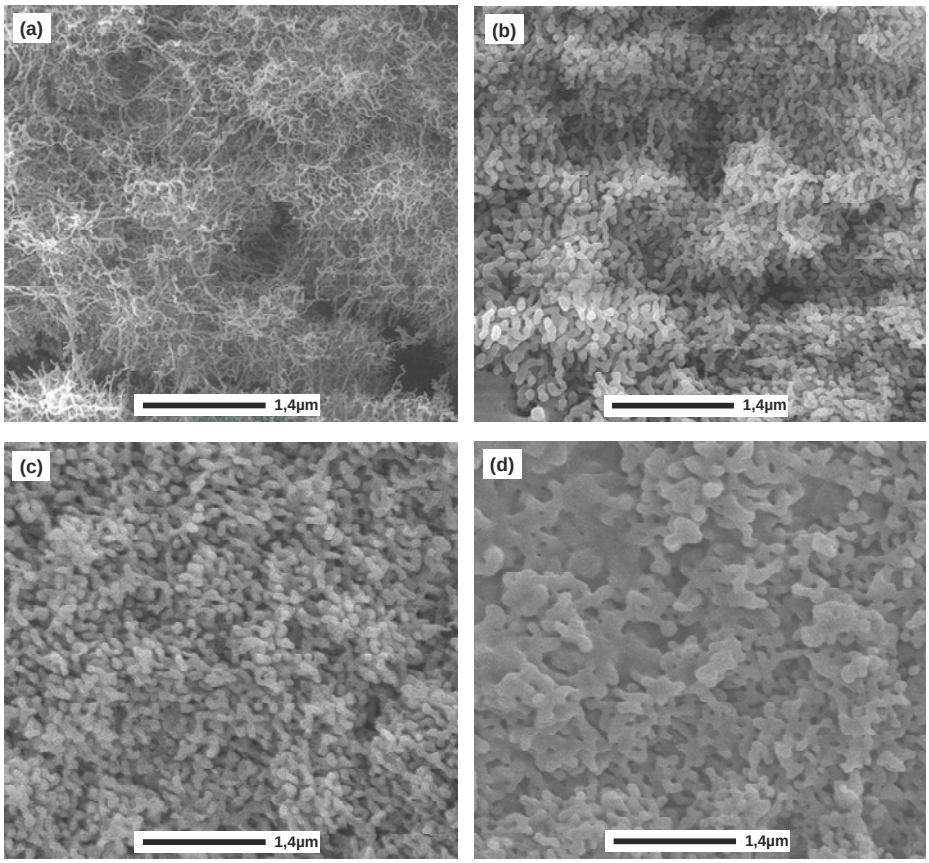


**Figure 4.27 SEM images of Al·$Al_2O_3$ nanowires (a) as-deposited and after laser treatment at scanning speeds of (b) 5 mm/s, (c) 4 mm/s and (d) 3 mm/s.**

Figure 4.27 shows SEM micrographs of Al·$Al_2O_3$ nanowires before and after the laser treatment. Figure 4.27a shows the chaotic Al·$Al_2O_3$ nanowires prior to laser treatment.

Figure 4.27b shows a clear growth and coalescence of the nanowires into fractal structures after laser treatment at a high scanning speed (ca. 5mm/s). Although there is a clear heat induced growth following the laser treatment, still 1D structures are characteristic features of the morphology. The rod-like structures are 200 nm in diameter which is nearly 10 times larger than that of deposited nanowires. Increasing the laser exposure time with lowering the scanning speed down to 4 mm/s leads to further growth and coalescence, as shown in Figure 4.27c. When the scanning speed is lowered to 3 mm/s, 1D structures totally disappear (Figure 4.27d). This can be thought as the early stage of a densification. It is believed that such a densification occurs as a consequence of the melting of the Al core and coalescence of the oxidized Al and former oxides.

#### 4.7.3.3 Effect of the Laser Power on the Morphology

As seen in the previous experimental section, a clear densification is observed at a scanning speed of 3 mm/s. In this context, the same scanning speed was employed to optimize the laser energy power to get fully dense layers. The laser power was increased gradually to see the effect on the densification and morphology. Figure 4.28 shows SEM micrographs of laser-treated $Al{\cdot}Al_2O_3$ nanowires at different laser powers.

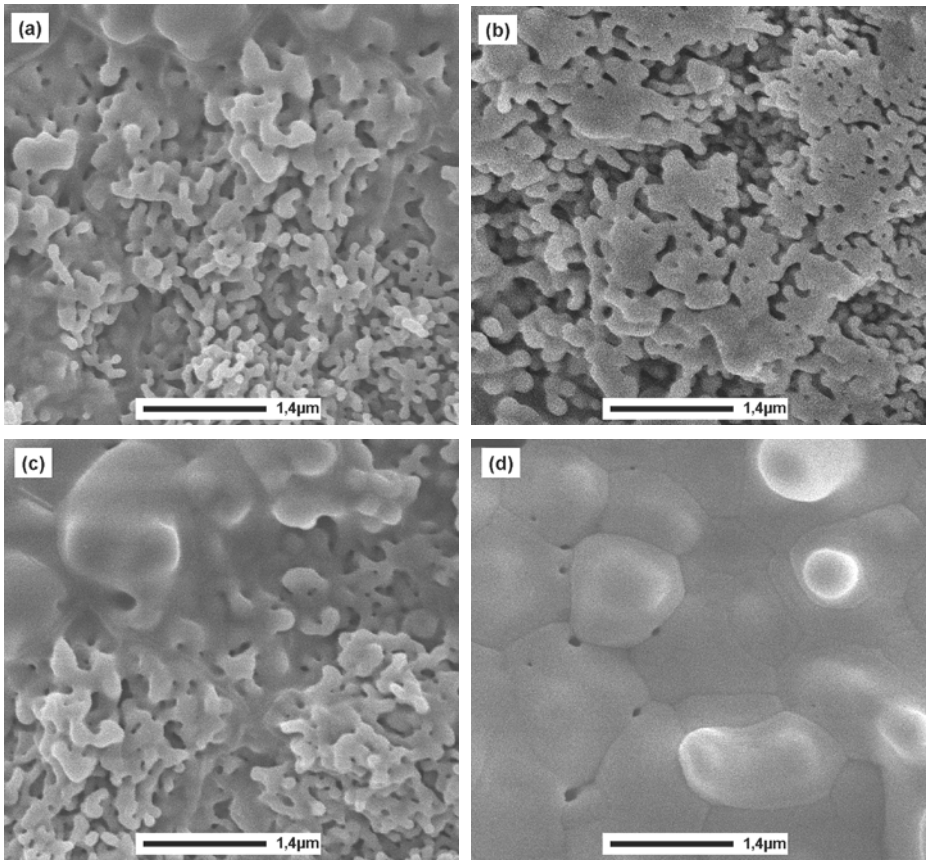


**Figure 4.28 SEM images of $Al{\cdot}Al_2O_3$ nanowires after laser treatment at a power of (a) 1 W, (b) 1.5 W, (c) 2 W and (d) 2.5 W.**

As shown in Figure 4.28a, at a laser power of 1 W worm-like structures grow and interact with each other. The coalescence of the structures resembles to the neck formation during sintering of ceramic particles. When the laser power is increased to 1.5 W the change in morphology becomes more evident (Figure 4.28b). Due to extreme laser heating, fractal-like structures seem to be fused together so that the individual particles can not be distinguished anymore. Wavy structures in Figure 4.28c can be the indication of a possible flow of molten Al. When the laser energy is increased to 2.5 W,

a full densification is achieved (Figure 4.28d). The morphology of the particles evolves into a spherical shape and the surface becomes smoother after the laser treatment, which reveals the existence of full densification.

#### 4.7.3.4 Effect of the Laser Wavelength on the Morphology

In laser assisted photo-thermal patterning applications the minimum feature size depends on the capability of focusing and confining the laser beam. Similar to other optical patterning applications, the resolution is limited with half of the wavelength of the light source (Abbè diffraction [253]). Although in a photo-thermal processing the heat dissipation also affects the resolution, the clear effect of the wavelength can be seen while switching from IR wavelengths to VIS wavelengths.

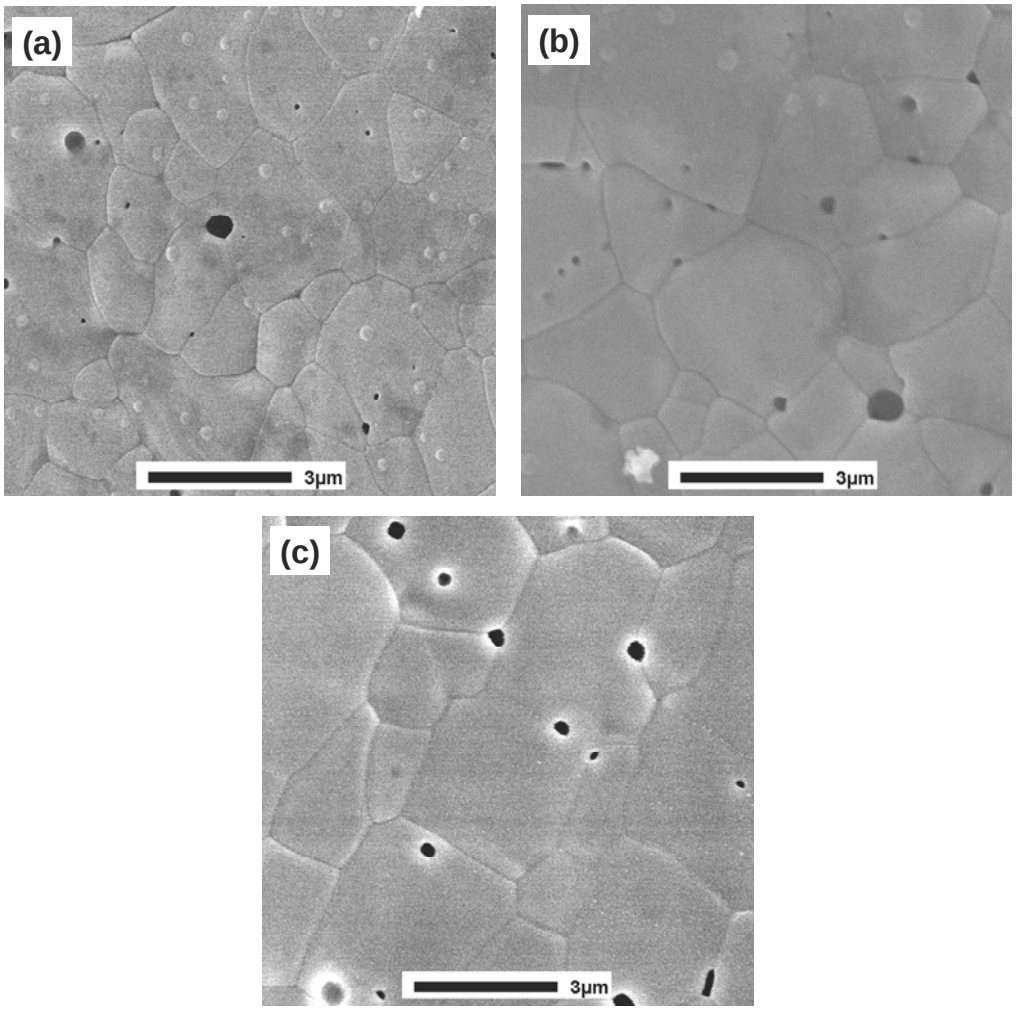


**Figure 4.29 SEM images of argon laser treated layers. (a) 1.5 W, (b) 2 W (2mm/s) and (c) 2 W (1mm/s).**

On the other hand, we observed that the wavelength also has an impact on the morphology of the laser treated $Al{\cdot}Al_2O_3$ layers. Figure 4.29 shows the SEM images of $Al{\cdot}Al_2O_3$ layers treated with the argon ion laser.

Figure 4.29a shows fine grains of $Al_2O_3$ formed after the argon laser treatment (1.5 W). Due to the fast cooling rates some defects are also seen in the image. These defect structures are in the forms of pores and small particles or inclusions. During the fast heating, some gaseous product may form small bubble-like structures. When the laser power is increased (2 W), the grains grow, as seen in Figure 4.29b. In addition, the amount of holes or pores within the grains decreases with the increase in the laser intensity. There are also negligible pores at the grain boundaries which are usually observed in sintering processes. When the laser exposure time is kept longer, the holes within the grains disappear but the pores at grain boundaries remain (Figure 4.29c). Naturally grain growth exits due to heating but the effect is not strong.

In the case of a crack-free sintering with a $CO_2$ laser operating at a comparable power density with that of the argon ion laser, larger grains are observed upon re-solidification, as shown in Figure 4.30a. The effect becomes more dominant when the exposure time is increased (Figure 4.30b).

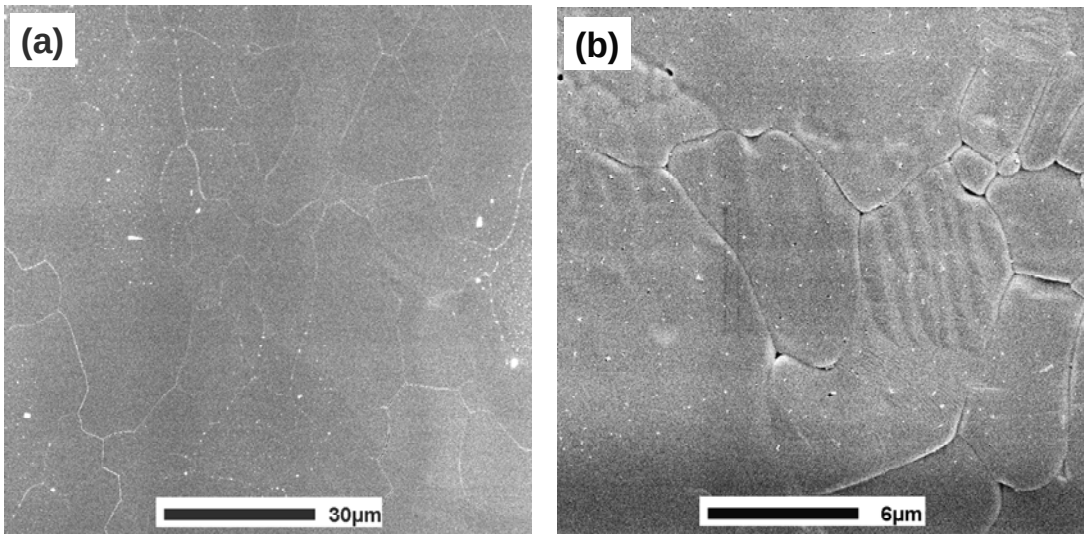


**Figure 4.30 SEM images of layers treated with $CO_2$ laser at a scanning speed of (a) 1 mm/s and (b) 0.5 mm/s.**

In the case of $CO_2$ laser treatment the IR (10.6 µm) wavelength is absorbed by both $Al{\cdot}Al_2O_3$ nanowires and also newly formed $Al_2O_3$ layer upon transformation. When the

laser beam irradiates a thin layer of Al·$Al_2O_3$ nanowires, firstly the composite layer transforms into $Al_2O_3$. Afterwards the grain growth takes place due to the strong absorption of the laser energy by newly formed $Al_2O_3$, as explained schematically in Figure 4.31. It is believed that this causes a non-controlled heat treatment which mostly results in crack formation.

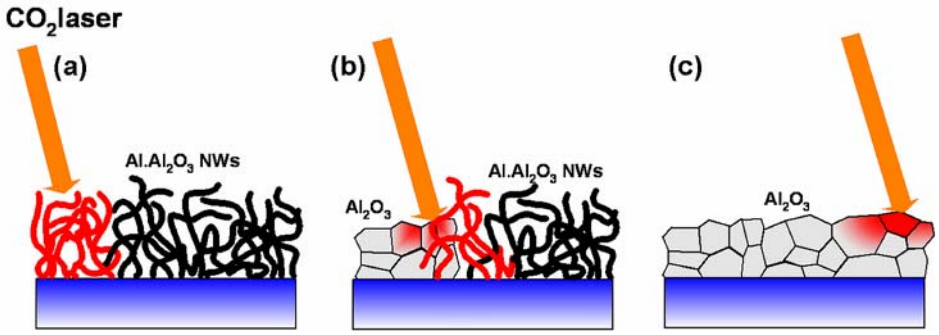


**Figure 4.31 Schematic illustration of the $CO_2$ laser treatment of Al·$Al_2O_3$ nanowires. (a) Absorption of laser light by the nanowires and starting transformation to $Al_2O_3$. (b) Absorption of laser light by the freshly formed dense $Al_2O_3$ layer and nanowires. (c) Excessive heating of the $Al_2O_3$ layer due to strong absorption of laser light.**

In the case of argon ion laser treatment, visible (514 nm) wavelengths are absorbed strongly by Al·$Al_2O_3$ nanowires, but it is reflected back from the white $Al_2O_3$ layer just formed after a short laser heating. This dynamic change in the reflection hinders further heating of the layer, as explained schematically in Figure 4.32. In addition, a visible wavelength radiation is reflected strongly by metal substrates.

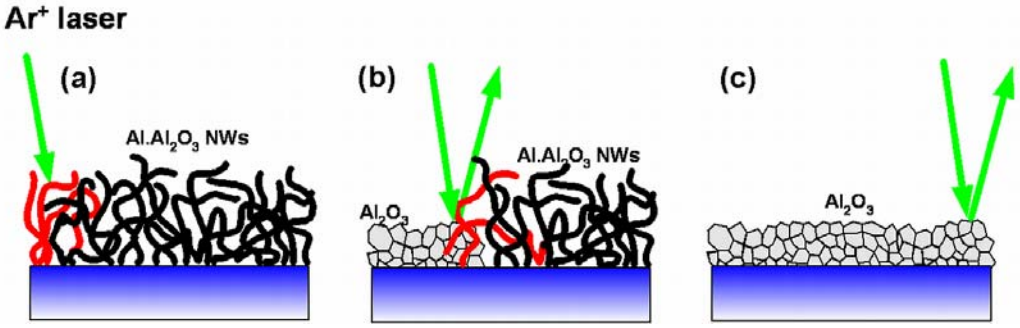


**Figure 4.32 Schematic illustration of the argon laser treatment of Al·$Al_2O_3$ nanowires. (a) Absorption of the laser light by the nanowires and starting transformation to $Al_2O_3$. (b) Reflection of the laser light from the freshly formed dense $Al_2O_3$ layer. (c) Formation of fine grain sized $Al_2O_3$ as excessive heating was prevented by laser light reflection.**

This makes the argon ion laser an effective tool for sintering of thin layers of $Al{\cdot}Al_2O_3$ nanowires deposited on metal substrates and therefore preparing thin alumina coatings without having any substrate deformation.

#### 4.7.3.5 Effect of the Laser Wavelength on the Densification Depth

As shown previously, the wavelength affects the final morphology due to the change in reflection after the laser induced heating. The change in reflection also affects the penetration depth of the laser. When the argon ion laser (514 nm) irradiates the surface of $Al{\cdot}Al_2O_3$, a dense layer of $Al_2O_3$ forms, as shown in Figure 4.33a.

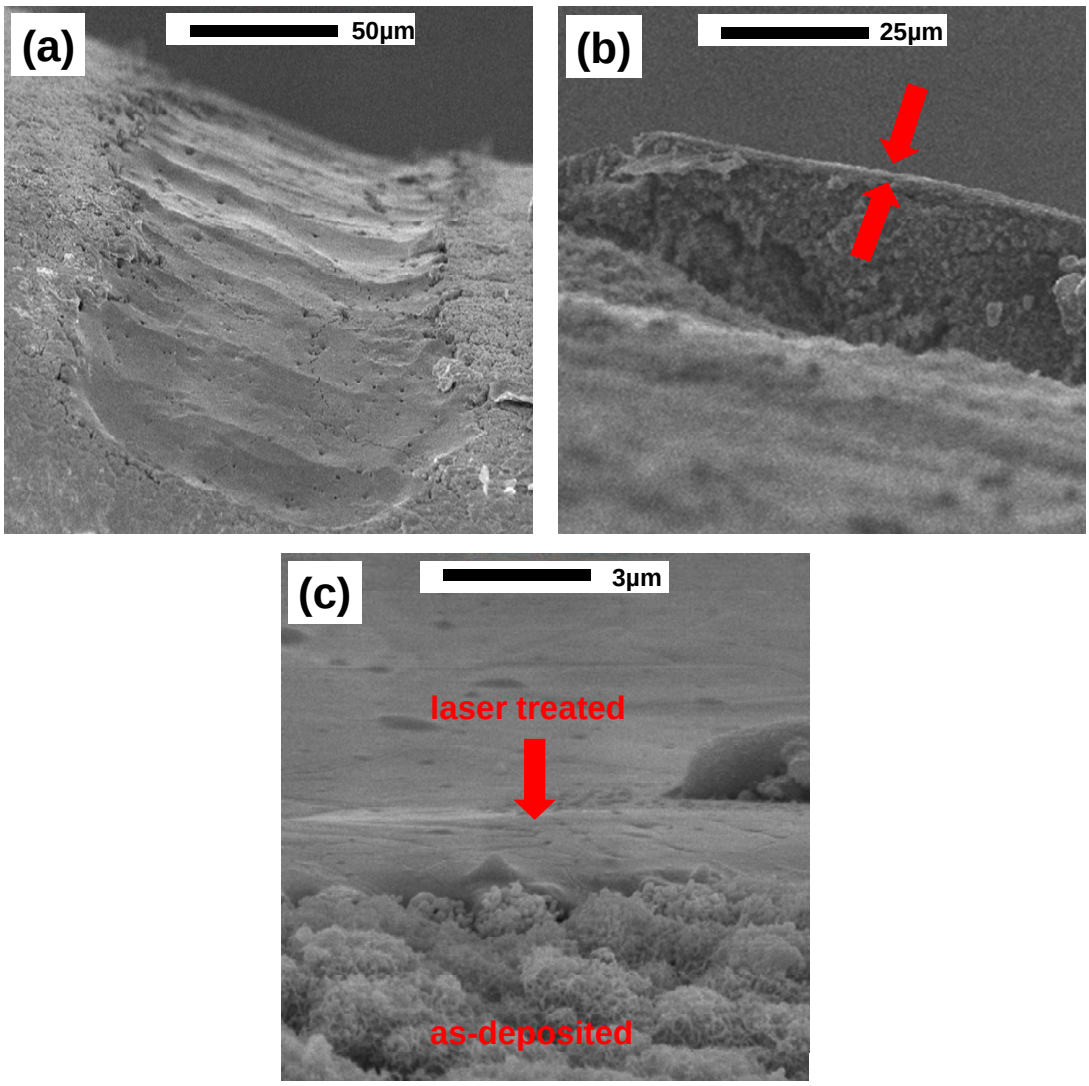


**Figure 4.33 SEM images of argon laser treated layers. (a) Laser induced track on the surface of the deposited layer. (b) Cross-sectional view showing the densified thin layer (shown by red arrows). (c) Laser treated dense layer over non-treated nanowires as deposited.**

The penetration depth of the laser is limited to a few micrometers. As seen in the cross-sectional SEM image given in Figure 4.33b, while the top 2-3 µm thick layer is totally densified, the layers beneath stay as deposited. This can be explained by the change of surface reflection upon laser heating. When the argon laser interacts with the surface layers, it is absorbed and this absorbed energy induces melting of the Al core. After re-solidification and densification, the newly formed dense white $Al_2O_3$ layer reflects the argon laser beam and this hinders the absorption of the laser energy by the layers beneath. The effect can be seen clearly in Figure 4.33c. While the surface layers absorbing the laser energy are densified, the bottom layers keep their 1D nanostructure morphology.

On the other hand, as explained previously, $CO_2$ laser light is absorbed by both $Al{\cdot}Al_2O_3$ and $Al_2O_3$ layers formed during the laser treatment. As shown in the cross-sectional SEM images (Figure 4.34a and b), thicker layers can be densified by the $CO_2$ laser. This clearly shows the effect of the laser wavelength on the penetration depth. As a summary, an argon ion laser is suitable for treatment of thin $Al{\cdot}Al_2O_3$ layers and for thicker layers $CO_2$ laser provides a better densification.

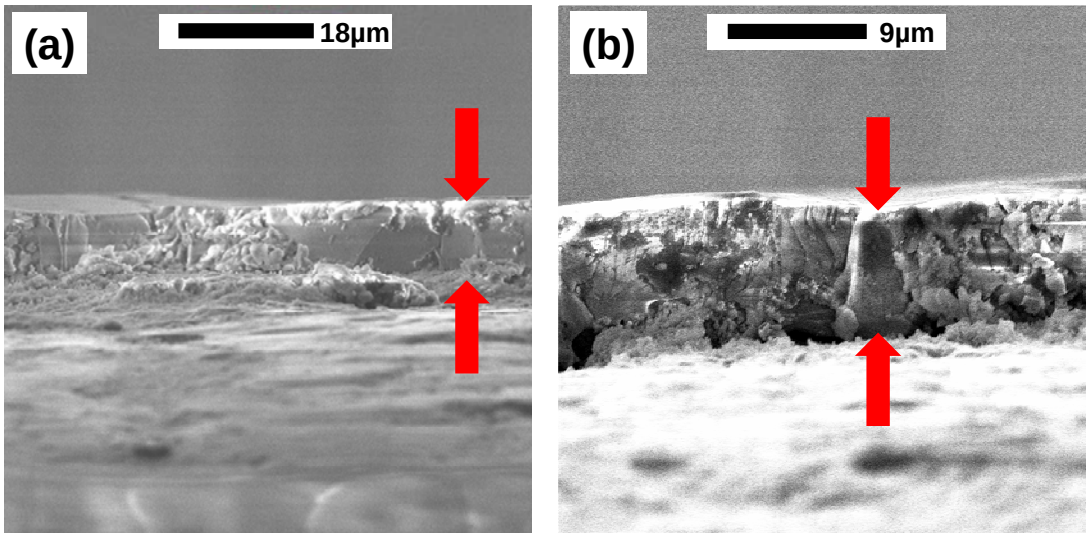


**Figure 4.34 Cross-sectional SEM images of layers (shown by red arrows) densified by the $CO_2$ laser. (a) Low magnification. (b) High magnification.**

### 4.7.4 Laser Induced Crystallization and Structural Analysis

#### 4.7.4.1 XRD Analysis

X-ray diffractograms of deposited Al·$Al_2O_3$ nanowires and the laser treated layers at various scanning speeds are given in Figure 4.35a.

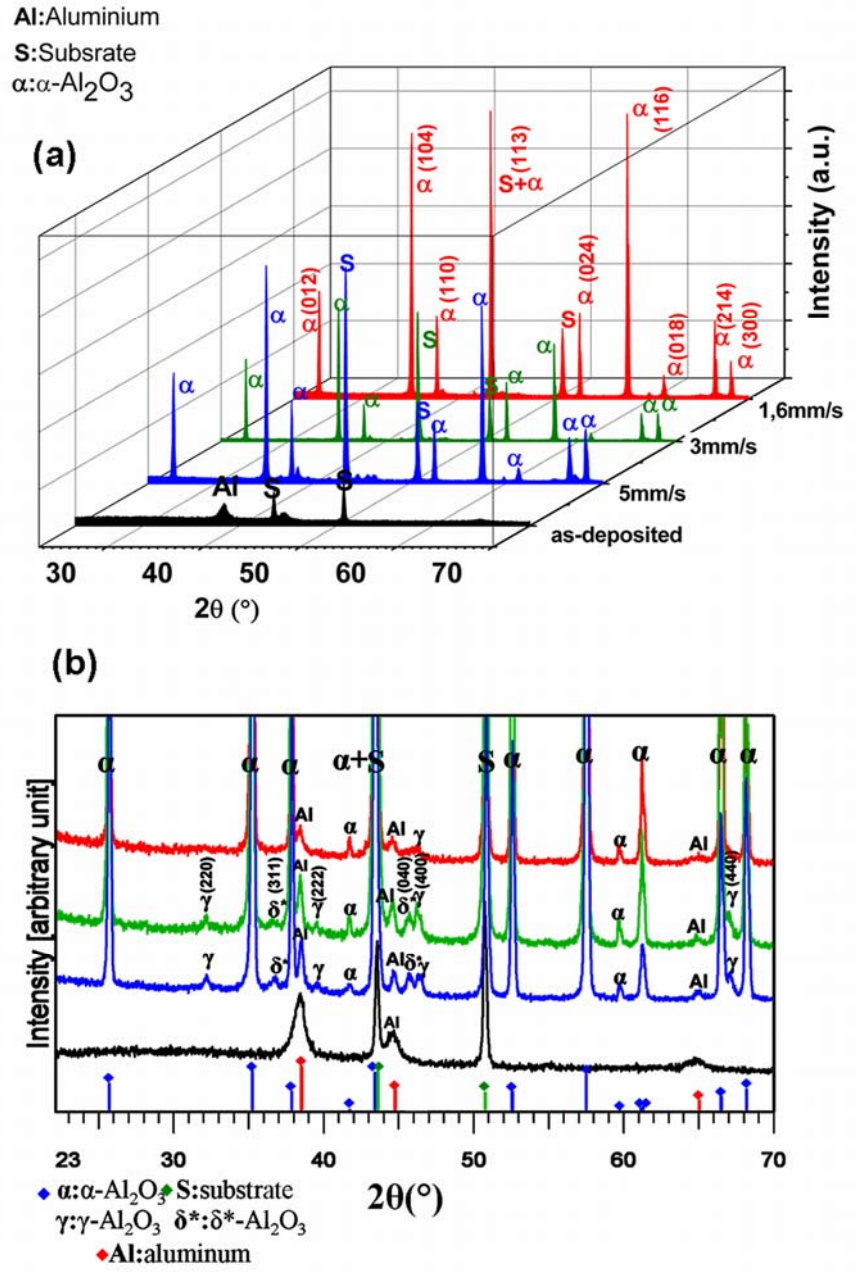


**Figure 4.35 X-ray diffractograms of laser treated surfaces at different scanning speeds. (a) 3D view showing α-$Al_2O_3$ formation. (b) High magnified 2D view showing metastable phases with extremely low intensities.**

The X-ray analysis indicated the formation of a stable α-alumina phase (PDF: 46-1212) with all the scanning speeds employed in the present study. Prior to the laser treatment, the X-ray diffractogram of $Al{\cdot}Al_2O_3$ shows that only the detectable crystalline phase apart from the steel substrate (PDF: 85-1410) is aluminum (PDF: 85-1327). The amorphous background may be attributed to $Al_2O_3$.

It is difficult to get sharp crystalline peaks in the case of nanocrystalline and extremely thin oxide layers. It is accepted that such effects are known to lead to very broad features in the diffractograms [254]. As presented previously in Chapter 3, the HR-TEM images showed that some of the observed lattice distances can either be attributed to the γ-or δ-phase of $Al_2O_3$. Such a mixture of metastable alumina phases seems to be transformed into stable α-$Al_2O_3$ by the laser treatment. Similar studies indicated that laser surface processing can transform, for instance the metastable γ-$Al_2O_3$ in plasma sprayed coatings into more stable α-$Al_2O_3$ [255].

The observation of only α-$Al_2O_3$ peaks is a sign of an effective phase transformation which is promising for the preparation of pure α-$Al_2O_3$ layers. On the other hand, at high resolution XRD diffractograms (Figure4.36b) we detected some additional peaks at very low intensities in comparison to α-$Al_2O_3$ peaks. These peaks can be attributed to other metastable alumina phases. At a high scanning speed of 5 mm/s, we observed some additional peaks. For instance, these diffraction peaks can be attributed to (220), (222), (400) and (440) γ-$Al_2O_3$ peaks (PDF: 10-425), as shown in Figure 4.35b. It is clear that at high scanning speeds the deposited layer is less exposed to the laser irradiation. When the scanning speed is decreased to 3 mm/s, the intensity of these γ-$Al_2O_3$ peaks increases. This is a clear indication of a gradual γ-$Al_2O_3$ transformation. On the other hand, when the scanning speed is decreased 1.6 mm/s, all γ-$Al_2O_3$ peaks except (400) diffraction, totally disappear. The magnitude of this (400) γ-$Al_2O_3$ peak is very low when compared to that of α-$Al_2O_3$. Comparing the magnitudes of the strongest (400) γ-peak and of the strongest (113) γ-peak, an estimate of the γ/α (%) proportion is obtained to some 2 %.

Besides the γ-phase, especially at high scanning rates one can see other diffraction peaks with very low intensities within the noisy diffractograms which can be attributed to other metastable alumina phases including δ-, $\delta^c$-, $\delta^*$- and θ-phases. Two peaks at

36.60° and 46.50° respectively can be assigned to the $\delta^*$-phase (e.g. (311) and (006) crystallographic orientations, PDF 46-1215). Actually, $\delta^*$-phase alumina and metallic Al have diffraction peaks between 44° and 45°; such very close peak positions make the phase analysis difficult. It is not easy to resolve the corresponding individual peaks. Similar to $\gamma$-$Al_2O_3$, $\delta$-$Al_2O_3$ peaks disappear at the lowest scanning speed. The polymorphism may occur from the possibility of different oxygen layer stacking sequences during laser induced temperature gradients. At longer irradiation times the localized laser heating can be sufficient for reconstruction of the stacking sequence to form the most stable $\alpha$-$Al_2O_3$.

At all scanning speeds the $\alpha$-$Al_2O_3$ formation is observed. At high scanning speeds the laser-surface interaction is limited to a few seconds. It is known that the average laser fluence decreases at high scanning speeds ($v_s$). This effect becomes even more evident when $v_s > 10^4$ μm/s [145]. The Gaussian beam profile and the change in the laser fluence result in temperature distributions on the irradiated area. Such temperature gradients seem to be the reason of the formation of metastable $Al_2O_3$ phases in addition to the stable $Al_2O_3$ phase. When the laser exposure time is kept short (high scanning speeds), the penetration depth of the laser light and heat flow is also limited. While the surface layer is heated efficiently, the layer beneath may be subjected less to the heating. As a consequence, the X-ray analysis may detect the formation of other metastable $Al_2O_3$ phases. In this context, it is difficult to talk about the presence of a texture or orientated growth. In addition, a very low metallic Al peak is also seen in the diffractograms after the laser treatment. Such an Al peak can be also attributed to non-transformed layers left beneath the surface at high scanning speeds.

At lower scanning speeds, longer laser heating induces thermal relaxation of non-equilibrium $\gamma$-$Al_2O_3$, which has a defect spinel structure, and this relaxation is followed by the restoration of thermodynamically stable $\alpha$-$Al_2O_3$. In order to analyze the phase transformation in detail, the intensities of the diffractograms obtained from the laser treatment of composite layers at different scanning speeds were normalized with respect to the (104) $\alpha$-$Al_2O_3$ reflection, since (113) the $\alpha$-$Al_2O_3$ reflection overlaps with the substrate reflection (Figure 4.36). The theoretical and measured intensities of the

reflection peaks are given in Table 4.8. As seen from the table, the intensities are not matching with the theoretical intensities.

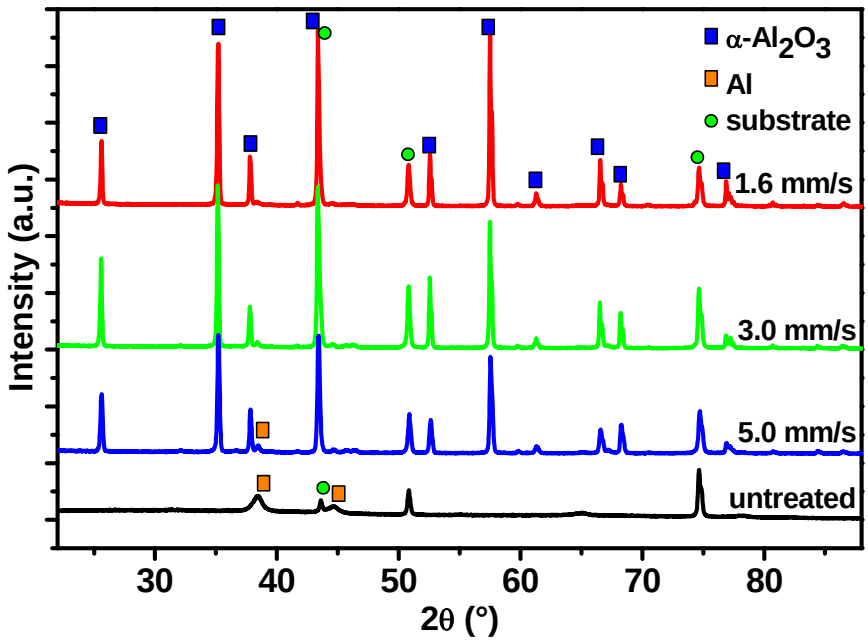


**Figure 4.36 X-ray diffractograms (normalized with respect to the (104) α-$Al_2O_3$ reflection) of the laser treated layers with different scanning speeds.**

The relative intensities of these patterns reveal different degrees of random texturing rather than a preferred orientation. This can be explained as a result of the non-homogenous surface heating which leads to the observation of different thermodynamic conditions locally depending on the temperature distribution. In addition, melting of the Al core and the oxidation also induce local changes in terms of temperature rise and stoichiometry. The (113) and (116) α-$Al_2O_3$ diffractions exhibit a systematic intensity enhancement with the decreasing scanning speed. A similar effect is also observed in the (024) and (018) α-$Al_2O_3$ reflections. When the scanning speed is decreased further from 3 mm/s to 1.6 mm/s, such an enhancement is not observed anymore. In this context, there is no clear orientation after the laser treatment. Safely, it can be mentioned that the amount of the left metastable alumina is less than 2 %.

| 2θ (°) | *hkl* | Theo. $I_{th}$ (%) | 5 mm/s $I_1$ (%) | 3 mm/s $I_2$ (%) | 1.6 mm/s $I_3$ (%) |
|---|---|---|---|---|---|
| 25.578 | 012 | 45 | 25.8 | 31.2 | 18.8 |
| 35.152 | 104 | 100 | 100 | 100 | 100 |
| 37.776 | 110 | 21 | 49.2 | 35.1 | 33.4 |
| 43.355 | 113 | 66 | N.A. | N.A. | N.A. |
| 52.549 | 024 | 34 | 76.9 | 122.3 | 74.3 |
| 57.496 | 116 | 89 | 272 | 260.7 | 285.8 |
| 61.298 | 018 | 14 | 28.5 | 26.9 | 30.2 |
| 66.519 | 214 | 23 | 143.5 | 129.8 | 120.9 |
| 68.212 | 300 | 27 | 135 | 120.9 | 60.8 |
| 76.869 | 1010 | 29 | 45.8 | 34.8 | 64.9 |
| 77.224 | 119 | 12 | 60.9 | 69.6 | 58.4 |

**Table 4.8 Theoretical and measured intensities of the reflection peaks (N.A.:These peaks can not be measured due to overlapping with the substrate peaks).**

### 4.7.4.2 Micro-Raman Spectroscopy and Observation of In-situ Crystallization

The XRD analysis showed that Al·$Al_2O_3$ layers transformed to α-alumina after the laser treatment. As shown previously, the highest crystallinity was observed at a laser power of 5 W and a scanning speed of 1 mm/s. Using the same parameters, Al·$Al_2O_3$ composite layers were treated with the laser.

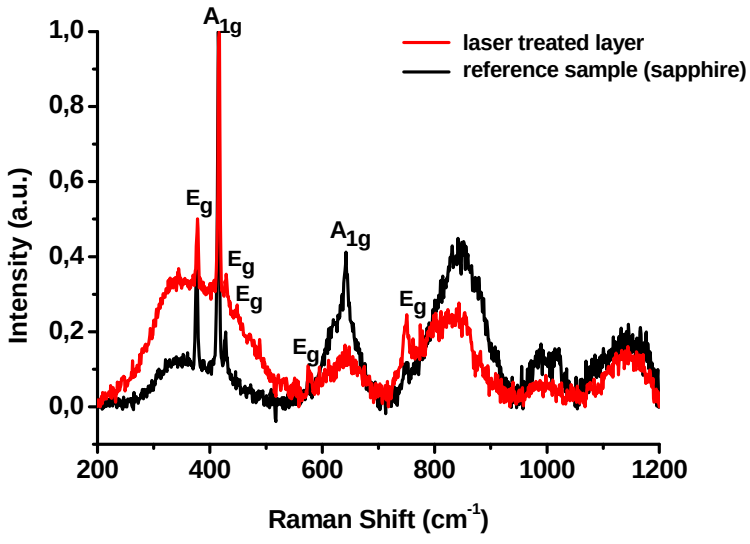


**Figure 4.37 Raman spectra of a laser treated layer and a reference sapphire sample.**

Following the laser treatment, the sample and a reference sapphire sample were characterized by micro-Raman spectroscopy. The Raman spectra of the laser treated sample and the reference sapphire are shown in Figure 4.37. One can see that the reference sapphire and the laser treated sample show similar Raman bands. The peak positions match well with α-$Al_2O_3$ peaks reported by Mirsa et al. [256] and Proto et al. [257]. Krishman et al. [258] showed also similar Raman spectra from α-$Al_2O_3$ synthesized by high energy laser treatment of metastable $Al_2O_3$ phases. In all these reported analyses, Raman bands of alumina are discussed up to a shift of 800 $cm^{-1}$. In this interval α-$Al_2O_3$ with R3c space group (rhombohedral) is known to exhibit seven Raman modes (2 $A_{1g}$ and 5 $E_g$), as shown in the spectra (Figure 4.37). It is seen clearly that the observed peaks match well with these Raman modes. The reduction of the full-width at half-maximum (FWHM) and the presence of sharp peaks resemble to sapphire, which is an indication of the high crystallinity.

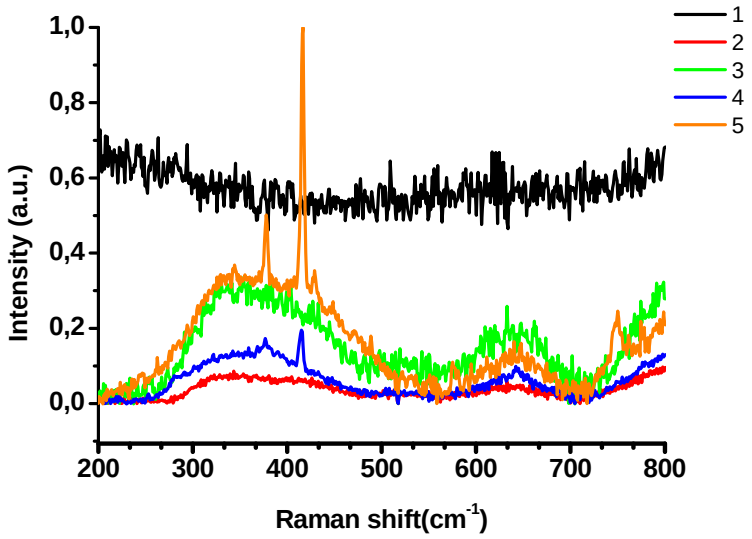


**Figure 4.38 Raman spectra of layers. (1) As deposited, 50 % reduced laser power and 30 seconds laser exposure time. (2) As deposited, 100 % laser power and 300 seconds laser exposure time. (3) Post-laser treated, 100 % laser power and 300 seconds laser exposure time. (4) Au sputtered, 50 % reduced laser power and 300 seconds laser exposure time. (5) Post-laser treated and Au sputtered, 50 % reduced laser power and 300 seconds laser exposure time.**

In comparison to α-$Al_2O_3$, γ-$Al_2O_3$ with Fd3m (cubic) does not show any Raman mode [258]. In another experiment Al·$Al_2O_3$ nanowires as-deposited were also

characterized by Raman spectroscopy. The recorded spectra at different laser exposure periods and intensities are shown in Figure 4.38.

There is no definite specific Raman band in the spectrum of $Al{\cdot}Al_2O_3$ nanowires (Figure 4.38, curve 1) treated with a 50 % reduced laser power for 30 seconds. Very broad bands at 280-480 $cm^{-1}$ and 570-720 $cm^{-1}$ intervals are observed in the case of 300 seconds exposure with a 100 % laser power (Figure 4.38, curve 2). Although sharp crystalline peaks are absent, the peak positions remind of the reported Raman spectra of $\alpha$-$Al_2O_3$ given in the literature [257 and 258]. This may be an indication of early stages of the transformation to $\alpha$-$Al_2O_3$.

Interestingly, a white spot appears on the surface after 300 seconds laser exposure. The optical images taken before and after the exposure to a weak Raman laser are given in Figure 4.39a and b respectively. The color change on the laser irritated area can be seen clearly. Following the laser irradiation, the microscope coupled to Raman spectroscopy became out of the focus. This can be explained by a possible change in the focal plane distance due to topography and structure changes within the laser irradiated local area. The inserts at the optical microscope images, Figure 4.39a and b, show laser scattering on the surface of the deposited layers at the beginning and end of the Raman analysis, respectively.

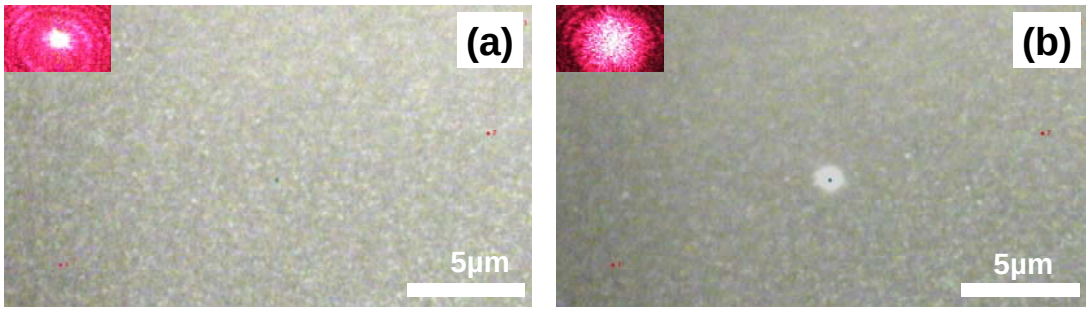


**Figure 4.39 Optical microscope images of the deposited layers (a) before and (b) after the Raman spectroscopy analysis (inserts show the scattering of the laser on the surface).**

The laser is more scattered after 300 seconds exposure. This is another indication of a possible change in the surface structure. These observations may be the indications of an in-situ phase transformation during the Raman analysis. Popochii et al. showed a similar effect concerning in-situ crystallization of amorphous Si nanoparticles while recording Raman spectra. In his work he showed that Si particles of 20–30 nm can be

heated up to 1500 K using only 1 mW visible continuous laser light focused to a spot of 2 μm in diameter [259].

In order to prove the existence of an in-situ transformation by X-ray analysis, a larger surface area was post-treated with a laser operating at a power density close to that of the Raman laser. Although the output power is relatively high (ca. 300 mW) in comparison to the weak Raman laser, the focused beam size is adjusted (18 μm) to apply the same power density. The exposure time was also kept comparable to that of the Raman laser using a computer controlled moving stage. The Raman spectrum of the laser treated layer exhibits also very broad Raman bands (Figure 4.38, curve 3). On the other hand, the XRD analysis of the same layer (Figure 4.40b) shows sharp peaks of α-$Al_2O_3$. This shows that previously observed broad peaks in the Raman spectra of $Al{\cdot}Al_2O_3$ nanowires after 300 seconds laser irradiation seem to be the fingerprints of an in-situ crystallization to the α-$Al_2O_3$ phase. Actually, the Raman signal is very low to resolve different modes in the recorded spectra to give more details about this in-situ transformation.

In order to increase the Raman scattering efficiency, a very thin layer of Au was sputtered to the surface of the laser treated layer, which was analyzed by XRD previously. The interaction between the electromagnetic field of the laser excitation and the nanostructured surface covered with the thin Au layer enhanced the Raman signal as expected. The Au coated and laser treated layer shows distinct sharp Raman bands (Figure 4.38, curve 5) which we were not able to resolve prior to Au sputtering. The observed peaks match with characteristic Raman bands of α-$Al_2O_3$ reported by Porto et al [257]. Similarly, Au coated $Al{\cdot}Al_2O_3$ nanowires exhibit sharp Raman peaks (Figure 4.38, curve 4) in comparison to bare $Al{\cdot}Al_2O_3$ nanowires following 300 seconds laser exposure at 50 % laser power (Figure 4. 38, curve 2).

The optical microscope image given as an insert in Figure 4.40a shows a distinct color change in the single line scanned under the focused laser beam. This color change is similar to the appearance of the white spot, which occurred after the irradiation of the surface by the weak laser during the Raman analysis. Although the focused laser beam size was kept at ca. 18 μm, the width of the white line is ca. 40 μm in the optical image. This may be due to the Gaussian beam profile of the laser and heat dissipation during

excessive heating of the surface. The SEM image of the scanned line shows a clear thermal induced growth (Figure 4.40a). The nanowires lost their 1D structure and formed a fractal network. As mentioned previously, the X-ray diffractograms recorded prior to the laser treatment show that the only detectible crystalline phase besides the substrate is metallic Al. After the laser treatment the transformation to $\alpha$-$Al_2O_3$ is clearly seen in diffractograms. The SEM image indicates that a low power density of the laser is not enough to induce a complete transformation and densification.

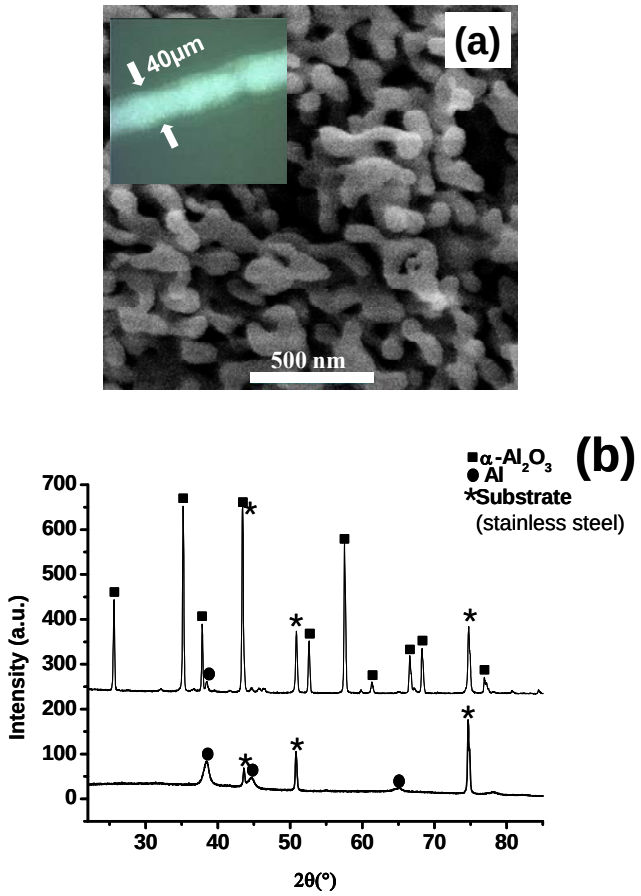


**Figure 4.40 (a) SEM image of a single track induced by laser (the insert shows the optical microscope image of the same track). (b) X-ray diffractogram of the deposited (black) and laser treated (red) layers.**

The observed effect is associated with the strong absorption and enormous enhancement of the electrical field due to the crossed core-shell metal-dielectric nanowires. Also the weak heat exchange of nanowires with each other and the environment is believed to induce a local heating rather than dissipation of heat to a

larger area. In addition, the oxidation of the Al core leads to a further increase of the temperature, as shown previously by the thermal camera measurements (see 4.7.2.2). This heating procedure can be used for some technological applications including permanent data recording.

### 4.7.5 Surface and Mechanical Properties upon CW Laser Treatment

#### 4.7.5.1 Surface Roughness and Wetting

The surface roughness was estimated from the mean value ($R_a$). The measurements were carried out using a surface profilometer. Crack-free and crack containing laser-treated surfaces were prepared using the typical power densities and processing speeds given previously in 4.7.2. For each sample eight profiles were taken along and across the laser tracks, at different locations, and the average value was calculated.

It was presented previously that the porosity of the deposited $Al{\cdot}Al_2O_3$ composite layers depends on deposition parameters such as the flow rate, pressure, temperature and thickness. An untreated $Al{\cdot}Al_2O_3$ layer deposited at a high flow rate at 600°C exhibits a $R_a$ value of 6.18 μm. Following the laser treatment at a scanning speed of 3 mm/s and at a laser power of 2.5 W, an effective densification takes place. Such laser treated dense and crack-free surfaces exhibit a $R_a$ value of 4.25 μm. On the other hand, surfaces treated under the same conditions but containing cracks show $R_a$ values varying between 5.00 and 9.2 μm.

The $R_a$ values for the crack containing surfaces increase with the laser power density and scanning speed. As the power density is increased, the surfaces are exposed to conditions of an increasing thermal shock, resulting in a rise of the number of thermally induced cracks on solidification, thereby producing a rougher surface. The increase in the number of cracks and the development of crack-networks are also reasons for the increase in the surface roughness with the processing speed. An increase in the processing speed expands the forced convection heat transfer rate, resulting in an overall increase in the heat removal rate and higher cooling rates, exposing the surface to a severe thermal shock.

The wetting characteristics of the surfaces were evaluated by measuring the contact angle between the surface and de-ionised water droplets, based on the standard sessile

drop test. An optical contact angle meter was used to take the measurements. The mean of the values for the angle from both sides of each drop was used. For each sample five measurements were taken at different positions and the average value was calculated.

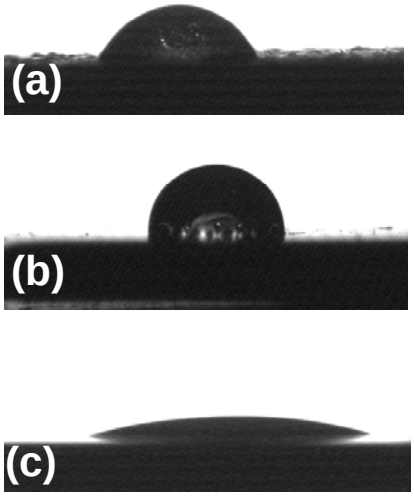


**Figure 4.41 Contact angles measured at different locations of the laser-treated surfaces containing cracks.**

Figure 4.41a, b and c show the contact angles measured at different locations of the laser-treated surfaces containing cracks. While the contact angle for untreated layers (chaotic nanowires as deposited) is below 10°, the contact angle of the laser treated surfaces containing cracks exhibit a wide variation from area to area and sample to sample. The contact angle values vary in the range of 10–60°. It is not possible to define a definite relationship between the laser power density and the contact angle, since the laser treatment does not provide a homogenous surface topography.

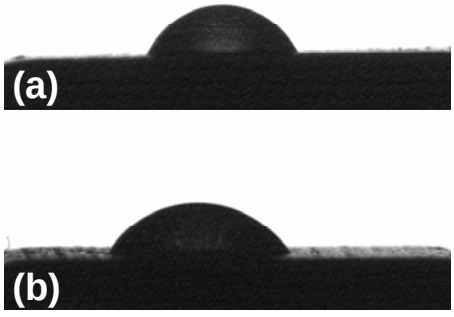


**Figure 4.42 Contact angles measured at different locations of the laser-treated crack-free surfaces.**

In comparison, the crack-free laser treated layers exhibit contact angles which vary in a narrow range of 25-30°, as shown in Figure 4.42a and b. This can be attributed to the more homogeneous surface topography of the crack-free laser treated surfaces.

In addition to totally melted and densified surfaces, the laser treatment also induced partial melting and transformations, as shown in the SEM micrographs in Figure 4.27b, c and d previously. Nano- and microstructures co-exist in such partially melted surfaces. Interestingly, such surfaces treated at relatively low laser power densities exhibit a hydrophobic behavior as shown in Figure 4.43. At some instances, the contact angle reaches to 140°. On the other hand, it is not easy to mention the presence of superhydrophobicy which requires also a low contact angle hysteresis to be defined. Although the water droplet can be moved easily on the surface with a small tilt angle, it is difficult study the hysteresis experimentally due to the inhomogeneous surface features induced by laser treatment [260]. Because of laser induced thermal gradients the surface may show local changes in terms of the crystal structure, texture, surface topography and chemistry. There are similar results reported concerning the hydrophobic behavior of laser treated alumina surfaces where the reason could not be figured out due to the formation of inhomogeneous surface properties after laser treatment [261].

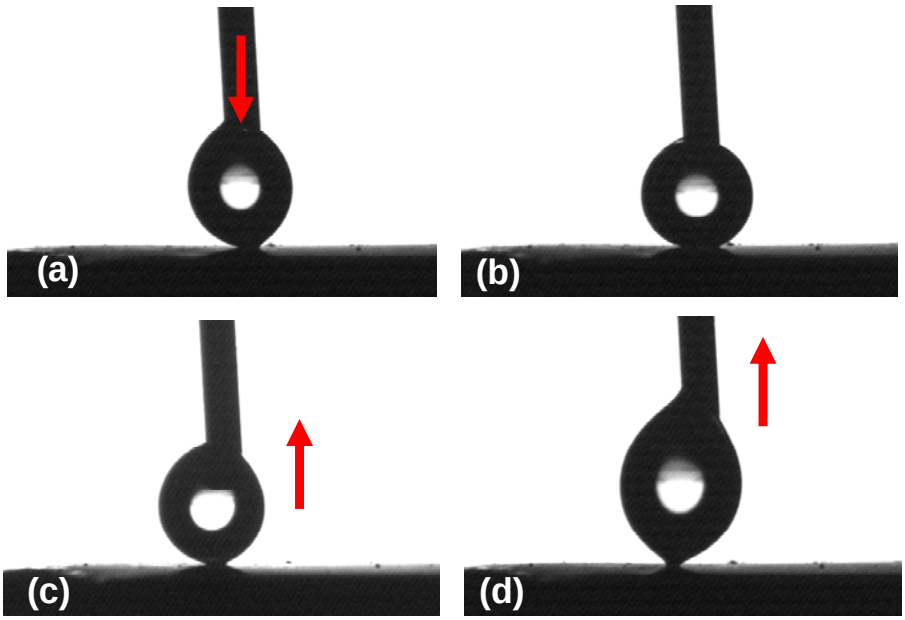


**Figure 4.43 (a) Pumping of the water through the syringe. (b) Static contact angle. (c) Withdrawing of the syringe. (d) Further withdrawing of the syringe.**

As a summary, laser treated surfaces exhibit higher contact angles than untreated surfaces; the wetting properties depend on the local compositional and morphological characteristics of the surface, which leads to large variations in the contact angles from area to area. The cracked surfaces show a tendency for an increasing contact angle with the roughness, but inhomogeneity causes a wide variation in the contact angles. Crack-free laser treated surfaces exhibit relatively homogenous surfaces with contact angles in a range from 25° to 30°.

#### 4.7.5.2 Mechanical Characterization of Laser Treated Al·$Al_2O_3$ Layers

The mechanical properties of laser treated Al·$Al_2O_3$ layers were investigated using the technique of nanoindentation with a Berkovich diamond indenter (three-sided pyramidal tip, 142.3°), which was calibrated carefully for its area function on a standard material, e.g. fused quartz. The loading profiles included five segments: loading to a peak load of 3000 µN; holding at the peak load; unloading back to 10 % of the peak load; holding at 10 % of the peak load; unloading back to the zero load. Separating the thermal drift from the creep in the material was possible by a comparison of the displacement in the two holding load segments [262]. As a result, no considerable thermal drift during our measurements was observed. The loading rate for all indents was set to 300 µN/s. A typical load displacement curve during nanoindentation of the sample is shown in Figure 4.44.

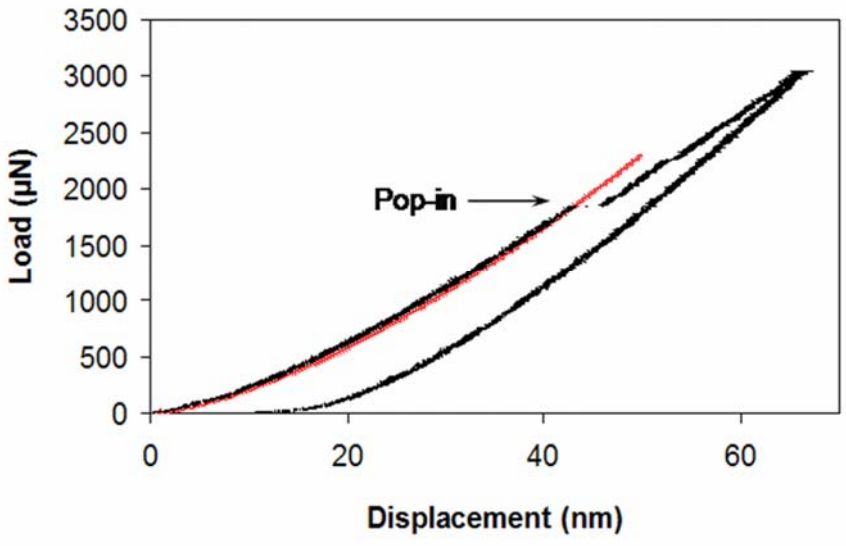


**Figure 4.44 Load-displacement curve during the nanoindentation of the laser treated surface.**

The hardness and elastic modulus according to the Oliver-Pharr method were calculated and shown in Figure 4.45 which is in a very good agreement with reported values in the literature [263]. Additionally, pop-in usually was observed during nanoindentation of laser treated layers, as shown in Figure 4.44.

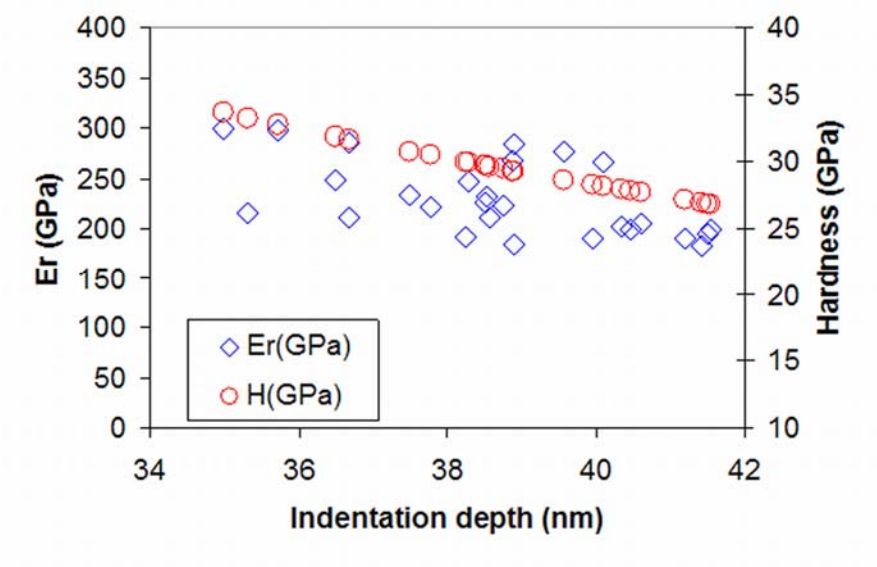


**Figure 4.45 Hardness and elastic modulus of the laser treated surface.**

In Figure 4.46 a typical nanoindentation curve without pop-in observation is shown, where obviously loading and unloading parts of the curve are lying above each other. This is presented also in the displacement-time curve of the same nanoindentation test in Figure 4.47.

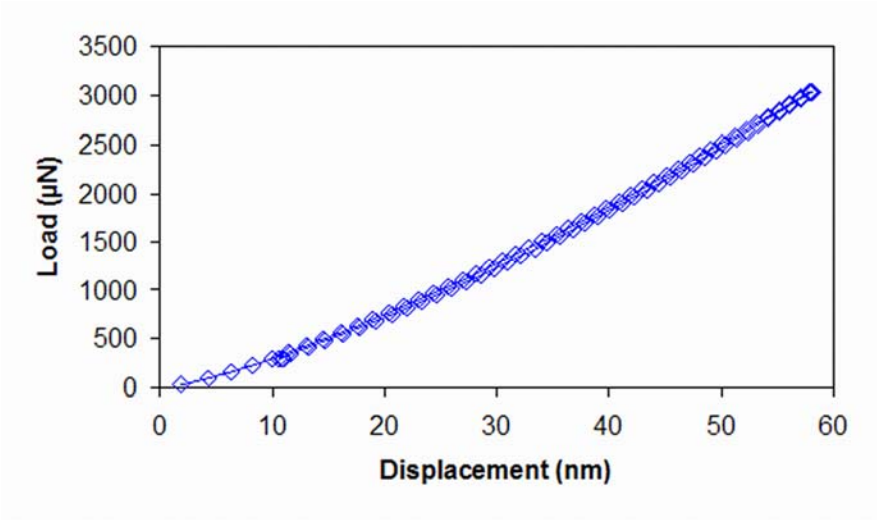


**Figure 4.46 Load-displacement curve of the laser treated surface.**

If no pop-in occurs during nanoindentation, this means that there is no plastic deformation and the material behaves completely elastic. Fitting the loading part of the curve before pop-in with a Hertzian contact also shows that the deformation of the material prior to pop-in is elastic. Therefore it can be assumed that the pop-in is the transition from elastic to plastic deformation in the sample.

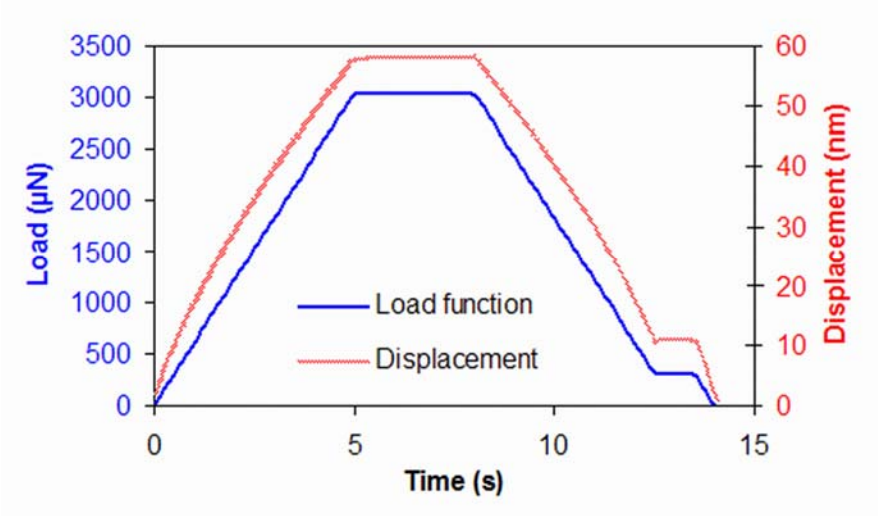


**Figure 4.47 Displacement-time curve of the nanoindentation test.**

According to the continuum mechanics, the maximum shear stress acting on a point is 0.48 times the contact radius below the sample surface. The computer simulations showed that dislocations are nucleating at this point [264]. The position of this maximum shear stress $z_{\tau(max)}$, and its value $\tau_{max}$, are given by (4.17) and (4.18),

$$z_{\tau(\max)} = 0.48\left(\frac{3PR}{4E_r}\right)^{\frac{1}{3}} \qquad \textbf{(4.17)}$$

$$\tau_{\max} = 0.31\left(\frac{6E_r^2}{\pi^3 R^2}P\right)^{\frac{1}{3}} \qquad \textbf{(4.18)}$$

where $P$ is the applied load, $R$ is the radius of the tip curvature and $E_r$ is the reduced modulus, given by (4.19),

$$\frac{1}{E_r} = \frac{1-\nu_1^2}{E_1} + \frac{1-\nu_2^2}{E_2} \qquad \textbf{(4.19)}$$

where $\boldsymbol{E}$ is the elastic modulus of the material, $\boldsymbol{\nu}$ is Poisson's ratio and the subscripts 1 and 2 indicate the tip and the sample, respectively. For α-$Al_2O_3$ and a diamond tip the equation (4.19) gives $E_r$=309 GPa. Substituting the tip radius of 250 nm and the observed pop-in load, we obtain a maximum shear stress of 24 GPa from equation (4.18). We can define the theoretical strength with a first order approximation, as given in (4.20),

$$\tau_{th} \approx \frac{G}{2\pi} \qquad \textbf{(4.20)}$$

where $\boldsymbol{G}$ is the shear modulus. Hence, the measured value lays in the order of the theoretical strength for α-$Al_2O_3$ of 26 GPa [265]. This proves that the laser treatment of the coating results in a very low defect density in the coating.

### 4.7.6 Pulsed Laser Treatment: Surface Structuring Approach

Pulsed Nd:YAG lasers were used for processing the ceramic as they are capable of delivering superior peak powers with an excellent beam quality due to which they are used in the manufacturing industries widely. As the laser pulse interacts with the surface of the material, high cooling rates and corresponding temperature changes in the material will cause the material to melt and re-solidify with dendritic structures. Such a laser-material interaction also affects the porosity between these dendrites. Various attempts have been made to optimize this inter-dendritic porosity so that it could be used for different applications, as each application may require variable levels of porosity. Similarly, we performed pulsed laser surface treatment of Al·$Al_2O_3$ composite layers in order to determine the potential of this technology to fabricate structured alumina surfaces.

The pulsed laser treatment leads to a variety of nano- and microstructures on the surface in addition to the transformation of Al·$Al_2O_3$ to $Al_2O_3$ (such transformation

induced by CW laser is presented in detail in Chapter 4.7.4). Following the pulsed laser treatment, porous surfaces are created rather than dense alumina layers. Such surfaces can not be compared with the dense α-alumina layers synthesized by the CW laser treatment in terms of their mechanical properties. On the other hand, such structures are interesting for cell-surface interaction studies because of the combination of nano and micro topographic features. In the next sections the pulsed laser treatment of $Al{\cdot}Al_2O_3$ nanowires will be covered and the use of such laser treated surfaces for cell interaction studies will be presented separately in Chapter 5.

#### 4.7.6.1 Surface Morphology after Laser Pulses at Near-damage-threshold Fluence

The following section delivers the experimental results performed by a Q-switched Nd:YAG laser with a beam size of 12 mm at 532 nm wavelength (SHG) radiation, which is nearly matching with the wavelength of the CW argon ion laser used to treat the thin layers of $Al{\cdot}Al_2O_3$ nanowires (Chapter 1.7.2).

Figure 4.48 demonstrates the SEM images of the surface topography produced by nanosecond laser processing at the near-damage-threshold fluence of F=0.2 J/cm$^2$ for different numbers of laser shots, whether the main features are random nanopores, nanoprotrusions or micro-nano hillocks.

After a single laser pulse, the extreme temperature rise induces a local surface melting, as clearly seen in Figure 4.48a. The regions on the surface, which are covered with relatively dense and highly interpenetrated nanowires, exhibit a stronger absorption. These regions seem to be melted partially and the molten material flows over the surface. Micro-grooves and protrusions form due to the fast solidification of the expelled liquid on the boundary of the solid state material. The change in the color of the deposited layers from black to white also reminds of the transformation of the $Al{\cdot}Al_2O_3$ composite to $Al_2O_3$ which is similar to our previous observations in the case of CW laser treatment (Chapter 1.7.2). The second laser pulse creates a relatively smooth surface due to re-melting of the layer, as shown in Figure 4.48b.

The surface becomes smoother after four laser pulses but it seems that repeating thermal shocks create cracks on the surface (Figure 4.48c). After eight pulses a splitting of the film is observed. This is an indication of extremely high thermal shocks. Li et al

[266] and Guo et al. [267] showed similar deformations and splitting of the layers after repeated high energy pulses. Higher resolution SEM micrographs, given in Figure 4.49, show more hints on the pulsed laser modification of deposited layers.

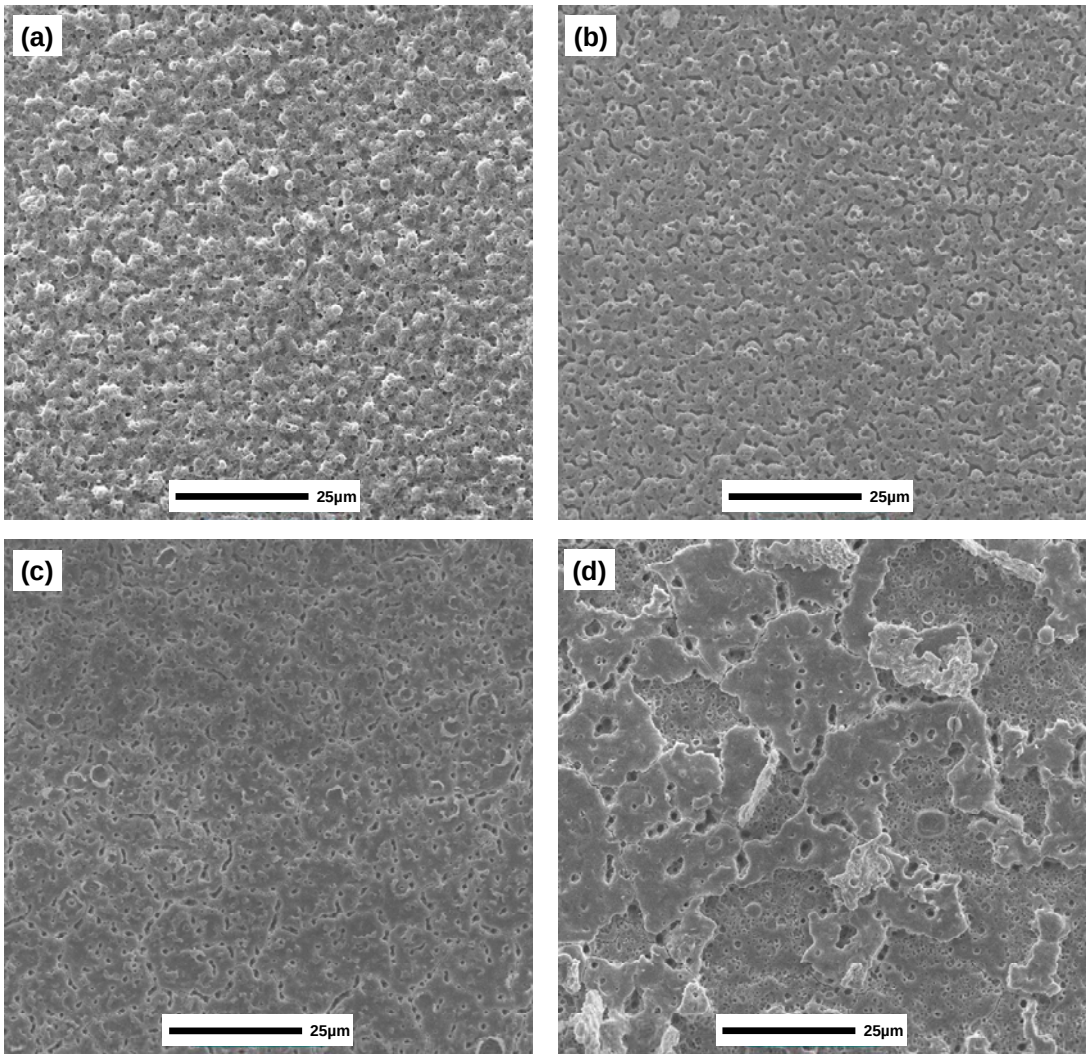


**Figure 4.48 SEM images of the deposited layers after (a) 1X laser pulse, (b) 2X laser pulses, (c) 4X laser pulses and (d) 8X laser pulses.**

It is shown clearly in Figure 4.49a that the first laser pulse melts the surface layers. The sudden increase of the temperature induces fast melting and solidification. While the top layer transforms into $Al_2O_3$, micro cracks and pores form due to the high cooling rates. One can see through a pore that the layer beneath the surface seems to be not melted by the laser pulse. Such a surface hosting both micro- and nanostructures is quite interesting to study cell-surface interactions. Moreover, $Al_2O_3$ is a well known bio-

compatible material [268]. There are various research works concerning the cell adhesion on structured $Al_2O_3$ layers [269].

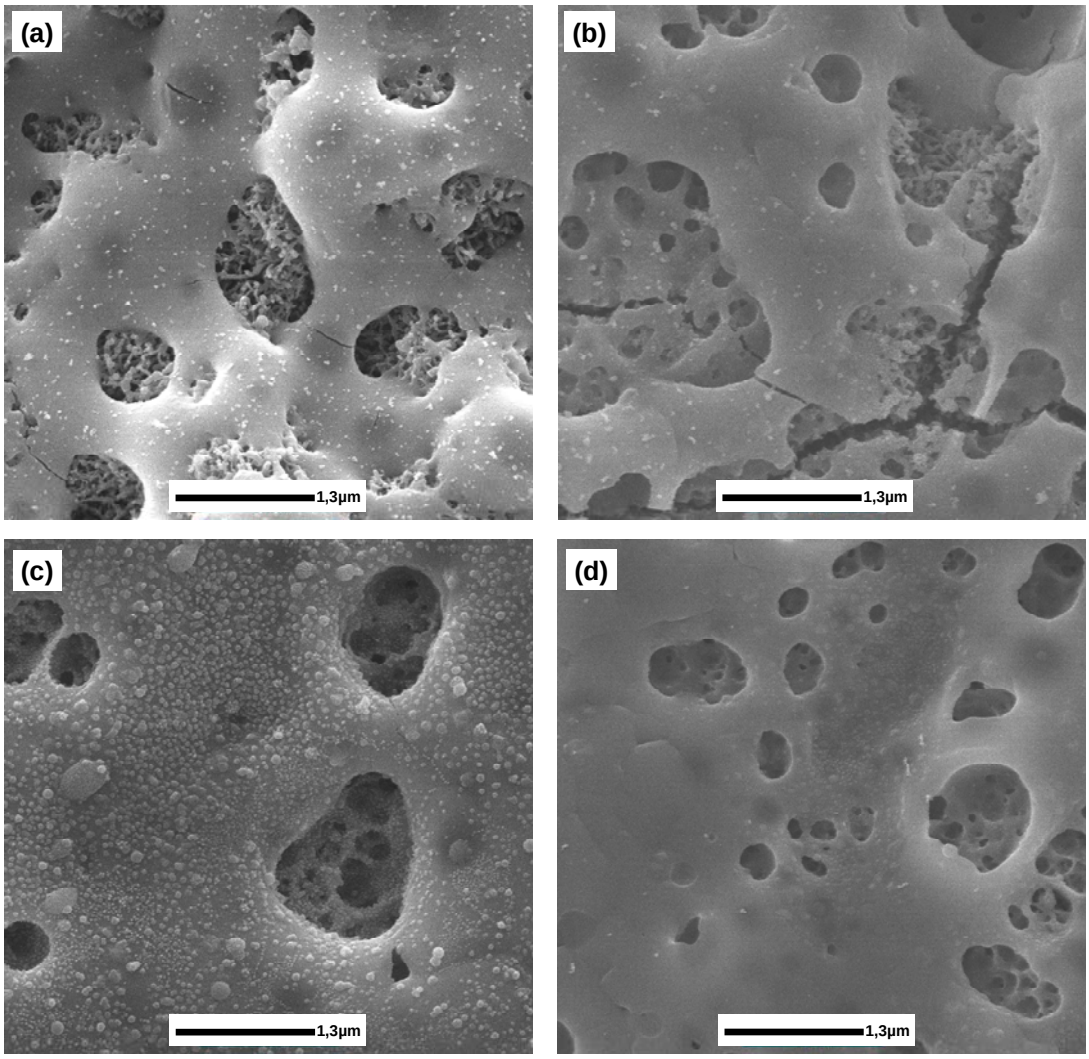


**Figure 4.49 High resolution SEM images of the deposited layers after (a) 1X laser pulse, (b) 2X laser pulses, (c) 4X laser pulses and (d) 8X laser pulses.**

During the second laser pulse the laser light is believed to pass through the pores and melt the nanowires which are not melted after the first laser pulse (Figure 4.49b). The laser light seems to be not absorbed by previously melted and oxidized regions (white in color), which reminds of the change of reflection of the deposited layers during the argon laser treatment (Chapter 1.7.2). Further laser pulses modify the nanostructures left in the pores and molten droplets are ejected on the surface, as seen in Figure 4.49c. On the other hand, the size of the open pores decreases and some cracks are filled with

the ejected melt. After eight pulses the nanowires within the pores are totally melted and the size of the pores becomes smaller (Figure 4.49d). Finally, micro-pores having some nano-cavities are the main characteristic features of the surface topography.

In order to see all intermediate stages of the pulsed laser interaction with $Al{\cdot}Al_2O_3$ nanowires, a consecutive pulse regime (1 to 6) at a lower laser fluence was applied and high resolution SEM was used to analyze morphology changes within a pore formed after the first laser pulse. In Figure 4.50 consecutive changes are shown in detail. After the first laser pulse, the surface is melted and some pores form. Following the second pulse, the nanowires within the pores coalesce.

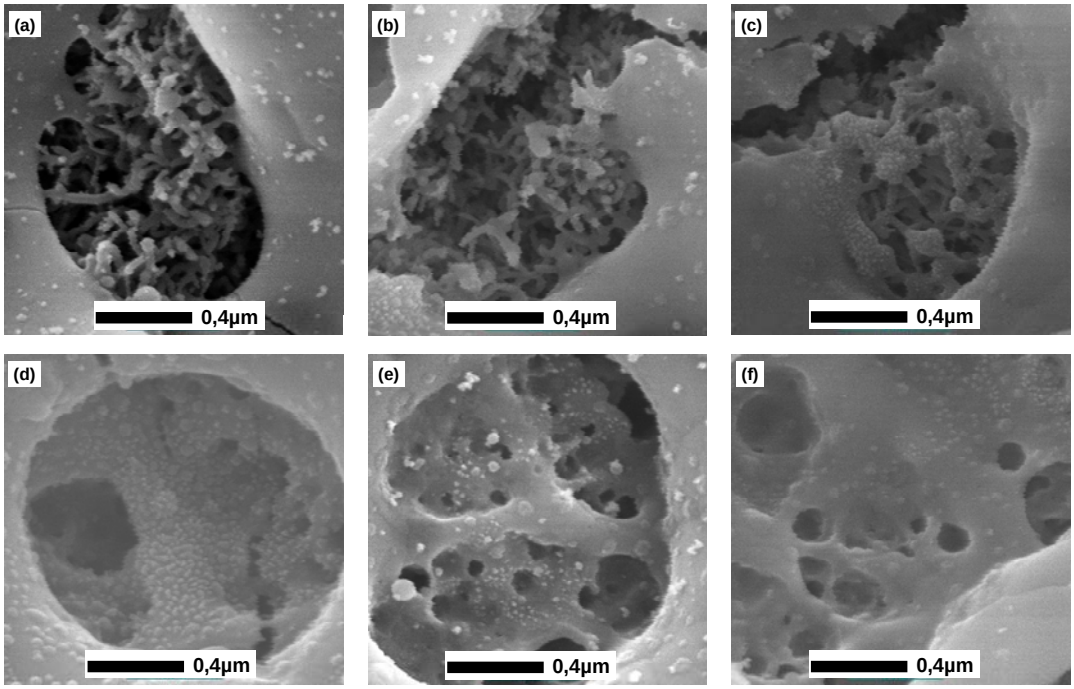


**Figure 4.50 High resolution SEM images of the deposited layers after (a) 1X laser pulse, (b) 2X laser pulses, (c) 3X laser pulses, (d) 4X laser pulses, (e) 5X laser pulses and (f) 6X laser pulses.**

After the third pulse the agglomeration of the nanostructures within the pore becomes more evident. Furthermore, some molten droplets are seen on the agglomerates. Following the fourth pulse, 1D nanostructures within the pore disappear and more molten droplets are seen over the inner walls of the pore. After the fifth pulse pores of 40-50 nm become the main characteristic feature. There is no significant change in the morphology after further laser pulses. It is believed that the whole surface reflects the laser light back and this decreases the absorption, so the laser energy is not enough

anymore to induce further modifications. By this simple method, it is shown that the porosity and overall morphology can be varied in a controlled way. These highly porous layers of alumina can be interesting for catalysis and bio-applications.

#### 4.7.6.2 Surface Morphology after Laser Pulses Exceeding Damage-threshold Fluence

When the laser fluence is increased to F= 0.3 J/cm$^2$, nanopores and spherical nanoprotrusions having diameters of 60-90 nm form after a single laser pulse. The examination of the SEM images (Figure 4.51a and b), showing the surface topography after the laser treatment, suggests the following mechanism for the formation of such nanopores and spherical nanoprotrusions: The nanopores are always accompanied near by nanoprotrusions, indicating a nano-scaled material transport to an adjacent site. It is believed that a high temperature gradient induces a radial surface tension gradient which expels the spherical liquid droplets to the periphery of the molten material. This may be the reason for the formation of spherical nanostructures upon solidification.

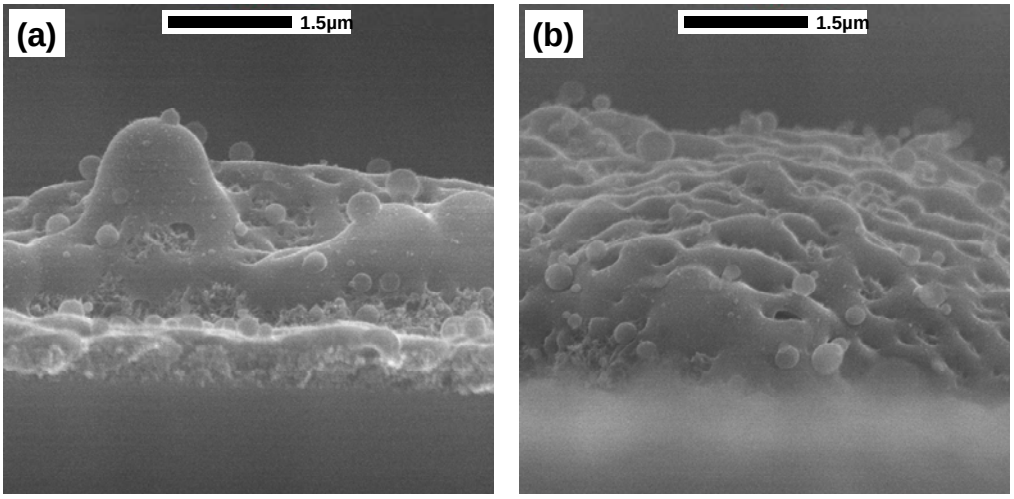


**Figure 4.51 SEM images of the deposited layers after a single laser pulse.**

With further laser pulses spherical nanoprotrusions are not observed anymore (Figure 4.52a). It is believed that nanostructures formed after laser pulses exhibit a higher reflection than non-treated chaotic surfaces. Therefore, further repeated pulses are not absorbed as strong as the first laser pulse. Repeated pulses will be absorbed mostly because of the randomly formed nanoprotrusions and holes formed just after the first laser pulse. Figure 4.52b shows that repeated pulses increase the surface roughness,

since every previous pulse creates randomly distributed nano-micro-structures which induce inhomogeneous optical absorption. Following the pulses, re-melted surface layers accumulate and form micro-hillocks.

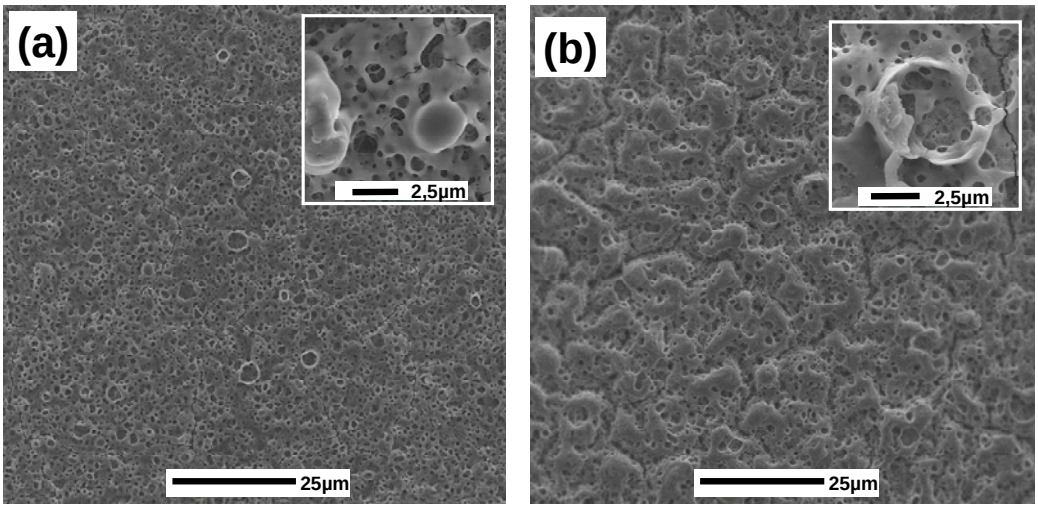


**Figure 4.52 SEM images of the deposited layer after (a) 3X laser pulses and (b) 6X laser pulses.**

At a high number of laser pulses (N > 10), island-like microstructures form. Indeed, these structures are in the form of deep columnar channels (Figure 4.53a). The characteristic size of this type of micro-roughness is in the range of 5-15 µm. Following the repeated laser pulses, such micro texture becomes the common feature all over the surface. This forms a homogenous surface showing the same level of micro-roughness as shown in Figure 4.53b.

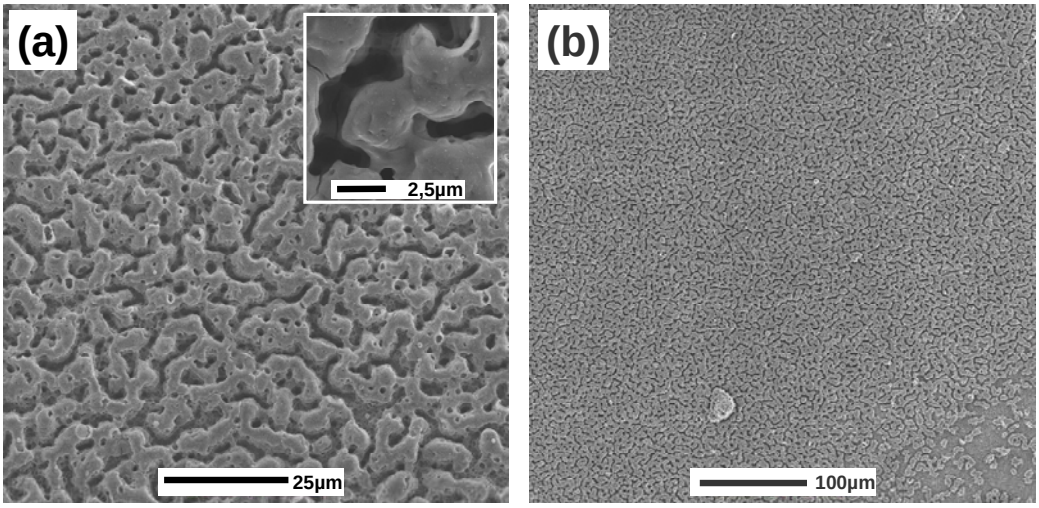


**Figure 4.53 SEM images of the deposited layers after (a) 12X laser pulses and (b) 20X laser pulses.**

#### 4.7.6.3 Surface Composition and Structure after Laser Pulses

It was shown that the molten Al core oxidizes to $Al_2O_3$ after the CW laser treatment and the XRD analysis showed clearly the formation α-alumina, as presented in Chapter 1.7.2. On the other hand, short laser pulses can heat only a thin layer on the surface. In Figure 4.54a it is shown that at a fluence of F=0.12 J/cm$^3$ melting is observed at the upper 70-80 nm of the layer. When the laser fluence is increased to F=0.23 J/cm$^3$, the melt thickness increases to 100-130 nm (Figure 4.54b). At a higher fluence of F=0.30 J/cm$^3$, the laser melted layer thickness reaches to ca. 200 nm (Figure 4.54c).

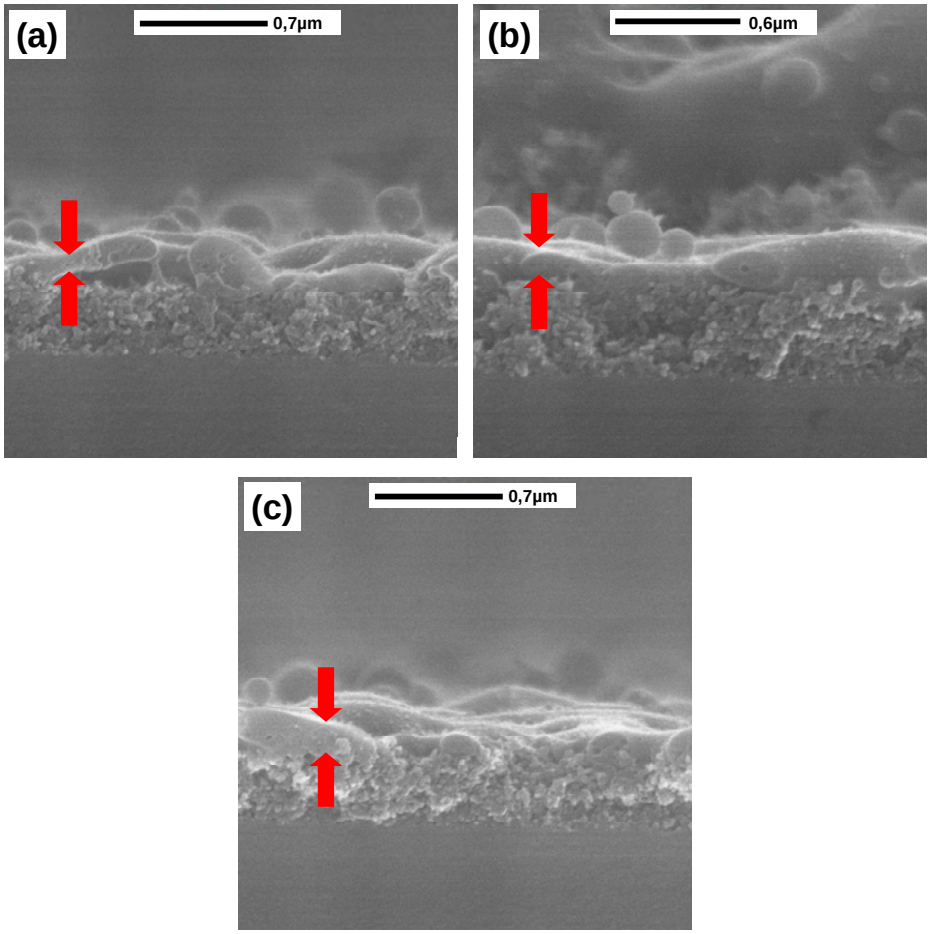


**Figure 4.54 Cross-sectional SEM images of layers after a single laser pulse at a fluence of (a) 0.12 J/cm$^3$, (b) F=0.23 J/cm$^3$ and (c) F=0.30 J/cm$^3$ (the arrows show the melted layers).**

In this context, the XRD technique is not relevant to analyze the phase transformation after a few laser pulses (N<5). Since a local phase analysis is needed on the surface, micro Raman spectroscopy is preferred. Figure 4.55 shows the Raman

spectra of layers treated with various laser pulses. A reference sapphire sample was also characterized under the same conditions for the comparison. After the first laser pulse there is no clear indication of a transformation besides some broad Raman bands. Such broad bands are also observed in the case of CW laser treatment which was presented previously in Chapter 1.7.4.2.

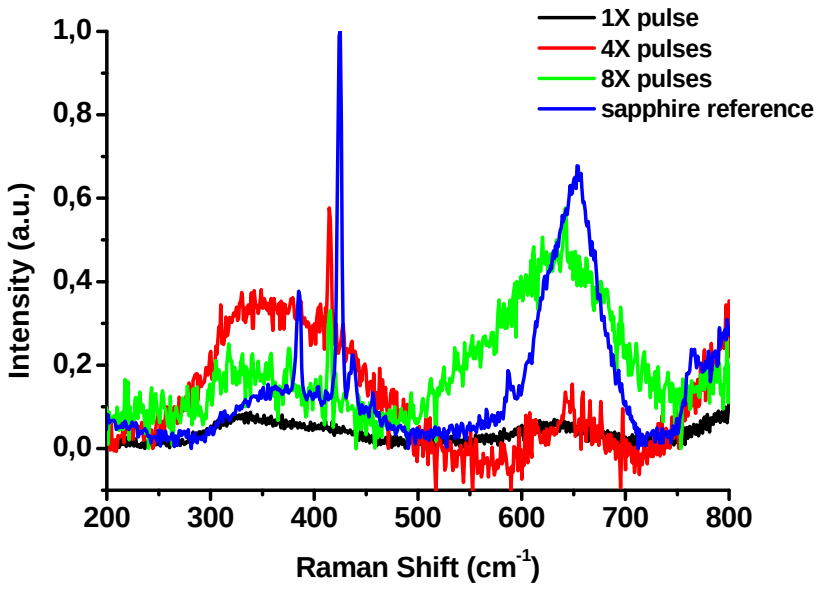


**Figure 4.55 Raman spectra of the deposited layer after various laser pulses and of the sapphire reference.**

Following the repeated laser pulses, α-alumina bands are observed in the spectra (Figure 4.55). The Raman bands and corresponding peak positions match with the ones observed previously in the case of high energy CW laser modification. The peak positions also show agreement with the standard sapphire spectra. This is a clear indication of the transformation of $Al{\cdot}Al_2O_3$ to $\alpha$-$Al_2O_3$.

The surface composition was analyzed using EDX after single and repeated laser pulses. As presented in Figure 4.56, there is no contamination after the high energy pulses. While the Al:O at. % is 47.06:52.94 after the single laser pulse, this ratio becomes 37.83:62.17 after 3 laser pulses, which may be a clear sign of the oxidation of more Al and transformation to $Al_2O_3$.

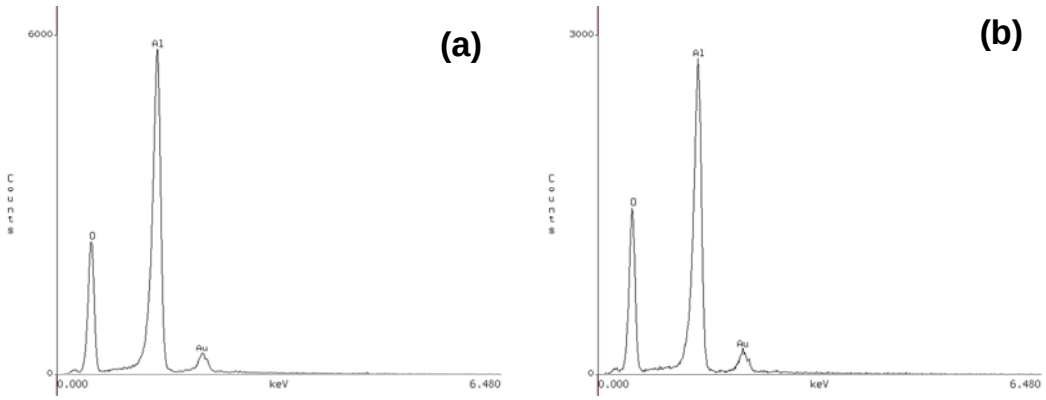


**Figure 4.56 EDX spectra of the deposited layers after (a) 1X laser pulse and (b) 3X laser pulses.**

Figure 4.57a and b demonstrate the XPS spectra of the $Al{\cdot}Al_2O_3$ layer before and after a single laser pulse. The peaks originate from the ejection of Al 2p, Al 2s, O 1s and C 1s core electrons. In addition, the O (KLL) Auger signals are easily identified.

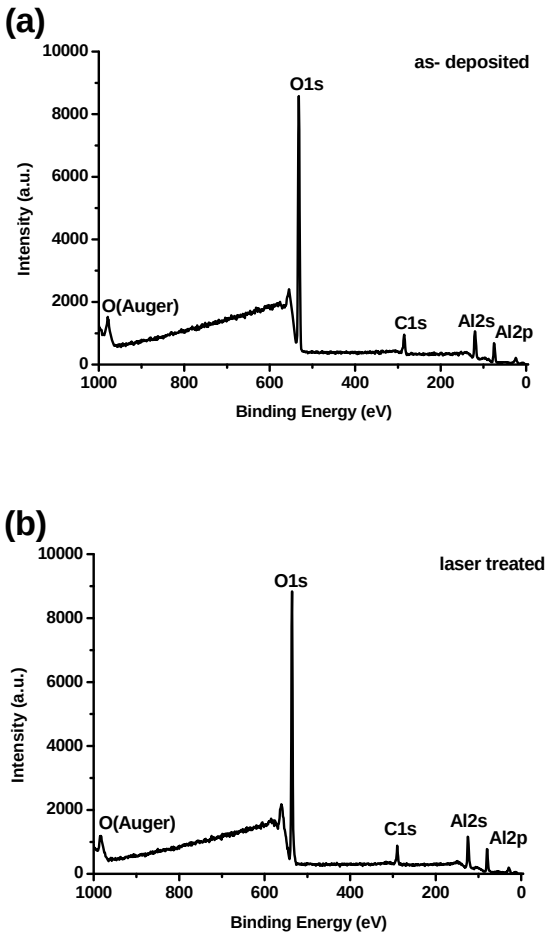


**Figure 4.57 XPS spectra of the deposited layer (a) before and (b) after a single laser pulse.**

The elemental analysis shows that Al:O:C (%) is 23.10:62.95:13.95 for the deposited layer. This value is 26.15:61.69:12.15 after the laser treatment. The low carbon content seems to be accumulated during the sample-handling. After the laser treatment the carbon content does not change drastically, which indicates that no extra contamination forms following the laser pulse.

# 5. Interactions of Cells with Nano- and Microstructured Surfaces Prepared by CVD and Pulsed Laser Treatment

Alumina ceramics have been used for implants and prostheses for several decades. Alumina exhibits an excellent biocompatibility, a good mechanical performance and long-term durability [270]. In numerous in-vitro and in-vivo studies the surface topography of alumina implants has been shown to be important in the enhancing implant performance [271]. It has been reported that modified surfaces have a higher early level of cell attachment than the untreated alumina surfaces [272].

A basic understanding and knowledge of cell-biomaterial surface interaction is of immense interest in tissue engineering and also other related biomedical applications. Studies have shown the effect of the micro- and nanoscaled surface topographies on cellular functions including morphology, adhesion, motility, proliferation and gene regulation [273]. Thus, various topographic features, namely pores, ridges, grooves, fibers, nodes and combinations of these features, were created by a wide range of fabrication techniques [274].

In this work we have studied the cell interactions on random nanofiber porous $Al{\cdot}Al_2O_3$ surfaces prepared by CVD. We performed laser surface treatment of such layers in order to produce a large variety of micro- and nanostructures for comparing the cell interactions on such different topographies. Pulsed laser treatment of $Al{\cdot}Al_2O_3$ nanowires produces a richer variety of surface structures than CW laser treatments. In the following sections cell interactions on such structures including nanowires, nanopores, nanoprotrusions and sub-micron sphere-like structures are presented in detail.

## 5.1 Basics of Cell-Surface Interaction

The adsorption of cell adhesion-mediating molecules in an appropriate amount, spectrum, spatial conformation, flexibility and accessibility for receptors involved in cell adhesion is influenced by physical as well as chemical properties of the material surface layer. Physical properties include surface roughness and topography, mechanical properties (rigidity or flexibility), crystallinity and porosity. Chemical properties comprise wettability, electrical charge, solubility, pH or the presence of chemical functional groups, e.g. amine groups or oxygen groups. In this context, interesting

correlations have been found in-vitro for specific cell types with the variation of parameters, such as the density of surface hydroxyl (-OH) or sulfonic groups ($-SO_3H$), surface C-O functionalities, surface free energy or surface wettability, hydrogenated amorphous 'unsaturated' carbon phases, fibronectin adsorption and equilibrium water content [275].

Surfaces exhibiting an intermediate wettability are known to provide better protein absorption and cell adhesion. Contrarily, cell adhesion is worse on most of the polymers including polyethylene, polyurethane, polypropylene or polystyrene which exhibit hydrophobic states. Such polymers are uncharged and hydrophobic in nature, meaning they repel water or are non-wettable. Cells usually avoid spreading on such hydrophobic surfaces and this results in poor and very uneven cell attachment and growth. It is proved experimentally that peptides and proteins adhere and fold on hydrophobic interfaces in a different manner than on hydrophilic surfaces [276].

In addition to wetting, macro mechanical properties of the substrate play a critical role in the cell adhesion. If the adhesion substrate is very firm, rigid and non-deformable, e.g. ECM molecules adsorbed on extremely hydrophobic surfaces, the cells are not able to reorganize these molecules in order to access the ligands for the integrin receptors and recruit these receptors into focal adhesion plaques, which is a prerequisite for the delivery of signals ensuring the viability of anchorage-dependent cells. On the other hand, if the material is too elastic, compliant, flexible and irreversibly deformable, it does not allow the anchorage of cells, even if the ligands for integrin receptors are present in satisfactory amounts and accessibility, and are bound by these receptors. Such type of substrate can not resist the cell tractional forces generated by the assembling cytoskeleton [277].

The surface texture of a cell culturing surface may have a significant effect on the behaviour of cells. In-vivo studies showed that in comparison to smooth surfaces, roughened surfaces show improved osseointegration, improved percutaneous implant integration and reduced fibrous encapsulation with enhanced integration of breast implant materials [278]. These improvements happen due to the increased adhesion of connective tissue cells onto roughened surfaces, resulting in a closer apposition of the tissue to the implant.

The study of the response of cells to surface structures began in 1911 when the reactions of cells grown on spider web fibers were described [279]. In the 1960s it was found that cells grown on cylindrical glass fibers would align on the fibers and were very sensitive to curvature. In many cases cells orient and migrate along fibers or ridges in the surface, a phenomenon that has been called 'contact guidance' originating from the earliest studies on neuronal cell cultures [280]. Today it is known that the behaviour of cultured cells on surfaces with edges, grooves or other features is significantly different from the cell behaviour on smooth surfaces [281].

## 5.2 Cell Behavior towards Surface Topography

Cell-biomaterial surface interaction became a core research topic in biomedical applications, especially in the field of tissue engineering following the improvements in understanding the extraordinary properties of nanomaterials and introduction of various advanced techniques to synthesize such materials. Cells exhibit highly sensitive interactions with the surrounding environment of chemistry and topography [282]. Surface topography with a definite chemistry has been shown previously to affect the cell adhesion, orientation, cell activation and migration significantly, but the mechanisms mediating such cell responses still remain unclear.

Different micro and nano fabrication approaches including various state-of-the-art top-down and bottom-up methods are employed to fabricate various topographic features in order to study the cell-surface interactions. While well known top-down methods, such as electron beam- and photo-lithography, provide regular and ordered patterns, random structures are mostly prepared by colloid/wet-chemical processes and gas phase deposition methods. On the other hand, the choice of the materials is also the incidence determining the synthesis approach. While embossing, casting and other soft lithography approaches can be easily applied to polymers to create well defined patterns [283], glass or other ceramic surfaces, which exhibit good biocompatibility, can not be patterned with the same ease.

The structure of the extra cellular matrix (ECM), which mainly supports the interaction of the cell with the outer environment, is composed of sub-structures of different length scales varying from millimeter to nanometer [284]. Most of the studies

have examined cell responses to micro- or nanoscaled features, whereas very few have investigated the effect of the combination of these length scales. The fabrication of complex structures including various length scales is of interest for understanding cell-surface interactions. Development of new synthetical strategies providing ease of use, large area, fast and low cost patterning for cell-surface interaction studies is still a challenge. In addition, the choice of the material is also critical due to compatibility requirements. In this context, synthesis of nano-/microstructured bio-ceramics, especially alumina ceramics, is of interest due to their proven cell compatibility.

## 5.3 Nano-/Microstructured Alumina as Bio-material

### 5.3.1 Cell-Alumina Surface Interactions

Alumina, especially $\alpha$-$Al_2O_3$, is a ceramic oxide material which has been used as a biomedical implant material since the early 1970s due to its excellent biocompatibility, corrosion resistance and phase stability [285]. In addition, superior mechanical properties of alumina including high hardness, wear resistance, scratch resistance, low coefficient of friction and sufficient mechanical strength to resist fatigue make it one of the strongest candidate for implant applications among other ceramics [286]. Basically, the composition and microstructure of alumina ceramics are the main incidents to define their use in a biomaterial. With over 30 years of use, the alumina ceramic implants can be divided into first, second and third generation implants. While the first and second generation of alumina ceramics were low-density materials with a coarse microstructure, today's third generation alumina ceramic materials have a high density with small grain sizes, high chemical purity and stable crystalline structures.

Besides the biocompatibility of alumina, the cell-alumina surface interaction is crucial to design biomaterials. Recent in-vitro studies provided evidence of increased osteoblast (the bone-forming cells) adhesion on nanophase alumina (e.g., those with grain sizes less than 100 nm) compared to larger conventional grain size alumina [287]. Such studies demonstrated that enhanced osteoblast adhesion was independent of the surface chemistry and the phase of ceramic, but was dependent on the surface topography of nanophase ceramics. More detailed studies showed the evidence of enhanced proliferation with an increase in the alkaline phosphate activity and the

concentration of calcium within the extra cellular matrix (ECM), when osteoblast were cultured on nanophase alumina compared to conventional alumina [288].

Webster and his co-workers studied the effect of the grain size on the adhesion of the osteoblast cells on alumina surfaces [289]. They used three different alumina surfaces having average grain sizes of 177 nm, 49 nm and 23 nm respectively. They showed, in the presence of 10 % fetal bovine serum, that the osteoblast adhesion on nanophase alumina with a average grain size of 23 nm was significantly higher than the adhesion on the borosilicate glass (reference substrate) and the conventional alumina (with an average grain size of 177 nm) after 0.5, 1, 2 and 4 hours. In their detailed work the osteoblast adhesion is increased up to 46 % on nanophase alumina compared to conventional alumina. Such alumina surfaces with different grain sizes were synthesized by sintering of conventional γ-alumina powders at different temperatures. While the surface properties of sintered alumina powders, including wetting and roughness, are presented systemically, there is no information about the composition and the phase analysis.

Swan et al. studied the interaction of osteoblast cells on nanostructured alumina surfaces prepared by a two-step anodization process [290]. The first anodization in oxalic acid is carried out to grow an oxide layer. Following an etching step to form nucleation sites, a second anodization again in oxalic acid was carried out to synthesize a porous alumina layer. By changing the anodization voltage, different pore sizes ranging from 30 to 80 nm in diameter are achieved. The SEM analysis showed that the cells were extending to adhere to the nanopores. These findings confirmed that the osteoblasts interacted with the nanotopography and this can be accepted as a short term cellular response limited by a 4 days cell culture. On the other hand, a comparative study was not carried out concerning the adhesion of the same type of cells on a control substrate.

Popat et al. using a similar two-step anodization method showed the effect of the nanotopography on the long term cell response [291]. In his detailed study nano-porous alumina membranes with a pore size in the range of 60-90 nm showed improved short-term osteoblast adhesion and proliferation similar to findings of Swan et al. In addition, osteoblasts were cultured over these surfaces for a period of 4 weeks to investigate long-term effects of the surface topography on the cellular functions. The cells cultured on

nanoporous alumina membranes showed higher protein content as indicated by BCA assay and XPS results. This shows that the interaction between ceramic nanostructures and proteins affects the cellular functions. While a detailed analysis was carried out on the cell biology, there is no information about the surface properties in terms of wettability and roughness. Although some of the prepared layers are designated as amorphous, the presented experimental data shows crystallinity besides the amorphous state of the anodized layers at some instances.

When compared to microscaled conventional ceramic materials, nanomaterials have an increased number of atoms and crystal grains at their surfaces and posses a higher surface area to volume ratio. Literature reports indicate that the cumulative adsorption of proteins from bodily fluids is significantly higher on smaller, nanometer grain sized materials [292]. Webster et al. correlated enhanced vitronectin adsorption, conformation and bioactivity to the increased osteoblast adhesion on nanophase alumina [293]. Such findings indicate that nanostructures affect the cellular activities rather than only improving simply the surface attachment.

It is known that several cellular activities, such as adhesion; proliferation, migration, differentiation and cell shape, are influenced by the ECM. The natural ECM is composed of various protein fibrils and fibers interwoven with a hydrated network of collagen and glycosaminoglycan chains. Such fibrous structures are found in many tissues such as bone, skin, tendons, ligaments and other connective tissues. The ECM is composed of various structures at different length scales. For example, specifically for the bone, hydroxyapatite is between 2 and 5 nm in width and 50 nm in length, whereas Type I collagen is a triple helix of 300 nm in length, 0.5 nm in width and has a periodicity of 67 nm [275]. Besides these components in the range of several nanometers, microscale features such as macrophages are also found in the ECM. In this context, 3D artificial structures composed of mainly fibrous structures but also accommodating pores for relatively larger micro features became interesting for studying cell-surface interactions.

It is shown that the functions of osteoblasts increased on alumina fibers (2 nm diameter and 50 nm length) synthesized by sol–gel methods, followed by aging, filtration, and subsequent drying and heat treatment at 400°C [294]. The osteoblasts deposited the most calcium when cultured on θ-and δ-phase nanofiber alumina compared

to any other substrate tested. This study also showed the first evidence of increased deposition of calcium containing mineral by osteoblasts according to the following trend of crystalline phases in nanofiber alumina: θ+δ> γ+δ> γ>α.

Similar responses of osteoblast cells to crystalline alumina structures were shown previously by Nishio et al. [190] who reported that osteoblastic differentiation on composites containing conventional grain sized γ-phase alumina allowed direct bone formation, whereas the composite containing the conventional grain sized α-phase alumina did not. On the other hand, the mechanism of recognition of the alumina crystal structure by the osteoblasts was not understood clearly. Tepper et al. showed that the osteoblast adhesion increases on alumina fibers but in his study there is no reliable information about the crystalline phase of alumina that was used [295].

Such nanofibrous structures have a high surface area-to-volume ratio, providing more space for cell attachment and therefore a higher cell density per unit of space compared to other structures. Recently, electro-spinning processes have attracted a great deal of attention as a way to mimic the structure of the natural ECM by means of producing fibers down to 5 nm [296]. This technique is used to fabricate nanofibrous structures from natural and synthetic polymers, such as collagen [297], chitosan [298], silk fibroin [299] and poly (L-lactide-co-e caprolactone) [300], poly (lactide) [301], polyurethane [302] and polycaprolactone [303].

In addition to ceramic and polymer nanofibrous structures, other well established 1D nanostructures such as carbon nano-tubes (CNTs) are also used to improve the cell-surface interaction. It is shown that CNTs embedded in polyurethane (PU) increase the osteoblast adhesion compared to a pure PU surface [304]. On the other hand, increasing the weight percentage of the CNTs in the PU matrix resulted in the decrease of the fibroblast adhesion. CNTs were used as vehicles to deliver macromolecules, which are normally unable to pass through the cellular membrane, into cells [305]. On the other hand, Bellucci et al showed that CNTs cause apoptosis of human T-cell lines. In addition, due to the hydrophobicity and tendency to aggregate, they are harmful to living cells in culture [306]. Very little is yet known about the cytotoxicity of CNTs, which exist in many different forms and can be chemically modified and/or functionalized with bio-molecules. In this context, while the effect of 1D structures is being investigated, the

effect of the material itself should also be studied in parallel investigations. It is believed that using biomaterials which proved their bio compatibility, such as $Al_2O_3$, $ZrO_2$ or other bio-ceramics, is more relevant for studying the effect of 1D structures on the cell behaviour.

In studying cell-surface interactions one should keep in mind that the ECM components are not composed of nano features only, but also of different structures varying at a length scale from micro- to millimeter. The effects of nano surface features on the cell behaviour has been examined by using nanoscaled patterns such as columns [307], dots [308], pits [309], pores [310], gratings [311], meshwork [312] and random surface roughness [313]. Before the development of advanced nanopatterning methods, intensive research was carried out on microscale patterned surface-cell interactions. Micro fabricated surfaces have been used to control the cell adhesion at the microscale [314]. It is known that the topography of the surface alters the cell proliferation and differentiation [314]. Studies showed that cells prefer attaching to surfaces which are composed of different topographical length scales. Such an effect is shown by using micro/nano carbon tubes together [316] and the addition of chemical micro domains to substrates composed of nanogrooves [317].

It is clear that, in addition to the topography effect on the cell behaviour, a substrate which is well understood in terms of biocompatibility is needed to get viable results. Alumina is one of the ceramic materials which are mostly used in bio-medical applications and tested in-vivo and in-vitro in terms of bio-compatibility. In this context, layers prepared by deposition of $(^tBuOAlH_2)_2$ and alumina structures synthesized by the laser treatment of these layers, can act as model systems to explore the effect of combinations of micro- and nano-structures with a controlled surface chemistry.

### 5.3.2 Background of Biocompatibility Studies on Surfaces Prepared by CVD of $(^tBuOAlH_2)_2$

First biocompatibility studies on the $Al{\cdot}Al_2O_3$ 1D nanostructures were reported in the doctoral thesis of Petersen supervised by Prof. Veith [128]. In his work different cells were employed to study their responses on the nanostructured surfaces of $Al{\cdot}Al_2O_3$ composite as well as on a HAlO layer. Oberringer and Petersen showed that the behaviour of the cells was different on HAlO and $Al{\cdot}Al_2O_3$ layers [318].On the other

hand, the work of Petersen and Schütze concerning fibroblast cells interactions showed that there was no distinguishable difference between the monocytes of cells deposited on the HAlO and $Al{\cdot}Al_2O_3$ composite layer [319]. During the experimental studies carried out in the Cell PROM project (Cell Programming by Nanoscaled Devices - EU funded project), the Leibniz-INM CVD group showed the differences between the response of normal human dermal fibroblast (NHDF) cells deposited on HAlO and $Al{\cdot}Al_2O_3$ layers.

Following the preliminary results concerning the different behaviour of the NHDF cells, a detailed work of Petersen proved that NHDF cells on HAlO layers showed a similar behaviour to those cultured on a Si-wafer which is used as the control substrate in terms of general biocompatibility, adhesion, proliferation and cell differentiation [128]. In comparison, NHDF cell cultures on $Al{\cdot}Al_2O_3$ composite layers resulted in poor cell adhesion and proliferation. Petersen tried a chemical modification of the $Al{\cdot}Al_2O_3$ nanowires without altering their geometry and structures in order to improve the cell compatibility. It is shown that following the surface modification with aminopropyl-triethoxy silane (APTS), the cell compatibility is increased. ESEM images show that cells formed several filopodia on nanowires following the chemical modification, although the morphology of the nanowires remains unchanged. Petersen stated that the $Al{\cdot}Al_2O_3$ nanowires exhibit an unusual behaviour in terms of biocompatibility when compared with the other alumina surfaces.

In these preliminary biocompatibility studies on $Al{\cdot}Al_2O_3$ nanowires the effect of morphology on cell interaction was the main topic of interest. Although no quantitative data has been given on the increase of the biocompatibility, APTS modified nanowires show a better cell adhesion. Since the chemical modification does not change the morphology, it is clear that the nanofibrous structure should have an effect also on the cell response. On the other hand, Bizios et al showed that, while osteoblast-like cell growth is enhanced on nanophase-alumina, an opposite effect is observed in the case of fibroblast cells [320]. It is clear that the cell-surface interaction can vary from one cell type to the other. For example, epithel cells do not react to 30-nm-wide pits, but blood platelets do, while epithel cells react to 40- and 80-nm-deep pits [321].

In this thesis a more detailed work is conducted on the biocompatibility of the $Al{\cdot}Al_2O_3$ nanowires with a better control of the morphology. Firstly, the main intention

is given to the morphology and topography effects on the cell interaction without a chemical surface modification. Different cell lines are employed to understand whether the responses of the cells are specific for one cell type or not. In addition to basic fibrous $Al{\cdot}Al_2O_3$ structures, different morphologies prepared by the laser treatment of $Al{\cdot}Al_2O_3$ nanowires were tested in terms of the biocompatibility. Depending on the laser intensity and pulse numbers various structures composed of both nano and micro features were produced. Such surfaces are composed of different length scaled features and believed to be helpful to understand the effect of the topography as a combination of micro- and nanostructures.

## 5.4 Experimental Approach

### 5.4.1 Preparation of the Micro- and Nanostructured Surfaces

The biocompatibility tests were performed on layers composed of $Al{\cdot}Al_2O_3$ nanowires and micro-/nanostructured surfaces fabricated by pulsed laser treatment of these composite nanowires. $Al{\cdot}Al_2O_3$ nanowires were deposited on glass cover-slips (12 mm) by the simple decomposition of $(^tBuOAlH_2)_2$ at 550-600°C for 20-30 minutes, as described in Chapter 3.

For the surface texturing we used an Nd:YAG laser system that generates laser pulses of 4 to 8 ns, with a maximum pulse energy of 2000 mJ, at a repetition rate of 10 Hz and with a fundamental wavelength of 1064 nm. By frequency doubling a wavelength of 532 nm is used for texturing of the deposited layers due to their strong absorption covering UV to NIR wavelengths. The number of laser shots, N, was controlled with an electromechanical shutter. The surface structuring is studied by applying different laser fluences and numbers of pulses, N, as described in Chapter 4.

### 5.4.2 Cell Compatibility Analysis

#### 5.4.2.1 Testing of $Al{\cdot}Al_2O_3$ layers

The following cell culture suspensions (Qiagen) were used to test the bio-compatibility of the $Al{\cdot}Al_2O_3$ coated cover-slips (additionally polystyrene, poly-L-Lysine coated glass and standard glass cover-slips were used for comparison):

- Jurkat (suspension human T-cell line)
- K562 (suspension human B-cell line)
- THP1 (suspension human monocytic cell line)
- MCF7 cells (adherent human breast cancer cell line)
- MOLT-14 (suspension human T-cell leukaemia)
- BE13 (suspension human T-cell leukaemia)
- Raji (suspension human macrophage cell line)

In order to remove the contaminations from coated and uncoated glass cover-slips the following procedure was applied:

- Transferring the substrates to the 24-well culture plate with the coated side up.
- Adding 500 µl ethanol (70 %) to each well.
- Washing the substrates with 500 µl water (3X) after staying in ethanol for 5 minutes at room temperature (RT).
- Washing the substrates with 500 µl PBS (phosphate buffered saline) (3X).

Sterile poly-L-Lysine and polystyrene coated cover-slips (BD Biosciences) were washed only. Additionally, cells were cultured without cover-slips directly in the 24-well cell culture plate.

The cells were plated in 1 ml of serum containing the cell culture medium in appropriate densities (typically $4\text{-}8\cdot10^4$ cells per well) and cultured at 37°C with 5 % $CO_2$ and 100 % humidity. Afterwards they were cultured for up to 72 hours and inspected daily by light microscopy. After that non-adherent cells were washed away by flushing the wells and cover-slips twice with 1000 µl PBS. The remaining attached cells were fixed in 500 µl ethanol (100 %) for 5 minutes at room temperature. After the removal of ethanol the cell nuclei were stained by adding 500 µl of Hoechst 33342 (Invitrogen, 0.1% in PBS). Microscopic pictures were taken using a fluorescence microscope. The cells remaining after the detachment by addition of a Trypsin/EDTA (ethylene diamine tetraacetic acid) solution were imaged once more to understand the adhesion mechanism. The detailed explanation of a standard trypsinization procedure is given in the next section. To allow a better quantification of the adhesion, the adhered cells were stained using Calcein-AM (calcein-acetoxymethylester), a fluorescence dye

which is enriched in viable cells so that the fluorescence intensity on each cover-slip could be measured by a fluorimeter.

### 5.4.3 Testing of $Al{\cdot}Al_2O_3$ layers and Surfaces Prepared by Pulsed Laser Treatment

Normal human dermal fibroblast cells (NHDF, Promocell) were cultivated in Quantum 333 (cell medium for fibroblasts, PAA-laboratories) in 75cm$^2$ tissue flasks (GrinerBioOne) under standard incubation parameters (37°C, 95 % humidity and 5% $CO_2$) until they reached confluency. The substrates were fixed on standard microscopic glass slides with UHU all purpose glue. The sterilization of the substrates was done subsequently according to the following protocol:

- Washing with sterile PBS (3X).
- Rinsing 5 minutes in ethanol (70 %).
- Rinsing in sterile PBS (2X).

To detach the cells from the flasks the following trypsinization procedure was applied:

- Aspirating the cell culture medium from the confluent cell layer.
- Washing with sterile PBS (37°C).
- Addition of Trypsin/EDTA (5 ml, PAA).
- Incubation for 3 minutes at 37°C.

In order to control the complete detachment of the cells with the microscope, the cell suspension was transferred from the flask into a centrifuge tube (10 ml). Afterwards the flask was washed with 5 ml Q 333 to add remaining cells to the cell suspension. The suspension was centrifuged at 1000 rpm for 3 minutes. The supernatant was discarded, the cell pellet was re-suspended in 8 ml of a Q 333 medium and the cell density per milliliter was determined using the CASY®-cell counter (Schärfe Systemtechnik). The substrates on the slides and standard microscopic slides serving as control were inoculated with an initial cell seeding density of 63 cells/mm$^2$. The incubation was done in Quadripem devices (Greiner BioOne) in 4 ml Q 333 medium for 3 days.

Since the substrates are opaque, the cells were stained with a constitutive marker for fibroblasts to visualize the cell morphology. The nuclei were counterstained with 4,6-

diamidino-2-phenylindole (DAPI). After removing this medium the cells were washed (3X) with sterile PBS (37°C), incubated in KCl (0.05 M) at 37°C for 5 minutes and fixed in methanol (-20°C) for at least 10 minutes. Following the air drying, the substrates were incubated (2X) in PBS containing 0.5 % Tween (polyoxyethylene sorbitol ester used as blocking agent) for 5 minutes in order to permeabilize the membranes. To reduce unspecific binding of the antibodies the substrates were rinsed in PBS containing 0.1 % Bovine Serum Albumin (BSA). A goat anti-human CD 90 antibody (protein in the fibroblastic membrane, Dianova) was diluted to 1:200 in PBS-BSA (0.1 %) and 75 µl of this medium was applied to every slide (incubated at room temperature in a dark humidified chamber, 30 minutes). After washing the slides (3X) with PBS-0.5 % Tween a secondary antibody (goat anti mouse with Cy3 labeling) was applied and the incubation was carried out as described above. Then the slides were washed (3X) again in PBS-0.5 % Tween. The fixation of the staining was done in paraformaldehyd (4 %) in PBS for 5 minutes, followed by an additional washing step in PBS-0.5 % Tween. After dehydrogenating in alcohol (70-80-96%) the slides were stored under mounting medium containing DAPI for nuclear counterstaining (Vectashield, Vector Laboratories) at 4°C until the microscopic analysis. The microscopic analysis was done using a Zeiss Axioscope microscope and the Axiovision software at 400X magnification. Cells on 20 visual fields were counted and the mean values and standard deviations were calculated.

For the electron microscopy analysis another procedure was applied. Firstly, in order to remove the Q 333 medium, the substrates and the control slides were washed (2X) with PBS at 37°C. Then fixation was done using 1 % paraformaldehyde and 1 % glutardialdehyde in 0.12 M PBS for 2 hours at room temperature under movement. Following the fixation, the samples were incubated in osmiumteroxide (4 %) for 2 hours under movement in the dark. The substrates were stored in distilled water at 4°C overnight. The water was removed by washing the substrates twice in ethanol under movement at 4°C for 5 minutes (30-50-70-80-90%). Dehydrating was completed by washing (3X) in ethanol (100 %) for 15 minutes under movement at 4°C. Then the samples were dried by Critical Point Drying (Polaron CPD 7501, Quorom Technolgies) and sputtered with gold-palladium (Polaron, Sputter Coater) before analyzing them in a FEI XL 30 ESEM FEG scanning electron microscope.

## 5.5 Results and Discussions

### 5.5.1 T-Cells on Nanowires

In Figure 5.1 optical images of every cell line (MCF7, Jurkat, THP1 and K562) on different test surfaces (glass-without Poly-L-Lysin, glass-with Poly-L-Lysin, polystyrene and $Al{\cdot}Al_2O_3$) are shown. The fluorescence intensity is slightly lower in the case of $Al{\cdot}Al_2O_3$ coated glass cover slips, because the coating absorbs light strongly. Nevertheless, it is obvious that the adherence of Jurkat cells is increased on the $Al{\cdot}Al_2O_3$ coated cover slips compared to the other substrates. Unexpectedly, this effect is restricted to Jurkat cells only. The adherence and growth of an intrinsically adherent cell line like MCF7 is not disturbed by the $Al{\cdot}Al_2O_3$ coating.

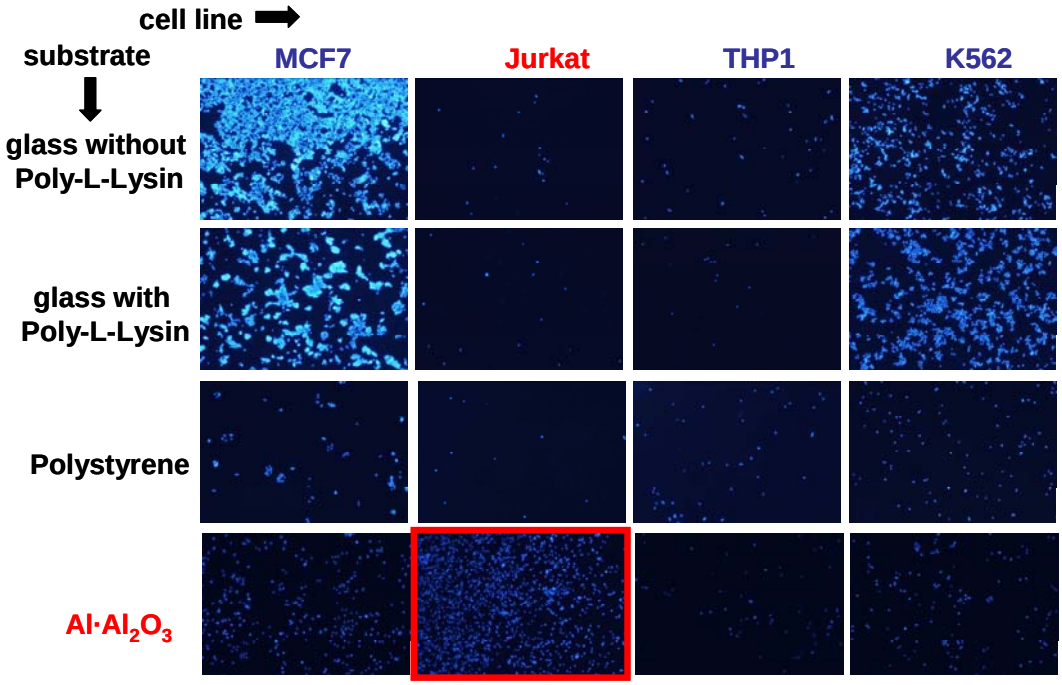


**Figure 5.1 Optical images of different cell types (MCF7, Jurkat, THP1 and K562) on different test surfaces.**

In another set of experiments Raji cells (human macrophage suspension cell line) were used instead of THP1 cells. After 24 hours the cells were washed with PBS and their nuclei were stained without fixing the cells by ethanol. Microscopic images were taken and the cells were detached by adding a Trypsin/EDTA (T/E) solution. After washing the detached cells away with PBS, the remaining cells were photographed once more. In this experiment the increased adhesion of Jurkat cells on the $Al{\cdot}Al_2O_3$ coating

is observed again (Figure 5.2). The adherent cells could be detached from the coating by trypsination indicating protein mediated adhesion.

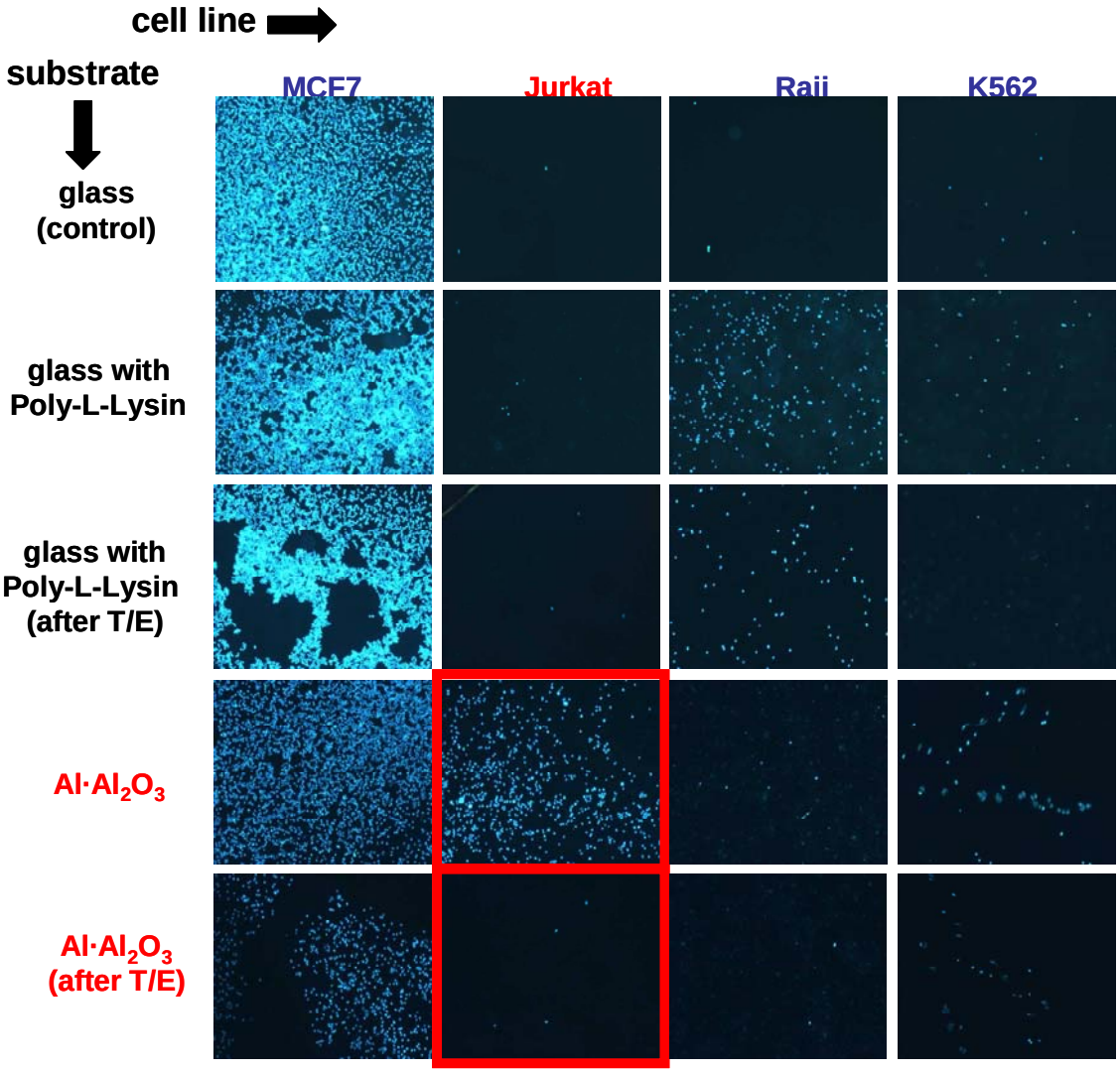


**Figure 5.2 Optical images of different cell types (MCF7, Jurkat, Raji and K562) on different surfaces before and after adding Trypsin/EDTA (T/E).**

In order to understand whether the increased adhesion is just a Jurkat cell-specific or a general T-cell effect, additional cell types were used to test the adhesion. The tested cell types can be listed as MCF7, MOLT-14, BE13, K562 and Jurkat. In Figure 5.3 and 5.4 phase contrast optical images are shown before and after washing the surfaces with PBS to detect non-adhering cells, respectively.

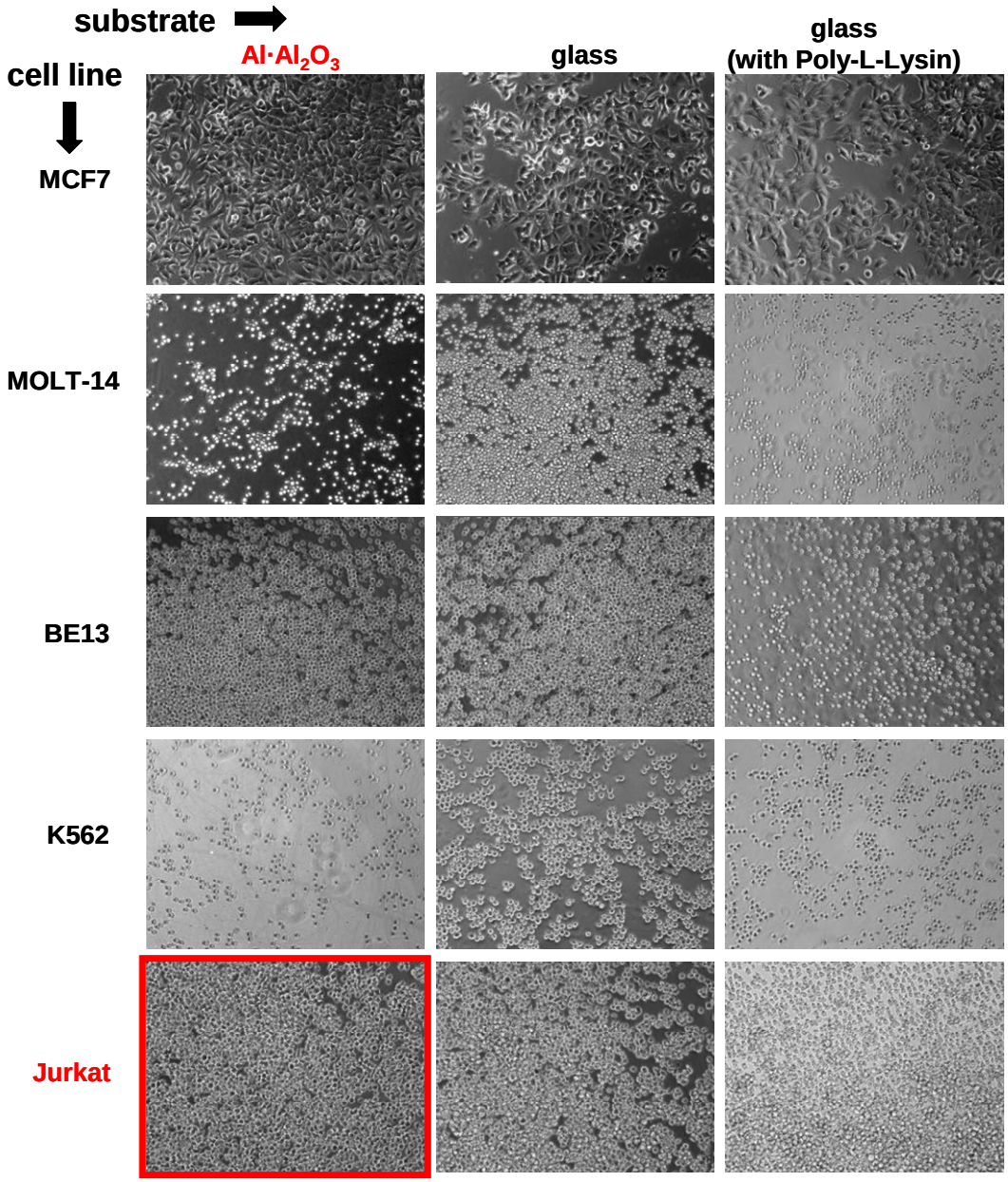


**Figure 5.3 Phase contrast optical images of different cells on test surfaces before washing with PBS.**

It is seen clearly that Jurkat cells adhere on the surface of the $Al{\cdot}Al_2O_3$ coating specifically. Also MOLT-14 cells show a slightly increased adhesion on the $Al{\cdot}Al_2O_3$ coating. BE13 and K562 cells show a bad adhesion since they are easily detected by washing with PBS. MCF7 cells adhere on every substrate, so there is no specific effect which can be attributed to the surface structure.

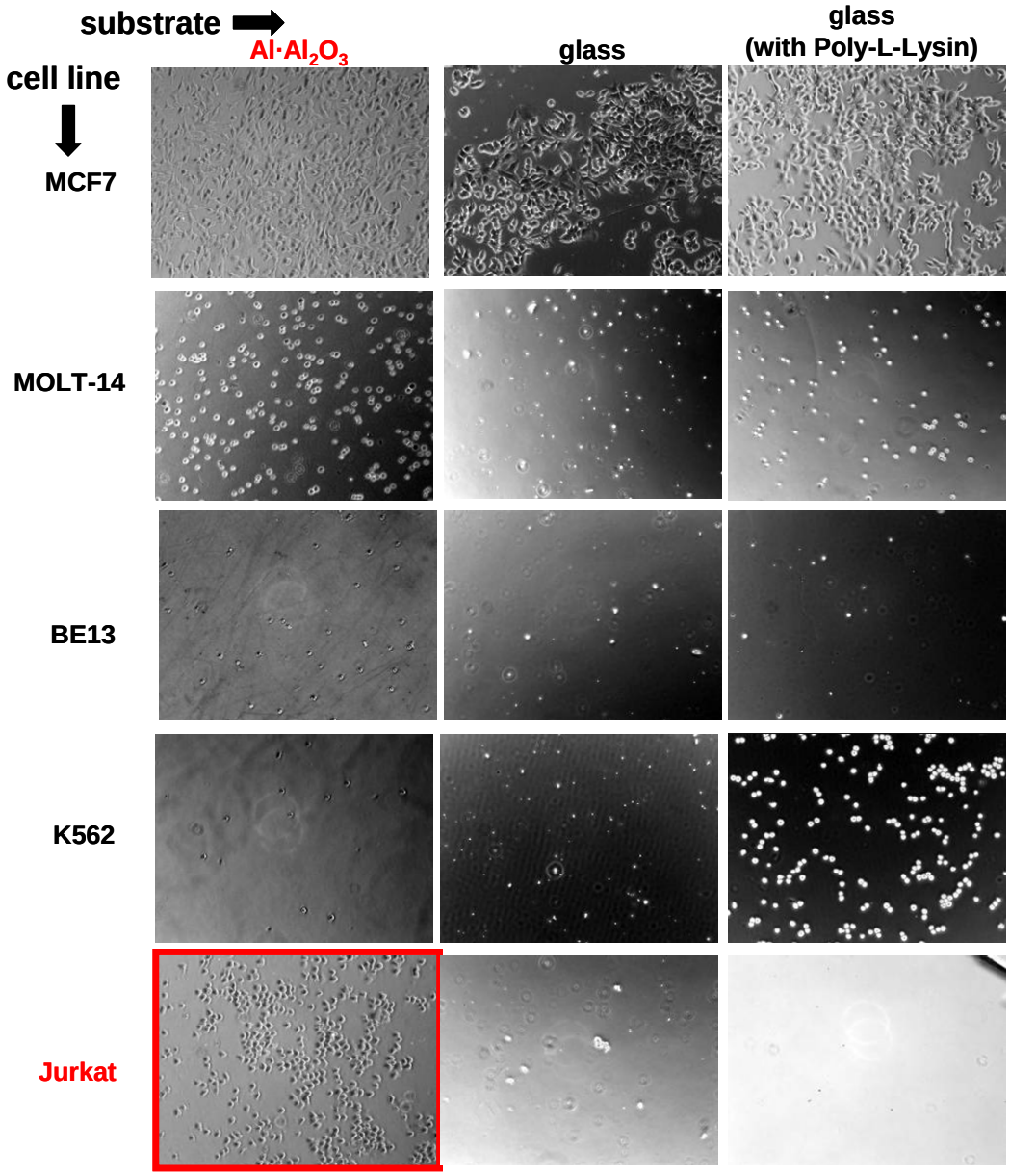


**Figure 5.4 Phase contrast optical images of different cells on test surfaces after washing with PBS.**

In order to get a better quantification of cell adhesion, the adhered cells were stained using Calcein-AM, a fluorescence dye which is enriched in viable cells. The fluorescence intensity on each cover slip was measured using a fluorometer by analyzing several spots on each glass cover slip. As MCF7 cells show a complete adhesion on all substrates these values were set to 100 % and the fluorescence intensities on other substrates are shown relatively to the corresponding MCF7 value. The following graph

in Figure 5.5 shows that the adhesion of Jurkat cells (two different sources) is clearly increased on the Al·$Al_2O_3$ surface again. Using this quantitative assay, K562 cells also show an increased adherence.

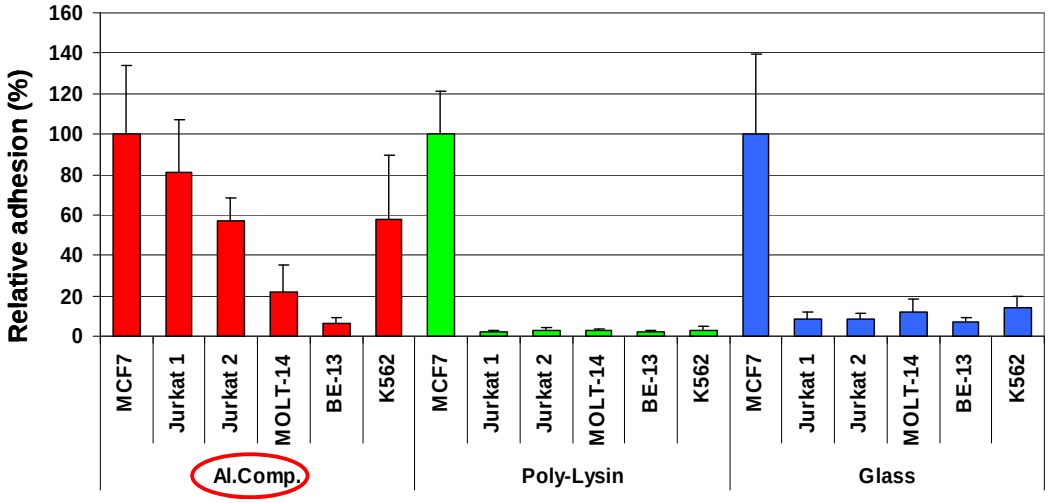


**Figure 5.5 Relative adhesion of MCF7, Jurkat, MOLT-14, BE-13 and K562 cells on Al·$Al_2O_3$ coated cover-slips (Al.Comp.), Poly-Lysin coated cover-slips (Poly-Lysin) and non-coated glass cover-slips (Glass).**

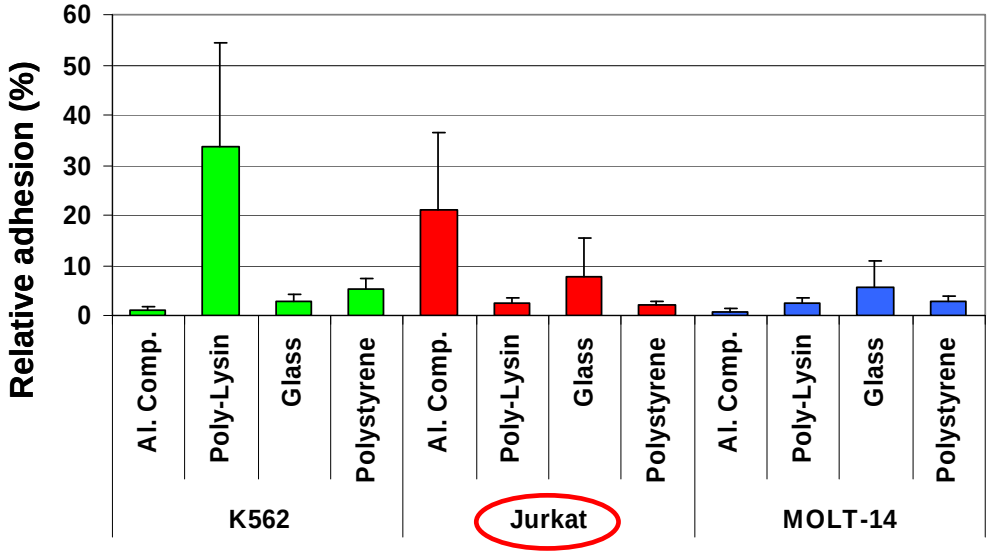


**Figure 5.6 Relative adhesion of K562, Jurkat and MOLT-14 cells on Al·$Al_2O_3$ coated cover-slips (Al.Comp.), Poly-Lysin coated cover-slips (Poly-Lysin), non-coated glass and polystyrene cover-slips.**

Excluding the totally adhering MCF7 cells, the fluorometer measurements were repeated by using three cell types; MOLT-14, Jurkat and K562. MOLT-14 cells exhibit very low adhesion (Figure 5.6). They nearly show no adhesion on any of the surfaces and the lowest adhesion is observed on $Al{\cdot}Al_2O_3$ surfaces. The adhesion of Jurkat cells increases on $Al{\cdot}Al_2O_3$. K562 cells show the best adhesion on polystyrene and poly-L-Lysin coated glass cover-slips. No adhesion is observed on glass and $Al{\cdot}Al_2O_3$ coated glass cover-slips.

The fluorometer measurements were also conducted on two different cover-slips coated with $Al{\cdot}Al_2O_3$ using BE-13 cells in addition to the previously used three cell types: MOLT-14, Jurkat and K562. Similar to earlier observations, MOLT-14 and BE-13 cells do not exhibit an adhesion on any of the substrates (Figure 5.7). There is a clear increase in the Jurkat cell adhesion on $Al{\cdot}Al_2O_3$ coated cover-slips again. On the other hand, there is a slight difference between two cover-slips coated with $Al{\cdot}Al_2O_3$. This can be explained by the thickness gradient between the two coatings. K562 cells again show the best adhesion on polystyrene coated glass cover slips and no significant adhesion on glass and $Al{\cdot}Al_2O_3$ coated glass cover slips.

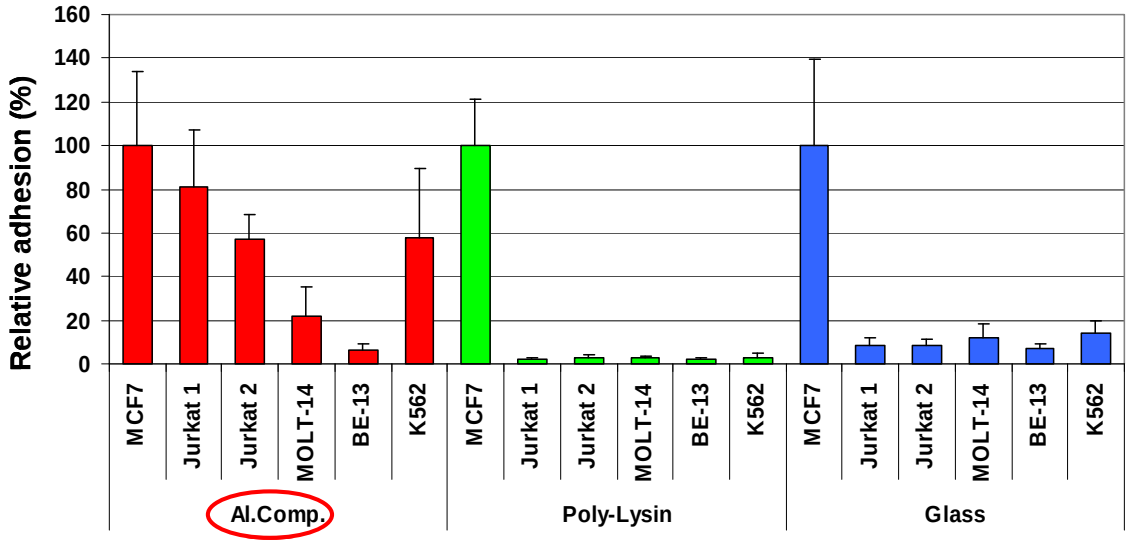


**Figure 5.7 Relative adhesion of Jurkat, K562, MOLT-14 and BE-13 cells on $Al{\cdot}Al_2O_3$ coated cover-slips (Al.Comp. 1/2), non-coated glass and polystyrene cover-slips.**

As a summary, the obtained data indicates that there is no general T-cell-line adhesion inducing effect of the $Al{\cdot}Al_2O_3$ coating. The **adherence of Jurkat cells lines on $Al{\cdot}Al_2O_3$ coated cover slips can be seen regularly** (however to varying extents), whereas such an effect is **not** seen in the case of the **other two T-cell lines (Molt-14 and BE-13).**

### 5.5.2 Fibroblast Cells on Nanowires and Laser Treated Surfaces

Fibroblasts cultured on the control substrates (glass cover-slips) proliferated and almost covered the material with cells of a normal morphology (Figure 5.8a). The cell growth seems dense and the morphology looks normal. In 20 visual fields seven mitotic cells are found. When the cells are cultured on $Al{\cdot}Al_2O_3$ nanowires, there is a distinguishable decrease in the cell density when compared to those cultured on the glass substrates (Figure 5.8b). In addition, the size of the cells look relatively smaller but their nuclei look healthy. The observation of mitoses indicates that the cell activity continues as under normal circumstances although they are much smaller than the ones cultured on the control samples.

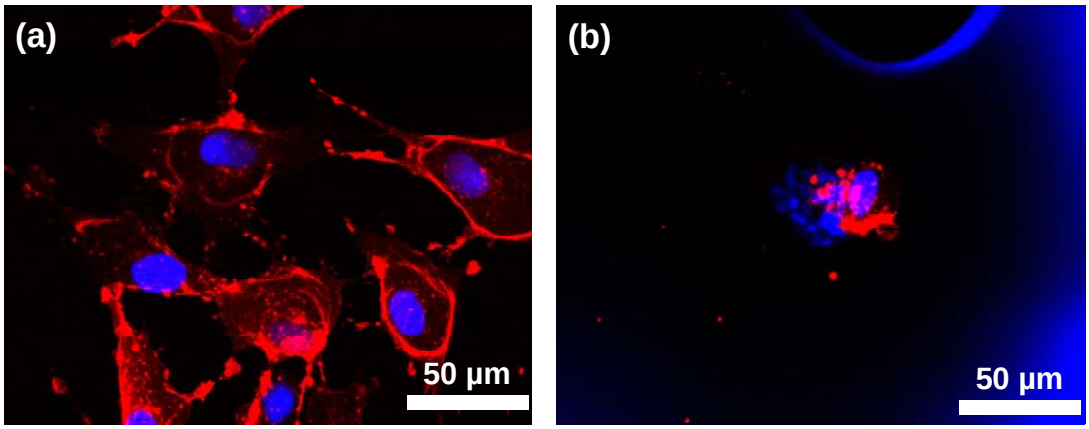


**Figure 5.8 Optical microscope images of fibroblasts cultured on a (a) non-coated glass cover-slip and (b) $Al{\cdot}Al_2O_3$ coated cover-slip.**

Cells cultured on $Al{\cdot}Al_2O_3$ composite treated with a single laser pulse show a slight difference (Figure 5.9a and b) compared to the ones cultured on nanowires (Figure 5.8b). The cell morphologies and sizes are comparable with those cultured on the control substrate. On the other hand, the cell density is lower than the control. The presence of some mitotic cells indicates that the cells are healthy.

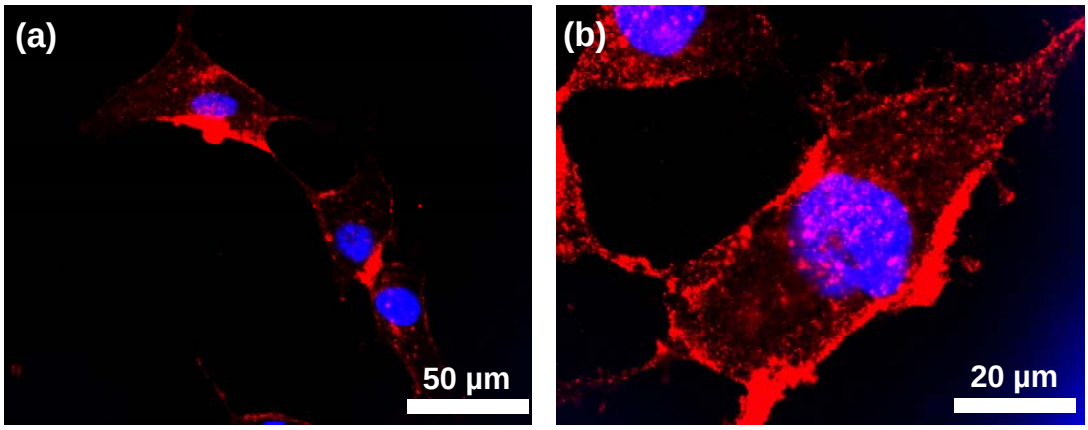


**Figure 5.9 Optical microscope images of fibroblasts cultured on Al·$Al_2O_3$ nanowires treated with a single laser pulse. (a) Low magnification. (b) High magnification.**

Similar results are observed in the case of cells cultured on the Al·$Al_2O_3$ nanowires treated with two laser pulses (Figure 5.10a and b). The cell morphology looks normal. The nuclei of the cells look larger than the ones cultured on the control samples (glass cover-slips) but they do not show any abnormality in terms of shape and cellular functions. The cell density is less than that of cultures deposited on Al·$Al_2O_3$ nanowires treated with a single laser pulse.

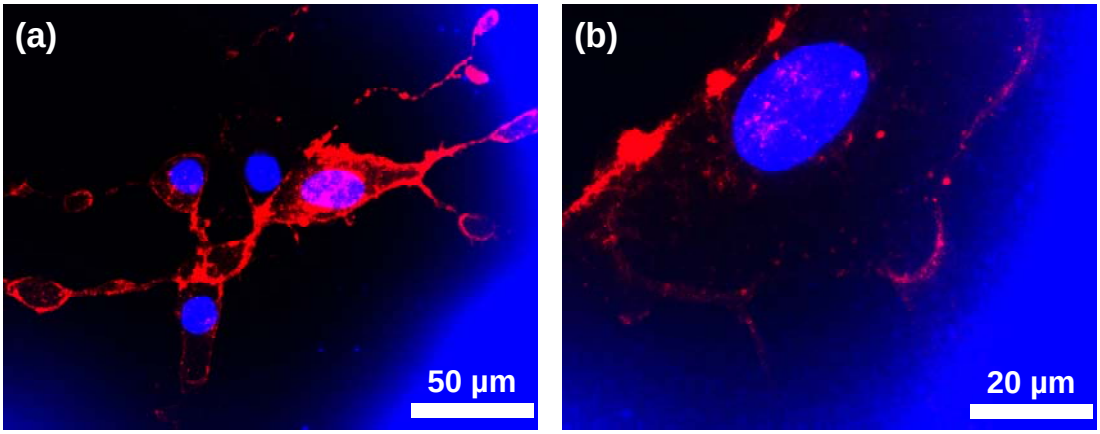


**Figure 5.10 Optical microscope images of fibroblasts cultured on Al·$Al_2O_3$ nanowires treated with two laser pulses. (a) Low magnification. (b) High magnification.**

Further repeating of the laser pulses yields a big difference in the cell's behaviors in terms of morphology and nuclei, as seen Figure 5.11a and b. The nuclei can not be seen clearly and they exhibit untypical structures. The cells are very small and there is no presence of any mitosis. On the other hand, due to optical interference effects the quality

of the images becomes worse. Nevertheless, the difference in the cell morphology and nuclei appearance indicates that the cells do not look healthy.

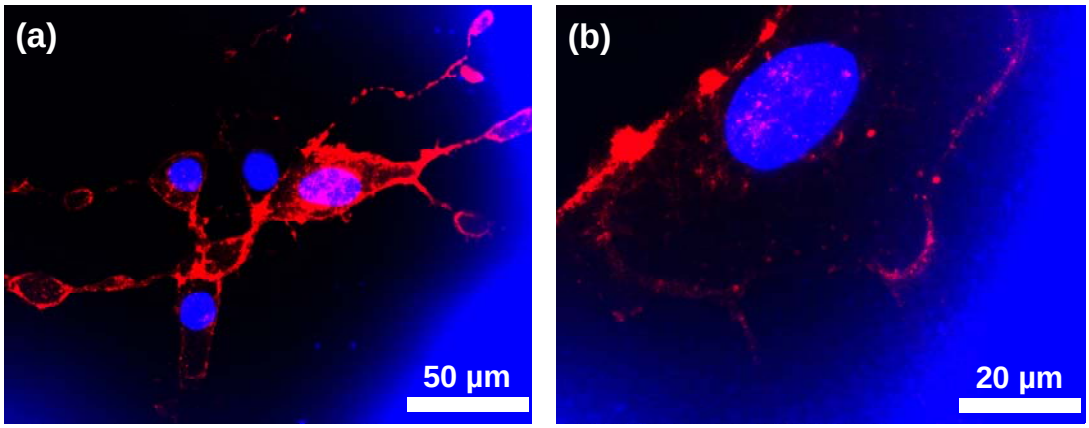


**Figure 5.11 Optical microscope images of fibroblasts cultured on Al·$Al_2O_3$ nanowires treated with three laser pulses. (a) Low magnification. (b) High magnification.**

A comparison of cell densities on nanowires (as-deposited) and laser treated surfaces is shown in Figure 5.12. It is clear that the cell density on the laser treated surfaces is less than that on the glass control in every case. When the densities between the Al·$Al_2O_3$ coated and laser treated surfaces are compared, single pulse laser treated surfaces show the highest density.

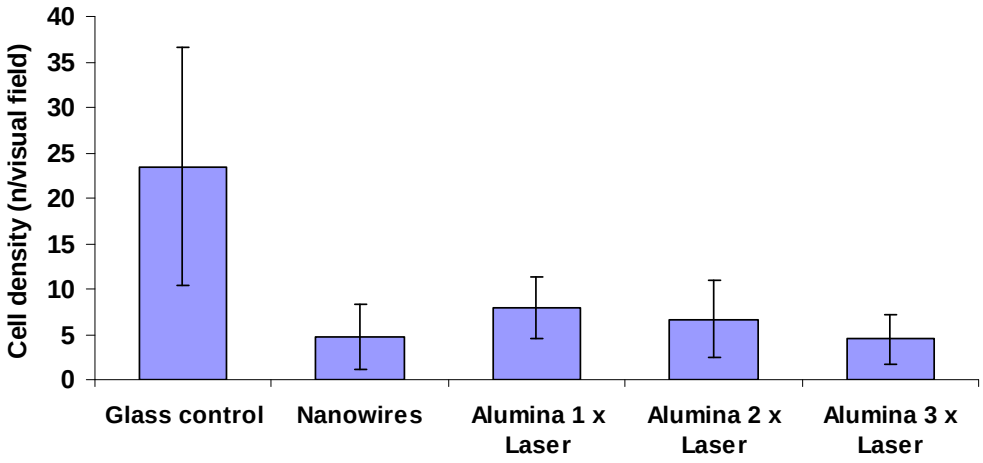


**Figure 5.12 Relative cell densities on glass, Al·$Al_2O_3$ nanowires andAl·$Al_2O_3$ nanowires treated with one, two and three laser pulses.**

The cell density decreases on the surfaces which were prepared by repeated laser pulses. The same trend can be observed in Figure 13, which shows that the wetting behavior of these surfaces changes with repeated laser pulses. The inserts in the graph show the SEM images of the prepared surfaces. Their detailed characterization is provided in Chapter 4.7.6.

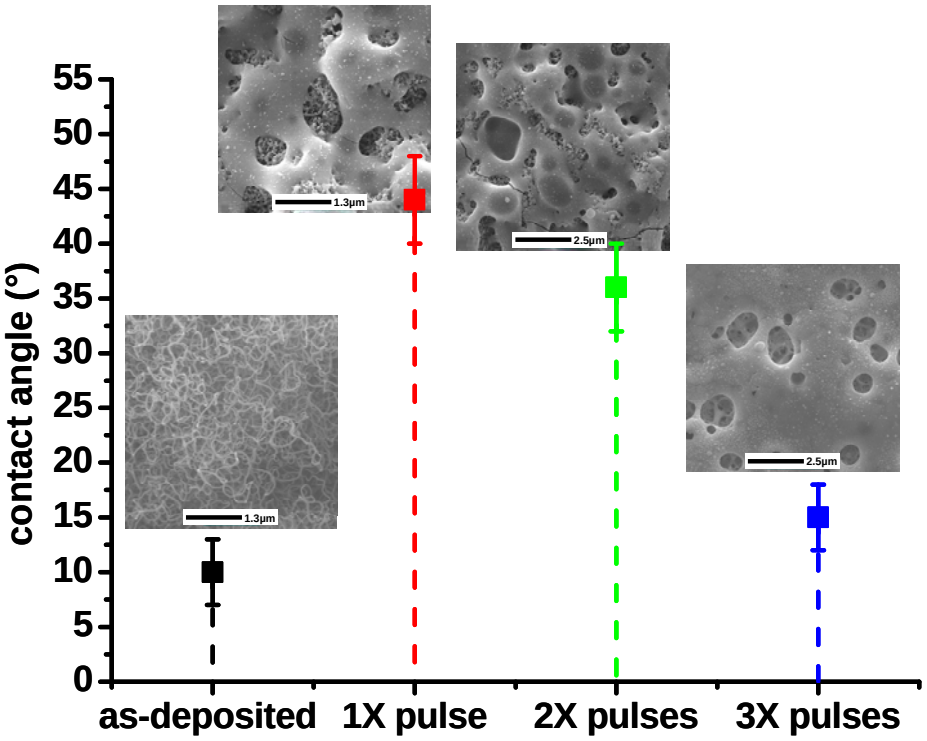


**Figure 5.13 Contact angles of deposited and laser treated layers. The inserts show the SEM images of corresponding surfaces.**

In order to understand the cell-surface topography interaction better, SEM was used to visualize the behavior of fibroblasts on nanowires (as-deposited) and laser treated surfaces. The SEM images of fibroblasts on the control substrate (glass cover-slip) show that the cells grow well across the whole surface with a normal morphology (Figure 5.14a). While less filopodia are seen at the cell edges, the amount of the filopodia increased at the proximity of neighbouring cells. This is an indication of cell-cell interaction which can be attributed to early stages of cell-cell adhesion [324]. In the images with a higher resolution (Figure 5.14c), it is seen that the filopodia-like structures

protrude to a mushroom-shaped structure which reminds of the dendritic spine formation in a neuronal growth cone [325]. On the other hand, cells do not spread well over the nanowires and have a relatively more ruffled membrane. As seen in Figure 5.14b, the cell exhibits an elongated morphology and a few filopodia are observed. In the higher magnification SEM image of a cell edge (Figure 5.14d) a few filopodia can be seen clearly. When they are compared with the ones observed on glass substrate, the main difference is the absence of the dense and branched dendritic filopodia.

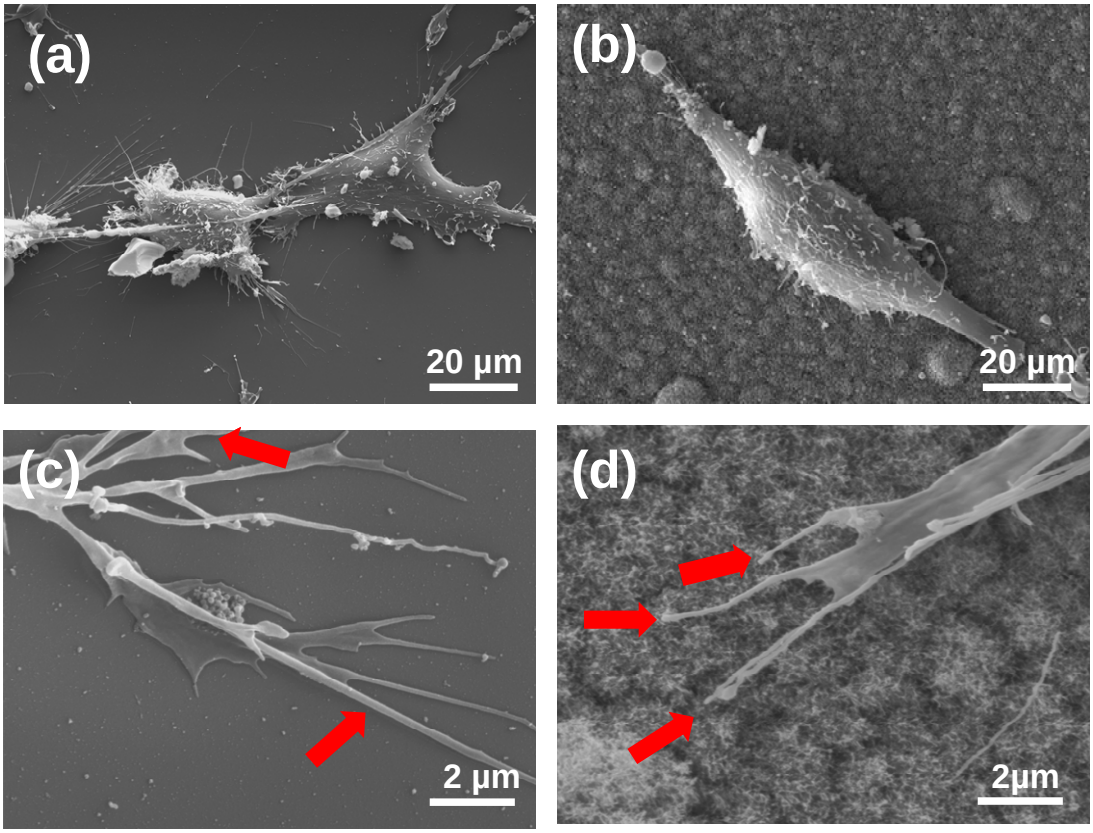


**Figure 5.14 SEM images of fibroblasts on glass cover-slips in (a) low and (c) high resolution and fibroblasts on Al·$Al_2O_3$ nanowires in (b) low and (d) high resolution.**

The cells show different responses to nanowires and surfaces treated with a single laser pulse. As seen in the SEM image given in Figure 5.15a, several filopodia form on the edge of the cell cultured on a laser treated surface. In comparison, very less filopodia formation is observed on the surface of the deposited nanowires (Figure 5.15b). The second noticeable difference is that the cells on the nanowires seem to probe the environment which is relatively far away from the cell periphery using longer filopodia when compared to cells cultured on the laser treated surface. In the case of laser treated

surfaces there is a clear interaction between the cell and the micro/nano structures near by the cell periphery. The cells cultured on the nanowires do not exhibit such an aggressive interaction and they prefer searching and probing the environment away from the cell periphery.

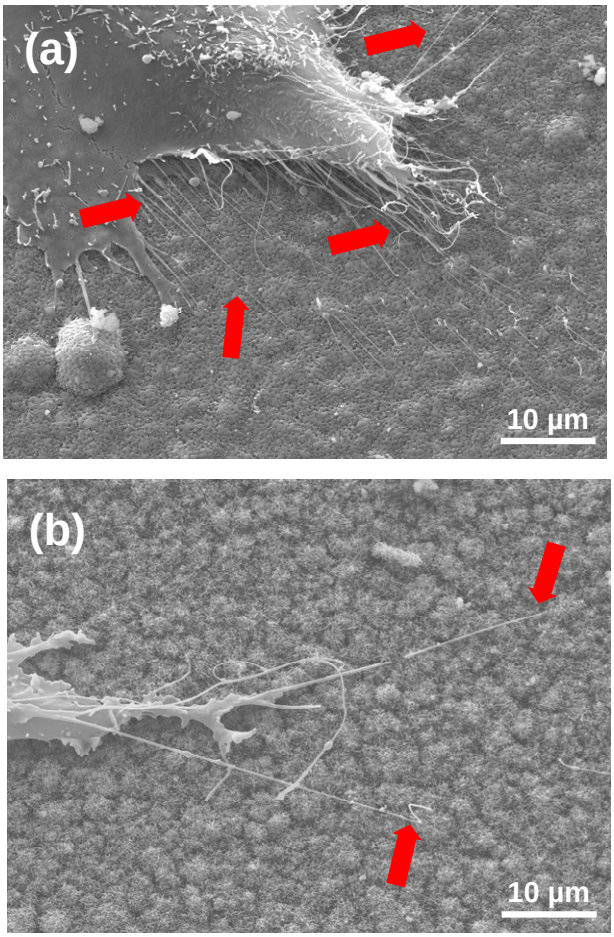


**Figure 5.15 SEM images of fibroblasts on (a) Al·$Al_2O_3$ nanowires treated with a single laser pulse and (b) Al·$Al_2O_3$ nanowires as deposited.**

After the second laser pulse the surface becomes smoother, as shown previously in Figure 4.48b. This change in the topography is directly sensed by the cells. As seen in Figure 5.16a, the cell tries to spread over the surface which is treated with a single laser pulse. In comparison, cells do not spread in the same manner on the surface treated with two laser pulses (Figure 5.16b). In Figure 5.16b the main characteristic feature is the growth at the edge of the fibroblast which reminds of the retraction fibers observed during the disassembling of the cell at one edge and forming new adhesions with substrate on the other edge. In the high magnification image (Figure 5.16a), various

filopodia are seen on the surface of the nanowires treated by a single laser pulse. There are relatively less filopodia on the surfaces treated by two laser pulses (Figure 5.16d).

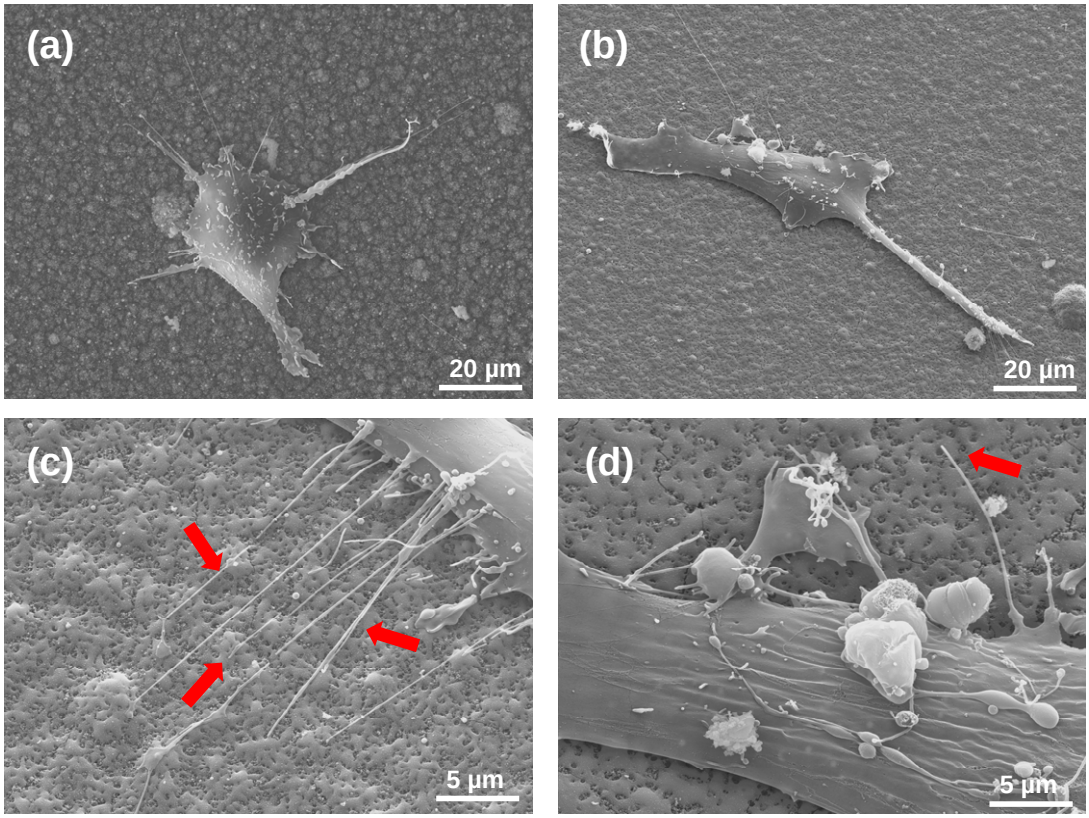


**Figure 5.16 SEM images of fibroblasts on Al·$Al_2O_3$ nanowires treated with a single laser pulse in (a) low and (c) high resolution and on Al·$Al_2O_3$ nanowires treated with two laser pulses in (b) low and (d) high resolution.**

After repeating laser pulses microgrooves are produced over a layer composed of micro and nano features (nanowires within the submicron cavities shown in detail in Figure 4.52). Actually, the surface can be separated into three regions where different characteristic morphologies can be observed due to the Gaussian distribution of the laser beam. In the first type the spacing between the microgrooves is ca. 5-6 µm (Figure 5.17a and b, red arrows) which is much larger than the average size of the microgrooves. In such conditions, cells do not spread over the surface and they only attach to the large grooves. Interestingly, while the cell probes the microgrooves by filopodia formation, it does not show any response to the layer beneath (Figure 5.17a and b).

A second type of morphology can be defined where the spacing between the microgrooves is comparable with the dimensions of the grooves (Figure 5.17c). The microgrooves again cover a layer composed of micro/nano features and they are closer to each other. Under these circumstances the cell spreads well over the micro features. As seen in the SEM image (Figure 5.17c), over the cell surface at the three leading edges, actin stress fibers can be seen partly. At the edges filopodia form to sense the substrate features to make new attachments. It seems that in principle the cell recognizes firstly the microgrooves and spreads over them, but later it tries to probe the smaller structures. It also looks like the cells hang on microgrooves.

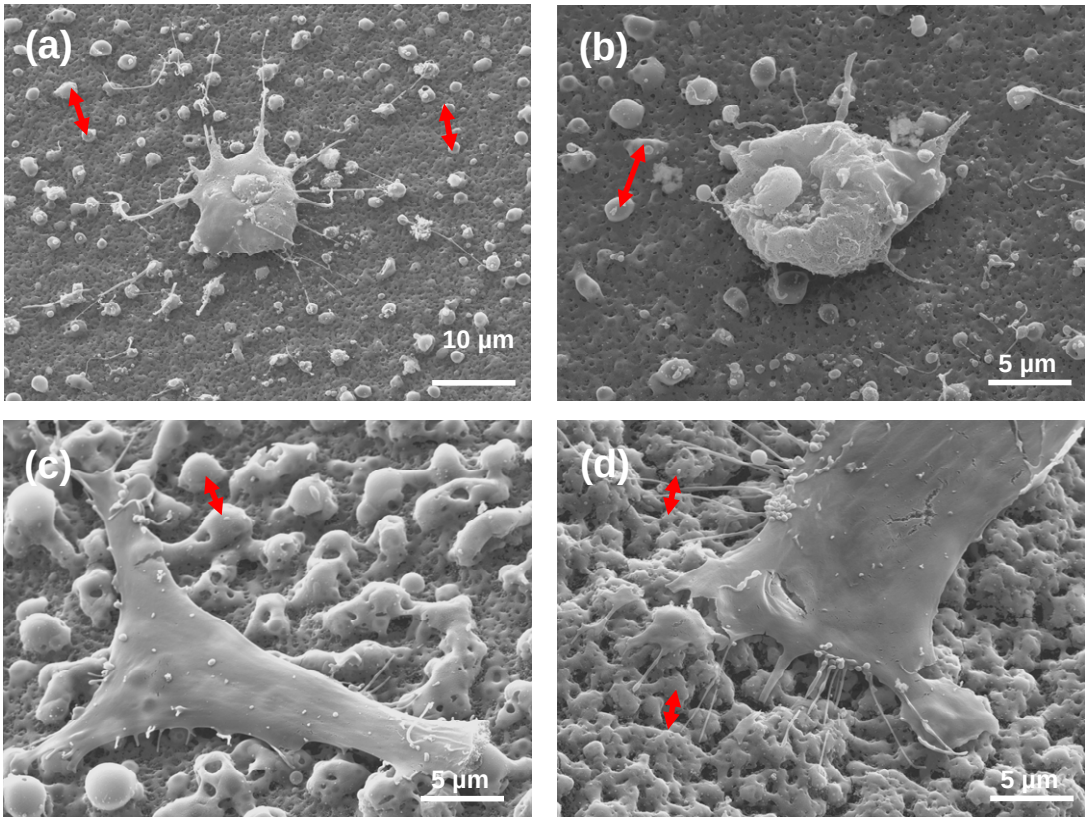


**Figure 5.17 SEM images of the surfaces after repeated laser pulses. (a) Microgrooves with interstices larger than their average sizes (type 1). (b) High magnification image of type-1-microgrooves. (c) Microgrooves with interstice dimensions comparable to their own sizes (type 2). (d) Microgrooves forming a continuous layer (type 3).**

The last type of morphology can be explained by adjacent microgrooves which form a continuous layer (Figure5.17d). Between or over some of these microgrooves there are sub-micron pores. The inner parts of these pores are partially covered with nanowires, as

shown previously in Figure 4.52. Under these conditions the cell spreads over the surface and forms many filopodia. When the spacing between the microgrooves is larger (larger than the size of a microgroove), the cells hang over these hill-like structures. In comparison, when a continuous landscape composed of adjacent microgrooves is created, the cells spread over the whole surface.

In high magnification SEM images (Figure 5.18a and b) it is clearly seen that, when the spacing between the microgrooves is larger, the cell identifies each groove as a separate structure rather than as a continuous landscape.

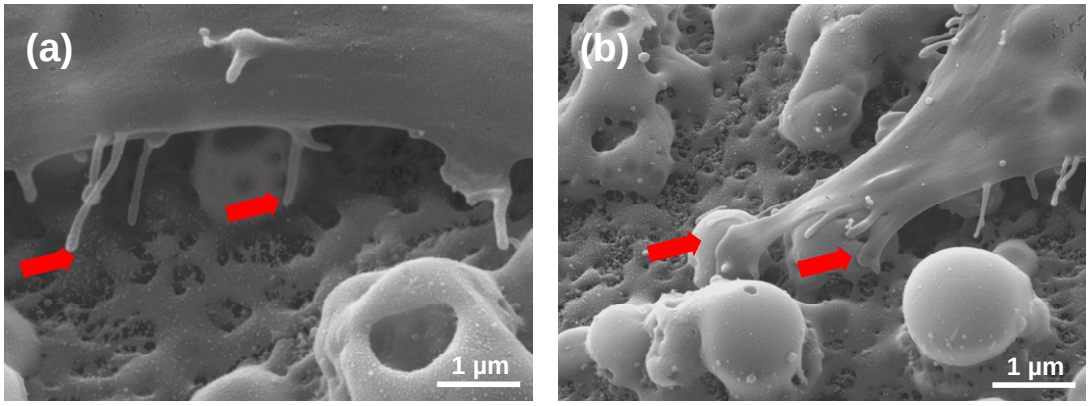


**Figure 5.18 SEM images of fibroblast cells on microgrooves. (a) Filopodia formation towards the nanostructures. (b) Transformation of filopodia into branch-mushroom-like structures.**

On the other hand, the filopodia formation towards the nanostructures shows that the cell tries to probe the smaller structures beside the microgrooves (as illustrated by the arrows in Figure 5.18a). Such tiny filopodia transform into branched mushroom-like structures at the leading edge of the fibroblast which is in contact with the microgrooves (as illustrated by the arrows in Figure 5.18b).

As a summary;

- Nanowires act as a less adhering medium for the fibroblast cells.
- Fibroblast cells show better responses to surfaces composed of nano- and microstructures.
- Microroughness and nanoporous combinations are recognized better by the fibroblast cells.
- The interstices between the structures or periodicity play also a major role for the cell behaviour.

### *5.5.3* Future Aspects: Neuronal Cell Growth on Nanowires

Nanotechnology and nanomaterials are used more and more for biomedical applications in basic and clinical neurosciences. Different nanostructured materials including quantum dots, nanowires or nanorods are used to study the interaction and stimulation of neurons at the molecular level [326], the transport of drugs and small molecules across the blood–brain barrier [327], neuronal differentiation from progenitor cells, neural regeneration [328] and the communication/signaling mechanism of neurite networks [329].

1D structures were employed in neurosciences for a long time. For example, micropipette electrodes and micro fabricated electrode arrays are well established tools to explore the electrical behaviors of individual neurons and neuronal networks [330]. Such micro structures are not small enough to deal with neuronal activities at the level of individual axonal or dendritic outgrowth. In this context, nanowires might be attractive tools for the coupling of neurons to technical surfaces, to improve for example the interfacing between neurons and electrodes. Lieber et al. showed that a nanowire contacted to a single axon can measure a conductance peak when the neuron is stimulated [331]. Similarly, an impulse applied to the nanowire creates a spike in the action potential of the neuron.

Nanowires also found applications in transporting foreign genes into cells which is a process of central importance in molecular biology. McKnight et al. showed that penetration of DNA-modified carbon nanofibers into living cells provides efficient delivery and expression of exogenous genes, similar to "microinjection" methods [332]. Since the carbon nanofibers bunch used in this work is in the size of micro scale, an external force was required to push the cells onto the tips, for the DNA to be injected. Nanowires may either penetrate the membranes passively or, considering that the cells might try to engulf them, do it actively without an external manipulation. Such a direct interaction was shown by Hällström et al. using gallium phosphide (GaP) nanowires grown vertically from a gallium phosphide surface [333]. In his work it is shown that the neuron cell survival was better on nanowire deposited substrates than on planar control substrates. The cells interacted with the nanowires and they penetrated into cells. After a long-term interaction nanowires were bended due to forces exerted by the cells.

In the present study we started investigating the interaction of neuron cells with $Al{\cdot}Al_2O_3$ nanowires. In a preliminary study neurons isolated from dorsal root ganglia (DRG) were seeded on top of $Al{\cdot}Al_2O_3$ coated glass cover-slips to demonstrate the biocompatibility on one side, and also delivering first insights into their influence upon neuronal growth and the formation of neuronal networks.

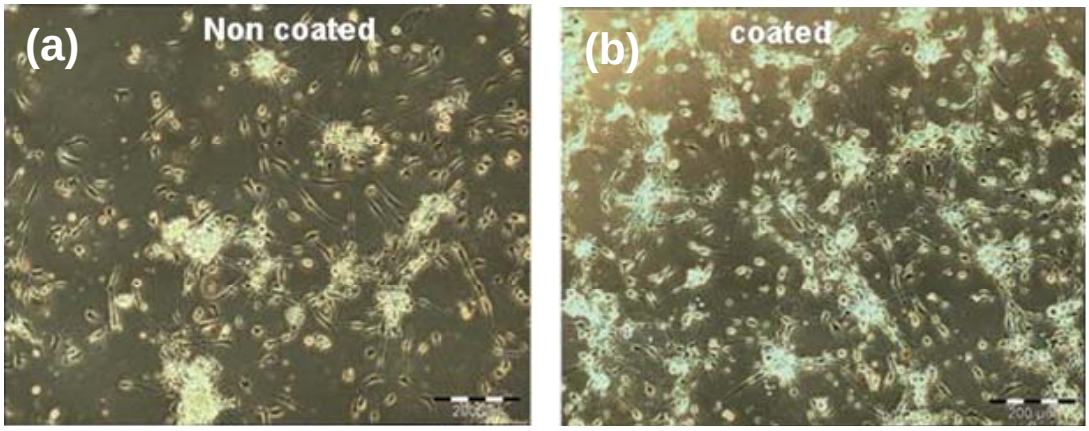


**Figure 5.19 Optical microscope images of neuronal and glial cell cultures on (a) non-coated glass cover-slips and (b) $Al{\cdot}Al_2O_3$ coated glass cover-slips.**

Our preliminary observations show that DRG neuron cells can be grown on $Al{\cdot}Al_2O_3$ nanowires and that the neurite network formation is influenced by the nanostructures. Phase contrast micrographs (Figure 5.19) already show the different growth of neuronal and glial cell cultures on glass and $Al{\cdot}Al_2O_3$ coated glass cover-slips.

To investigate the influence on the neurite formation, cultures were fixed in 4 % formaldehyde and immunohistochemically stained for the neuronal marker tubulin. It could be demonstrated clearly that DRG neurons (Figure 5.20b) form a much denser neurite network on the $Al{\cdot}Al_2O_3$ surface, as seen in the control samples (Figure 5.20a), thus giving evidence for their response to the nanotopography of the $Al{\cdot}Al_2O_3$ layer. Due to the random distribution of the nanowires neurites grow outward from the ganglia without preference to any specific direction. These observations indicate the potential of $Al{\cdot}Al_2O_3$ to support the formation of a communicative neural network in three dimensions. Future investigations using nanostructures of varying composition or topography will reveal the interaction of the topography and neuronal and glial cells in-vitro in much more details, thus delivering the base for possible uses in either improving

the neuronal-electrode interaction or even in actively influencing the differential fate of neural stem cells when grown on nanostructured surfaces.

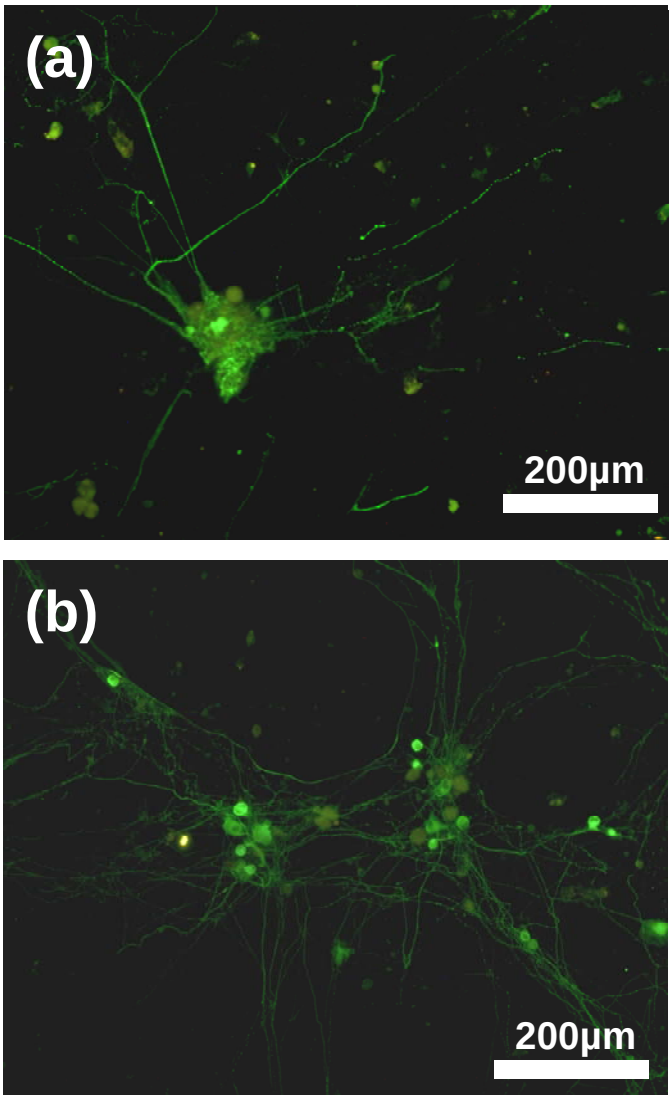


**Figure 5.20 Optical images of DRG neurons cultured on (a) non-coated glass cover-slips and (b) Al·$Al_2O_3$ coated cover-slips.**

This preliminary study on neurons showed that Al·$Al_2O_3$ nanowires provide an enhanced cellular adhesion and growth which can be interesting for various applications in the medical field as well as biosciences. We believe that Al·$Al_2O_3$ nanowires can be used to study cellular communication and neural signaling. The development of new nano-engineered scaffolds which can mimic the extra cellular matrix and provide better physical and biocompatible environments for neuron cells is considered one of the primary tasks for the future investigation of the Al·$Al_2O_3$ nanowires.

# 6. Conclusion

Recently, one-dimensional (1D) nanostructures have attracted considerable interest of nanoscience studies as well as nanotechnology applications. In particular, 1D nanostructures of metal oxides, such as ZnO, $SnO_2$, $Fe_2O_3$, $WO_3$, $Ta_2O_5$ and $Al_2O_3$ so-called functional materials, have been studied widely. Especially, 1D hetero structural nanowires with a two different material combination, for instance metal/metal oxides, hold a great potential for various photonic and electronic applications. In this context, $Al{\cdot}Al_2O_3$ core-shell nanowires, which were firstly reported by Veith et al., form an interesting class of such hetero 1D structures. Although some research activities were carried out on such composite nanowires previously, there are still open questions to answer.

In this PhD thesis the first attention is given to gain an understanding of the underlying mechanisms controlling the 1D growth of $Al{\cdot}Al_2O_3$ nanostructures. By systematically altering the deposition temperature a further understanding of the formation of such nanostructures was achieved. At high temperatures above the melting point of Al it seems that firstly an Al seed forms and the directional growth starts from this self-catalyst seed. Our detailed study revealed that the local temperature change plays an important role on the morphology of the deposited 1D structures. The dynamic changes on the surface temperature and flow rate affect the catalyst Al seed density which is the critical point for random and chaotic arrangement of 1D nanostructures. At high temperatures it is believed that repeated melting and re-solidification of Al seed leads to formation of branched nanowires.

For the first time the formation of loop-like 1D nanostructures was observed at low deposition temperatures. It is believed that when the temperature of the substrate is below the melting point of Al, firstly large particles nucleate. Following the nucleation step, such particles assemble and form clusters together. The deposition of further gaseous species leads to the formation of 1D worm-like structures by assembling the particles between adjacent former clusters. Finally, this directional growth ends up into closed loop-like exotic structures. In addition to the temperature, other process parameters like the flow rate of the precursor play a role in determining the morphology of such structures, but appear to be less significant.

We employed a new mask-less local deposition method which we named as selective CVD (SCVD). This study presents the selective heating of thin metal film structures deposited on glass substrates by applying magnetic induction. Basically, localized heating and various temperature regions can be achieved simultaneously on the substrate by applying an external high-frequency magnetic field. A controlled thermal gradient on the surface leads to the deposition of various structures and observation of stepwise 1D growth. As a continuation of the local deposition approach, this thesis reports, for the first time, about the possibility to grow 1D complex structures by thermal laser assisted CVD of a $(^{t}BuOAlH_2)_2$ precursor. An LCVD system has been designed, fabricated and tested during this PhD thesis. Careful thermal control has permitted the fabrication of 1D structures that can be used as building blocks for larger three-dimensional (3D) objects. Especially, similarities between the morphology of deposited layers and the extra cellular matrix (ECM) are promising results for possible scaffold applications. On the other hand, this process still needs further optimization.

$Al{\cdot}Al_2O_3$ nanowires exhibit broad plasmon absorption which is believed to be due to their dielectric-metal core-shell combination and chaotic 1D geometry. Highly crossed nanowires may enhance the applied electromagnetic field intensity which leads to the "hot spot" formation. Since the plasmon absorption peak of Al is in the UV wavelengths, optical characterization faces with severe difficulties. Although the underlying mechanism is not well understood, such a broad absorption is interesting for some applications, for instance laser assisted synthesis of $\alpha$-$Al_2O_3$. In most of the laser processings of alumina ceramics $CO_2$ lasers are preferred due to the IR wavelengths absorption of alumina. In comparison, $Al{\cdot}Al_2O_3$ nanowires provide a wide spectrum of wavelength flexibility in laser processing.

In particular, two laser processing approaches were investigated: continuous wave (CW) laser and pulsed laser treatments. This research work provided a detailed description of the design of prototype laser processing stations and experimental details about photothermal laser processing of the $Al{\cdot}Al_2O_3$ composite system. The design of the prototype laser stations was conducted from a *systems design* perspective, to demonstrate the interaction between the individual elements of the laser processing steps. Part of the goal was to establish an automated laser direct-write device.

Laser induced heating of $Al{\cdot}Al_2O_3$ nanowires leads to dense $\alpha$-$Al_2O_3$ layers. Our detailed nanoindentation experiments showed that hardness and elastic modulus values (calculated according to the Oliver-Pharr method) are in a very good agreement with reported values in the literature. Additionally, pop-ins usually were observed during nanoindentation of laser treated layers. The shear modulus value lays in the order of the theoretical strength for $\alpha$-$Al_2O_3$ of 26 GPa. This proves that the laser treatment of layers seems to result in $\alpha$-$Al_2O_3$ layers with a very low defect density. The depth of the laser densified region varies depending on the type of the laser in addition to laser power and scan speed. In the case of photo-thermal laser treatment of $Al{\cdot}Al_2O_3$ layers with an argon-ion laser the depth of the densified region is limited to a few microns. Just after the transformation of $Al{\cdot}Al_2O_3$ layers to $\alpha$-$Al_2O_3$, the argon-ion laser beam is reflected back and this hinders the excessive heating of the densified layer. In comparison to the argon-ion laser, the $CO_2$ laser is absorbed by both $Al{\cdot}Al_2O_3$ layers (as-deposited) and freshly formed dense $\alpha$-$Al_2O_3$ layer. This causes excessive heating of the layers which induce high thermal shocks. In addition to CW laser processing, we performed a detailed study of surface structures produced by pulsed laser treatment. The effects of the laser fluence and the number of applied pulses on laser induced topography were studied. We found that short laser pulses (4-8 nanoseconds) produce a large variety of surface structures such as nanopores, nanoprotrusions and microgrooves. These surfaces composed of micro and nano features provide optimal conditions for studying cell-surface interactions.

Micro-/nanostructured surfaces prepared by direct deposition of $(^tBuOAlH_2)_2$ and post-laser treatment were tested for biocompatibility. Different cell types including T-cell lines, normal human dermal fibroblast (NHDF) and neuron cells were cultured on synthesized surfaces. Interestingly, Jurkat cells exhibit a selective adhesion on the $Al{\cdot}Al_2O_3$ nanowires. It is believed that it is a protein mediated specific adhesion due to the observed detachment in the trypsination stage. Such a specific Jurkat cell interaction can lead to a device application in cancer diagnosis and treatment. On the other hand, NHDF cells do not adhere well on the $Al{\cdot}Al_2O_3$ nanowires. The adhesion of NHDF cells is improved after the laser treatment of nanowires. The laser treatment of $Al{\cdot}Al_2O_3$ nanowires can be extended to control the selective adhesion of similar cell lines locally.

Our preliminary experimental work shows that neuron cells grow better on $Al{\cdot}Al_2O_3$ coated cover-slips compared to non-coated control glass cover-slips. These observations indicate the potential of the $Al{\cdot}Al_2O_3$ nanowires to support the formation of a communicative neural network in three dimensions. By applying laser modification and local deposition techniques presented so far (SCVD and LCVD), $Al{\cdot}Al_2O_3$ composite can be used to improve neuron-electrode interactions which is the most critical issue in neuronal prostheses applications.

# 7. List of Publications

The following publications were realized in the frame of this PhD thesis.

**Publications in refereed journals:**

I. **Chemical Vapor Deposition of Aluminum based Micro- and Nanostructured Surfaces for Biological Applications.**
   M. Veith, C. Petersen, **O. C. Aktas**, W. Metzger, M. Oberringer, T. Pohlemann, M. Müller, S. Gerbes, Mater. Lett. 62, 23 (2008), 3842
II. **The Transformation of Core/Shell Aluminum/Alumina Nanoparticles into Nanowires.**
   M. Veith, E. Sow, C. Petersen, U. Werner, **O. C. Aktas**; Europ. J. Inorg. Chem.; in press (published online)
III. **Fibroblast Cell Attachment on Laser Modified Al·$Al_2O_3$ Surfaces.**
   M. Veith, **O. C. Aktas**, W. Metzger, M. Oberringer, G. Wennemuth, T. Pohlemann; to be submitted
IV. **α-$Al_2O_3$ Synthesis by Low Energy Laser Heating of Al·$Al_2O_3$ Nanowires.**
   M. Veith, **O. C. Aktas**; to be submitted
V. **Nanoindentation on α-$Al_2O_3$ prepared by Laser Treatment of Al·$Al_2O_3$ Nanocomposite.**
   M. Veith, **O. C. Aktas**, A. Barnoush, H. Vehoff; to be submitted

**Patents:**

I. **Verfahren zur Herstellung von Korund aus einem Komposit durch Energiezufuhr.**
   **O. C. Aktas**, M. Veith, Y. Wolf, S. Albayrak, B. Siegert; AZ: 10 2007 053 023.6-43 (pending).

# 8. References


[1] J. G. Lu, P. Chang, Z. Fan; Mater. Sci. Eng. 52 (2006), 49

[2] A. Kolmakov, Y. Zhang, M. Moskovits; Nano Lett. 3, 8 (2003), 1125

[3] S. J. Wu, R. Venugopal, Y. T. Chen; J. Chin. Chem. Soc. 52 (2005), 725

[4] Y. Zhang, K. Suenaga, C. Colliex, S. Iijima; Science 281 (1998), 973

[5] Z. L. Wang, Z. R. Dai, R. P. Gao, Z. G. Bai, J. L. Gole; Appl. Phys. Lett. 77 (2000), 3349

[6] Y. D. Yin, Y. Lu, Y. G. Sun, Y. N. Xia; Nano Lett. 2 (2002), 427

[7] R. R. He, M. Law, R. Fan, P. Yang; Nano Lett. 2 (2002), 1109

[8] L. J. Lauhon, M. S. Goudakäsen, C. L. Wang, C. M. Lieber; Nature 420 (2002), 57

[9] J. Y. Lao, J. G. Wen, Z. F. Ren; Nano Lett. 2 (2002), 1287

[10] S. Iijima; Nature 354 (1991), 56

[11] U. Landman, R. N. Barnett, W. D. Luedtke; Z. Phys. D: At., Mol. Clusters 40 (1997), 282

[12] M. H. Velez; Thin Solid Films 495 (2006), 51

[13] G. S. Snider, R. S. Williams; Nanotechnology 18, 3 (2007), 035204

[14] M. Law, L. E. Greene, J. C. Johnson, R. Saykally, P. Yang; Nat. Mater. 4, 6 (2005), 455

[15] L. Tong, L. Hu, J. Zhang, J. Qiu, Q. Yang, J. Lou, Y. Shen, J. He, Z. Ye; Opt. Express 14, 1 (2006), 82

[16] W. Wang, F. Jla, J. Zhu, J. Zhang; Thermoelectrics 682 (2003), 17

[17] Q. Li, S. M. Koo, M. D. Edelstein, J. S. Suehle, C. A. Richter; Nanotechnology 18 (2007), 315202

[18] S. J. Tan, I. K. Lao, H. M. Ji, A. Agarwal, N. Balasubramanian, D. L. Kwong; J. Phy. Conf. Ser. 34 (2006), 626

[19] S. Liang, R. Islam, D. J. Smith, P. A. Bennett, J. R. O'Brien, B. Taylor; Appl. Phys. Lett. 88 (2006), 113111

[20] K. B. Lee, S. M. Lee, J. Cheon; Adv. Mater. 13, 7 (2006), 517

[21] C. E. Morosanu; Thin Films by CVD, Elsevier, Amsterdam (1990)

[22] T. Kodas, M. Hampden-Smith; The Chemistry of Metal CVD, VCH Publisher, New York (1997)

[23] R. S. Wagner, W. C. Ellis; Appl. Phys. Lett. 4, 5 (1964), 89

[24] Y. Wu., P. J. Yang; J. Am. Chem. Soc.123, 13 (2001), 1365

[25] J.Hu, T. W. Odom, C. M: Lieber; Acc. Chem. Res. 32, 5 (1999), 435

[26] Z.Q Liu, W. Y. Zhou, L. F. Sun, D. S. Tang, X. P. Zou, Y. B. Li, C. Y. Wang, G. Wang, S. S. Xie; Chem. Phys. Lett. 341 (2001), 523

[27] T. I. Kamins, R. S. Williams, D. P. Basile, T. Hesjedal, J. S. Harris; J. Appl. Phys. 89, 2 (2000),1008

[28] C. C. Chen, C. C. Yeh, C. H. Chen, M. Y. Yu,H. L. Liu, J. Wu, K. H. Chen, L. C. Chen, J.Y. Peng, Y. F. Chen; J. Am. Chem. Soc. 123, 12 (2001) 2791

[29] J. C. Harmand, G. Patriarche, N. P. Laperne, M. N. Combes, L. Travers, F. Glas; Appl. Phys. Lett. 87, 20 (2005), 2031013

[30] A. D. Kimberly, D. Knut, T. Martensson, L. Samuelsen, B. Mandl, W. Seifert; Nano Lett. 5, 4 (2005), 761

[31] M. H. Huang, Y. Wu, H. Feick, N. Tran, E. Weber, P. Yang; Adv. Mater. 13, 2 (2001), 113

[32] Z. Q. Liu, S. S. Xie, L. F. Sun, D. S. Tang, W. Y. Zhou, C. Y. Wang, W. Liu, Y. B. Li, X. P. Zou, G. Wang, J. Wang; J. Mater. Res. 16, 3 (2001), 683

[33] R. S. Wagner; Whisker Technology, Wiley-Interscience, New York (1970)

[34] A. Umar, S. H. Kim, Y. S. Lee, K. S. Nahm, Y. B. Hahn; J. Cryst. Growth, 282, 1 (2005), 131

[35] A. Vomiero, M. Ferroni, E. Comini, G. Faglia, G. Sberveglieri; Nano Lett. 7, 12 (2007), 3553

[36] X. Liu, C. Li, S. Han, J. Han, C. Zhou; Appl. Phys. Lett. 82, 12 (2003), 1950

[37] X. Yang, Y. J. Wu, F. Zhu, Y. F. Zhang; Phys. Stat. Sol. 201, 14 (2004), 3051

[38] J. Hu, Y. Bando, Z. Liu, F. Xu, T. Sekiguchi, J. Zhan; Chem. Eur. J., 10, 2 (2004), 554

[39] L. M. Russell, K. Y. Donaldson, D. P. H. Hasselman, N. D. Corbin, J. J. Petrovic, J. F. Rhodes; J. Am. Cer. Soc. 74, 4 (2005),874

[40] Z. R. Dai, Z. W. Pan, Z. L. Wang; Adv. Funct. Mater. 13, 1 (2003), 9

[41] Y. Wang, L. Zhang, G. Meng, C. Liang, G. Wang, S. Sun; Chem. Commun. 24 (2001), 2632

[42] J. H. Park, Y. J. Choi, J. G. Park; J. Cryst. Growth, 280, 1 (2005), 161

[43] X. Kong, X. Sun, Y. Li; Chem. Lett. 32, 6 (2003) 546

[44] Y. C. Lin, W. T. Lin; Nanotechnology 16, 9 (2005), 1648

[45] Y. Zhang, R. Li, X. Zhou, M. Cai, X. Sun; J. Nanomater. (2008), 250370

[46] S. Sharma, M. K. Sunkara; J. Am. Chem. Soc. 124, 41 (2002), 12288

[47] D. Calestani, M. Zha, A. Zappettini, L. Lazzarini, L. Zanotti; Chem. Phys. Lett. 445, 4 (2007), 251

[48] F. Wang, G. Q. Jin, X. Y. Guo; J. Phys. Chem. B 110, 30 (2006), 14546

[49] Y. Baik, K. Shanker, J. R. McDermid, R. A. L. Drew; J. Am. Ceram. Soc. 77, 8 (2005), 2165

[50] C. N. R. Rao, G. Gundiah, F. L. Deepak, A. Govindaraj, A. K. Cheetham; J. Mater. Chem. 14, 4 (2004), 440

[51] H. Zhao, M. Lei, X. Yang, J. Jian, X. Chen; J. Am. Chem. Soc. 127, 45 (2005), 15722

[52] V. G. Sevastyanov, Y. S. Ezhov, E. P. Simonenko, N. T. Kuznetsov; Mater. Sci. Forum 457 (2004), 59

[53] G. Gundiah, F. L. Deepak, A. Govindaraj, C. N. R Rao; Chem. Phys. Lett. 381, 5 (2003), 579

[54] H. Zhang, M. Zuo, S. Tan, G. Li, S. Zhang, J. Hou; J. Phys. Chem. B 109, 21 (2005), 10653

[55] N. Wang, Y. H. Tang, Y. F. Zhang, C. S. Lee, S. T. Lee; Phys. Rev. B 58, 24 (1998), 16024

[56] S. T. Lee, N. Wang, Y. F. Zhang, Y. H. Tang; MRS Bull. (1999), 36

[57] W. S. Shi, Y. F. Zheng, N. Wang, C.S. Lee, S. T. Lee; Chem. Phys. Lett. 345, 5 (2001) 377

[58] W. S. Shi, Y. F. Zheng, N. Wang, C. S. Lee, S. T. Lee; Appl. Phys. Lett. 78, 21 (2001), 3304

[59] R. Q. Zhang, Y. Lifshitz, S. T. Lee; Adv. Mater. 15, 7 (2003), 635

[60] Y. F. Zhang, Y. H. Tang, N. Wang, C. S. Lee, I. Bello, S. T. Lee; Phys. Rev B 61,7 (2000), 4518

[61] Y. D. Yin, G. T. Zhang, Y. N. Xia; Adv. Funct. Mater. 12, 4 (2002), 293

[62] A. Vertova, L. Borgesel, G. Cappelletti, C. Locatelli, A. Minguzzi, C. Pezzoni, S. Rondinini; J. Appl. Electrochem. 38, 7 (2008), 973

[63] J. C. Carbery, C. B. Alcock; US-Patent 5028404

[64] K. S. Shamala, L. C. S. Murthy, K. R. Narasimha; Mater. Sci. Eng. B 106, 3 (2004), 269

[65] H. Bartzsch, D. Glosz, B. Bocher, P. Frach, K. Goedicke; Surf. Coat. Technol. 174 (2003), 774

[66] H. Exner, A.-M. Reinecke, M. Nieher; J. Ceram. Process. Res. 3, 2 (2002), 66

[67] D. Godlinski, M. Kuntz, G. Grathwohl; J. Am. Ceram. Soc. 85, 10 (2002), 2449

[68] J. Kim, Y. C. Choi, K. S. Chang, S. D. Bu; Nanotechnology 17, 28 (2006) 355

[69] K. S. Mazdiyasni; Fiber Reinforced Ceramic Composites, Noyes Publications (1990)

[70] J. Soro, A. Smith, C. Gault; J. Eur. Ceram. Soc. 27, 2 (2007), 1469

[71] F. T. Wallenberger, N. E. Weston, S. D. Brown; Mater. Lett. 11, 8 (1991), 229

[72] R. Gras, J. L. Duvail, T. Mine, M. Dubosc, P. Y. Tessier, L. Cagnon, P. Coronel, J. Torres; Microelec. Eng. 83, 11 (2006), 2432

[73] J. Zhang, Y. Huang, J. Lin, X. X. Ding, C. Tang, S. R. Qi; J. Solid State Chem. 178, 7 (2005), 2262

[74] A. Jagminas, J. Kuzmarskyte, L. Malferrari, M. Cuffiani; Mater. Lett. 61, 14 (2007), 2896

[75] B. C. Satishkumar, A. Govindaraj, E. M. Vogl, L. Basumallick, C. N. R. Rao; J. Mater. Res. 12, 3 (1997), 604

[76] Y. Zhang, J. Liu, R. He, Q. Zhang, X. Zhang, J. Zhu; Chem. Phys. Lett. 360, 5 (2002), 579

[77] N. Che, D. W. Readey, J. J. Moore; Ceram. Eng. Sci. Proc. 77 (1994), 170

[78] V. Valcàrcel, A. Souto, F. Guitiàn; Adv. Mater. 10, 2 (1998), 138

[79] C. C. Tang, S. S. Fan, P. Li, M. L. Chapelle, H. Y. Dang; J. Cryst. Growth 224, 1 (2001), 117

[80] J. Zhou, S. Z. Deng, J. Chen, J. C. She, N. S. Xu; Chem. Phys. Lett. 365, 5 (2002), 505

[81] X. S. Peng, L. D. Zhang, G. W. Meng, X. F. Wang, Y. W. Wang, C. Z. Wang, G. S. Wu; J. Phys. Chem. B 106, 43 (2002), 11163

[82] X. S. Fang, C. H. Ye, X. X. Xu, T. Xie, Y. C. Wu, L. D. Zhang; J. Phys.: Condens. Matter 16, 23 (2004), 4157

[83] Q. Zhao, X. Xu, H. Zhang, Y. Chen, J. Xu, D. Yu; Appl. Phys. A 79, 7 (2004), 1721

[84] Z. Wang, Q. Zhao, Y. Zhang, B. Xiang, D. P. Yu; Eur. Phys. J. D 34, 1 (2005), 303

[85] M. Zhao, X. L. Chen, X. N. Zhang, H. Li, H. Q. Li, L. Wu; Chem. Phys. Lett. 388, 1 (2004), 7

[86] J. Proost, S. Van Boxelb; J. Mater. Chem. 14 (2004), 3058

[87] G. Gundiah, F. L. Deepak, A. Govindaraj, C. N. R. Rao; Topics in Cataly. 24, 1 (2003), 137

[88] C. Ma, Y. Berta, Z. L. Wang, Solid State Commun. 129, 10 (2004), 681

[89] O. Vazquez-Mena, G. Villanueva, V. Savu, J. Brugger; Microelectronics Engineering, 85, 5 (2008), 1237

[90] Y. Ekinci, H. H. Solak, J. F. Löffler; Int. Symp. Optomech. Tech., SPIE Proceed. 19 (2007), 6717

[91] S. K. Park, J. S. Noh, W. B. Chin, D. D. Sung; Current Applied Physics 7, 2 (2007), 180

[92] P. M. Hamrick; Simulation of the Concentration Field During Physical Vapor Deposition onto a Nanofiber Substrate, Master Thesis, University of Akron (2006)

[93] H. J. Chen, Y. Y. Chen, C. H. Hsieh, S. J. Lin, L. J. Chou, W. Kuang; Appl. Phys. Lett. 90 (2007), 023111

[94] T. W. Odom, J. L. Huang, C. M. Lieber; J. Phys.: Condens. Matter 14, 6 (2002), 145

[95] K. Kim, T. B. Norris, S. Ghosh, J. Singh, P. Bhattacharya; Appl. Phys. Lett. 82 (2003), 1959

[96] M. S. Dresselhaus, Y. M. Lin, O. Rabin, M. R. Black, G. Dresselhaus; Mater. Sci. Eng. C 23, 1 (2003), 129

[97] D. A. Wharam, T. J. Thorton, R. Newbury, M. Repper, H. Ahmed, J. E. F. Frost, D. G. Hasko, D. C. Peacock, D. A. Ritchie, G. A. C. Jones; J. Phys. C: Solid State Phys. 21 (1998), 209

[98] Y. Li, F. Qian, J. Xiang, C. M. Lieber; Mater. Today 9, 10 (2006), 18

[99] P. Basudev, S. K. Batabyal, J. P. Amlan; Appl. Phys. Lett. 89 (2006), 233109

[100] D. Atkinson, D. S. Eastwood, L. K. Bogart; Appl. Phys. Lett. 91 (2007), 133119

[101] C. Liang, K. Terabe, T. Hasegawa, M. Aono; Nanotechnology 18, 48 (2007), 485202

[102] C. P. T. Svensson, T. Mårtensson, J. Trägårdh, C. Larsson, M. Rask, D. Hessman, L. Samuelson, J. Ohlsson; Nanotechnology 19, 30 (2008), 305201

[103] K. D. Buddharaju, N. Singh, S. C. Rustagi, S. H. G. Teo, G. Q. Lo, N. Balasubramanian, D. L. Kwong; Solid State Electron. 52, 9 (2008), 1312

[104] T. Makita, K. Doi, K. Nakamura, A. Tachibana; J. Chem. Phys. 119, 1 (2003), 538

[105] D. W. Bushmire; IEEE Reliab. Phys. (1976), 55

[106] T. Wada, M. Sugimoto, T. Ajiki; Reliability, IEEE Transactions on 38, 5-1 (1989), 565

[107] T. A. Palomaki, S. K. Dutta, H. Paik, H. Xu, J. Matthews, R. M. Lewis, R. C. Ramos, K. Mitra, P. R. Johnson, F. W. Strauch, A. J. Dragt, C. J. Lobb, J. R. Anderson, F. C. Wellstood; Phys. Rev. B 73 (2006), 014520

[108] M. T. Tuominen, J. M. Hergenrother, T. S. Tighe, M. Tinkham; IEEE Trans. Appl. Supercond. 3, 1 (1975)

[109] J. W. Lee, J. H. Lee, B. S. Kim, S. W. Hwang, D. Whang; Mater. Res. Soc. Symp. Proc. 1080 (2008)

[110] U. Kreibg, M. Vollmer; Optical Properties of Metal Clusters (1995)

[111] H. Tamada, T. Doumuki, T. Yamaguchi, S. Matsumoto; Opt. Lett. 22, 6 (1997), 419

[112] J. J. Wang, L. Chen, X. Liu, P. Sciortino, F. Liu, F. Walters, X. Deng; Appl. Phys. Lett. 89, 14 (2006), 141105

[113] Y. Ekinci, H. H. Solak, C. David, H. Sigg; Optics Express 14, 6 (2006), 2323

[114] J. C. Johnson, H. Yan, R. D. Schaller, P. B. Petersen, P. Yang, R. J. Saykally; Nano Letters 2 ,4 (2002), 279

[115] H. Yamada, M. Shirane, T. Chu, H. Yokoyama, S. Ishida, Y. Arakawa; Jpn. J. Appl. Phys. 44 (2005), 6541

[116] E. Tutuc, J. Appenzeller, M. C. Reuter, S. Guha; Nano letters 6, 9 (2006), 2070

[117] X. Duan, Y. Huang, Y. Cui, J. Wang, C. M. Lieber; Nature 409, 66 (2001)

[118] M. H. Huang, S. Mao, H. Feick, H. Yan, Y. Wu, H. Kind, E. Weber, R. Russo, P. Yang; Science 292, 5523 (2001), 1897

[119] T. Thurn-Albrecht, J. Schotter, G. A. Kästle, N. Emley, T. Shibauchi, L. Krusin-Elbaum, K. Guarini, C. T. Black, M. T. Tuominen, T. P. Russell; Science 290, 5499 (2000), 2126

[120] N. Elfström, J. Linnros; J. Phys: Conf. Ser.100, 5 (2008), 052042

[121] F. Patolsky, G. F. Zheng, O. Hayden, M. Lakadamyali, X. W. Zhuang, C. M. Lieber; Proc. Natl. Acad Sci. 101, 39 (2004), 14017

[122] M. Veith; Z. Phys. Chem. 222 (2008), 287

[123] M. Veith, S. Faber, R. Hempelmann, S. Janssen, J. Prewo, H. Eckerlebe; J. Mater. Sci. 31 (1996), 2009

[124] M. Veith, S. J. Kneip, S. Faber, E. Fritscher; Mater. Sci. Forum 269 (1998), 303

[125] M. Veith, K. Andres; J. Metastable and Nanocrystalline Materials 15 (2003), 279

[126] M. Veith, K. Andres, S. Faber , J. Blin, M. Zimmer, Y. Wolf, H. Schnöckel, R. Köppe, R. de Masi, S. Hüfner; Eur. J. Inorg. Chem. (2003), 4387

[127] Y. Wolf; Neue Festkörper-Phasengemische im ternären System, Wasserstoff-Aluminium-Sauerstoff, Dissertation, Universität des Saarlandes (2005)

[128] C. Petersen; Mikro- und nanostrukturierte Schichten mittels Gasphasenabscheidung von $(H_2AlO^tBu)_2$ für den Einsatz in der Nanobiotechnologie (2007)

[129] E. Sow; Dissertation, Universität des Saarlandes (2008)

[130] M. Veith, S. Faber, H. Wolfganger, V. Huch; Chem. Ber. 129 (1996), 381

[131] R. Haimbaugh; Practical Induction Heat Treating, ASM International (2001)

[132] H.-A. Yang, C.-W. Lin, C.-Y. Peng, W. Fang; J. Micromech. Microeng. 16 (2006), 1314

[133] S. Semancik, R. Cavicchia; Chem. Res. 31 (1998), 279

[134] V. Rudnev, D. Lovelss, R. Cook, M. Black, Handbook of Induction Heating, CRC Press (2002)

[135] S. Kimura, C. Munakata; Opt. Lett. 12 (1987), 552

[136] C. T. Forwood, L. M. Clarebrough; Electron Microscopy of Interfaces in Metals and Alloys, Institute of Physics Puplishing (1991)

[137] C. Rentenberger, T. Waitz, H. P. Karnthaler, Mater. Sci. Eng. A 462, 1 (2007), 283

[138] Y. Q. Wang, R. Smirani, G. G. Ross, F. Schiettekatte; Phys. Rev. B 71 (2005), 161310

[139] M. Veith, C. Petersen, E. Sow; Patent DE10 2006 013 (2006)

[140] E. J. Davies; Conduction and Induction Heating, IEE Power Engineering Series III (1989)

[141] C. Pacholski, A. Kornowski, H. Weller; Angew. Chem. 41, 7 (2002), 1188

[142] A. E. Paladino, R. L. Coble; J. Am. Ceram. Soc. 46, 3 (2006), 133

[143] Q. S. Mei, K. Lu; Progress in Materials Science 52, 8 (2007), 1175

[144] D. Bäurle; Chemical Processing with Lasers, Springer-Verlag (1986)

[145] D. Bäurle; Laser Processing and Chemistry, Springer-Verlag (2000)

[146] G. A. Abrams, S. L. Goodman, P. F. Nealey, M. Franco, C. G. Murphy; Cell Tissue Res. 39 (2000), 299

[147] S. P. Harimkara, N. B. Dahotre; Materials Characterization 5, 9 (2008), 700

[148] R. J. Dmani, P. Kakrocy; J. Eur. Ceram. Soc. 20 (2000), 867

[149] J. F. Li, L. Li, F. H. Stott; Acta Mater. 52 (2004), 4385

[150] J. W. Barlow, N. K. Vail; US Patent 6,048,954 (1997)

[151] U. Lakshminarayan, H. L. Marcus; Proceedings of the Solid Freeform Fabrication Symposium, Texas-Austin (1991), 205

[152] P. K. Subramanian, H. L. Marcus; Mater. Manuf. Processes 10, 4 (1995), 689

[153] M. Allmen, A. Blatter; Laser-Beam Interactions with Materials, Physical Principles and Applications Series: Springer Series in Materials Science (1995, Auflage 2)

[154] H. Kogelnik, T. Li; Appl. Phys. 5,10 (1996), 1550

[155] W. M. Steen; Laser Material Processing, Springer (2003)

[156] R. C. Crafer, P. J. Oakley; Laser Processing in Manifacturing, Chapmann and Hall (1993)

[157] M. Davist, P. Kapadiat, J. Dowden,W. M. Steen, C. H. G. Courtney; J. Phys. D: Appl. Phys. 19 (1986), 1981

[158] C. Wei, D. Deng, G. Tian, H. He, J. Shao, Z. Fan; Int. J. Light Electron Optics 119, 13 (2008), 624

[159] T. M. Yue, K. J. Huang, H. C. Man; Surf. Eng. 23, 2 (2007), 142

[160] A. S. Korhonen, E. Harju; J. Mater. Eng. Perform. 9, 3 (2000), 302

[161] J. G. Heinrich, A. Gahler, J. Günster, M. Schmücker, J. Zhang, D. Jiang, M. Ruan; J. Mater. Sci. 42 (2007), 5307

[162] M. Jasim, R. D. Rawlings, D. R. F. West; J. Mater. Sci. 27 (1992), 3903

[163] H. Su, J. Zhang, J. Tian, L. Liu, H. Fu; J. Appl. Phys. 104 (2008), 023511

[164] D. Triantafyllidis, L. Li, F. H. Stott; Mater. Sci. Eng., A 390, 1 (2005), 271

[165] T. R. Jervis, M. Nastasi, A. J. J. Griffin, T. G. Zocco, T. N. Taylor, S. R. Foltyn; Surf. Coat. Technol. 89, 1 (1997), 158

[166] L. Hao, J. Lawrence; J. Mater. Sci. - Mater. Med. 18, 5 (2007), 807

[167] J. Qi, K. L. Wang, Y. M. Zhu; J. Mater. Process. Technol. 139, 1 (2003), 273

[168] N. H. Rizvi, P. Apte; J. Mater. Process. Technol. 127, 2 (2002), 206

[169] C. S. Lim, M. H. Hong, Y. Lin, G. X. Chen, A. S. Kumar, M. Rahman, L. S. Tan, G. C. Lim; J. Mater. Process. Technol. 192 (2007), 328

[170] D. J. Hwang, A. Chimmalgi, C. P. Grigoropoulos; J. Appl. Phys. 99 (2006), 044905

[171] D. Bäuerle; Laser Processing and Chemistry: Recent Developments, Applied Surface Science 186 (2002), 1

[172] V. Yordanova, K. Starbova, W. Hintz, J. Tomas, U. Wendt; J. Optoelectron. Adv. Mater. 7, 5 (2005), 2601

[173] H. J. Lee, R. K. Prud'homme et al.; J. Mater. Res. 16, 12 (2001), 3536

[174] R. Ruizpalacios; Laser direct-write of optical components prepared using the sol-gel process, Dissertation, University of Austin, Texas (2004)

[175] V. G. Gregson; Laser Heta Treatment Procesing, North-Holland (1984)

[176] L. Miaja-Avila, C. Lei, M. Aeschlimann, J. L. Gland, M. M. Murnane, H. C. Kapteyn, G. Saathoff; Phys. Rev. Lett. 97, 11 (2006), 113604

[177] A. P. Horsfield, D. R. Bowler, H. Ness, C. G. Sánchez, T. N. Todorov, A. J. Fisher; Rep. Prog. Phys. 69, 4 (2006), 1195

[178] M. S. Anderson; Appl. Phys. Lett. 87 (2005), 144102

[179] F. E. Pfefferkorn, F. P. Incropera, Y. C. Shin; Int. J. Heat Mass Transfer 48, 10 (2005), 1999

[180] J. Mazumder; Laser Heat Treatment: The State of the Art, J. Met. 35, 5 (1983), 18

[181] I. W. Boyd; Laser Processing of Thin Films and Microstrutures, Springer-Verlag (1987)

[182] K. A. Nowakowski; Laser beam interaction with materials for microscale applications, Dissertation,Worcester Polytechnic Institute (2005)

[183] J. D. Majdumar, I. Manna; Sadhana 28, 3 (2003), 495

[184] W. M. Steen, C. Courtney; Metal. Technol. 6, 12 (1979), 456

[185] R. H. Bube; Electrons in Solids, Academic Press (1988)

[186] P. Gianluca; Determination of the Structure of Gamma Alumina Using Empirical and First Principles Calculations combined with Supporting Experiments, Dissertation, Curtin University of Technology (2004)

[187] I. Levin, D. Brandon; J. Am. Ceram. Soc. 81, 8 (2005), 1995

[188] S. P. Harimkar; J. Appl. Phys. 100 (2006), 024901

[189] A. Larsson, M. Halvarsson, S. Ruppi; Surf. Coat. Technol. 111 (1999), 191

[190] K. Nishio, M. Neo, H. Akiyama, Y. Okada, T. Kokubo, T. Nakamura; J. Biomed. Mater. Res. 55, 2 (2001), 164

[191] H.-C. Kao, W.-C. Wei; J. Am. Ceram. Soc. 83, 2 (2000), 362

[192] T. Hübert, S. Svoboda, B. Oertel; Surf. Coat. Technol. 201 (2006), 487

[193] W. D Kingery, H. K. Bowen, D. R. Uhlmann; Introduction to Ceramics, John Wiley and Sons, New Yowrk (1976)

[194] P. S. Santos, H. S. Santos, S. P. Toledo; Materials Research 3, 4 (2000), 104

[195] Y. Wu, K.-L. Choy; Surf. Coat. Technol. 180 (2004), 436

[196] Zhaoxia Bi; Journal of Cryst. Growth 300, 1 (2007), 123

[197] H. O. Pierson; Handbook of Chemical Vapor Deposition, Noyes Publications (1999)

[198] J. L. Zilko; Handbook of Thin-Film Deposition Processes and Techniques, Noyes Publications, Park Ridge, NJ (1988)

[199] D. A. Glocker, S. I. Shah; Handbook of Thin Film Process Technology, IOP Publishing Ltd., Bristol (1995)

[200] J. S. Kim, H. A. Marzouk, P. J. Reucroft, J. D. Robertson, C. E. Hamrin Jr.; Thin Solid Films 230 (1993), 156

[201] W. Koh, S.-J. Ku, Y. Kim; Thin Solid Films 304 (1997), 222

[202] T. W. Kim, S. S. Yom, W. N. Kang et al.; Appl. Surf. Sci. 65 (1993), 854

[203] A. Devi, S. A. Shivashankar, A. G. Samuelson; J. de Phys. IV, 12 (2002), 139

[204] M. P. Singh, S. A. Shivashankar; Surf. Coat. Technol. 161 (2002), 135

[205] S. Blittersdorf, N. Bahlawane, K. Kohse-Höinghaus, B. Atakan, J. Müller; Chemical Vapor Depoisition 9, 4 (2003), 194

[206] K. L. Choy; Prog. Mater Sci. 48, 2 (2003), 57

[207] K.-H. Zum Gahr, J. Schneider; Ceram. Int. 26 (2000), 363

[208] L. Bradley, L. Li, F. H. Stott; Appl. Surf. Sci. 138 (1999), 233

[209] M. F. Modest; J. Laser Appl. 13 (2001), 111

[210] D. Triantafyllidis, L. Li, F. H. Stott; Appl. Surf. Sci. 186 (2002), 140

[211] J. A. Benda, A. Parasco; US Patent 6,007,764 (1999)

[212] J. W. Barlow, N. K. Vail; US Patent 6,048,954 (2000)

[213] H. Zheng, J. Zhang, S. Lu, G. Wang, Z. Xu; Mater. Lett. 60 (2006), 1219

[214] S. Liu, U. Fooken, C. M. Burba, M. A. Eastman, R. J. Wehmschulte; Chem. Mater. 15 (2003), 2803

[215] E. W. Fritscher; Chemical Vapor Deposition mit Silanen, Heterometallalkoxiden und Hydridoalkoxiden sowie Anwendungen, Dissertation, Universität des Saarlandes (1997)

[216] O. Seeger, S. Faber, M. Veith, E. Fritscher, M. Dausch, R. Schmid; US Patent 6,187,390 (2001)

[217] K. Andres; Umfassende Untersuchungen zur Oxoaluminiumhydridschicht ”HAlO” und zu Al/Al2O3 Kompositschichten, Dissertation, Universität des Saarlandes (2002)

[218] M. Veith, K. Andres, C. Petersen, C. Daniel, C. Holzapfel, F. Mücklich; Adv. Eng. Mater. 7, 1 (2005), 27

[219] J. Blin; Herstellung und Reaktivität von Hydridoaluminiumalkoxi- und siloxiverbindungen und Herstellung von Eisen-Zinn heterobimetallischen Komplexen, Dissertation,Universität des Saarlandes (1999)

[220] Z. Liu, Surface structuring with laser interference by high power pulsed UV-laser, Dissertation, Universität des Saarlandes (2002)

[221] Chety-Gimondo; Etude par ionisation laser couplee a la spetrometrie de masse de films minces d’hydrure d’oxoaluminium et d’oxoborate de gadolinium et de calcium, PhD Thesis, Universite de Metz (2002)

[222] C. Petersen, A. Lasagni, C. Holzapfel, C. Daniel, F. Mucklich, M. Veith; Appl. Surf. Sci. 253, 19 (2007), 8022

[223] N. He, W. Jia, M. Gong, L. Huang; Sens. Actuators, A 125, 2 (2006), 482

[224] J. Bartl, M. Baranek; Measurement Science Review 4, 3 (2004), 31

[225] V. Rosenband; Combustion and Flame 137 (2004), 366

[226] A. Biswas, O. C. Aktas, U. Schürmann, U. Saeed, V. Zaporojtchenko, F. Faupel; Appl. Phys. Lett. 84, 14 (2004), 2655

[227] A. Biswas, O. C. Aktas, J. Kanzow, U. Saeed, T. Strunskus, V. Zaporojtchenko, F. Faupel; Mater. Lett. 58 (2004), 1530

[228] K. S. Lee, I. H. Kim, T. S. Lee, B. Cheong, J. G. Park, J. G. Ha, W. M. Kim; Surf. Coat. Technol. 198, 1 (2005), 51

[229] C. G. Granqvist; Adv. Mater. 15, 21 (2003), 1789

[230] V. Teixeira, E. Sousa, M. F. Costa, C. Nunes, L. Rosa, M. J. Carvalho, M. Collares-Pereira, E. Roman, J. Gago; Thin Solid Films 392 (2001), 320

[231] C. Sellla, A. Kaba, S. Berthier, J. Lafait; SPIE. Optical Materials Technology for Energy Efficiency and Solar Energy Conversion 653 (1986)

[232] J. A. Thornton, J. L. LAMB; Sol. Energy Mater. 9, 4 (1984), 415

[233] G. A. Niklasson, C. G. Granqvist; Mater. Sci. Solar Energy Conversion Syst. 4 (1991)

[234] C. Langhammer, M. Schwind, B. Kasemo, I. Zoric; Nano Lett. 8, 5 (2008), 1461

[235] H. A. Atwater, J. A. Dionne, L. A. Sweatlock; Subwavelenght-scale plasmon waveguides, Springer-Verlag (2007)

[236] M. Gadenne, V. Podolskiy, P. Gadenne, P. Sheng, V. M. Shalaev; Europhys. Lette. 53, 3 (2001), 364

[237] E. Anno, M. Tanimoto; Phys. Rev. B: Condens. Matter 64 (2001), 165407E

[238] G. L. Hornyak, K. L. N. Phani, D. L. Kunkel, V. P. Menon, C. R. Martin; Nanostruct. Mater. 6, 5 (1995), 839

[239] J. Liu, A. I. Maaroof, L. Wieczorek, M. B. Cortie; Advanced Materials Early View 17, 10 (2005), 1276

[240] V. A Podolskiy, A. K Sarychev, E. E. Narimanov, V. M. Shalaev; Journal of Optics A: Pure and Applied Optics 7, 2 (2005), 32

[241] S. M. Prokes, O. J. Glembocki, R. W. Rendell, M. G. Ancona; Appl. Phys. Lett. 90 (2007), 093105

[242] V. Shalev; Handbook of Nanostructured Materials and Nanotechnology, Academic Press (2002, Auflage 4)

[243] A. Rai, K. Park, L. Zhou, M. R. Zachariah; Combust. Theor. Model. 10, 5 (2006), 843

[244] S. C. Sanchez-Lopez, A. Fernandez, C. F. Conde, A. Conde, C. Morant, J. M. Sanz; Nanostructured Materials 7, 8 (1996), 813422

[245] Z. Yang, L. He, J. Chen, H. Cong, H. Ye; J. Mater. Res. 18, 2 (2003)

[246] M. A. Trunov, S. M. Umbrajkar, M. Schoenitz, J. T. Mang, E. L. Dreizin; J. Phys. Chem. 110 (2006), 13094

[247] V. I. Levitas, B. W. Asay, S. F. Son, M. L. Pantoya; (2006). Appl. Phys. Lett. 89 (2006), 071909-1

[248] V. Rosenband; Combust. Flame 137 (2004), 366

[249] T. Campbell, R. K. Kalia, A. Nakano, P. Vashishta, S. Ogata, S. Rodgers; Phys. Rev. Lett. 82 (1999), 4866

[250] G. A. Storaska, J. M. Howe; Mater. Sci. Eng., A 368, 1 (2004), 183

[251] T. Maruyama, M. Ichida; J. Mater. Sci. Lett. 19 (2000), 1833

[252] O. Boldus, S. Schreck, M. Rohde; J. Eur. Ceram. Soc. 24, 15 (2004), 3759

[253] T. A. Klar, E. Engel, S. W. Hell; Phys. Rev. E 64 (2001), 066613

[254] B. E. Warren; X-Ray Diffraction, Dover Publications, New York (1990)

[255] R. Krishnan, S. Dash, C. B. Rao, R. V. S. Rao, A. K. Tyagi, B. Raj; Scr. Mater. 45 (2001), 693

[256] A. Misra, H. D. Bist, M. S. Navati, R. K. Thareja, J. Narayan; Mater. Sci. Eng. B 79 (2001), 49

[257] S. P. Porto, R. S. Hrishnan; J. Chem. Phys. 47, 3 (1967), 1009

[258] R. Krishnan, R. Kesavamoorthy, S. Dash, A. K. Tyagi, B. Raj; Scr. Mater. 48 (2003), 1099

[259] V. Poborchii, T. Tada, T. Kanayama; J. Appl. Phys. 97 (2005), 104323

[260] D. Quéré; Annu. Rev. Mater. Res. 38 (2008), 71

[261] D. Triantafyllidis, L. Li, F. H. Stott; Thin Solid Films 453 (2004), 76

[262] A. Barnoush, H. Vehoff; Corros. Sci. 50 (2008), 259

[263] C. Lu, Y. W. Mai, P. L. Tam, Y. G. Shen; Philos. Mag. Lett. 87, 6 (2007), 409

[264] J. Li, K. Van Vliet, T. Zhu, S. Yip, S. Suresh; Nature 418 (2002), 307

[265] A. Krell, S. Schädlich; Int. J. Refract. Met. Hard Mater. 19 (2001), 237

[266] H. Li, S. Costil, V. Barnier, R. Oltra, O. Heintz, C. Coddet; Surf. Coat. Technol. 201 (2006), 1383

[267] A. Y. Vorobyev, C. Guo; Appl. Surf. Sci. 253 (2007), 7272

[268] A. Ravaglioli, A. Krajewski; Biomaterials, Chapman and Hall, London (1992)

[269] E. E. L. Swan, K. C. Popat, C. A. Grimes, T. A. Desai; J. Biomed. Mater. Res. A 72, 3 (2005), 288

[270] P. Boutin., P. Christel, J. M. Dorlot, A. Meunier, A. Roquancourt, D. Blanquaert, S. Herman, L. Sedel, J. Witvoet; J. Biomed. Mater. Res. 22 (1988), 1203

[271] G. Balasundarama, T. J. Webster; J. Mater. Chem. 16 (2006), 3737

[272] R. L. Price, K. M. Haberstroh, T. J. Webster; Med. Biol. Eng. Comput. 41 (2003), 372

[273] J. Vitte, A. M. Benoliel; A. Pierres, P. Bongrand; Eur. Cell. Mater. 7 (2004), 52

[274] R. G. Flemming, C. J. Abrams, S. L. Goodman, P. F. Nealey; Biomaterials 20 (1999), 573

[275] A. Blau; Interactions between Biological and Non-Biological Devices, University of Kaiserslautern, Gradaute Course (2007)

[276] M. C. Beckerle; Cell Adhesion 39 (2001), New York, Oxford University Press

[277] A. Garcia, D. Boettiger; Biomaterials 20 (1999), 2427

[278] I. Yoshihiro; Biomaterials 20 (1999), 2333

[279] R. G. Harrison; Science 34 (1911), 279

[280] A. M. Rajnicek, S. T. Britland, C. D. McCaig; J. Cell Sci. 7, 110 (1997), 2905

[281] A. Curtis, C. Wilkinson; Biomaterials 18 (1997), 1573

[282] R. Singhvi, G. Stephanopoulos, D. I. C. Wang; Biotechnol. Bioeng. Mater. 43 (1994), 764

[283] S. Y. Chou, P. R. Krauss, P. J. Renstrom; Appl. Phys. Lett. 67 (1995), 3114

[284] F. M. Watt; Trends Biochem. Sci. 11 (1986), 482

[285] D. L. Wise, D. J. Trantolo, D. E. Altobelli, M. J. Yaszemski, J. D. Gresser; Human Biomaterials Applications, Humana Press, Totowa, New Jersey (1996)

[286] C. C. Berndt, G. N. Haddadt, A. J. D. Farmer, K. A. Gross; Mater. Forum 14 (1990), 161

[287] T. J. Webster, R. W. Siegel, R. Bizios; Scr. Mater. 44 (2001), 1639

[288] M. Karlsson, E. Palsgard , P. R. Willshaw, L. Di Silvio; Biomaterials 24 (2003), 3039

[289] T. J. Webster, R. W. Siegel, R. Bizios; Biomaterials 20 (1999), 1221

[290] E. E. Swan, K. C. Popat,T. A. Desai; Biomaterials 26, 14 (2005), 1969

[291] K. C. Popat; Biomaterials 26, 22 (2005), 4516

[292] E. M. Christenson, K. S. Anseth, J. J. J. P. van den Beucken, C. K. Chan, B. Ercan, J. A. Jansen, C. T. Laurencin, W.-J. Li, R. Murugan, L. S. Nair, S. Ramakrishna, R. S. Tuan, T. J. Webster, A. G. Mikos; J. Orthopaed. Res. 25, 1 (2007), 11

[293] T. J. Webster, L. S. Schalder, R. W. Siegel, R. Bizios; Mat. Res. Soc. Symp. Proc. 662 (2001)

[294] T. J.Webster, E. L.Hellenmeyer, R. L.Price; Biomaterials 26 (2005), 953

[295] T. J. Webster, L. G. Gutwein, F. Tepper; 26th Annu. Conf. Compos., Adv. Ceram., Mater. Struct. B: Ceram. Eng. Sci. Proceed. 23, 4

[296] J. R. Venugopal, S. Low, A. T. Choon, A. B. Kumar, S. Ramakrishna; J. Biomed. Mater. Res. Part A 85A, 2 (2007), 408

[297] X. M. Mo, C.Y. Xu, M. Kotaki, S. Ramakrishna; Biomaterials 25 (2004) 1883

[298] N. Bhattarai, D. Edmondson, O. Veiseh, F. A. Matsen, M. Zhang; Biomaterials 26, 31 (2005), 6176

[299] K. H. Kim; J. Biotechnol. 120 (2005), 327

[300] I. K. Kwon, S. Kldoki, T. Matsuda; Biomaterials 26 (2005), 3929

[301] S. R. Bhattarai, N. Bhattarai, P. Viswanathamurthi, H. K. Yi, P. H. Hwang, H. Y. Kim; J. Biomed. Mater. Res. A 78A, 2 (2006), 247

[302] Y. Zhang, C. T. Lim, S. Ramakrishna, Z. M. Huang; J. Mater. Sci. Mater. Med. 16 (2005), 933

[303] K. Tuzlakoglu; J. Sci. Mater. in Med. 16 (2005), 1099

[304] T. J Webster, M. C Waid, J. L McKenzie, R. L Price, J. U Ejiofor; Nanotechnology 15 (2004), 48

[305] L. Lacerdaa, S. Raffab, M. Pratoc, A. Biancod, K. Kostarelosa; nanotoday 2, 6 (2007)

[306] M. Bottini, S. Bruckner, K. Nika, N. Bottini, S. Bellucci, A. Magrini, A. Bergamaschi, T. Mustelin; Toxicol. Lett. 160, 2 (2006), 121

[307] S. Turner, L. Kam, M. Isaacson, H. G. Craighead, W. Shain, J. Turner; J. Vac. Sci. Technol. B 15 (1997), 2848

[308] K. B. Lee, S. J. Park, C. A. Mirkin, J. C. Smith, M. Mrksich; Science 295 (2002), 1702

[309] A. S. G. Curtis, N. Gadegaard, M. J. Dalby, M. O. Riehle, C. D. W. Wilkinson, G. Aitchison; IEEE Trans. Nanobios. 3 (2004), 61

[310] A. V. Sapelkin, S. C. Bayliss, B. Unal, A. Charalambou; Biomaterials 27 (2006), 842

[311] N. W. Karuri, S. Liliensiek, A. I. Teixeira, G. Abrams, S. Campbell, P. F. Nealey, C. J. Murphy; J. Cell Sci. 117 (2004), 3153

[312] L. Zanello, B. Zhao, H. Hu, R. C. Haddon; Nano Lett. 6 (2006), 562

[313] D. C. Miller, A. Thapa, K. M. Haberstroh, T. J. Webster; Biomaterials 25 (2004), 53

[314] X. F. Walboomers, J. A. Jansen; Odontology 89 (2001), 2

[315] K. E. Gonsalves, C. R. Halberstadt, C. T. Laurencin, L. S. Nair; Biomedical Nanostructures, Wiley-Interscience (2008)

[316] M. T. Eliason; Combined micro and nanopatterning for cell substrates, M.Sc. Thesis, Georgia Institute of Technology (2007)

[317] J. L. Charest, M. T. Eliason, A. J. Garcia, W. P. King, A. A. Talin, B. A. Simmons; J. Vac. Sci. Technol., B 23, 6 (2005), 3011

[318] CellPROM Project, internal meeting, presentation (2004)

[319] CellPROM Project, internal meeting, presentation (2005)

[320] R. Bizios; Mater. Res. Soc. Symp. Proc. 845 (2005)

[321] A. Curtis; Tutorial on the biology of nanotopography NanoBioscience, IEEE Transactions 3, 4 (2004), 293

[322] W. Metzger, N. Grenner, S. E. Motsch, R. Strehlow, T. Pohlemann, M. Oberringer; Tissue Eng. 13, 11 (2007), 2751

[323] The Qiagen Transfection Book, 2. Edition (2007)

[324] T. M. Svitkina, E. A. Bulanova, O. Y. Chaga, D. M. Vignjevic, S.-I. Kojima, J. M. Vasiliev, G. G. Borisy; J. Cell Biol. 160 (2003), 409

[325] P. K. Mattila, P. Lappalainen; Nat. Rev. Mol. Cell Biol. 9 (2008), 446

[326] G. A. Silva; Nat. Rev. Neurosci. 7 (2006)

[327] U. Schroeder, P. Sommerfeld, S. Ulrich, B. A. Sabel; J. Pharm. Sci. 87 (1998), 1305

[328] F. Yang, R. Murugan, S. Ramakrishna, X. Wang, Y. X. Ma, S. Wang; Biomaterials 25, 10 (2004), 1891

[329] D. H. Kim, M. Abidian, D. C. Martin; J. Biomed. Mater. Res. A 71 (2004), 577

[330] J. S. Wegman, A. Dwarka, M. Holzer, W.-K. Lye, M. L. Reed, E. Herzog, T. N. Blalock; Mat. Res. Soc. Symp. Proc. 773 (2003)

[331] M. C. Lieber Y. Li, J. Xiang; Mater. Today 9, 10 (2006), 18

[332] T. E. McKnight, A. V. Melechko, G. D. Griffin, M. A. Guillorn, V. I. Merkulov, F. Serna, D. K. Hensley, M. J. Doktycz; Nanotechnology 14 (2003), 551

[333] W. Hällström, T. Martensson, C. Prinz, P. Gustavsson, L. Motelius, L. Samuelson, M. Kanje; Nanoletters 7, 10 (2007), 2960